



The Effects of Ionizing Radiation on Microelectromechanical Systems  
(MEMS) Actuators: Electrostatic, Electrothermal, and  
Residual Stress

THESIS  
Jared R. Caffey  
2d Lt, USAF

AFIT/GE/ENG/03M-05

DEPARTMENT OF THE AIR FORCE  
AIR UNIVERSITY

**AIR FORCE INSTITUTE OF TECHNOLOGY**

Wright-Patterson Air Force Base, Ohio

Approved for public release; distribution unlimited.

The views expressed in this thesis are those of the author and do not reflect the official policy or position of the United States Air Force, the United States Department of Defense or the United States Government.

AFIT/GE/ENG/03M-05

The Effects of Ionizing Radiation on Microelectromechanical Systems  
(MEMS) Actuators: Electrostatic, Electrothermal, and  
Residual Stress

THESIS

Presented to the Faculty of the Graduate School of Engineering and Management  
of the Air Force Institute of Technology  
Air University  
In Partial Fulfillment of the  
Requirements for the Degree of  
Master of Science in Electrical Engineering

Jared R. Caffey, B.S.E.E.  
2d Lt, USAF

25 March 2003

Approved for public release; distribution unlimited.


The Effects of Ionizing Radiation on Microelectromechanical Systems  
(MEMS) Actuators: Electrostatic, Electrothermal, and  
Residual Stress

THESIS

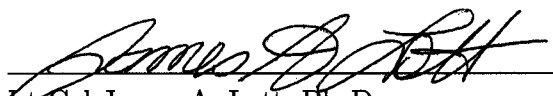
Jared R. Caffey, B.S.E.E.

2d Lt, USAF

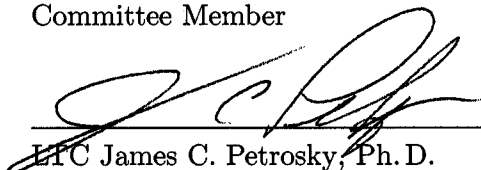
Approved:

  
Capt Paul E. Kladitis, Ph. D.  
Assistant Professor of Electrical Engineering  
Thesis Advisor

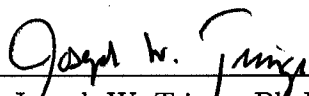
13 MAR 03  
Date

  
Lt Col James A. Lott, Ph. D.  
Professor of Electrical Engineering  
Committee Member

05 MARCH 2003  
Date

  
LTC James C. Petrosky, Ph. D.  
Assistant Professor of Nuclear Engineering  
Committee Member

05 MAR 03  
Date

  
Capt Joseph W. Tringe, Ph. D.  
Air Force Research Laboratory  
Committee Member

5 Mar 03  
Date



## *Acknowledgements*

I am forever grateful to my family, friends, instructors, and “lab-mates” for their help and support during my time at AFIT. I wish to also thank my committee members, Capt. Kladitis, Lt Col Lott, LTC Petrosky and Capt. Tringe for their added wisdom and guidance. A special thanks to LTC Petrosky for providing a firm background in the area of radiation effects. His patience and teaching philosophy made delving into the unfamiliar topic an extremely pleasant experience.

I am indebted to the sponsors who supported my research effort: AFIT Cooperative Research and Development Agreement Funds, New Faculty Startup Program ENR Proposal # 2002-025; and the Air Force Research Laboratory, Space Vehicles Directorate, Space Electronics and Protection Branch (AFRL/VSSE).

I am, also, indebted to the laboratory technicians, both at AFIT and AFRL/SN, for their valuable time and knowledge. Rick Patton and Bill Trop were instrumental in maintaining and instructing on the use of equipment located in the AFIT MEMS Test Laboratory and the AFIT Clean Room. A special thanks to Larry Callahan (AFRL/SNDD) for the time he spent wire-bonding all my actuators, Kevin Leedy (AFRL/SNDI) for time spent operating the interferometric microscope, and Dave Via for time spent operating the scanning electron microscope.

Most of all, I offer my thanks to my wife and son, for their love, support, understanding, patience and prayers during this 18 month process.

## *Table of Contents*

	Page
Acknowledgements . . . . .	iv
List of Figures . . . . .	x
List of Tables . . . . .	xviii
List of Abbreviations . . . . .	xxi
Abstract . . . . .	xxiii
 I. Introduction . . . . .	 1-1
1.1 Motivation . . . . .	1-1
1.1.1 Applications of MEMS Devices in Radiation En- vironments . . . . .	 1-2
1.1.2 Scientific Merit . . . . .	1-2
1.1.3 Scientific Contributions . . . . .	1-2
1.2 Problem Statement . . . . .	1-3
1.2.1 Accomplishments . . . . .	1-3
1.3 Thesis Scope and Approach . . . . .	1-3
1.4 Main Results . . . . .	1-4
1.5 Thesis Overview . . . . .	1-5
 Bibliography . . . . .	 1-7
 II. Background . . . . .	 2-1
2.1 Radiation Environments . . . . .	2-1
2.1.1 Space . . . . .	2-1
2.1.2 Nuclear Weapons . . . . .	2-4

	Page
2.1.3 Nuclear Reactors . . . . .	2-5
2.2 Radiation Measurement . . . . .	2-6
2.3 Interaction of Radiation with Solid Materials . . . . .	2-6
2.3.1 Photon Interactions . . . . .	2-7
2.3.2 Charged Particle Interactions . . . . .	2-8
2.3.3 Neutron Interactions . . . . .	2-9
2.4 Effects of Radiation on Semiconductor Materials . . . . .	2-9
2.4.1 Ionizing Radiation Effects . . . . .	2-10
2.4.2 Displacement Effects . . . . .	2-11
2.5 Microelectromechanical Systems . . . . .	2-13
2.5.1 MEMS Fabrication Techniques . . . . .	2-14
2.5.2 Electrostatic Piston Actuator . . . . .	2-17
2.5.3 Electrothermal Actuator . . . . .	2-18
2.5.4 Residual-Stress Cantilever . . . . .	2-19
2.6 Previous Radiation Testing of MEMS Devices . . . . .	2-19
2.6.1 MEMS Comb-drives . . . . .	2-20
2.6.2 Micro-engines . . . . .	2-27
2.6.3 Electrothermal Actuators . . . . .	2-30
2.6.4 Summary of MEMS Radiation Testing . . . . .	2-31
2.7 Conclusions . . . . .	2-31
Bibliography . . . . .	2-33
III. Device Design . . . . .	3-1
3.1 Designing . . . . .	3-1
3.2 MUMPs® Fabrication process . . . . .	3-1
3.3 Design of Test Actuators . . . . .	3-5
3.3.1 Electrostatic Piston Actuator Design . . . . .	3-5

	Page
3.3.2 Electrothermal Actuator Design . . . . .	3-9
3.3.3 Residual Stress Cantilever Design . . . . .	3-13
3.4 Conclusions . . . . .	3-15
Bibliography . . . . .	3-16
IV. Analytical Models . . . . .	4-1
4.1 Electrostatic piston actuator . . . . .	4-1
4.2 Electrothermal actuator . . . . .	4-8
4.3 Residual stress cantilever . . . . .	4-13
4.4 Conclusions . . . . .	4-18
Bibliography . . . . .	4-19
V. Experimental Setup . . . . .	5-1
5.1 Image Capture . . . . .	5-1
5.2 Test Equipment . . . . .	5-3
5.2.1 Measurement Equipment . . . . .	5-3
5.2.2 Connection Boxes . . . . .	5-4
5.3 Radiation Sources . . . . .	5-4
5.3.1 Cobalt 60 Gamma Source . . . . .	5-6
5.3.2 Low Energy X-ray Source . . . . .	5-9
5.4 Post-processing of MUMPs® Die . . . . .	5-11
5.4.1 Packaging Process . . . . .	5-12
5.4.2 Release Process . . . . .	5-12
5.4.3 Wire Bonding Process . . . . .	5-16
5.4.4 Sealing Process . . . . .	5-17
5.5 Device Characterization . . . . .	5-18
5.5.1 Electrostatic Piston Actuator . . . . .	5-18

	Page
5.5.2 Electrothermal Actuator . . . . .	5-26
5.5.3 Residual stress cantilever . . . . .	5-32
5.6 Conclusions . . . . .	5-34
VI. Results and Analysis . . . . .	6-1
6.1 Characterization of Electro-static Piston Actuator . . .	6-1
6.1.1 Comparison of Analytical Model and Experimental Measurements . . . . .	6-1
6.1.2 Characterization of Electrostatic Piston Actuator Subjected to Low Energy X-rays . . . . .	6-5
6.1.3 Characterization of Electrostatic Piston Actuator Subjected to Gamma rays . . . . .	6-18
6.2 Characterization of Electrothermal Actuator . . . . .	6-21
6.2.1 Comparison of Analytical Model and Experimental Measurements . . . . .	6-21
6.2.2 Characterization of Electrothermal Actuator Subjected to Low Energy X-rays . . . . .	6-22
6.2.3 Characterization of Electrothermal Actuator Subjected to Gamma rays . . . . .	6-31
6.3 Characterization of Residual Stress Cantilever . . . . .	6-36
6.3.1 Analytical Model Results . . . . .	6-36
6.3.2 Results for Residual Stress Cantilever irradiated with LEXR Source . . . . .	6-38
6.3.3 Results for Residual Stress Cantilever irradiated with Co-60 Gamma Source . . . . .	6-38
6.4 Conclusion . . . . .	6-39
Bibliography . . . . .	6-41

	Page
VII. Conclusions . . . . .	7-1
7.1 Actuator Characterization . . . . .	7-1
7.2 Contributions to Scientific Community . . . . .	7-2
7.3 Future Work . . . . .	7-3
7.3.1 Testing Actuators in Different Radiation Environments . . . . .	7-3
7.3.2 In-situ Characterization . . . . .	7-3
7.3.3 Quantify and Model Changes in Resistance Due to Joule Heating . . . . .	7-3
7.3.4 Redesign Electrostatic Actuator and Confirm Snap-down Behavior . . . . .	7-4
7.4 Conclusions . . . . .	7-4
Bibliography . . . . .	7-5
Appendix A. Matlab® Script for Modelling Electrostatic Piston Actuator . . . . .	A-1
Appendix B. Matlab® Script for Modelling Electrothermal Actuator . . . . .	B-1
Appendix C. Agilent VEE Pro Programs . . . . .	C-1
C.1 Agilent VEE Pro Program Used for Electrostatic Piston Actuator . . . . .	C-1
C.2 Agilent VEE Pro Program Used for Electrothermal Actuator . . . . .	C-4
Appendix D. PolyMUMPs Designs . . . . .	D-1
D.1 PolyMUMPs Run 48 Designs . . . . .	D-1
D.2 PolyMUMPs Run 49 Designs . . . . .	D-7
D.3 PolyMUMPs Run 51 Designs . . . . .	D-9
D.4 PolyMUMPs Run 52 Designs . . . . .	D-14
D.5 PolyMUMPs Run 53 Designs . . . . .	D-15

## *List of Figures*

Figure		Page
2.1.	Photon interaction probability as a function of photon energy and atomic number of target [10]. . . . .	2-8
2.2.	Illustration of the five effects of radiation induced defect centers in the forbidden energy band [11]. . . . .	2-12
2.3.	Linear rack assembly fabricated in the SUMMiT <sup>TM</sup> surface micromachining process [20]. . . . .	2-15
2.4.	Example bulk micromachined structure etched in a silicon substrate [21]. . . . .	2-15
2.5.	Various MEMS gears fabricated using the LIGA process [20].	2-16
2.6.	Illustration of electrostatic Piston actuator without bottom attracting plate. . . . .	2-17
2.7.	Illustration of horizontally deflection electrothermal actuator.	2-18
2.8.	Diagram of a comb-drive accelerometer detailing the moving (X) and the stationary (Y & Z) electrodes [32]. . . . .	2-21
2.9.	Cross-section view of a comb-drive based accelerometer detailing the movable (X) and stationary (Y & Z) electrodes for equilibrium and acceleration. The figure details the series capacitance of the three electrodes. . . . .	2-22
2.10.	Test results for ADXL50 for dose rate of $25 \frac{rad(Si)}{s}$ [31]. . . .	2-23
2.11.	Test results for whole device and sensor only irradiation [31].	2-24
2.12.	Typical comb-drive design. . . . .	2-28
2.13.	Frequency response of standard comb-drive for electron irradiation [33]. . . . .	2-29
2.14.	Frequency response of standard comb-drive for proton irradiation [33]. . . . .	2-29

Figure		Page
3.1.	L-edit layout (a) and scanning electron micrograph (b) of a 100 $\mu\text{m}$ square piston actuator connected to four residual stress cantilevers. . . . .	3-2
3.2.	Drawing of the different layers available in the MUMPs <sup>®</sup> process. The layer names, layer thicknesses, and mask names are given. . . . .	3-3
3.3.	Electric field orientation and direction of travel for radiation induced charges for (a) Positive bias and (b) Negative bias. The thickness of the individual layers are not drawn to scale. . .	3-7
3.4.	Electric field orientation, direction of travel for radiation induced charges and formation of interface traps for electrostatic piston actuator under snapdown biasing. . . . .	3-8
3.5.	(a) L-Edit layout (b) and scanning electron micrograph illustrating top view of the electrostatic piston actuator tested in this research. . . . .	3-10
3.6.	Isometric drawing of horizontally deflection electrothermal actuator detailing the dimension notation used in this research.	3-11
3.7.	(a) L-Edit layout, (b) scanning electron micrograph illustrating top view and (c) scanning electron micrograph illustrating isometric view of the horizontally deflection electrothermal actuator tested in this research. . . . .	3-12
3.8.	(a) L-Edit layout, (b) scanning electron micrograph looking straight down, and (c) scanning electron micrograph illustrating an isometric of 300 $\mu\text{m}$ by 20 $\mu\text{m}$ , residual stress cantilever tested in this research. . . . .	3-14
4.1.	Top and cross-sectional views of electrostatic piston actuator detailing the detailing the geometrical parameters used in deriving the analytical model. . . . .	4-2
4.2.	Illustration of s-shaped flexures used in the derivation of the analytical model for the electrostatic piston actuator. . . . .	4-4
4.3.	Schematic diagram of a cross-section of an electrostatic piston actuator with a sheet charge placed at the air-dielectric interface.	4-7



Figure		Page
4.4.	Top view of electrothermal actuator unwrapped along x axis and side view of actuator with elevation of actuator above substrate surface, $d$ , and actuator thickness, $t$ , labelled. . . . .	4-9
4.5.	Definition of variables used in the derivation of the analytical model used to calculate radius of curvature and tip deflection of a residual stress cantilever . . . . .	4-13
4.6.	Isometric view of cantilever used to derive analytical model.	4-14
5.1.	Photograph of Micromanipulator Probe Station, test equipment rack and video image processing cart. . . . .	5-2
5.2.	Photograph of International Scientific Instruments WB-6 scanning electron microscope during this research. . . . .	5-2
5.3.	Picture of test bed used to provide electrical connections to the test die during irradiation. Each of the fourteen leads are connected to one of the BNC connectors on the side of the box.	5-5
5.4.	Picture of splitter box built to facilitate electrical connections between the DUT and the measurement equipment. . . . .	5-5
5.5.	Cobalt decay scheme. . . . .	5-6
5.6.	Experimental setup used for irradiating devices with the Co-60 source. . . . .	5-7
5.7.	Picture of test bed mounted next to Co-60 source tube. . . .	5-8
5.8.	Picture of test equipment setup in Co-60 source building. . .	5-8
5.9.	Experimental setup used for irradiating devices with the LEXR source. . . . .	5-10
5.10.	Picture of the exterior of the LEXR source room. The LEXR control panel, test equipment and computer are positioned outside the room. . . . .	5-10
5.11.	Picture of X-ray tube, test bed and DUT inside the LEXR source room. . . . .	5-11
5.12.	(a) Illustration and leading particulars of ceramic package used in this research and (b) picture of MUMPs <sup>®</sup> die packaged in ceramic 14 pin DIP. . . . .	5-13

Figure		Page
5.13.	Picture of typical setup used to release packaged die in AFIT Class 10,000 Clean Room. . . . .	5-14
5.14.	Autosamdri <sup>®</sup> -815 CO <sub>2</sub> dryer. . . . .	5-15
5.15.	Picture of released, MUMPs <sup>®</sup> die mounted in well of 14 pin ceramic DIP and wire bonded to package bond pads. . . . .	5-16
5.16.	Picture of MUMPs <sup>®</sup> die mounted in 14 pin ceramic package and sealed with cellophane tape. . . . .	5-17
5.17.	Picture illustrating the electrical connection between the electrostatic piston actuator and the 100 $\mu$ m by 100 $\mu$ m bond pad, and the 100 $\mu$ m by 100 $\mu$ m substrate bond pad. . . . .	5-19
5.18.	(a) Illustration of L-Edit schematic detailing the wire bond connections. (b) Picture of MUMPs <sup>®</sup> Die, containing the electrostatic piston actuators, wire bonded to to 14 PIN ceramic DIP.	5-20
5.19.	Picture of 14 pin ceramic package, containing MUMPs <sup>®</sup> Die, mounted in the test bed. . . . .	5-21
5.20.	General test configuration used to measure capacitance-voltage relationship for electrostatic piston actuator. . . . .	5-21
5.21.	Electrical connections required to measure capacitance-voltage relationship for electrostatic piston actuator tested under positive and snapdown biasing configurations. . . . .	5-22
5.22.	Electrical connections required to measure capacitance-voltage relationship for electrostatic piston actuator tested under negative biasing configuration. . . . .	5-23
5.23.	Picture illustrating the electrical connections between the electrothermal actuator and the 100 $\mu$ m by 100 $\mu$ m bond pads. .	5-27
5.24.	(a) Illustration of L-Edit schematic detailing the wire bond connections for the electrothermal actuators. (b) Picture of MUMPs <sup>®</sup> Die containing the electrothermal actuators wire bonded to to 14 PIN ceramic DIP. . . . .	5-28
5.25.	Picture of packaged MUMPs <sup>®</sup> die containing electrothermal actuators mounted in test bed. . . . .	5-29

Figure		Page
5.26.	Test configuration used to measure resistance-voltage relationship for an electrothermal actuator. . . . .	5-30
5.27.	Cross-sectional profile plots of residual stress cantilever plotted using MetroPro Software distributed by Zygo Corporation. . .	5-33
6.1.	Change in capacitance versus actuation voltage predicted by Model #1, Model #2, and experimentally measured. . . . .	6-3
6.2.	(a) Analytical predictions of Capacitance versus voltage when 1.7 pC of charge is placed at the nitride-air interface. The x- and y-axis are scaled in (b) to emphasize the differences between the two model prior to snapdown. . . . .	6-4
6.3.	Change in capacitance versus actuation voltage for piston actuator irradiated to total dose of 500 krad(Si) (Die #2, Table 5.1) with (a) 10 volts actuation voltage applied during irradiation and (b) no actuation voltage applied during irradiation. . . .	6-7
6.4.	Capacitance versus actuation voltage for piston actuator irradiated to total dose of 500 krad(Si) (Die #2, Table 5.1) with (a) 10 volts actuation voltage applied during irradiation and (b) no actuation voltage applied during irradiation. . . . .	6-8
6.5.	Scanning electron micrograph showing the flexures of the electrostatic piston actuator stuck to the silicon-nitride layer. . .	6-10
6.6.	Change in capacitance versus actuation voltage for piston actuator irradiated to total dose of 750 krad(Si) (Die #3, Table 5.1) with (a) 10 volts actuation voltage applied during irradiation and (b) no actuation voltage applied during irradiation. . . .	6-12
6.7.	In-situ measured change in capacitance versus total ionizing dose for piston actuator irradiated to total doses of 250 (Die #1, Table 5.1) (a), 500 (Die #2, Table 5.1) (b), 750 (Die #3, Table 5.1) (c), and 1000 krad(Si) (Die #4, Table 5.1) (d) while biased with 10 volts. . . . .	6-13

Figure		Page
6.8.	Change in capacitance versus actuation voltage for piston actuator irradiated to total dose of 500 krad(Si) (Die #6, Table 5.1). The top plot illustrates changes for an actuator held at a -10 volt constant bias during irradiation. The bottom plot illustrates changes for an actuator with no actuation voltage applied during irradiation. . . . .	6-14
6.9.	In-situ measured change in capacitance versus total ionizing dose for piston actuator bias with -10 volts and irradiated to total dose of 500 krad(Si) (Die #6, Table 5.1). . . . .	6-15
6.10.	Change in capacitance versus total ionizing dose for two piston actuators irradiated to total dose of 1000 krad(Si) using the snapdown biasing configuration. (a) represents changes in capacitance when snapdown voltages were applied after absorbing a total dose of 500 krad(Si) (Die #10, Table 5.1). (b) represents changes in capacitance when snapdown voltages were applied after absorbing a total dose of 750 krad(Si) (Die #11, Table 5.1). . . . .	6-17
6.11.	Change in capacitance versus actuation voltage for piston actuator irradiated to total dose of 750 krad(Si) (Die # 7, Table 5.2). The top plot illustrates changes for an actuator held at a -10 volt constant bias during irradiation. The bottom plot illustrates changes for an actuator with no actuation voltage applied during irradiation. . . . .	6-19
6.12.	Change in capacitance versus total ionizing dose for piston actuator irradiated to total doses of 250 (Die #1, Table 5.2) (a), and 500 krad(Si) (Die #2, Table 5.2) (b) while biased with -10 volts. . . . .	6-20
6.13.	Analytical prediction and pre-characterization measurement of Electrothermal actuator tip deflection versus voltage. . . . .	6-23
6.14.	Pre- and post-irradiation deflection measurements for 250 $\mu$ m long electrothermal actuators subjected to total ionizing doses of (a) 250 krad(Si), (b) 500 krad(Si), (c) 750 krad(Si), and (d) 1000 krad(Si) in LEXR source. . . . .	6-25

Figure		Page
6.15.	Pre- and post-irradiation resistance measurements for 250 $\mu\text{m}$ long electrothermal actuators subjected to total ionizing doses of (a) 250 krad(Si) (Die #1, Table 5.3), (b) 500 krad(Si) (Die #2, Table 5.3), (c) 750 krad(Si) (Die #3, Table 5.3), and (d) 1000 krad(Si) (Die #4, Table 5.3) in LEXR source. . . . .	6-26
6.16.	In-situ resistance measurements taken on 250 $\mu\text{m}$ long electrothermal actuators subjected to total ionizing doses of (a) 500 krad(Si), and (b) 750 krad(Si), at a dose rate of $134.5 \frac{\text{rad}(\text{Si})}{\text{s}}$ , in LEXR source. . . . .	6-27
6.17.	(a) Current measurements for 250 $\mu\text{m}$ electrothermal actuator taken immediately before irradiating the actuator to a total ionizing dose of 500 krad(Si) (Die #2, Table 5.3) in LEXR source. (b) Average resistance for first two and last five cycles of the pre-irradiation resistance measurements plotted in (a). (c) Pre- and post-irradiation resistance measurements. . . . .	6-28
6.18.	Pre and post break-in tip deflection measurements for electrothermal actuators not subjected to ionizing radiation. . .	6-30
6.19.	(a) Current measurements for electrothermal actuators not subjected to ionizing radiation. (b) Average resistance for pre and post break-in of electrothermal actuator not subjected to ionizing radiation. . . . .	6-30
6.20.	Pre- and post-irradiation deflection measurements for 250 $\mu\text{m}$ long electrothermal actuators subjected to total ionizing doses of 250 (Die #1, Table 5.4), 500 (die #2, Table 5.4), 750 (Die #3, Table 5.4) and 1000 krad(Si) (Die #4, Table 5.4) in Co-60 gamma source. . . . .	6-32
6.21.	Pre- and post-irradiation resistance measurements for 250 $\mu\text{m}$ long electrothermal actuators subjected to total ionizing doses of 250 (Die #1, Table 5.4), 500 (Die #2, Table 5.4), 750 (Die #3, Table 5.4), and 1000 krad(Si) (Die #4, Table 5.4) in Co-60 gamma source. . . . .	6-33

Figure		Page
6.22.	In-situ resistance measurements taken on 250 $\mu\text{m}$ long electrothermal actuator subjected to total ionizing dose of 750 krad(Si) (Die #3, Table 5.4), at a dose rate of $130.8 \frac{\text{rad}(\text{Si})}{\text{s}}$ , in Co-60 gamma source. . . . .	6-34
6.23.	Pictures of electrothermal actuator before irradiation and after irradiating to 1000 krad(Si) in Co-60 gamma source. . . . .	6-35
6.24.	Modelled and experimentally measured deflection of 300 $\mu\text{m}$ by 20 $\mu\text{m}$ cantilever. . . . .	6-37

## *List of Tables*

Table		Page
2.1.	Maximum electron radiation levels found in the Van Allen Belts [2]. . . . .	2-2
2.2.	Estimated electron flux in the Van Allen Belts [2]. . . . .	2-3
2.3.	Maximum proton radiation levels found in the Van Allen Belts [2]. . . . .	2-3
2.4.	Estimated proton flux in the Van Allen Belts [2]. . . . .	2-3
2.5.	Typical Total Ionizing Dose from Electrons and Protons in $\frac{rad(Si)}{yr}$ for satellites in specified orbits [4]. . . . .	2-4
2.6.	Range of radiation environments possible in nuclear plant containment building [7]. . . . .	2-5
3.1.	Zero-deflection capacitance for a square piston actuator having the indicated side lengths. . . . .	3-8
3.2.	Dimensions used in the design of the electrothermal actuator. Figure 3.6 illustrates the correlation of the dimension notation to the electrothermal actuator design. . . . .	3-11
5.1.	Irradiation time, Dose, Dose rate and biasing configuration for the 12 piston actuator die irradiated with 50 keV X-rays from the LEXR. . . . .	5-25
5.2.	Irradiation time, Dose, Dose rate and biasing configuration for the 12 piston actuator die irradiated with 1.25 MeV gamma rays from the Co-60 source. . . . .	5-25
5.3.	Irradiation time, Dose and Dose rate for the 4 electrothermal actuator die irradiated with 50 keV X-rays from the LEXR source. . . . .	5-31
5.4.	Irradiation time, Dose and Dose rate for the 4 electrothermal actuator die irradiated with 1.25 MeV gamma rays from the Co-60 source. . . . .	5-32

Table		Page
6.1.	Geometrical parameters used in the analytical model of the piston actuator. . . . .	6-2
6.2.	Material parameters used in the analytical model of the piston actuator. . . . .	6-2
6.3.	Time table detailing the time elapsed between the ten measurements taken, and the duration of the measurements, for electrostatic piston actuators irradiated to the specified total dose using the LEXR Source. T is taken to be the start of the pre-irradiation capacitance measurements. . . . .	6-5
6.4.	Time table detailing the time elapsed between the ten measurements taken, and the duration of the measurements, for electrostatic piston actuators irradiated to the specified total dose using the Co-60 Source. T is taken to be the start of the pre-irradiation capacitance measurements. . . . .	6-18
6.5.	Material parameters used in the electrothermal actuator analytical model. . . . .	6-22
6.6.	Geometrical parameters used in the electrothermal actuator analytical model. . . . .	6-22
6.7.	Time table detailing the time elapsed between the eight measurement taken, and the duration of the measurements, for electrothermal actuators irradiated to the specified total dose using the LEXR Source. T is taken to be the start of the pre-irradiation resistance measurements. . . . .	6-24
6.8.	Time table detailing the time elapsed between the eight measurement taken, and the duration of the measurements, for electrothermal actuators irradiated to the specified total dose using the Co-60 Source. T is taken to be the start of the pre-irradiation resistance measurements. . . . .	6-31
6.9.	Parameters used in analytical model of residual stress cantilever.	6-37
6.10.	Measured Tip deflection and standard deviation for residual stress cantilever prior to after being irradiated with LEXR source to specified total ionizing dose. The percent change is given for comparison purposes. . . . .	6-39



Table		Page
6.11.	Measured Tip deflection and standard deviation for residual stress cantilever prior to after being irradiated with Co-60 source to specified total ionizing dose. The percent change is given for comparison purposes. . . . .	6-39

## *List of Abbreviations*

Abbreviation		Page
MEMS	Microelectromechanical Systems . . . . .	1-1
NASA	National Aeronautics and Space Administration . . . . .	1-2
DoD	Department of Defense . . . . .	1-2
USAF	United States Air Force . . . . .	1-2
MUMPs®	Multi-User MEMS Processes . . . . .	1-3
DoD	Department of Defense . . . . .	1-4
Co-60	Cobalt-60 . . . . .	1-4
LEXR	Low Energy X-Ray . . . . .	1-4
keV	Kilo-electron-volts . . . . .	2-2
MeV	Mega-electron-volts . . . . .	2-2
GEO	Geosynchronous Orbit . . . . .	2-4
GPS	Global Positioning Satellite . . . . .	2-4
LEO	Low Earth Orbit . . . . .	2-4
DMS	Defense Meteorological Satellite . . . . .	2-4
rad	Radiation Absorbed Dose . . . . .	2-6
Gy	Gray . . . . .	2-6
MOS	Metal Oxide Semiconductor . . . . .	2-10
SiO <sub>2</sub>	Silicon Dioxide . . . . .	2-10
eV	Electron-volts . . . . .	2-10
LIGA	Lithographie Galvanoformung Abformung . . . . .	2-16
JPL	Jet Propulsion Laboratory . . . . .	2-20
°	Degrees . . . . .	2-20
Si	Silicon . . . . .	2-21
Co-60	Cobalt-60 . . . . .	2-21
SEM	Scanning Electron Microscope . . . . .	2-22

Abbreviation		Page
H	Hydrogen . . . . .	2-22
He	Helium . . . . .	2-22
C	Carbon . . . . .	2-22
CMOS	Complementary Metal on Semiconductor . . . . .	2-27
IV	Current versus Voltage . . . . .	2-30
SEM	Scanning Electron Micrograph . . . . .	3-1
PSG	Phosphosilicate Glass . . . . .	3-2
LPCVD	Low Pressure Chemical Vapor Deposition . . . . .	3-2
mm	millimeter . . . . .	3-2
POCl <sub>3</sub>	Phosphorus Oxychloride . . . . .	3-3
nm	nanometer . . . . .	3-3
RIE	Reactive Ion Etch . . . . .	3-3
μm	micrometer . . . . .	3-3
°C	Degrees Centigrade . . . . .	3-3
FEM	Finite Element Method . . . . .	4-8
DUT	Device Under Test . . . . .	5-3
DC	Direct Current . . . . .	5-3
GPIB	General Purpose Interface Bus . . . . .	5-3
AC	Alternating Current . . . . .	5-3
Ni-60	Nickle-60 . . . . .	5-6

*Abstract*

The effects of ionizing radiation on the operation of polysilicon microelectromechanical system (MEMS) electrostatic actuators, electrothermal actuators, and residual stress cantilevers were examined. Pre-irradiation, in-situ, and post-irradiation measurements were taken for the electrostatic and electrothermal actuators. The residual stress cantilevers were characterized before and after irradiation. All three devices were irradiated to a total ionizing dose of 1 megarad(Si) using both the Air Force Research Laboratory's low energy X-ray source and Co-60 gamma source. In both radiation environments, the electrostatic piston actuators exhibited a decrease in capacitance and thereby an increase in voltage per deflection. Both effects are attributed to dielectric charging phenomena. All devices irradiated under positive bias returned to pre-irradiation conditions within seven days of being irradiated. The electrothermal actuator operation was not affected by exposure to either type of ionizing radiation. The tip deflection measurements of the residual stress cantilevers showed a slight decrease between pre- and post characterization. The tip deflection of residual stress cantilevers irradiated with 50 keV X-rays, to 1 megarad(Si) total ionizing dose, decreased by less than 5 % from pre-irradiation measurements. Tip deflection of residual stress cantilevers irradiated with 1.25 MeV gamma rays, to 1 megarad(Si) total ionizing dose, decreased by less than 16.5 % of pre-irradiated measurements. No correlation was made between change in tip deflection and radiation dose.

# The Effects of Ionizing Radiation on Microelectromechanical Systems (MEMS) Actuators: Electrostatic, Electrothermal, and Residual Stress

## *I. Introduction*

### *1.1 Motivation*

The motivation for this research can best be summarized by General Lester Lyles, Air Force Material Command Commander, who said, “The mission of the Air Force is to fly and fight. In order to fly and fight we need to have great systems...” [1]. Microelectromechanical systems (MEMS) have a tremendous potential to enhance the systems utilized by today’s warfighter. However, before these potential benefits can be realized, any issues associated with the reliability of MEMS must be explored. Since MEMS technology is new, most of the research has been centered on technological advances and demonstrating the potential benefits available with MEMS , with little emphasis placed on understanding their reliability. The reliability of MEMS utilized within a warfighting system is compounded by the harsh warfighting environment. The successful application of MEMS into warfighting systems requires that reliability issues be thoroughly explored and understood.

One environmental factor of concern to the reliability of warfighting systems is radiation. Whether it be key systems orbiting the battlefield or directly employed in the hands of the front-line soldier, all must survive radiation exposure to some predetermined level. Thus, to successfully utilize MEMS devices for battlefield operations the effects of radiation on the devices must be thoroughly researched and understood. Researching and understanding these effects is the focus of this thesis.

*1.1.1 Applications of MEMS Devices in Radiation Environments.* MEMS show tremendous potential for space-based operations. The last decade has brought about a philosophical change in the National Aeronautics and Space Administration's (NASA) approach to space exploration [2]. The old approach of launching a few very specialized missions that took years to plan and develop has been discarded. The new plan focuses on creating smaller vehicles that are less expensive and more rapidly deployable. One major hurdle associated with the new philosophy is not sacrificing the capabilities of the older generation of space vehicle for reduced size, price and development time.

MEMS technology shows a tremendous potential in allowing such a reduction to occur while at the same time advancing current capabilities. Three characteristics of MEMS devices that make them attractive to space applications are their low mass, small size, and low power consumption. These key attributes of MEMS give them the potential to be critical mission enhancers in NASA's new approach to space exploration. In fact, several MEMS devices have already been suggested for space applications, such as micro-instrumentation, micro-laboratories, radio frequency communications and, docking systems for microsatellites [3].

*1.1.2 Scientific Merit.* Characterizing the effects of radiation on MEMS electrostatic, electrothermal and residual-stress actuators contributes knowledge to the ever-growing field of MEMS and will accelerate their insertion into fielded systems. This research will benefit the Department of Defense (DoD), NASA, and the United States Air Force (USAF) by accelerating the maturation of MEMS technology, thus enhancing the United States' current warfighting capabilities. In addition to benefiting DoD, NASA, and the USAF, this research will provide some noteworthy contributions to the scientific community.

*1.1.3 Scientific Contributions.* The following is a list of noteworthy scientific contributions made during this research.

- Test and characterizes electrostatic piston actuator in an ionizing radiation environment.
- Demonstrates that the operation of electrostatic piston actuators are affected by radiation induced charge trapping within exposed dielectric layers.
- Reports successful experimental packaging of MEMS devices for testing and post characterization in an ionizing radiation environment.
- Demonstrates high yields for MUMPs® fabricated MEMS devices for testing within radiation environments.
- Confirms previously published radiation testing results for the horizontally deflecting electrothermal actuator.

## 1.2 Problem Statement

With the possibility that MEMS actuators will be used to enhance current capabilities for systems operating in harsh radiation environments comes the reality that the actuators must be known to operate predictably in those environments. This research directly contributes to the reliability knowledge base.

*1.2.1 Accomplishments.* The objective of this thesis is to characterize operation of three MEMS actuators within an ionizing radiation environment. The three devices, an electrothermal actuator, an electrostatic piston actuator, and a residual-stress cantilever, are characterized with respect to their electrical and mechanical properties while operating in a radiation environment. All three actuators are fabricated using the Cronos Multi-User MEMS Processes (MUMPs®), surface micromachining foundry process [4].

## 1.3 Thesis Scope and Approach

The goal of this research is to discover any degradation in the operating parameters of three commonly used MEMS actuators when subjected to ionizing radiation.

The three actuators selected for testing in this research are the electrostatic piston actuator, the residual stress cantilever and the horizontally deflecting electrothermal actuator. No radiation testing has been found in the literature on the first two actuators, however, radiation testing has been reported on the electrothermal actuator. The research focus is on measurement methods that would allow in-situ deflection measurement in order to characterize transient effects associated with the radiation environment.

In order to operate in a space environment, MEMS actuators must be able to withstand ionizing radiation. This research focused on the effects of ionizing radiation. The radiation sources used in this research were selected due to their availability and utility. The Department of Defense (DoD) MIL-STD-883E, Method 1019.4 [5] suggests radiation testing of microcircuits be accomplished using a uniform field of Cobalt-60 gamma rays. In keeping with this recommendation, the actuators were subjected to ionizing radiation from a Cobalt-60 gamma ray source. In addition, a low energy X-ray source was utilized since the low energy X-rays have a different energy deposition profile when compared to the Co-60 gamma rays.

The actuators under test were packaged in a dual in-line package and sealed with double-sided cellophane tape. The operation of the packaged devices was characterized using current and capacitance measurements where applicable. The devices were subjected to gamma irradiation from a Cobalt-60 (Co-60) source and 50 keV X-rays from a Low Energy X-Ray (LEXR) source. During irradiation, the capacitance and current draw (as applicable) of each of the devices is monitored and compared to a control device. The final step is characterizing each of the devices after irradiation.

#### *1.4 Main Results*

Three types of MEMS actuators were tested for radiation hardness. They include an electrostatic actuators, electrothermal actuators, and a residual-stress cantilevers.



The electrostatic piston and electrothermal actuators were characterized prior to, during, and after irradiation in gamma and X-ray radiation environments. The testing of the electrostatic actuators revealed a small decrease in the deflection-voltage relationship and an increase in the snapdown voltage, both due to charging of the dielectric layer. The trapped charge annealed within seven days of being irradiated.

The operation of the electrothermal actuators was characterized by measuring current and deflection as a function of applied voltage. Although some degradation in tip deflection was noted for some actuators, it was attributed to actuator break-in and not radiation exposure. The testing accomplished on the electrothermal actuators confirmed results previously published [6, 7].

The residual stress cantilevers were characterized prior to and after irradiation. The residual stress cantilevers were characterized by tip deflection measured with a interferometric microscope. The tip deflection of residual stress cantilevers irradiated with 50 keV X-rays, to 1 Mrad(Si) total ionizing dose, decreased by less than 5 %. Tip deflection of residual stress cantilevers irradiated with 1.25 MeV gamma rays, to 1 Mrad(Si) total ionizing dose, decreased by less than 16.5 %. Although no correlation was made between the change in tip deflection and the radiation exposure, the research concludes that no permanent damage results from radiation exposure.

### *1.5 Thesis Overview*

This thesis is organized into seven chapters. The first chapter is a brief introduction into the operation of MEMS devices within a radiation environment. The scope of the research and its importance to the military community is presented. The second chapter, a literature review, provides background material for the rest of the thesis. It includes the operation and application of the three MEMS actuators to be tested, previous radiation testing of MEMS actuators, the effects of ionizing radiation on material properties, and the radiation sources used for the research.

Chapter three describes the actuator design process, the PolyMUMPs fabrication process and associated design criteria for each of the actuators. Chapter four presents the analytical models used to characterize the operation of the three actuators. Chapter five describes the experimental setup and procedures used to characterize the operation of the MEMS actuators within an ionizing radiation environment. Chapter six presents the results and analysis of the pre-irradiation, in-situ irradiation, and post-irradiation characterization of the three MEMS actuators. Chapter seven concludes the thesis with final comments on the research and suggests a direction for further research on MEMS actuators. Appendix A contains the Matlab<sup>®</sup> code used in the analytical model of the piston actuator. Appendix B contains the Matlab<sup>®</sup> code used in the analytical model of the electrothermal actuator. Appendix C contains the Agilent VEE code used for data acquisition. Finally Appendix D contains a summary of MUMPs<sup>®</sup> die designed throughout this research. To benefit the reader, references are listed at the end of each chapter.

## Bibliography

1. VanHook, L., "AFMC: living in a materielist world," *Leading Edge*, vol. 42, May 2000.
2. George, T., Y. Bae, I. Chakraborty, H. Cherry, C. Evans, B. Eyre, A. G. A. Hui, K. King, L. Kim, R. Lawton, G. Lin, C. Marrese, J. Mueller, J. Podosek, K. Shcheglov, T. Tang, T. VanZandt, S. Vargo, J. Wellman, V. White, D. Wiberg, and E.-H. Yang, "MEMS Technology at NASA's Jet Propulsion Laboratory," *Photonics for Space Environments VII, Proceedings of SPIE*, vol. 4134, pp. 16–24, 2000.
3. Kerns, D.V., Jr. and S. E. Kerns, "Challenges in the Migration of Commercial MEMS Accelerometers to Military Applications," *Proceedings of SENSORS EXPO. Baltimore*, pp. 53–7, 4-6 May 1999.
4. Koester, D., A. Cowen, R. Mahadevan, and B. Hardy, *PolyMUMPs Design Handbook: a MUMPS<sup>®</sup> process*. Revision 8.0, MEMSCAP, 2002.
5. "Department of Defence Test Method Standard: Microcircuits, MIL-STD-883E," December 1996.
6. Johnstone, R. W., K. F. Ko, J. C. Yang, M. Parameswaran, and L. S. Erhardt, "The effects of proton irradiation on electrothermal micro-actuators," *Canadian Journal of Electrical and Computer Engineering*, vol. 27, pp. 3–5, January 2002.
7. Taylor, E. W., A. H. Paxton, H. Schöne, J. H. Comtois, A. D. Sanchez, M. A. Michalicek, J. E. Winter, S. J. Mckinnew, M. Osinski, P. Perlin, R. F. Carson, J. P. G. Bristow, J. Lehman, and M. K. Hibbs Brenner, "Radiation induced effects research in emerging photonic technologies: vertical cavity surface emitting lasers, GaN light emitting diodes and microelectromechanical devices," *Photonics for Space Environments V, Proceedings of SPIE*, vol. 3124, pp. 9–20, July 1997.

## *II. Background*

This chapter is a compilation of topics relevant to the study of radiation effects on MEMS devices. Section 2.1 presents three radiation environments common to military operations. Section 2.2 discusses the units of radiation measurement. Section 2.3 is an overview of the different interactions that are possible between radiation and solid materials. The effects that radiation can have with semiconductor materials are covered in Section 2.4. The last two sections of the chapter are devoted to MEMS topics. Section 2.5 is a general overview of MEMS. The topics include general MEMS fabrication techniques along with a detailed description of the three actuators to be tested. The chapter concludes with Section 2.6, a discussion of radiation testing of MEMS devices as reported in the literature.

### *2.1 Radiation Environments*

Radiation-induced defects are encountered when a device is subjected to radiation. Radiation can originate from several sources encountered by a device over its lifetime. For this research, the sources can be classified into three environments: space radiation, nuclear blast, and nuclear reactor environments. A thorough description of these environments is undertaken by Ma [1] and Olesen [2]. These radiation environments will briefly be described in the following sections.

*2.1.1 Space.* Devices operating on satellites or other spacecraft are subjected to several ionizing radiation sources. The type of radiation encountered is dictated by the level of orbit of the spacecraft. The space radiation environment near the earth's surface, usually 1 to 10 earth radii, is of most interest since most spacecraft orbits range in altitude from 100 miles to 22,300 miles (geostationary orbit). Within this range of orbits spacecraft will encounter electrically charged particles trapped by the Earth's magnetosphere and high-energy particles from cosmic

rays. The two types of radiation commonly encountered within the space arena will now be described in detail.

*2.1.1.1 Trapped Electrons.* Energies of electrons trapped in the Earth's magnetosphere can range from low energies, kilo-electron-Volts (keV), to around 5 mega-electron-volts (MeV). These electrons are trapped in a region termed the Van Allen Belts which is centered on the geomagnetic equator and extends from approximately 1.2 to 11 Earth radii [3]. The region is commonly separated into two regions, the inner and outer belts. Although there is no distinct division, the outer extent of the inner belt is commonly taken to be 10,000 km. Table 2.1 lists the maximum electron radiation levels found in both the inner and outer belts. Table 2.2 lists the estimated particle flux for both inner and outer zones of the Van Allen Belts. Electrons in the outer zone are seen to have a higher peak flux than those of the inner zone. In addition, the energy of the outer zone electron spectra,  $\sim 7$  MeV, is higher than the energies of the inner zone spectra,  $< 5$  MeV [3].

Belt	Altitude (km)	Electrons > 20 keV	Electrons > 200 keV
		$(\frac{cm^2}{s})$	$(\frac{cm^2}{s})$
Inner	2000	$2 \times 10^9$	$< 10^8$
Outer	25,000	$10^{11}$	$< 10^8$

Table 2.1 Maximum electron radiation levels found in the Van Allen Belts [2].

*2.1.1.2 Trapped Protons.* Energies of protons trapped in the Earth's magnetosphere can range up to approximately 800 MeV. Trapped protons are generally found in the same region as are the trapped electrons; however, the regions of high flux are not coincidental for the two particles. Table 2.3 lists the maximum proton radiation levels found in both the inner and outer belts. Table 2.4 lists the estimated proton flux for both the inner and outer zone of the Van Allen Belts.

Electrons	Energy (keV)	Intensity ( $\frac{1}{cm^2-s}$ )
Heart of inner zone:		
	> 20	2 x 10 <sup>9</sup>
	> 600	10 <sup>8</sup>
Heart of outer zone:		
	> 20	10 <sup>11</sup>
	> 200	10 <sup>8</sup>

Table 2.2 Estimated electron flux in the Van Allen Belts [2].

Belt	Altitude (km)	Protons 0.1 to 5 MeV	Protons > 60 MeV
		( $\frac{cm^2}{s}$ )	( $\frac{cm^2}{s}$ )
Inner	2000	< 10 <sup>6</sup>	4 x 10 <sup>3</sup>
Outer	25,000	10 <sup>8</sup>	< 10 <sup>2</sup>

Table 2.3 Maximum proton radiation levels found in the Van Allen Belts [2].

Protons	Energy (MeV)	Intensity ( $\frac{1}{cm^2-s}$ )
Heart of inner zone:		
	> 40	2 x 10 <sup>4</sup>
	0.1 to 5	10 <sup>6</sup>
Heart of outer zone:		
	> 40	10 <sup>2</sup>
	0.1 to 5	10 <sup>8</sup>

Table 2.4 Estimated proton flux in the Van Allen Belts [2].

Orbit Name	Geosynchronous Orbit (GEO)	Global Positioning Satellite (GPS)	Low Earth Orbit (LEO)	Defense Meteorological Satellite (DMS)
Dose $\frac{rad(Si)}{yr}$	6,600	59,000	17,300	1,260

Table 2.5 Typical Total Ionizing Dose from Electrons and Protons in  $\frac{rad(Si)}{yr}$  for satellites in specified orbits [4].

The amount of total ionizing dose accumulated by a device in the space environment is dependent on the orbit of the satellite, the length of the mission, the solar activity and the amount of shielding on the satellite. Table 2.5 lists some yearly dose accumulations from electrons and protons for four orbits commonly used by the military.

*2.1.2 Nuclear Weapons.* The effects of nuclear weapons have been of interest to the military since the invention of the atomic bomb [5,6]. The environment of a nuclear blast is drastically different from that of conventional weapons; the amount of energy released by an atomic bomb is thousands of times greater than conventional weapons. Highly penetrating invisible electromagnetic rays are released during detonation, and radioactive substances are present after the explosion [5].

The presence of the radioactive substances create an environment flooded with gamma rays, neutrons, beta, and alpha particles. Two categories of radiation are defined for the nuclear weapon environment: initial and residual. Because of their short range, the effects of beta and alpha particles are usually insignificant and thus gamma and neutron radiation are typically considered in the environment of interest. Approximately three percent of the energy emitted during a nuclear explosion is carried off by gamma rays and neutrons. Gamma ray energies can range up to 12 MeV; however, the majority of gamma rays have energies less than 0.75 MeV. Neutron energies range up to 15 MeV. Both of these ranges are examples of possible spectra. The actual energy spectrum is dictated by the type and design of the weapon detonated.

*2.1.3 Nuclear Reactors.* By their very nature, nuclear power plants are a source of radiation. Electronics used to control and operate the plant are continuously subjected to radiation. A thorough discussion of the radiation environment within a nuclear reactor is undertaken by Gover [7]. The containment building of a nuclear reactor houses the majority of devices that must be radiation hard. Therefore the radiation environment of interest is within the containment building.

The radiation present within the containment building is primarily composed of gamma rays; however, neutrons are also present. In a possible accident the radiation environment can change drastically and therefore must be considered when designing control devices. Table 2.6 gives typical operating environments for a nuclear plant over a forty year period and worst case estimates for an accident situation.

Environment	Normal Operation (40-yr Aging)	Accident
Gamma		
rad(Si)	$10^3$ to $10^8$	$2 \times 10^7$
$\frac{\text{rad(Si)}}{\text{hr}}$	$10^{-3}$ to $10^2$	$10^6$
Neutron		
$\frac{n}{\text{cm}^2}$	$10^9$ to $10^{14}$	—
$\frac{n}{\text{cm}^2\text{s}}$	$10^0$ to $10^5$	—
Electrons/Protons		
rad(Si)	—	$2 \times 10^8$

Table 2.6 Range of radiation environments possible in nuclear plant containment building [7].

The three radiation environments presented here have a common link; all three have ionizing radiation present. This commonality steered this research toward exploring the effects of ionizing radiation on MEMS actuators. As recommended by the DoD MIL-STD-883E, Method 1019.4 [8], the actuators in this research will be subjected to ionizing radiation from a Co-60 source as well as a low energy X-ray source. However, before the effects of ionizing radiation can be investigated, one must understand how radiation exposure is quantified.



## 2.2 Radiation Measurement

The amount of radiation a given material is exposed to is given in several units: flux, fluence or dose. A thorough discussion on radiation dosimetry is found in Knoll's *Radiation Detection and Measurement* [9]. The dimensions of flux are particles per unit area per unit time. Fluence is simply the time integral of the flux and has dimensions of particles per unit area. Absorbed dose is defined as the amount of energy absorbed per unit mass of absorber. Since the absorbed dose is dependent on the mass of the absorber, different materials subjected to the same amount of radiation will absorb a different dose. For this reason the unit of absorbed dose will be annotated with the absorbing material. Absorbed dose is quantified using several different, but related, units. Historically, the unit of absorbed dose has been radiation absorbed dose, *rad*, and is defined as  $100 \frac{\text{ergs}}{\text{gram}}$ . The SI unit of absorbed dose is the *gray* (Gy), and is defined as  $1 \frac{\text{joule}}{\text{kilogram}}$ . A relationship between the *rad* and *gray* can be derived knowing that 1 erg is equivalent to  $10^{-7}$  Joules.

$$1\text{rad}(\text{absorber}) = 100 \frac{\text{ergs}}{\text{gram}} = 0.01 \frac{\text{Joules}}{\text{kilogram}} = 0.01\text{Gy}(\text{absorber}) \quad (2.1)$$

Now that the amount of energy deposited by radiation can be quantified, we must look at how radiation interacts with different materials. Understanding the interactions that are possible will lead to a broader knowledge on how radiation can effect MEMS devices.

## 2.3 Interaction of Radiation with Solid Materials

Radiation induced changes in physical and electrical properties of materials have been widely researched. J.R. Srour [10,11] gives a complete discussion on the basic mechanisms of radiation effects on electronic materials. The previously mentioned radiation environments contribute three different types of particles that can

interact with the materials to alter their physical and electrical properties: photons, charged particles, and neutrons. A thorough overview of different interactions of radiation with solid materials can be found in [10–12]. The interaction between the target material and the radiation depends on properties of both the target material and the incident radiation. The mass, charge, and kinetic energy of the particle along with the mass, charge, and density of the target material governs the interaction. Section 2.3.1 presents the possible interactions between photons and solid materials. The interactions possible between charged particles and solid materials are presented in Section 2.3.2. Section 2.3.3 discusses the interaction on neutrons and solid materials

*2.3.1 Photon Interactions.* Photons are electromagnetic rays with no rest mass and no electrical charge. X-rays and gamma rays are two types of photons distinguished from one another solely by their energy. There are several possible interaction mechanisms known for photons. However, three major interactions are found to contribute significantly to altering the physical and electrical properties of materials: photoelectric effect, Compton scattering, and pair production [9]. All three interactions lead to either partial or complete transfer of the photon energy to the target material as electron energy. The type of photon interaction depends on the photon energy and the atomic number of the material. Figure 2.1 illustrates this relationship. The solid lines, within the figure, represent an equal probability of occurrence between neighboring interactions. For Si, photon energies below about 50 keV will interact predominantly by the photoelectric effect. Energies between 50 keV and 20 MeV will lead to Compton Scattering. Pair production will be the dominant interaction for photons above 20 MeV.

During photoelectric interactions, the impinging photon collides with an atom of the target material. A photon with enough energy will free an outer shell electron, known as a photoelectron, which will absorb all of the incident photon energy. The absorption of the photon energy is what separates photoelectric interactions from

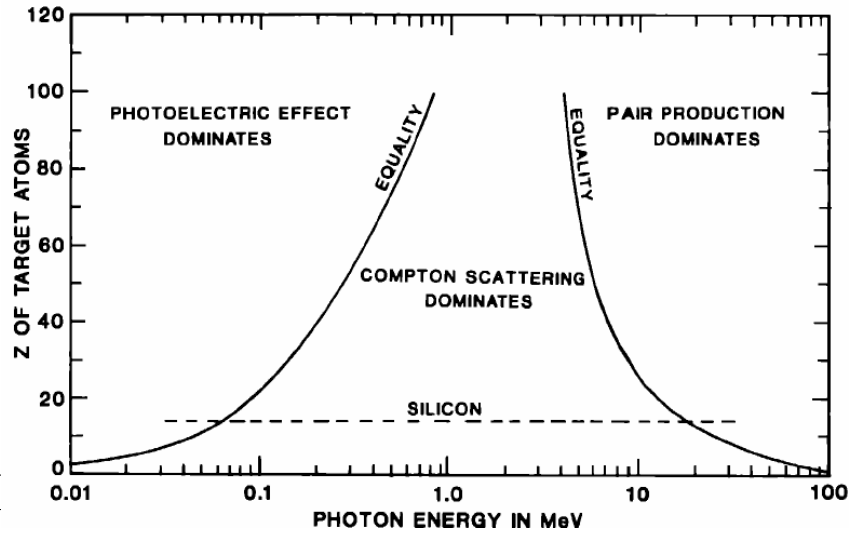


Figure 2.1 Photon interaction probability as a function of photon energy and atomic number of target [10].

Compton scattering. Compton scattering involves photons whose energy is much greater than the binding energy of atomic electrons. Thus, the photoelectron only absorbs a portion of the photon energy, while the remaining energy is contained in a scattered, lower energy, photon. Compton scattering has the probability of producing secondary photoelectrons with the scattered photon. Once incident photons reach the threshold energy of 1.02 MeV, they can interact through pair production. At this threshold energy, the incident photon will be completely absorbed creating a positron-electron pair. A positron is a positive charged particle with the same rest mass as an electron. All three of the above interactions yield energetic electrons which are free to interact with the host lattice as charged particles.

*2.3.2 Charged Particle Interactions.* Charged particles interact with the target material primarily through coulombic interactions, also known as Rutherford scattering. Rutherford scattering can result in displacement damage and excitation or ionization of atomic electrons. The effects of displacement damage and ionization are discussed in Section 2.4.2. Displacement damage and ionization are the dominant basic effects of radiation in electronic materials. Charged particles may also result

in nuclear interactions. The absorption of a proton by a target nucleus may result in the release of an alpha particle [10]. This type of interaction is similar to that which occurs with neutrons.

*2.3.3 Neutron Interactions.* Since neutrons, like gamma rays, carry no charge, they do not undergo coulombic interactions. When neutrons do interact with material, the interaction involves the nuclei of the target atoms. Such an interaction can result in elastic scattering, inelastic scattering, or transmutation. An elastic scattering event occurs when a neutron transfers a portion of its energy to an atom and can dislodge the atom from its initial lattice position. This displacement could result in secondary interactions within the material. Inelastic scattering occurs when an atom absorbs an incident neutron and subsequently reemits the neutron at a lower energy. The excited nucleus will eventually return to its original energy state with the emission of a gamma ray. The last neutron interaction is that of transmutation. Transmutation occurs with the absorption of a neutron by a nucleus and the subsequent emission of another nuclear particle such as a proton or alpha particle. The emission of a proton or alpha particle causes the atom to undergo transmutation, the conversion of an atom of one element into an atom of a different element.

The next logical step in progressing to understanding the effects of radiation on MEMS devices is to apply the different interactions just presented to semiconductor and insulating material. Understanding how these interactions can change the characteristics of semiconductor material will be instrumental in correlating changes in operating parameters of the MEMS actuators to radiation.

## *2.4 Effects of Radiation on Semiconductor Materials*

The three interactions discussed in Section 2.3 all lead to one of two consequences when radiation interacts with semiconductor materials: ionization or dis-

placement damage. Typically, as a particle passes through semiconductor materials, a portion of its energy will be transferred to the target material as ionization energy and the remainder as displacement damage. Ionizing radiation effects are presented in Section 2.4.1. Section 2.4.2 presents the effects of displacement on semiconductor material.

*2.4.1 Ionizing Radiation Effects.* Ionizing radiation is a widely researched area within microelectronics [1,10,11,13]. The vulnerability of Metal Oxide Semiconductor (MOS) devices to ionizing radiation has spurred much study to understand the role of the oxide-insulating layers in the radiation softness of devices [1]. Studies have shown that changes in threshold voltages, current gain, and device turn on/off times can be affected by ionizing radiation. Ma and Dressendorfer [1] and Messenger [13] attribute these changes to three main ionizing-radiation induced processes: electron-hole generation, electron-hole transport, and trapping.

Ionization is a bond breaking process that produces a free electron and a positive charged parent ion. The liberation of a valence band electron creates a mobile hole in the valence band through a process known as pair production. Even though the free electron and mobile hole never leave the target material, the electrical properties of the material are still changed. All of the photon interactions discussed in Section 2.3.1 are capable of ionization either as a primary or secondary effect.

*2.4.1.1 Electron-Hole Generation.* Electron-hole generation is dependent on incident material properties and the dose of radiation absorbed. The generation of electron-hole pairs will usually occur within 1 picosecond after irradiation. The generation of one electron-hole pair in silicon dioxide ( $\text{SiO}_2$ ) requires approximately 17 electron-volts (eV) of energy while in Si only 3.6 eV is required. The difference illustrates how the same absorbed dose can generate significantly different electron-hole pair concentrations in two different materials. The generated pair density is directly proportional to the dose absorbed by the material.

Of the electron-hole pairs generated, only those pairs that survive recombination are found to contribute to electrical parameter variations. The survival of the pairs is dependent on the carrier mobilities, applied electric field, and temperature.

*2.4.2 Displacement Effects.* As mentioned in Section 2.3.2, displacement damage and ionization are the two basic damage mechanisms that affect the electrical properties of materials. Srour [10, 11] covers both damage mechanisms in detail. Displacement of atoms occurs when the incident particles have enough energy to overcome the binding energy of the lattice. A minimum of 26 eV is enough energy for a photon to overcome the binding energy in a Si lattice. Displacement damage can also be a product of ionization. An electron would require 150 keV, and a proton 100 eV to cause displacement in Si. Once an atom becomes displaced, its original location is known as a vacancy. The new position of the atom, typically a non-lattice point, is termed an interstitial site. The displaced atom disrupts the periodicity of the lattice and thus introduces energy levels within the forbidden band of the material favorable to charge carriers. The introduction of favorable energy states within the bandgap alters the electrical properties of the material.

Figure 2.2 illustrates the energy bandgap in a semiconductor material and the five different ways that new energy levels could affect electrical properties.  $E_c$  denotes the conduction band and  $E_v$  denotes the valence band. The area between the conduction and valence band is known as the forbidden energy gap and typically contains no favorable energy levels. This forbidden energy gap is where radiation induced trap sites are formed. The position of these radiation induced trap sites dictates how the electrical properties of the semiconductor will be affected. The five ways in which the electrical properties can change are numbered in the figure and will now be discussed.

In Figure 2.2, process 1 illustrates a defect energy level near the mid-gap of the energy band. Thermal excitation could elevate a bound valence band electron

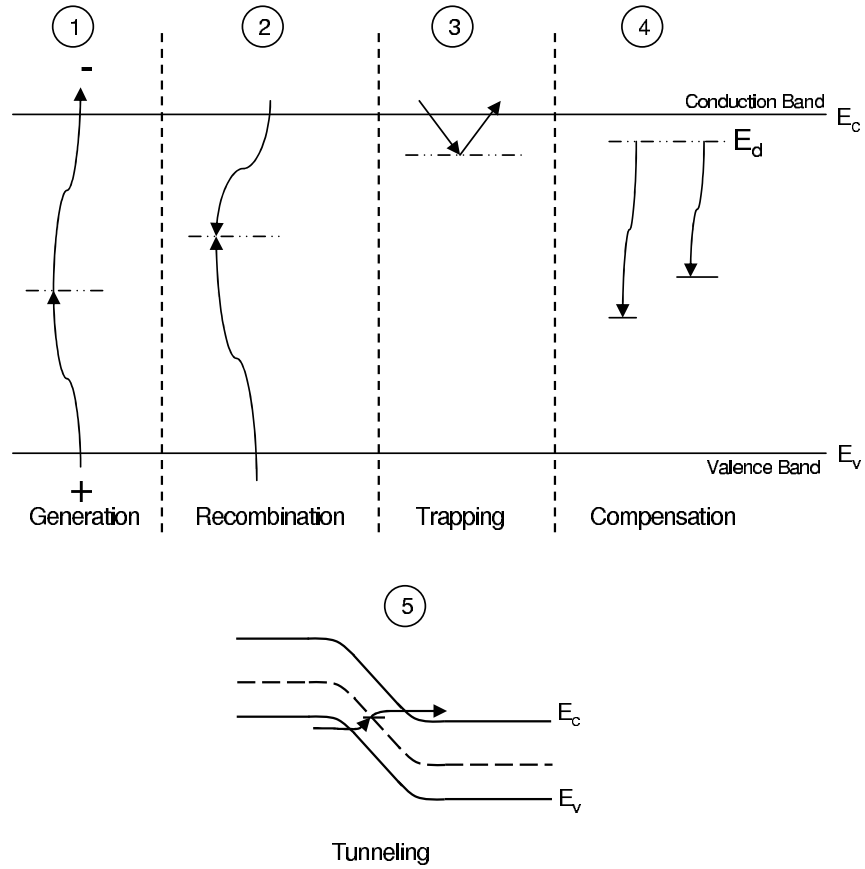


Figure 2.2 Illustration of the five effects of radiation induced defect centers in the forbidden energy band [11].

into the defect level, and a subsequent excitation could elevate the electron into the conduction band. The result is a thermally generated electron-hole pair. Process 2 is the recombination of electron-hole pairs. In this process, a free carrier is captured, from either the valence or conduction band, followed immediately by the capture of an opposite charged carrier; this double capture removes free charge carriers from the material. A recombination center effectively reduces the recombination lifetime of the carriers in a material.

Process 3 illustrates the loss of mobile carriers by trapping. In trapping a shallow defect center captures a carrier for a finite amount of time and reemits

the carrier back into its original band. Defects centers can occur near both the conduction and valence band thus majority and minority carriers can be trapped. Process 4 is the compensation of donors and acceptors by radiation induced traps. The radiation induced traps create a favorable energy level which is filled by electrons from donor atoms. Since the electrons from the donor atoms are meant to become mobile carriers in the conduction band, this process results in the reduction of the equilibrium majority carrier concentration. Tunnelling, detailed in process 5, is the result of defect centers within a depletion region. Carriers recombine by hopping to these defect centers located within the forbidden energy gap thus reducing the concentration of mobile carriers. This process is also referred to as defect-assisted or trap-assisted tunnelling.

The radiation background presented in the previous sections has led to the hypothesis that radiation could affect the operating parameters of MEMS actuators. The scope of the thesis is to research to what extent radiation affects the operating parameters of the electrostatic piston actuator, the electrothermal actuator, and the residual stress cantilever. Therefore, a brief overview of MEMS is required.

## 2.5 *Microelectromechanical Systems*

Microelectromechanical systems is a broad title given to devices with dimensions less than 1 mm but larger than 1  $\mu\text{m}$  [14]. MEMS utilize electrical and mechanical components to create small machines that can, among other things, be used for sensing and actuation on the micro-scale. Books by Kovacs [15], Madou [16] and Gad-el-Hak [14] are excellent sources that cover a wide array of topics associated with MEMS.

This section is focused on introducing the reader to some MEMS fabrication techniques and three commonly used MEMS actuators. Section 2.5.1 will introduce three different fabrication techniques used to create MEMS devices. Section 2.5.2 introduces the electro-static piston actuator and its principles of operation. The



horizontally deflecting electrothermal actuator is detailed in Section 2.5.3. Section 2.5.4 presents the residual stress cantilever and overviews its operation.

*2.5.1 MEMS Fabrication Techniques.* Many techniques used to fabricate micro-scale machines have been borrowed from the fast growing, integrated circuit industry. Three common fabrication techniques are surface micromachining, bulk micromachining and micromolding. An overview of each of these fabrication techniques is given in the following sections.

*2.5.1.1 Surface Micromachining.* Surface micromachining is an additive fabrication process in which three dimensional structures are created on the surface of substrate. The structures are created by depositing, patterning, and etching thin films. This fabrication process follows directly from those used to fabricate microelectronic circuits. Two different kinds of materials are used in surface micromachining: structural, and sacrificial. The materials are deposited and patterned so that removal of the sacrificial material leaves a movable, three dimensional structure. Sandia's SUMMiT<sup>TM</sup> process and Cronos' PolyMUMPs [17], SOIMUMPs [18] and MetalMUMPs [19] are all commercially-available surface micromachining processes. Cronos' PolyMUMPs process is detailed in Section 3.2. Figure 2.3 is a linear rack assembly fabricated in the SUMMiT<sup>TM</sup> process [20].

*2.5.1.2 Bulk Micromachining.* Bulk micromachining is a subtractive process in which three dimensional structures are created by etching away substrate material. Bulk micromachining is typically used where large structures of substantial mass and thickness are required. By capitalizing on anisotropic etching processes, substrate material can be bulk micromachined to form such structures as V-grooves and pyramidal pits. Figure 2.4 shows an example of a bulk micromachined structure etched in a silicon substrate [21].

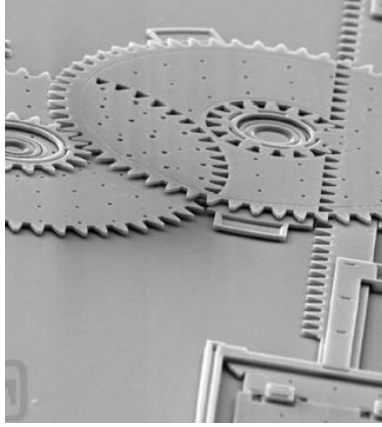


Figure 2.3 Linear rack assembly fabricated in the SUMMiT<sup>TM</sup> surface micromachining process [20].

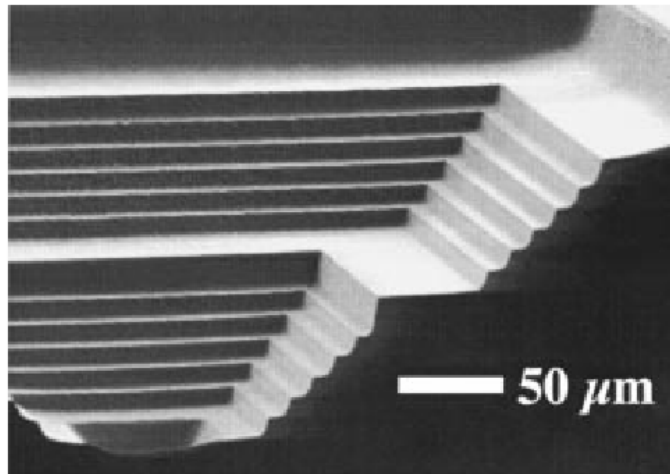


Figure 2.4 Example bulk micromachined structure etched in a silicon substrate [21].

2.5.1.3 *Micromolding.* Micromolding is a fabrication process capable of creating structures with extremely high aspect and depth-to-width ratios. The most common micromolding process, "*Lithographie, Galvanoformung, Abformung*," (LIGA), was developed by W. Ehrfeld, et al. [15]. A brief overview of the process is given here, however; a detailed outline of the process is given by Madou [16]. Figure 2.5 pictures various gears fabricated in the LIGA process [20].

The LIGA process begins by creating a three-dimensional resist structure, or mold, using an X-ray resist. The three-dimensional mold is then filled with metal by electrodeposition. After the deposition, the resist layer can be removed leaving a free standing metal structure. The advantage of LIGA is that this metal structure can be the final product or a precision plastic mold. The mold can be the start of an infinite micromolding loop when coupled with precision plastic injection molding.

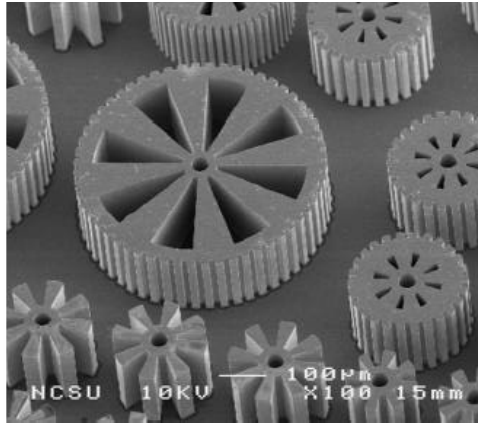


Figure 2.5 Various MEMS gears fabricated using the LIGA process [20].

The MEMS actuators tested in this research were fabricated using Cronos' PolyMUMPs [17] surface micromachining, fabrication process. Understanding the principles of operation for the three actuators is important for performing radiation testing. The following sections will present the operating principles of the electrostatic piston actuator, the electrothermal actuator and the residual stress cantilever.

*2.5.2 Electrostatic Piston Actuator.* Electrostatic actuation is probably the most widely used form of actuation within MEMS. Some of the advantages associated with electrostatic actuators are simple design, low power consumption and high operating frequency. Some of the disadvantages are a large area-to-force ratio and high drive voltages. The electrostatic piston actuator operation is governed by Coulomb's law, which states that charges of the same sign repel and charges of the opposite sign attract each other [22]. The actuator is composed of two electrically isolated plates. The top plate is suspended over the fixed, bottom attracting plate by four thin flexures. An illustration of the top electrostatic piston actuator plate is given in Figure 2.6. The four flexures serve two purposes in the actuator design. The first purpose of the flexures is to provide a mechanical linkage between the top actuating plate and the wafer. The second purpose is to provide a restoring force to the actuating plate. When a potential difference is applied between the two plates they are attracted to each other. The top actuating plate deflects toward the fixed bottom plate creating actuation perpendicular to the plane of the wafer.

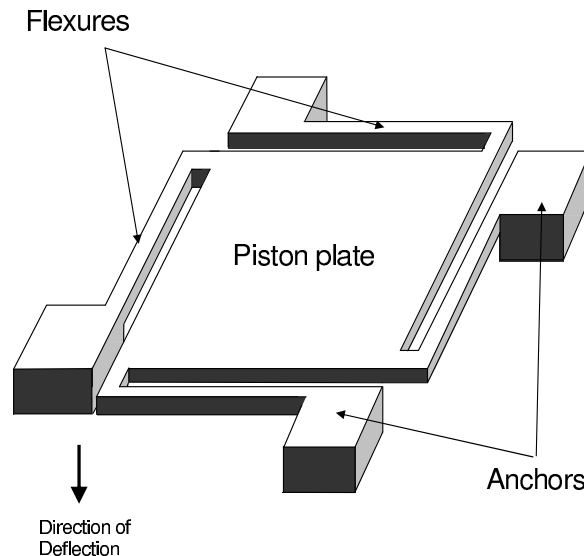


Figure 2.6 Illustration of electrostatic Piston actuator without bottom attracting plate.

*2.5.3 Electrothermal Actuator.* The theory of operation of the actuator is centered on the principle of joule heating. Figure 2.7 is an illustration of a horizontally-deflecting electrothermal actuator. The actuator is operated by applying a voltage across the two anchors of the actuator, which causes current to flow through the device. The current causes the device to heat up due to resistive losses, through a process known as joule heating. Since the current density in the thin flexure, called the hot arm, is greater than in the thicker flexure, the cold arm, the hot arm experiences more heating. The difference in temperatures between the two flexures causes the flexures to experience different degrees of thermal expansion. To accommodate the difference in expansion, the structure deflects toward the cold arm. This same principle applies to devices designed to deflect vertically, out of the plane of the substrate. The deflection of electrothermal actuators has been successfully used to assemble MEMS devices out of the plane of the substrate. Horizontally deflecting actuators have also been successfully used to drive micro-engines. Kladi-tis [23] demonstrated a novel idea of using horizontally deflecting actuators as legs for micro-robots.

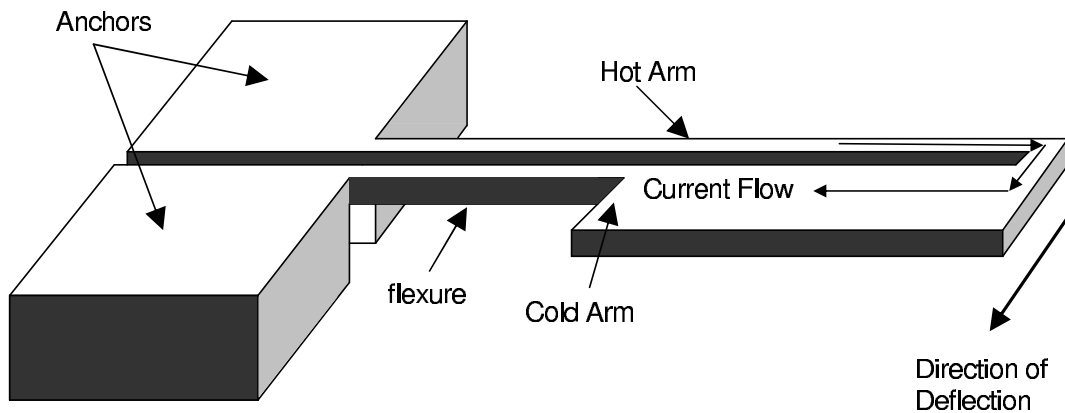


Figure 2.7 Illustration of horizontally deflection electrothermal actuator.

*2.5.4 Residual-Stress Cantilever.* The operation of the residual-stress cantilever capitalizes on mismatch in the coefficient of thermal expansion between two different thin film layers sandwiched together. When the device is cooled to room temperature from its fabrication temperature, or subjected to temperature changes during operation, the two layers expand, or contract, by different amounts. The difference in internal strain between the different layers causes the cantilever to curl out of the plane of the substrate. The residual stress cantilever is an ideal structure for sensing since several external stimuli can affect the temperature of the cantilever. The residual-stress cantilever has been successfully used as a photon detector [24], chemical sensors [25], and biosensors [26]. Residual-stress cantilevers have even been suggested for use in docking systems for microsatellites [27].

## *2.6 Previous Radiation Testing of MEMS Devices*

A thorough literature review reveals the effects of radiation on many types of MEMS devices are not well documented. This might be due to the lack of commercially available MEMS devices, and the fact that many of the devices are still in the developmental stages. Two devices that must be excluded from the previous statement are the MEMS comb-drive and horizontally deflecting electrothermal actuator. The following sections will explore radiation testing accomplished on these two devices. In some cases the radiation testing of these devices also included irradiating control circuitry co-located with the MEMS devices. Since the scope of this thesis is focused on radiation effects of MEMS actuators and the effects of radiation on electronic devices are well documented [1, 13, 28, 29], the effects of radiation on the control circuitry will not be discussed.

Section 2.6.1 presents an overview of radiation testing accomplished for MEMS comb drives. The radiation testing of MEMS micro-engines is presented in Section 2.6.2. Section 2.6.3 presents the results of radiation testing accomplished on the electrothermal actuators.

*2.6.1 MEMS Comb-drives.* Analog Devices and Motorola have both produced commercially available comb drive-based accelerometers. Accelerometers from both companies have been subjected to radiation testing by the Jet Propulsion Laboratory (JPL) at California Institute of Technology [30, 31]. In addition, Analog Devices has conducted their own research in conjunction with the Naval Research Laboratory on the effects of radiation on two of their accelerometers, the ADXL50 and ADXL04 [32]. A comb drive used as a microengine was also subjected to radiation testing at Sandia National Laboratories [33]. All the tests conducted have demonstrated that the operation of MEMS comb-drives is affected by radiation. A brief discussion on the principles of operation for a MEMS comb drive-based accelerometer will be undertaken prior to presenting the results of the radiation testing.

*2.6.1.1 MEMS Accelerometers.* Hirano [34] and Johnson and Warne [35] both give an in-depth presentation of the electrophysics of comb-drives and comb-drive accelerometers. The comb-drive accelerometer utilizes a differential capacitor sensor composed of two independent stationary plates and a moveable plate which will deflect during changes in relative motion. Figure 2.8 is an illustration of a comb-drive accelerometer. The flexures confine the movement of the capacitor plate (X) relative to the stationary capacitor plates (Y & Z). During operation, a voltage of the same magnitude is applied to the stationary plates (Y & Z) but the voltages are out of phase by  $180^\circ$ . This configuration, two series connected capacitors, creates a capacitive divider which is controlled by the moveable central plate. The voltage induced on the moveable plate is taken as the output of the accelerometer.

At the equilibrium position, the distances between the two moveable plates and the central plate ( $d_1$  &  $d_2$  in Figure 2.9) are equal and thus the capacitance is equal. The net voltage induced on the moveable plate is zero. Under acceleration, the moving plate shifts toward one of the stationary plates, creating an imbalance in capacitance between the two stationary plates and the moving plate. This imbalance in the series capacitance causes a voltage to be induced on the moveable electrode.

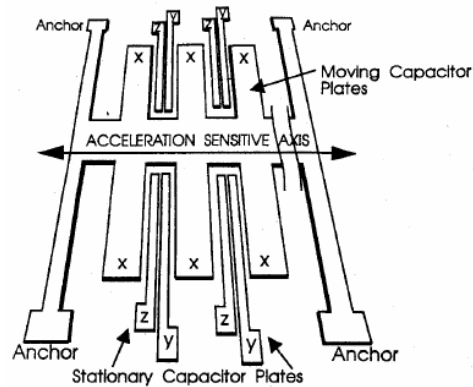


Figure 2.8 Diagram of a comb-drive accelerometer detailing the moving (X) and the stationary (Y & Z) electrodes [32].

This induced voltage is directly proportional to the acceleration applied to the sensor; a larger acceleration causes a larger deflection of the moveable mass creating a greater difference in capacitance between the two series capacitors and thus a large voltage is induced on the moveable mass. The phase of the induced voltage dictates the direction of acceleration. The equilibrium and acceleration configurations of the accelerometer are illustrated in Figure 2.9.

As mentioned in Section 2.6.1, three commercially-available MEMS accelerometers, Analog Devices' ADXL50 and ADXL04 and Motorola's XMMAS40G, have been tested for radiation hardness by two independent research groups, as well as by JPL and the Naval Research Laboratory. These are representative of devices that could be used within military applications and thus radiation environments. The accelerometers are fabricated on a single wafer of Silicon (Si), they are composed of a mechanical sensor for sensing motion, and an electronic circuit for supplying a voltage output. The ADXL50 and ADXL04 differ only in that the ADXL04 has a conducting polysilicon layer, which is electrically connected to the mechanical sensor to shield the dielectric layer. JPL tested the ADXL50 and XMMAS40G using four different sources: Cobalt-60 (Co-60) source, high-energy proton accelerator (155 MeV), low-energy proton accelerator (5.5 MeV), and a Scanning Electron Microscope



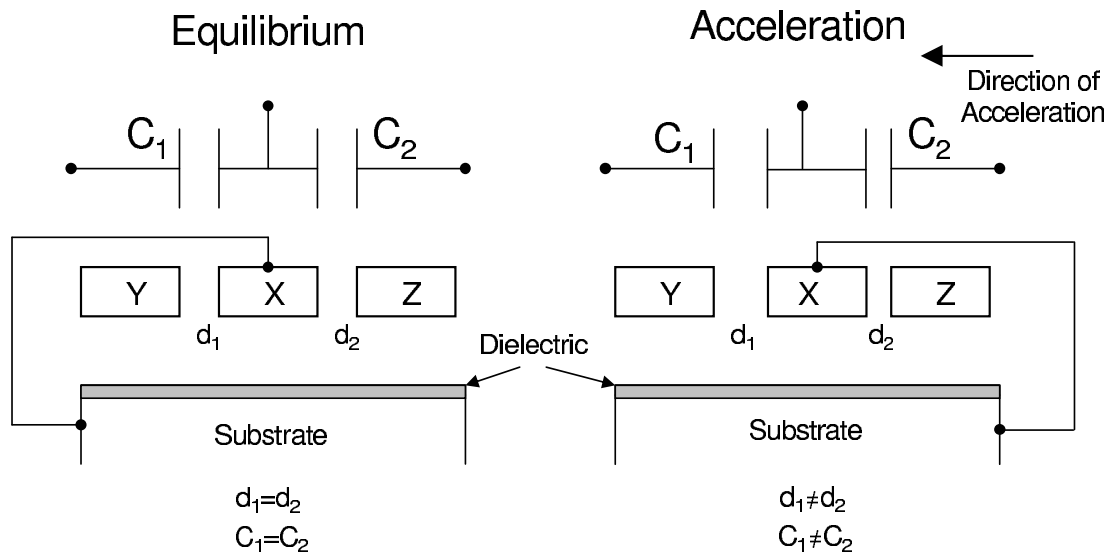


Figure 2.9 Cross-section view of a comb-drive based accelerometer detailing the movable (X) and stationary (Y & Z) electrodes for equilibrium and acceleration. The figure details the series capacitance of the three electrodes.

(SEM). The Navel Research Lab tested the ADXL50 by exposing it to 65 MeV protons along with Hydrogen (H), Helium (He), and Carbon (C) ions. They tested the ADXL04 by only exposing it to H ions.

*2.6.1.2 Radiation Testing of Analog Devices' ADXL50 and ADXL04 Accelerometers.* JPL subjected the ADXL50 to four different test configurations. Their first test irradiated the entire ADXL50 accelerometer to 1.17 and 1.33 MeV gamma particle irradiation from a Co<sup>60</sup> room type irradiator. Three devices were irradiated at a dose rate of  $25 \frac{\text{rad}(\text{Si})}{\text{s}}$ . When the devices were held at a normal operating bias and in a static condition, only a small shift in output voltage was noted for dose levels between 5 and 20 krad(Si). At high dose levels unusual failures were noted. At 25 krad(Si) and above, the output voltage was clamped at 50 mV until the device was subjected to accelerations greater then 30 g, at which point normal operation was restored. Normal operation could be maintained as long as the power remained on. Once the supply power was removed the device reverted to the

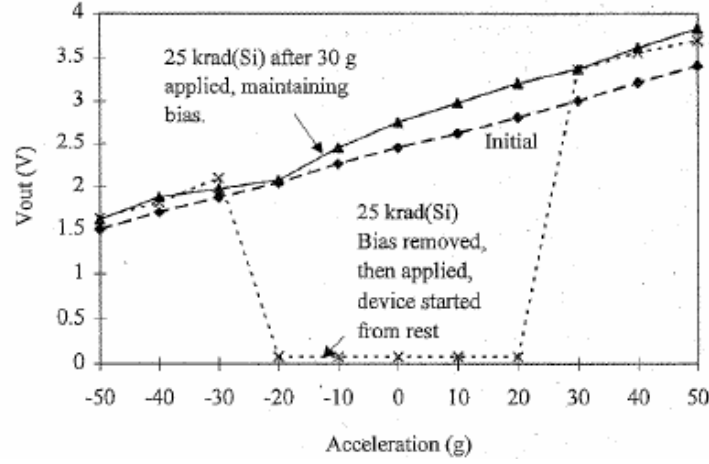


Figure 2.10 Test results for ADXL50 for dose rate of  $25 \frac{\text{rad}(\text{Si})}{\text{s}}$  [31].

clamped output of 50 mV. These results are illustrated in Figure 2.10. The dashed line represents pre-irradiation operating parameters. The solid line represents the operating parameters for total dose of 25 krad(Si) and after |30| g while maintaining normal operating bias. The dotted line and x illustrates the operating parameters after 25 krad(Si) and operating bias removed and reapplied.

After irradiating the three devices, an anneal study was undertaken. JPL, after irradiating to 25 krad(Si), found no signs of annealing after a 24 hour, room temperature anneal. However, after 144 hours at 100 °C, the operating parameters of one device returned to pre-irradiation standards. So that higher total dose effects could be investigated, this device was again irradiated to a total dose of 40 krad(Si). At 40 krad(Si), the device failed in the same manner as previously discussed for a total dose of 25 krad(Si); however, a complete recovery occurred after 1 hour of room temperature annealing. The results of this annealing test suggest that the failure mechanism is tied to dose rate and thus the accelerometer may survive a higher total dose when irradiated at a lower dose rate. When the ADXL50 was irradiated at a low dose rate of  $0.005 \frac{\text{rad}(\text{Si})}{\text{s}}$  the output voltage remained unchanged from non-irradiated

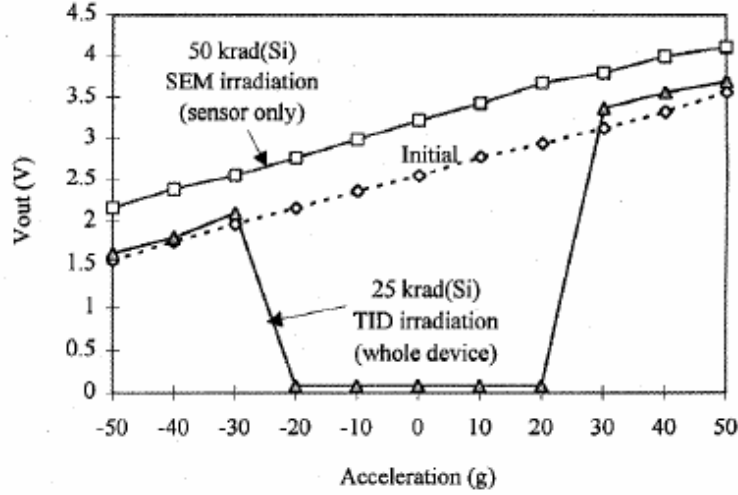


Figure 2.11 Test results for whole device and sensor only irradiation [31].

characterization up to a total dose of 25 krad(Si), and the hysteresis effects seen at the higher dose rate was not observed.

The high energy proton test involved irradiating only the sensor portion of the accelerometer using a SEM with a dose rate of  $1 \frac{\text{krad}(\text{Si})}{\text{s}}$ . The results are presented in Figure 2.11. The output voltage of the irradiated device remained linear, similar to that of the non-irradiated devices, increasing slightly when compared to the non-irradiated devices. This behavior was noted for all doses up to the final dose level of 50 krad(Si). The hysteresis response observed during irradiation of the whole device was not observed for this test configuration. Figure 2.11 illustrates the output voltage over a range of accelerations for pre-irradiation ( $\diamond$ ), 50 krad(Si) SEM irradiation ( $\square$ ), and 25 krad(Si) gamma irradiation ( $\triangle$ ). After irradiating the sensor to a total ionizing dose of 50 krad(Si), the output voltage increased by approximately 0.5 Volts over the pre-irradiated output voltage.

The low energy proton test also irradiated only the sensor element to a total dose of 100 krad(Si), but using 5.5 MeV protons. In this test the output voltage versus acceleration curve shifted by approximately -0.5 V. This shift was opposite

of that obtained during the SEM irradiation. Again, the hysteresis effect, observed during the  $\text{Co}^{60}$  test, was not noted for the low energy proton irradiation.

The final irradiation accomplished by JPL on the ADXL50 accelerometer was conducted using 155 MeV protons. Two devices, that had not been previously irradiated, were irradiated to a total dose of 100 krad(Si). One device, which had the sensor element previously irradiated to 100 krad(Si) with 5.5 MeV protons, was again irradiated. This time the entire device was irradiated to 100 krad(Si) with 155 MeV protons. The two unirradiated devices behaved differently after irradiation. The output of one of the devices decreases and seemed to be clamped at 0.115 V over the entire acceleration range. The output of the second device shifted upward and displayed the same hysteresis effects observed during gamma irradiation. However, after the high energy proton irradiation, the device would not function below  $|30|$  g. This difference was attributed to the difference in total doses absorbed during the two irradiations, 25 krad(Si) during gamma irradiation and 100 krad(Si) during high energy proton irradiation. The output of the previously irradiated device underwent a downward shift with the same hysteresis effects observed during the gamma irradiation.

Similar shifts in output voltages were obtained by the Naval Research Laboratory when they irradiated the ADXL50 with 65 MeV protons. They tested the ADXL50 in a static condition with normal operating bias applied. At low dose rates of  $< 50 \frac{\text{rads}(\text{Si})}{\text{s}}$  up to a total dose of 24 krad(Si), the output voltage increased. At a high dose rate of  $250 \frac{\text{rad}(\text{Si})}{\text{s}}$ , the output voltage decreased. The output voltage of the ADXL50 was also measured as a function of proton fluence with and without an applied bias. At low dose rates the differences in the output voltage with and without an applied bias were insignificant. At high dose rates, irradiating the device with power on caused a greater change in the output voltage than did irradiating the device with power off.

The researchers proposed two possible damage mechanisms that could explain the shift in output voltage. They are displacement damage and charge trapping within the dielectric layer. The primary effects of displacement damage is seen in the physical parameters of a material such as resistivity, density, elasticity, etc. It would be hard to explain the output voltage shift as a function of these material parameters. For example, any changes in the elastic constant would be offset by changes in the deflection and the same electrostatic force would restore the mass to its neutral position. The shift in output voltage, on the other hand, can be attributed to charge separation phenomena. Applying a bias causes the electrons and holes generated by the incident radiation to be separated. This separation of charge reduces carrier recombination allowing more charge to be available for trapping. The trapped charge changes the electric field distribution around the moveable mass which could cause the mass to move and thus the output voltage to shift. Edmonds et al. [30] gives an in-depth explanation of this electrostatic response. The validity of this response was confirmed by Knudson [32] during The Naval Research Laboratory's testing of the ADXL04 accelerometer.

Knudson subjected the ADXL04 accelerometer to 65 MeV proton irradiation with fluences up to  $3.5 \times 10^{10} \text{ cm}^2$ . There was no noticeable change in the output voltage for the irradiated device. As mentioned earlier, one main difference between the ADXL50 and ADXL04 is that the ADXL04 contains layer of conducting polycrystalline Si. The moveable element and the conducting layer are coupled electrically. Thus, any charge trapped within the dielectric layer of the device would have no effect on the electric field distribution influencing the sensing element. Knudson concluded that the output voltage shift observed for the irradiated ADXL50 devices is mainly due to charge trapping in the dielectric layers.

#### *2.6.1.3 Radiation testing of Motorola XMMAS40G Accelerometer.*

The Motorola XMMAS40G was also tested for radiation hardness by JPL [31]. The device was subjected to gamma radiation in a  $\text{Co}^{60}$  irradiator at a dose rate of 25

$\frac{\text{rad}(\text{si})}{\text{s}}$ . Small changes in output voltage were noted at low total doses. The device failed at a total dose of 4 krad(Si) when the output voltage clamped at 4.86V. After 24 hours of room temperature annealing, the output decreased to 27 mV and was nonfunctional after 168 hours of high temperature annealing at 100 °C . No local irradiation of the sensor element was possible due to the delidding problems. The sensitive radiation response and low total dose failure of the XMMAS40G were attributed to extremely sensitive complementary metal on semiconductor (CMOS) circuitry.

*2.6.2 Micro-engines.* It is appropriate here to also give a brief overview of the operation of a MEMS comb-drive microengine. A detailed discussion of MEMS comb-drive actuators is undertaken by Hirano [34] and Johnson and Warne [35]. Figure 2.12 illustrates a typical comb-drive design. The movable electrode is connected to two sets of fingers. Each of the fingers is interdigitated with another bank of fingers fixed to the substrate. The movable electrode is connected to the substrate by four flexure arms. The flexure arms confine the movement of the shuttle to primarily one direction as illustrated in Figure 2.12. When a potential is applied between the sets of interdigitated fingers, the resultant force causes lateral motion. The fingers are designed with a high thickness-to-length ratio so that the attractive force of the electrostatic potential is mainly due to the fringing electric field lines. The microengine utilizes two comb-drives to create rotational movement of a gear.

*2.6.2.1 Radiation Testing Microengine.* Testing the radiation response of a comb-drive powered microengine was accomplished at Sandia National Laboratories [33]. The test involved exposing the microengine to X-rays, electrons and protons. Three different biases were applied during the irradiation; floating, all pins grounded, and normal operating bias.

This research demonstrated that the biasing of a comb drive has significant effects on its radiation response. The comb drive was found to be operational up to

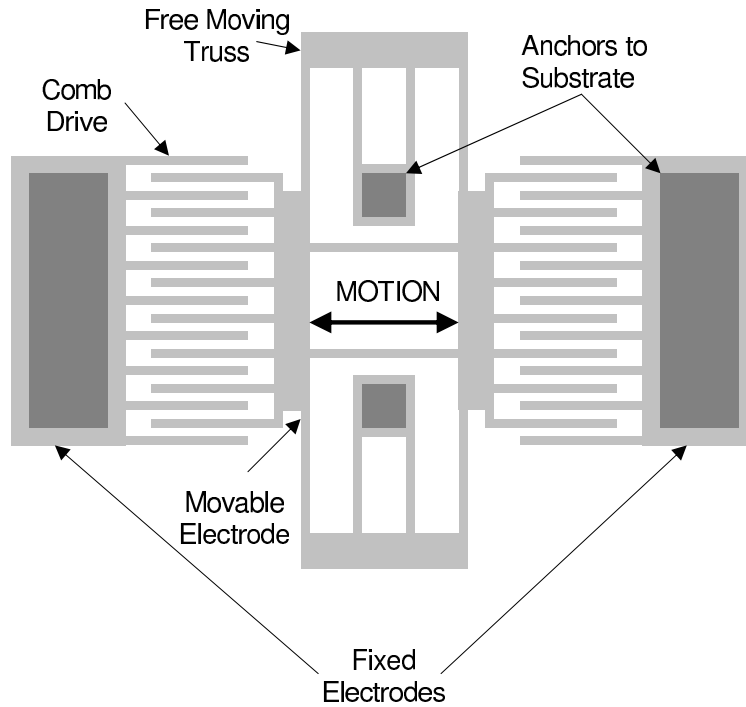


Figure 2.12 Typical comb-drive design.

fluence levels of  $10^6 \text{ cm}^{-2}$  when biased with a drive signal. When the floating and grounded biases were applied, the comb drive remained operation up to fluences of  $10^{13} \frac{\text{electrons}}{\text{cm}^2}$  and  $10^{14} \frac{\text{electrons}}{\text{cm}^2}$ , respectively. Two observed effects were linked directly to radiation degradation. The first effect attributed to radiation exposure was an increase in displacement of the comb drive due to dielectric charging. Figure 2.13 shows the increase in displacement, at resonance, for electron irradiation and Figure 2.14 illustrates the increase in displacement, at resonance, for proton irradiation. The increase is totally attributed to radiation because a control sample on the same chip, which was not irradiated, did not show the increased displacement.

The second effect attributed to radiation was linear and lateral clamping. The linear clamping was caused by charging of a nitride strip. A part of the comb-drive was found to be broken off and stuck to the comb base and the nitride-insulating strip below the base. The lateral clamping was caused when the shuttle travel increased

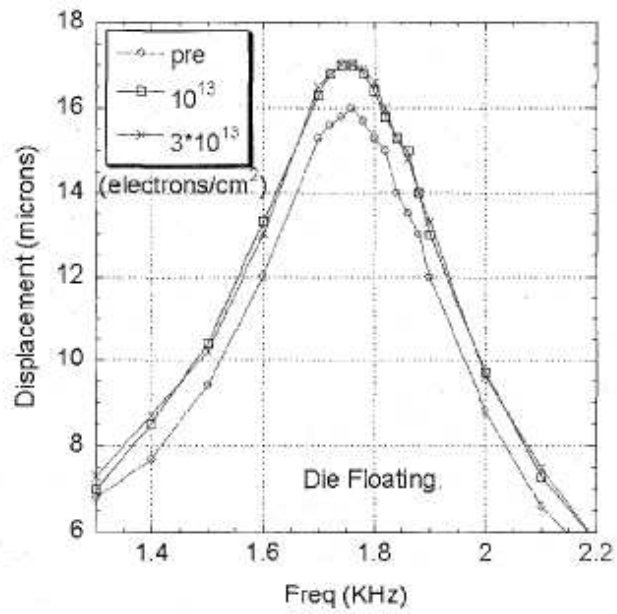


Figure 2.13 Frequency response of standard comb-drive for electron irradiation [33].

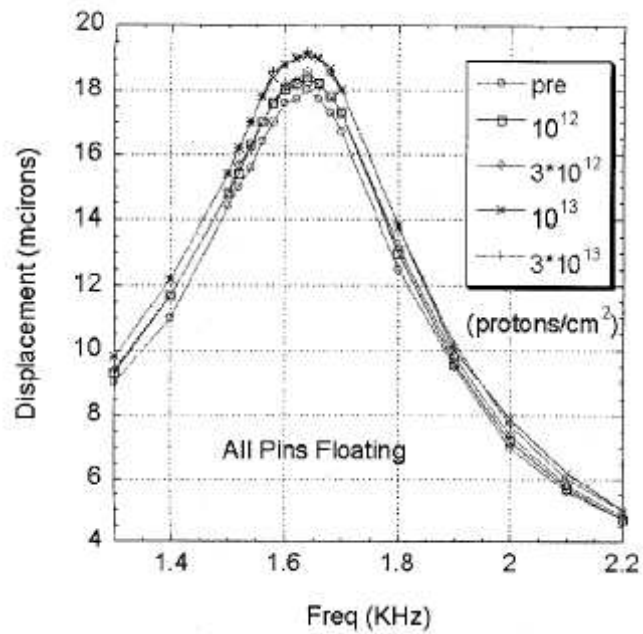


Figure 2.14 Frequency response of standard comb-drive for proton irradiation [33].



enough to cause the interdigitated fingers to touch the attracting bank of fingers. The other effects that were observed while testing the microengine dealt mainly with wear mechanisms associated with friction.

Unlike the MEMS accelerometers and microengines that were tested, researchers performing radiation testing on the electrothermal actuators found no evidence that the operating parameters were effected by exposure to radiation.

*2.6.3 Electrothermal Actuators.* As with the comb-drive actuators, it is appropriate to describe the operation of an electrothermal actuator before the effects of radiation are explored. A brief overview of the operating principles of the electrothermal actuator can be found in Section 2.5.3.

*2.6.3.1 Radiation Testing Electrothermal Actuators.* Two groups of researchers have tested horizontally deflecting electrothermal actuators within a radiation environment. Taylor et al. [36] irradiated the actuator with protons and gamma rays and Johnstone et al. [37] irradiated the device with only proton radiation.

Taylor et al. used an ion microbeam to irradiate specific sections of the actuator believed to be high tensile stress areas. They explored degradation in operability directly due to dielectric charging, a common byproduct of radiation. Their testing revealed that no ion induced degradation occurred. Furthermore, they found no cracking or degradation in deflection in the device as a result of the radiation. The researchers did point out that high fluences or different conditions could result in adverse charge build-up which could lead to system failure as a result of stiction.

Johnstone et al. [37] irradiated their devices with 50 MeV protons with total doses ranging from  $10^9$  to  $10^{13} \frac{\text{protons}}{\text{cm}^2}$ . There were no noticeable changes in the current versus voltage (IV) characteristics before or after irradiation. However, some changes were noted concerning the deflection between the pre-irradiated and post-

irradiated devices. This change was attributed to stiction. The researchers were unsure if the stiction was a result of the irradiation or just environmental contamination.

*2.6.4 Summary of MEMS Radiation Testing.* The MEMS radiation testing found in the published literature has demonstrated that radiation has the potential to affect the operation of the device. The extent that radiation will affect the operation is dependent on the device design, structural material and energy of the radiation.

When dielectric layers are exposed in the device design there is a high probability that the operating parameters could be affected. Dielectric layers exposed to the radiation will experience some level of charging. Charging of the dielectric will increase in the presence of an applied voltage. The applied voltage causes separation of the radiation-induced charges which reduces the amount of recombination. Since fewer charges recombine, more are available for trapping within the dielectric layer.

Although theoretically possible, the testing has not related any significant changes in physical parameters such as resistivity, density, and elasticity, of the structural materials, to radiation exposure.

The effects on device operation will be greatly dependent on the energy of the energy present in the radiation environment. The the energy deposition profile is dependent on the initial energy of the radiation. Higher incident energies would deposit more energy within the substrate. At lower energies, the polysilicon structural layers will absorb more energy and larger areas of damage will occur.

## *2.7 Conclusions*

The information in this chapter was compiled to form a solid foundation in pursuit of exploring effects of radiation on three MEMS actuators, an electrostatic piston actuator, an electrothermal actuator and a residual stress cantilever. An overview of applicable radiation physics was presented. The radiation physics will

be applied to the principles of operation of the actuators and results of previous radiation testing to build a test plan to successfully characterize the three actuators for operation in an ionizing radiation environment.

## Bibliography

1. Ma, T. P. and P. V. Dressendorfer, *Ionizing Radiation Effects in MOS Devices and Circuits*. New York: John Wiley and Sons, Inc., 1989.
2. Olesen, H. L., *Radiation Effects on Electronic Systems*. New York: Plenum Press, 1966.
3. Stassinopoulos, E. G., "Radiation environment of space." IEEE Nuclear and Space Radiation Effects Conference, July 16 1990.
4. King, D. P. and D. R. Alexander, "Space electronics overview," tech. rep., MRC Microelectronics, Albuquerque, New Mexico, July 2002.
5. Los Alamos Scientific Laboratory, *The Effects of Atomic Weapons*. U. S. Government Printing Office, September 1950.
6. Glasstone, S. and P. J. Dolan, *The Effects of Nuclear Weapons*. Washington D.C.: U. S. Department of Defense and U. S. Department of Energy, 3<sup>rd</sup> ed., 1977.
7. Gover, J. E., "Basic radiation effects in electronics technology," *IEEE Nuclear and Space Radiation Effects Conference Short Course*, July 1984.
8. "Department of Defence Test Method Standard: Microcircuits, MIL-STD-883E," December 1996.
9. Knoll, G. F., *Radiation Detection and Measurement*. New York: John Wiley and Sons, 3<sup>rd</sup> ed., 2000.
10. Srour, J. R., et al., *Radiation Effects on and Dose Enhancement of Electronic Materials*. Park Ridge: Noyes Publication, 1984.
11. Srour, J. R., "Basic mechanisms of radiation effects on electronic materials, devices, and integrated circuits," *IEEE Nuclear and Space Radiation Effects Conference Short Course*, 1982.
12. Dawes, W. R., Jr., R. B. McLean, P. A. Robinson, Jr., and J. J. Silver, *Hardening Semiconductor Components Against Radiation and Temperature*. New Jersey: Noyes Data Corporation, 1989.
13. Messenger, G. C. and M. S. Ash, *The Effects of Radiation on Electronic Systems*. New York: Van Nostrand Reinhold Co., 1986.
14. Gad-el-Hak, M., *The MEMS Handbook*. Boca Raton: CRC Press, 2002.
15. Kovacs, G. T. A., *Micromachined Transducers Sourcebook*. Boston: McGraw Hill, 1998.

16. Madou, M., *Fundamentals of Microfabrication*. Boca Roton: CRC Press, 1997.
17. Koester, D., A. Cowen, R. Mahadevan, and B. Hardy, *PolyMUMPs Design Handbook: a MUMPS<sup>®</sup> process*. Revision 8.0, MEMSCAP, 2002.
18. Walters, M., J. Carter, A. Cowen, and G. Hames, *SOIMUMPs Design Handbook: a MUMPS<sup>®</sup> process*. Revision 2.0, JDS Uniphase MEMS Business Unit, 2002.
19. Cowen, A, B. Dudley, E. Hill, M. Walters, R. Wood, S. Johnson, H. Wynands, and B. Hardy, *MetalMUMPs Design Handbook: a MUMPS<sup>®</sup> process*. Revision 1.0, MEMSCAP, 2002.
20. Marsh, G., "Micromachinery: rolling at last?," *Materials Today*, pp. 44–49, July/August 2002.
21. Kovacs, G. T. A., N. I. Maluf, and K. E. Petersen, "Bulk micromachining of silicon," *Proceedings of the IEEE*, vol. 86, pp. 1536–1551, August 1998.
22. Halliday, D., R. Resnick, and K. S. Krane, *Physics*, vol. Volume Two: Extended Version. New York: John Wiley and Sons, Inc., 4<sup>th</sup> ed., 1992.
23. Kladitis, P. E. and V. M. Bright, "Prototype microrobots for micro-positioning and micro-unmanned vehicles," *Sensors and Actuators A*, pp. 132–137, 2000.
24. Datskos, P. G., S. Rajic, and I. Datshou, "Detection of infrared photons using the electronic stres in metal-semiconductor cantilever interfaces," *Ultramicroscopy*, vol. 82, pp. 49–56, 2000.
25. Datskos, P. G., M. J. Sepaniak, C. A. Tipple, and N. Lavrik, "Photomechanical chemical microsensors," *Sensors and Actuators B*, vol. 76, pp. 393–402, 2001.
26. Raiteri, R, M. Grattarola, H. J. Butt, and P. Skladal, "Micromechanical cantilever-based biosensors," *Sensors and Actuators B*, vol. 79, pp. 115–126, 2001.
27. Terry, M., J. Reiter, K. F. B. J. W. Suh, and G. T. A. Kovacs, "A docking system for microsatellites based on MEMS actuator arrays," *Smart Materials and Structures*, vol. 10, pp. 1176–1184, 2001.
28. Larin, F., *Radiation Effects in Semiconductor Devices*. New York: John Wiley and Sons, 1968.
29. Van Lint, V. A. J., T. M. Flanagan, R. E. Leadon, J. A. Naber, and V. C. Rogers, *Mechanisms of Radiation Effects in Electronic Materials*, vol. 1. New York: John Wiley and Sons, 1980.
30. Edmonds, L. D., G. M. Swift, and C. I. Lee, "Radiation Response of a MEMS Accelerometer: An Electrostatic Force," *IEEE Transactions on Nuclear Science*, vol. 45, pp. 2779–2788, December 1998.

31. Lee, C. I., A. H. Johnston, W. C. Tang, and C. E. Barnes, "Total Dose Effects on Microelectromechanical Systems (MEMS): Accelerometers," *IEEE Transactions on Nuclear Science*, vol. 43, pp. 3127–3132, December 1996.
32. Knudson, A. R., S. Buchner, P. McDonald, W. J. Stapor, A. B. Campbell, K. S. Grabowski, and D. L. Knies, "The Effects of Radiation on MEMS Accelerometers," *IEEE Transactions on Nuclear Science*, vol. 43, pp. 3122–3126, December 1996.
33. Schanwald, L. P., J. R. Schwank, J. J. Sniegowski, D. S. Walsh, N. F. Smith, K. A. Peterson, M. R. Shaneyfelt, P. S. Winokur, J. H. Smith, and B. L. Doyle, "Radiation effects on surface micromachined comb drives and microengines," *IEEE Transactions on Nuclear Science*, vol. 45, pp. 2789–2798, December 1998.
34. Hirano, T., T. Furuhashi, K. J. Gabriel, and H. Fujita, "Design, Fabrication and Operation of Submicron Gap Comb-Drive Microactuators," *Journal of Microelectromechanical Systems*, vol. 1, pp. 52–59, March 1992.
35. Johnson, W. A. and L. K. Warne, "Electrophysics of micromechanical comb actuators," *Journal of Microelectromechanical Systems*, vol. 4, pp. 49–59, March 1995.
36. Taylor, E. W., A. H. Paxton, H. Schöne, J. H. Comtois, A. D. Sanchez, M. A. Michalick, J. E. Winter, S. J. McKinnew, M. Osinski, P. Perlin, R. F. Carson, J. P. G. Bristow, J. Lehman, and M. K. Hibbs Brenner, "Radiation induced effects research in emerging photonic technologies: vertical cavity surface emitting lasers, GaN light emitting diodes and microelectromechanical devices," *Photonics for Space Environments V, Proceedings of SPIE*, vol. 3124, pp. 9–20, July 1997.
37. Johnstone, R. W., K. F. Ko, J. C. Yang, M. Parameswaran, and L. S. Erhardt, "The effects of proton irradiation on electrothermal micro-actuators," *Canadian Journal of Electrical and Computer Engineering*, vol. 27, pp. 3–5, January 2002.

### *III. Device Design*

The creation of MEMS devices involves a three step process. First, a computer software suite is used to layout the desired structure. Second, the computer layouts are submitted to a commercial foundry for fabrication. Third, the fabricated devices are received from the foundry and post-processing is accomplished. This chapter discusses the first two steps of the creation process as they pertain to this research. Section 3.1 discusses the software package used to design and layout the MEMS devices. Section 3.2 discusses the commercial fabrication process used to fabricate the test devices. Finally, Section 3.3 presents all the devices designed and fabricated for this research.

#### *3.1 Designing*

The first step in creating MEMS devices is to layout the desired devices. L-Edit: The Layout Editor<sup>©</sup> was the design software package used for this research. L-Edit is a broad-featured integrated circuit mask layout tool. The program uses elements drawn on layers to represent the masks used in the particular foundry process used to fabricate the MEMS devices. A technology file is used to specify the available layers, relationship between layers and the type of mask file used. Each of the available layers are represented on the computer by different colors and patterns. Figure 3.1 (a) illustrates example of an L-Edit layout of a MEMS device and Figure 3.1 (b) is a scanning electron micrograph (SEM) of the same device. Once the desired layouts are obtained, the mask file is electronically sent to the commercial foundry for fabrication.

#### *3.2 MUMPs<sup>®</sup> Fabrication process*

All the devices tested in this thesis were fabricated by the Cronos Integrated Microsystems MUMPs<sup>®</sup> foundry. PolyMUMPs is a service, provided by Cronos, to

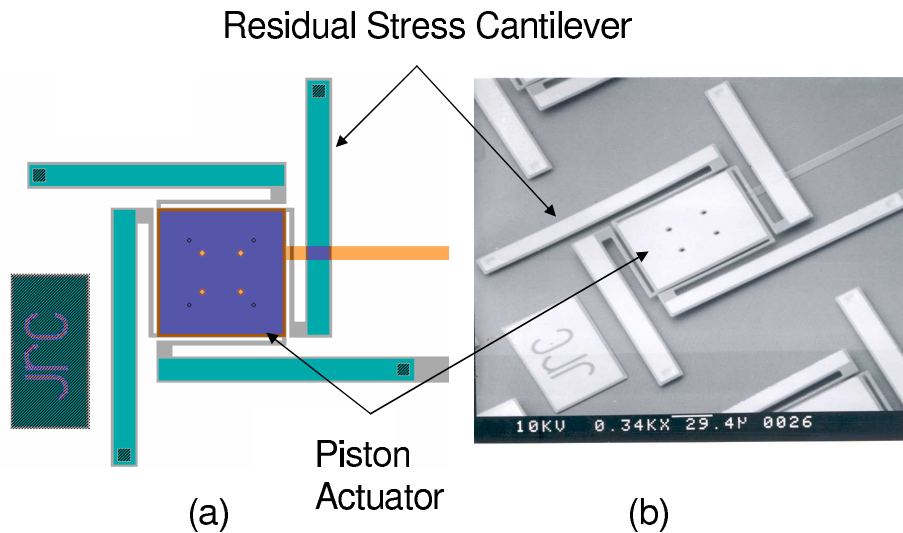


Figure 3.1 L-edit layout (a) and scanning electron micrograph (b) of a 100  $\mu\text{m}$  square piston actuator connected to four residual stress cantilevers.

the MEMS industry, that allows low-cost prototype fabrication of polysilicon surface micromachined devices. A description of their surface micromachined process, as well as design rules and considerations, can be found in the MUMPs<sup>®</sup> Design Handbook [1]. A brief discussion of the PolyMUMPs processing steps follows.

The PolyMUMPs process is a three layer surface micromachining process. Both the structural layers (polysilicon), and the sacrificial layers (phosphosilicate glass (PSG)), are deposited using Low Pressure Chemical Vapor Deposition (LPCVD). The first structural layer is electrically isolated from the substrate by a layer of silicon nitride, also deposited by LPCVD. The substrate is a (100) oriented, 100 millimeter (mm) n-type silicon wafer.

Figure 3.2 is an example of the different layers available and the different masks used in the PolyMUMPs process. The MUMPs<sup>®</sup> fabrication process will now be described. The reader may want to refer back to Figure 3.2 to clarify particular layers and masks as they are described.



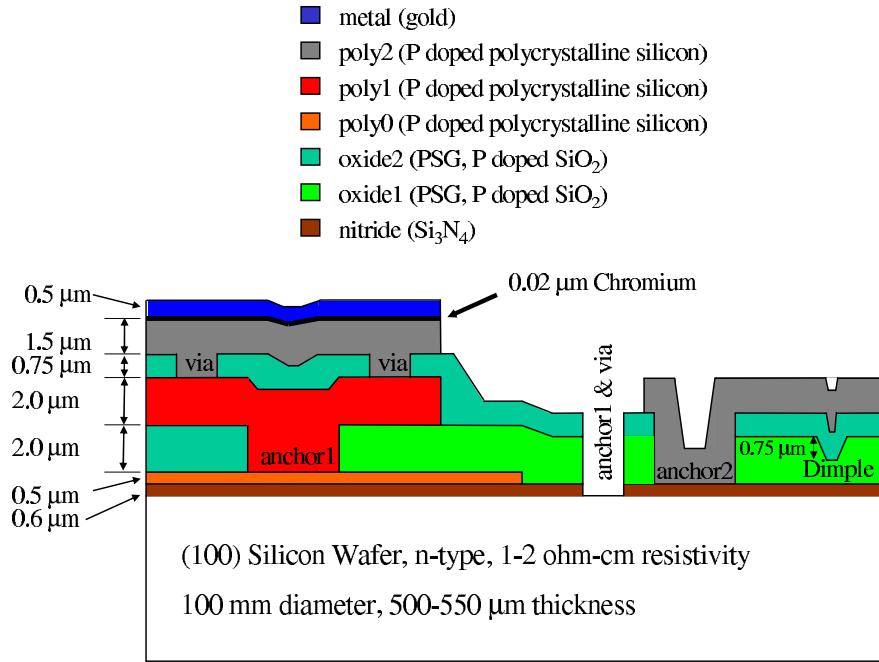


Figure 3.2 Drawing of the different layers available in the MUMPs® process. The layer names, layer thicknesses, and mask names are given.

The fabrication process begins by doping the surface of the substrate wafer. The doping is accomplished using a standard diffusion furnace and Phosphorus Oxychloride (POCl<sub>3</sub>) as a dopant source. The heavy doping mitigates the amount of charge feedthrough to the substrate from electrostatic devices. Next, a 600 nanometer (nm) thick layer of silicon nitride is deposited followed immediately by the deposition of a 500 nm thick layer of polysilicon, the first structural layer (Poly 0).

Poly 0 is then photolithographically patterned with POLY0 mask and subsequently etched using a Reactive Ion Etch (RIE) system. Once this is done, the first sacrificial layer (1<sup>st</sup> Oxide), a 2.0 micrometer (μm) thick layer of PSG, is deposited. The wafer is annealed in argon gas at 1050 degrees Centigrade (°C) for 1 hour. The 1<sup>st</sup> Oxide layer is lithographically patterned using the DIMPLES mask and etched to a depth of 0.75 μm using RIE. This etch step allows dimples to be created in the second structural layer (Poly 1). The 1<sup>st</sup> Oxide layer is again lithographically patterned, this time with the ANCHOR1 mask, and etched to create anchor holes

for Poly 1. The anchor holes allow the first releasable layer to be connected to the isolating nitride layer or Poly 0, which ever is exposed.

Next, a 2  $\mu\text{m}$  thick layer of polysilicon, Poly 1, is deposited followed directly by a 200 nm thick layer of PSG. At this point a second annealing process is completed, again at 1050 °C for 1 hour. This annealing dopes the structural layer using the 1<sup>st</sup> Oxide layer and the 200 nm thick PSG as limited diffusion sources and reduces the amount of stress in the Poly 1. The thin layer of PSG is then lithographically patterned, using the POLY1 mask, and etched to form a hard mask for the etching of the Poly 1 layer. The PSG hard mask is more resistant to the polysilicon etch chemistry and thus ensures accurate transfer of the polysilicon pattern. After Poly1 is etched the hard mask is removed by RIE.

Following the etch of Poly 1 and the removal of the hard mask, the second sacrificial layer (2<sup>nd</sup> Oxide) is deposited to a nominal depth of 0.75  $\mu\text{m}$  and the wafer is again annealed. This oxide layer is etched twice using two different masks. The first etch mask (*VIA*) provides etch holes in the 2<sup>nd</sup> Oxide layer down to Poly1. This step allows electrical and mechanical connection to be made between Poly1 and the second releasable layer (Poly2). The second etch mask (*ANCHOR2* ) is provided so that both sacrificial oxides can be etched in one step. Both the *VIA* and *ANCHOR2* layers are lithographically patterned and etched by RIE.

Poly2 is now deposited to a thickness of 1.5  $\mu\text{m}$  and directly followed by a 200 nm thick layer of PSG. The thin layer of PSG is again used as a hard mask and also as a limited diffusion doping source for Poly 2. A 1050°C anneal is again accomplished to both dope and reduce the residual stresses in the polysilicon layers. The Poly2 layer is lithographically patterned using the POLY2 mask and the PSG and Poly 2 are etched using RIE. The hard mask is then removed by RIE.

The final step in the process is the deposition of a metal layer to facilitate probing, bonding, provide electrical connections and highly reflective surfaces. This layer consists of 0.5  $\mu\text{m}$  thick layer of gold. The gold layer is lithographically pat-

tered using the METAL mask. A lift-off technique is then used to facilitate the removal of unwanted gold.

It is important, however, to consider all of the steps of the Cronos' PolyMUMPs process when designing devices. The following section will discuss this process as it relates to the design of the actuator that will be tested along with the issues associated with the actuators and this research.

### *3.3 Design of Test Actuators*

The utility of all three of the actuators tested in this research have been extensively demonstrated. For this reason, the design of the actuators entailed reaccomplishing layouts found in literature. However, accomplishing in-situ measurements of the electrothermal and the residual stress cantilever proved somewhat of a challenge. Because of this, much time had to be spent on preparing a test plan so that designs could be fabricated that would facilitate measuring the required parameters. Section 3.3.1 presents the design of the electrostatic piston actuator and issues applicable to this research. Section 3.3.2 discusses the electrothermal actuator design and modifications required to accommodate in-situ measurements. The design of the residual stress cantilever is explained in Section 3.3.3.

*3.3.1 Electrostatic Piston Actuator Design.* Based on the background information presented in Section 2.4, it is reasonable to expect that the operation of the piston actuator could be affected by radiation in two ways. First, if displacement damage were to occur in the polysilicon material making up the piston plate, then it is possible that certain material parameters could be influenced, especially Young's modulus. Any change in the Young's modulus of the polysilicon layer would change the amount of restoring force associated with the four flexures. This would result in altering the voltage-displacement relationship of the actuator. Second, trapping of charged carriers within the nitride layer could change the distribution of electric

field lines. Any change in the distribution of the electric field lines would influence the amount of electrostatic force felt by the piston plate and the voltage-deflection relationship would be altered.

The test plan for characterizing the piston actuator was created with these effects in mind. The plan is to irradiate the piston actuator under three different biasing configurations: positive bias, negative bias, and snap-down bias. The first two biasing configurations were chosen so that location and type of trapped charged could be explored. Figure 3.3 illustrates the electric field orientation and direction of travel of radiation induced charged carriers under a positive and negative bias. The figure is for illustration purposes, so the individual layers are not drawn to scale. Under a positive bias, the radiation-induced charge would be separated, with the holes being swept toward the nitride-substrate interface and electrons toward the nitride-air interface. Likewise, a negative bias would reverse the direction of travel of the separated charge with the electrons travelling toward the nitride-substrate interface and the holes travelling toward the nitride-air interface. Experimentally measured differences between these two biasing configurations can be related to the location and nature of the trapped charges. Under the positive bias configuration, holes would be swept toward the silicon nitride-substrate interface and trapped along the interface. Holes trapped in this location will oppose the positive bias applied to the actuator plate decreasing the amount of deflection associated with the applied voltage. Under the negative bias configuration, holes would be swept toward the silicon nitride-air interface and trapped. Holes trapped in this location will add to the negative bias applied to the actuator plate increasing the amount of deflection associated with the applied voltage.

The third biasing configuration was chosen to investigate the annealing properties of the nitride under high electric fields. Figure 3.4 illustrates the electric field orientation and the direction of movement of radiation-induced charge under a positive bias configuration. It illustrates the formation of trap sites at the dielectric-

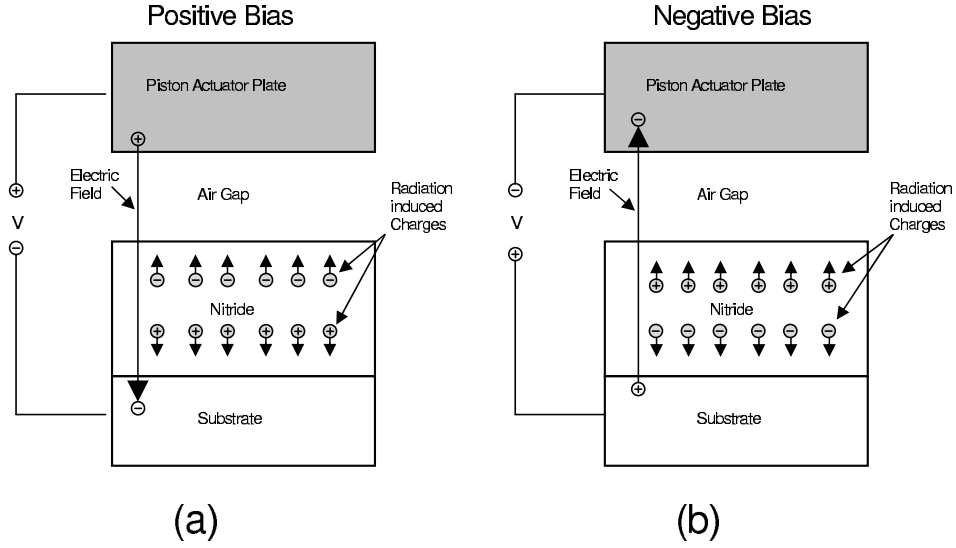


Figure 3.3 Electric field orientation and direction of travel for radiation induced charges for (a) Positive bias and (b) Negative bias. The thickness of the individual layers are not drawn to scale.

substrate interface. It was hypothesized that high electric fields could influence trapped charges so that they are swept out of the nitride.

The physical setup of the piston actuator allows the voltage-deflection relationship to be found with simple capacitance measurements. As will be shown in Section 4.1, the piston actuator can be modelled as an infinite parallel plate capacitor whose capacitance is given by:

$$C = \frac{\epsilon A}{d} \quad (3.1)$$

where  $\epsilon$  is the permittivity of the material separating the parallel plates,  $A$  is the area common to both plates and  $d$  is the distance between the two plates. Equation 3.1 illustrates the inverse relationship of the distance between the parallel plates and their capacitance. This relationship between capacitance and distance will allow characterization of the voltage-deflection relationship without any modifications to the typical design of an electrostatic piston actuator.

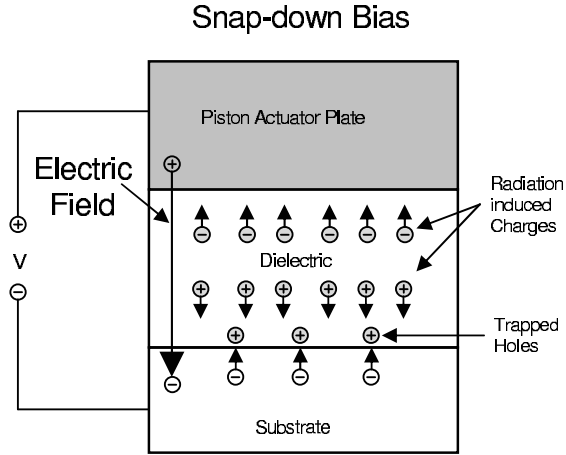


Figure 3.4 Electric field orientation, direction of travel for radiation induced charges and formation of interface traps for electrostatic piston actuator under snap-down biasing.

The only other consideration to be made in regard to designing the piston actuator was the magnitude of the capacitance that could be measured. Since the capacitance is seen to increase as the distance between the plates decrease, the smallest capacitance occurs at zero deflection. Zero-deflection capacitance measurements for square piston actuators with side lengths ranging from  $50\ \mu\text{m}$  to  $200\ \mu\text{m}$  were calculated using Equation 4.3, and material parameters given in Table 6.2. The results are illustrated in Table 3.1. Estimation of the capacitance associated with the electrostatic piston actuator is covered in Section 4.1.

Side lengths [ $\mu\text{m}$ ]	Capacitance [fF]
50	7.83
75	17.6
100	31.3
125	48.9
150	70.5
175	95.9
200	125

Table 3.1 Zero-deflection capacitance for a square piston actuator having the indicated side lengths.

With these values of capacitance in mind, I decided that a 200  $\mu\text{m}$  square piston mirror would suffice for this research. Before laying out the design; however, three more details had to be considered; including the size and position of etch holes, the width of the flexures, and the required electrical connections. Determining the size of the etch holes was easily solved by knowing that the minimum feature size recommended in the PolyMUMPs Design Handbook [1] is 2  $\mu\text{m}$ . Therefore, the size of the etch holes were set to 3  $\mu\text{m}$  to ensure they would be fabricated. The main consideration when placing the etch holes was to ensure that etchant would be able to reach the entire underside of the plate. This would ensure the structure would be completely released during the release process. The minimum feature size also was key in choosing the width of the flexures to be 3  $\mu\text{m}$ . Two electrical connections would be required to operate the piston actuator. Both the piston plate and the substrate need to be connected to voltage supplies. These connections were made using two 100  $\mu\text{m}$  square bond pads. One bond pad will be connected to the substrate and the other to the actuator piston plate.

The next step was to lay out the piston actuator design using the L-Edit software package. Figure 3.5 illustrates the L-Edit design (a) and a scanning electron micrograph (b) of the 200  $\mu\text{m}$  square piston actuator. Since only one electrical connection to the substrate is required, the substrate bond pad was positioned along the edge of the die to facilitate wire bonding.

*3.3.2 Electrothermal Actuator Design.* Based on previous radiation testing of the electrothermal actuator by Taylor [2] et al. and Johnstone et al. [3], (described in Section 2.6.3.1), it was hypothesized that radiation induced displacement damage could affect the operation of the electrothermal actuator. The deflection-voltage relationship of the electrothermal actuator is highly dependent on the resistivity of the structural material. Radiation-induced displacement damage could influence the carrier mobilities within the material and thus change the resistivity of the actuator. Any change in resistivity would change the current density and in turn the amount

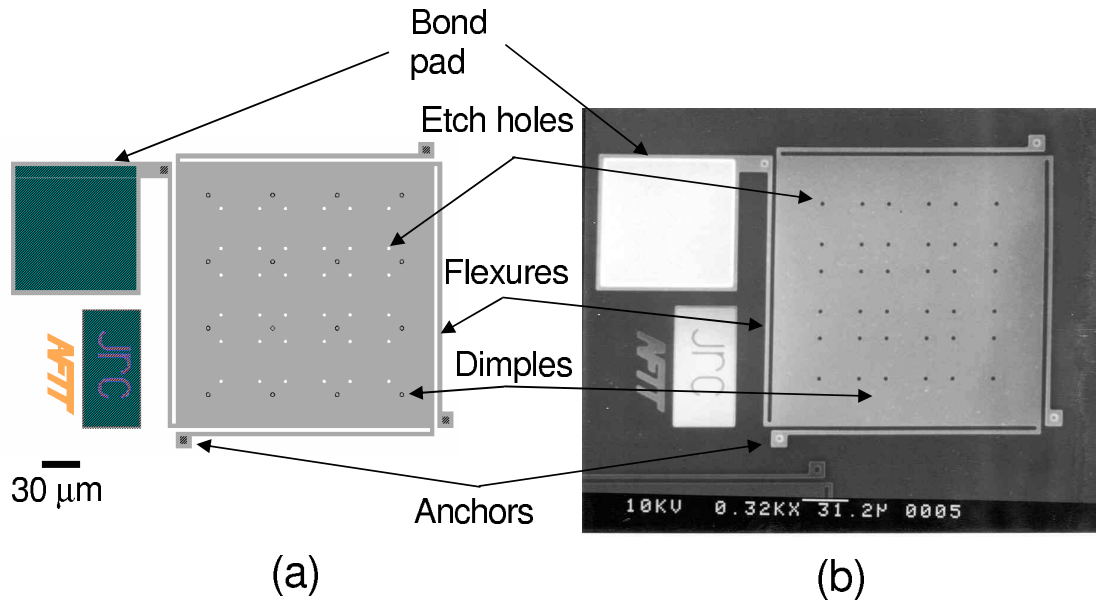


Figure 3.5 (a) L-Edit layout (b) and scanning electron micrograph illustrating top view of the electrostatic piston actuator tested in this research.

of joule heating that occurs within the actuator. The change in joule heating could influence the amount of thermal expansion experienced by the actuator and thus the voltage-deflection relationship could be affected.

The test plan for characterizing the electrothermal actuator was created with radiation-induced displacement damage in mind. The previous radiation testing accomplished by Taylor [2] and Johnstone [3] focused on deflection measurements, both during and after irradiation, and current measurements before and after irradiation. It was decided that in-situ current-voltage measurements would be taken since they have not been reported in the literature. The plan entailed measuring the deflection-voltage relationship prior to and after irradiation along with the current-voltage relationship during irradiation. Any change in the current-voltage relationship could in principle be correlated with changes in the deflection-voltage relationship.

Like the electrostatic piston actuator, the typical design of the electrothermal actuator allows in-situ current-voltage measurements to be taken without any modi-



fications. The deflection-voltage relationship can be measured with a simple micron gauge fabricated adjacent to the tip of the electrothermal actuator. The main decisions that had to be made with respect to the design of the electrothermal actuator concerned its dimensions. Comtois [4] performed a detailed study on maximizing the deflection of an electrothermal actuator by optimizing its geometry. Figure 3.6 illustrates all the elements of the electrothermal actuator and the dimension notation used. After consulting Comtois' research, the dimensions detailed in Table 3.2 were identified as optimal.

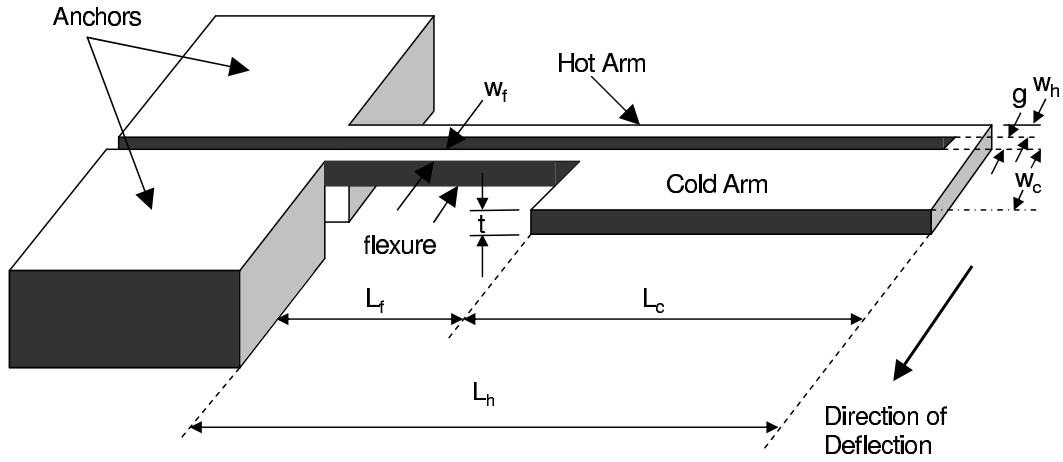


Figure 3.6 Isometric drawing of horizontally deflection electrothermal actuator detailing the dimension notation used in this research.

	Dimension [ $\mu\text{m}$ ]
$g$	2.5
$w_h$	2.5
$w_c$	18
$w_f$	2.5
$L_f$	50
$L_c$	250
$L_h$	200

Table 3.2 Dimensions used in the design of the electrothermal actuator. Figure 3.6 illustrates the correlation of the dimension notation to the electrothermal actuator design.

Figure 3.7 illustrates the L-Edit design for the electrothermal actuator that was characterized in this research. The  $100\text{ }\mu\text{m}$  square bond pads were used to make the required electrical connections. The lower substrate bond pad utilizes a combination of ANCHOR1 and VIA to breach the nitride so that an electrical connection to the substrate could be made. The deflection gage at the tip of the actuator was used to measure the deflection-voltage relationship.

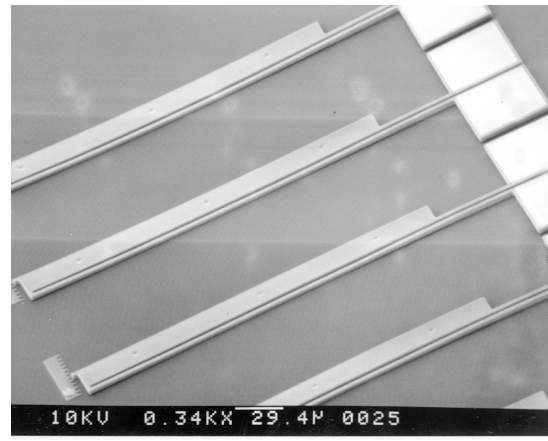
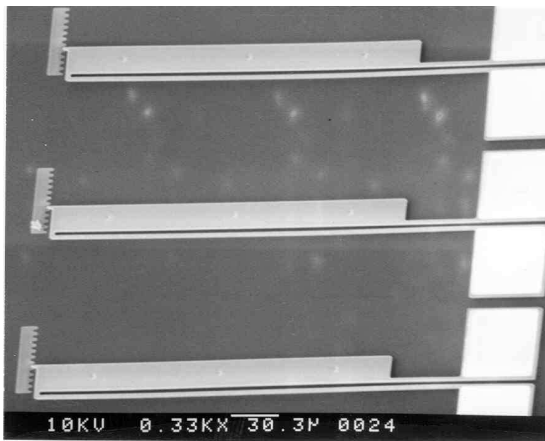
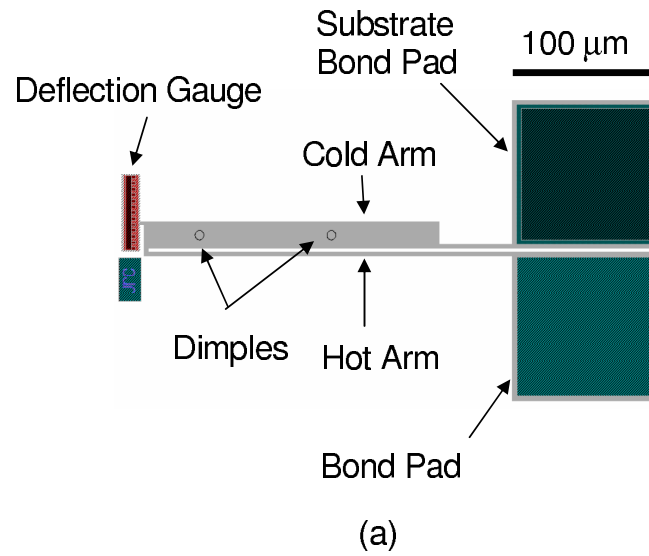


Figure 3.7 (a) L-Edit layout, (b) scanning electron micrograph illustrating top view and (c) scanning electron micrograph illustrating isometric view of the horizontally deflection electrothermal actuator tested in this research.

*3.3.3 Residual Stress Cantilever Design.* Section 2.5.4 explained how the deflection of the residual stress cantilever depends on the difference in coefficient of thermal expansion for the two thin film layers. It is this dependence on temperature that suggests that the residual stress cantilever will be affected by radiation. Wickramasinghe [5] showed that the absorption of photons by a solid can result in temperature changes. Therefore, it is hypothesized that absorption of ionizing radiation by the residual stress cantilever could cause a change in temperature and thus yield a change in tip deflection. The test plan for characterizing the residual stress cantilever centers on this temperature dependence.

The test plan for the residual stress cantilever is extremely simple when compared to the electro-static and electrothermal actuators. Although no biasing is required during the test, two separate designs were used. The first design is a simple residual stress cantilever. This actuator will not be characterized within a radiation environment. The design of the second actuator is somewhat more complex since it will be tested in-situ. The second cantilever design will consist of four residual stress cantilevers mechanically connected to a polysilicon plate. The principle of operation of this device is similar to the piston actuator discussed in Section 3.3.1. The physical setup will allow the capacitance to be measured while being subjected to ionizing radiation. Any change in capacitance can then be correlated to the change in deflection.

Figure 3.8 (a) illustrates the L-Edit layout of the simple residual stress cantilever. A scanning electron micrograph of the actual actuator is illustrated in Figure 3.8. The structural layer of the cantilever (POLY2) is 300  $\mu\text{m}$  in total length and 20  $\mu\text{m}$  wide. The thin gold layer is recessed on all sides by 2  $\mu\text{m}$  as directed by the PolyMUMPs Design Rules [1].

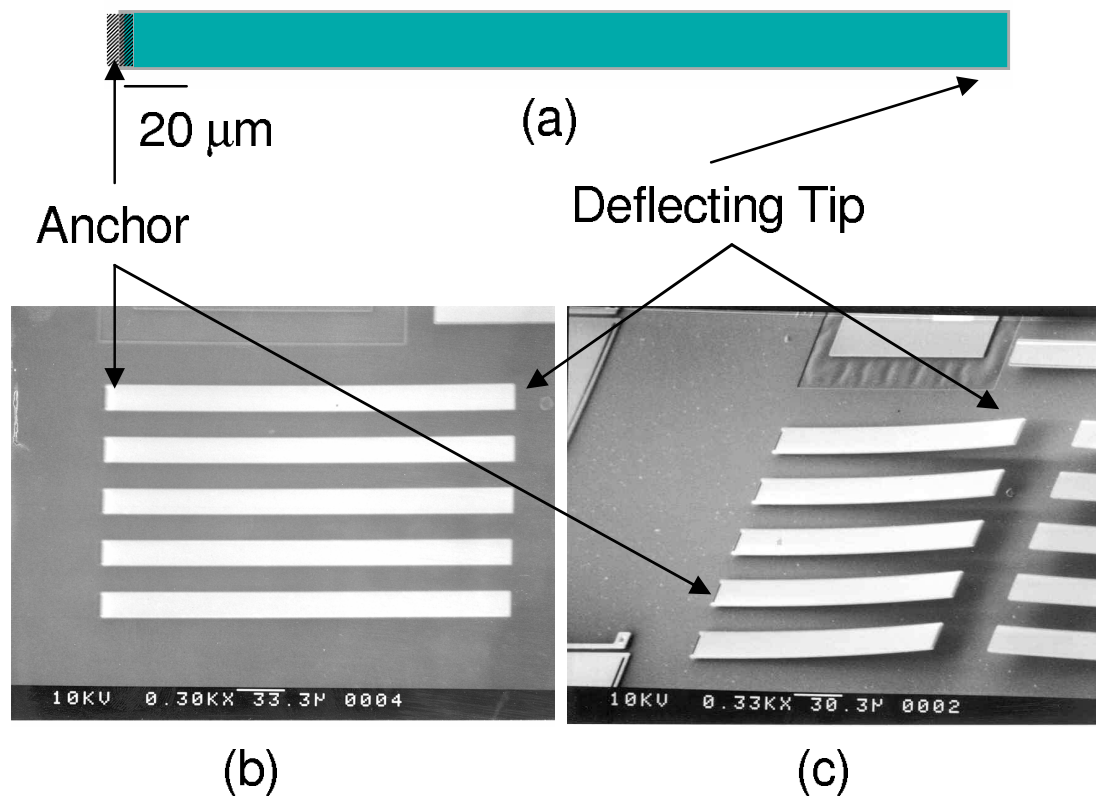


Figure 3.8 (a) L-Edit layout, (b) scanning electron micrograph looking straight down, and (c) scanning electron micrograph illustrating an isometric of  $300\ \mu\text{m}$  by  $20\ \mu\text{m}$ , residual stress cantilever tested in this research.

### *3.4 Conclusions*

The main goal of this research is to characterize the operation of the three MEMS actuators subjected to ionizing radiation. Three factors had to be considered during the design of the actuators: available test equipment, available fabrication processes, and the methods for characterization. All three factors were key in finalizing the actual design of the devices. Models must now be derived that can be used to predict the devices' operation.

## Bibliography

1. Koester, D., A. Cowen, R. Mahadevan, and B. Hardy, *PolyMUMPs Design Handbook: a MUMPS<sup>®</sup> process*. Revision 8.0, MEMSCAP, 2002.
2. Taylor, E. W., A. H. Paxton, H. Schöne, J. H. Comtois, A. D. Sanchez, M. A. Michalicek, J. E. Winter, S. J. Mckinnew, M. Osinski, P. Perlin, R. F. Carson, J. P. G. Bristow, J. Lehman, and M. K. Hibbs Brenner, “Radiation induced effects research in emerging photonic technologies: vertical cavity surface emitting lasers, GaN light emitting diodes and microelectromechanical devices,” *Photonics for Space Environments V, Proceedings of SPIE*, vol. 3124, pp. 9–20, July 1997.
3. Johnstone, R. W., K. F. Ko, J. C. Yang, M. Parameswaran, and L. S. Erhardt, “The effects of proton irradiation on electrothermal micro-actuators,” *Canadian Journal of Electrical and Computer Engineering*, vol. 27, pp. 3–5, January 2002.
4. Comtois, J. H., *Structures and Techniques for Implementing and Packaging Complex, Large Scale Microelectromechanical Systems Using Foundry Fabrication Processes*. PhD thesis, Air Force Institute of Technology, 1996.
5. Wickramasinghe, H. K., R. C. Bray, V. Jipson, C. F. Quate, and J. R. Salcedo, “Photoacoustics on a microscopic scale,” *Applied Physics Letters*, vol. 33, Dec, 1978.

## IV. Analytical Models

The role of analytical models within an experimental setting is to provide a basic understanding of device behavior without undertaking an extensive amount of computation. The following sections will develop simplified analytical models which will be used to predict and validate device operating parameters. In Section 4.1, a mathematical expression will be developed to model the deflection and capacitance as a function of applied voltage for an electro-static piston actuator. In Section 4.2 a simple computer program designed to model the deflection of a horizontally deflecting electrothermal actuator will be presented. Finally, in Section 4.3 two models will be developed to demonstrate the amount of deflection available from a residual-stress cantilever.

### 4.1 Electrostatic piston actuator

The following derivation of an analytical model for the piston actuator follows closely to the electro-static cantilever actuator model derived by Kovacs in *Micro-machined Transducers Sourcebook* [1].

A sensible place to start the derivation of an analytical model for the piston actuator is to compare the actuator to a parallel plate capacitor. The derivation for the analytical model of a piston actuator therefore begins with the equation for energy stored in a capacitor,

$$U = \frac{CV^2}{2} \quad (4.1)$$

where  $C$  is the capacitance between the piston plate and the bottom ground plane, and  $V$  is the voltage applied between the two conductors. Since the length of the sides of the piston plate are much greater than the distance between the two plates, the piston actuator can be modelled as an infinite parallel plate capacitor and the

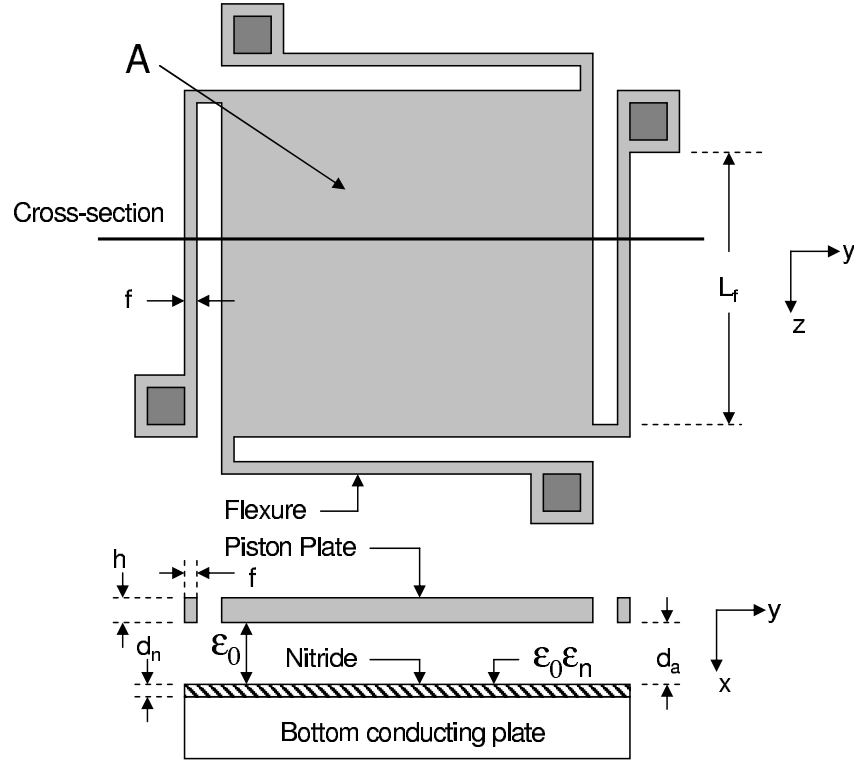


Figure 4.1 Top and cross-sectional views of electrostatic piston actuator detailing the geometrical parameters used in deriving the analytical model.

fringing electric field lines can be neglected. This simplification allows the capacitance to be represented as:

$$C = \frac{\varepsilon_o \varepsilon_r A}{d} \quad (4.2)$$

where  $\varepsilon_o$  is the permittivity of free space,  $\varepsilon_r$  is the relative permittivity of the dielectric material separating the conducting plates,  $A$  is the area common to the two conducting plates, and  $d$  is the separation between the two conducting plates.

Figure 4.1 illustrates the piston actuator and defines all the variables which will be used throughout the derivation of the analytical model. Note that subscript  $n$  denotes parameters associated with the nitride layer and subscript  $a$  denotes param-



eters associated with the air gap. Applying Equation 4.2 to the two series capacitors, formed by the top plate, air-gap, and air-nitride interface; and the air-nitride interface, nitride and bottom plate, the capacitance between the two plates of the piston actuator is:

$$C = \frac{\varepsilon_o \varepsilon_n A}{(\varepsilon_n d_a + d_n)} \quad (4.3)$$

where  $\varepsilon_n$  is the relative permittivity of the silicon nitride layer,  $d_a$  is the thickness of the airgap between the silicon nitride layer and the piston plate with zero deflection, and  $d_n$  is the thickness of the dielectric layer. Substituting Equation 4.3 into Equation 4.1 yields

$$U = \frac{1}{2} \frac{\varepsilon_o \varepsilon_n A V^2}{(\varepsilon_n d_a + d_n)} \quad (4.4)$$

If the amount of deflection the piston plate undergoes is defined as  $x$ , the distance between the silicon nitride layer and the piston plate can be defined as:

$$d_a - x : \quad 0 \leq x \leq d_a \quad (4.5)$$

Replacing  $d_a$  in Equation 4.4 with this new air-gap distance (Equation 4.5) yields an equation for the energy stored in the actuator as a function of the air-gap between the silicon nitride layer and the piston plate when the piston plate is deflected.

$$U = \frac{1}{2} \frac{\varepsilon_o \varepsilon_n A V^2}{(\varepsilon_n (d_a - x) + d_n)} \quad (4.6)$$

The attractive force applied between the two conducting plates is defined as:

$$F_E = -\frac{dU}{dx} = \frac{1}{2} \frac{\varepsilon_o \varepsilon_n^2 A V^2}{(\varepsilon_n (d_a - x) + d_n)^2} \quad (4.7)$$

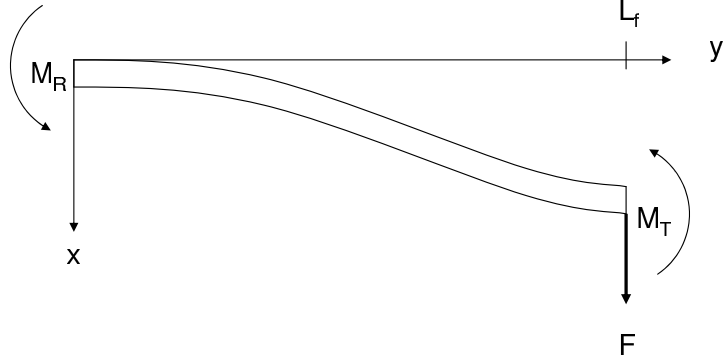


Figure 4.2 Illustration of s-shaped flexures used in the derivation of the analytical model for the electrostatic piston actuator.

Under static equilibrium the electrostatic force applied to the piston plate must be balanced by the restoring force applied to the plate by the four flexures. Therefore, the next step is to calculate the restoring force associated with the flexures. In order to calculate the restoring force associated with the flexures, it will be assumed the flexures behave as S-shaped cantilevers when deflected. Figure 4.2 illustrates the s-shaped flexure.

The governing equation for the flexure is:

$$\frac{\partial^3 x}{\partial y^3} = -\frac{F}{EI} \quad (4.8)$$

where  $F$  is the force applied to the tip of the flexure,  $E$  is the Young's modulus of the flexure material,  $I$  is the moment of inertia of the flexure,  $x$  is the deflection of the flexure and  $y$  is the distance along the flexure. The boundary conditions for the s-shaped flexure are

$$\begin{aligned} x(0) &= 0 \\ \left. \frac{\partial x}{\partial y} \right|_{y=L_f} &= 0 \\ \left. \frac{\partial x}{\partial y} \right|_{y=0} &= 0 \end{aligned} \quad (4.9)$$

where  $L_f$  is the length of the flexure. Integrating Equation 4.8 twice with respect to  $y$  and applying the boundary conditions in Equation 4.9 yields the deflection as a function of distance along the flexure:

$$x(y) = -\frac{Fy^3}{6EI} + \frac{FLy^2}{4EI} \quad (4.10)$$

Arranging Equation 4.10 into the form of Hooke's Law and evaluating at the tip of the cantilever yields the restoring force as a function of deflection for one flexure:

$$F(x) = \frac{12EIx}{L_f^3} \quad (4.11)$$

The total restoring force supplied by the four flexures is:

$$F_{restoring}(x) = 4F(x) = \frac{48EIx}{L_f^3} \quad (4.12)$$

Equating Equation 4.7 and Equation 4.12, yields the relationship between the applied voltage and the amount of deflection.

$$V(x) = \frac{4[\varepsilon_n(d_a - x) + d_n]}{L_f} \sqrt{\frac{6EI_yx}{\varepsilon_o\varepsilon_n^2L_fA}} \quad (4.13)$$

For a single flexure, illustrated in Figure 4.1, the second moment of area about the x-axis,  $I_y$  is defined as:

$$I_y = \frac{fh^3}{12} \quad (4.14)$$

where  $f$  is the width of the flexures, and  $h$  is the thickness of the flexures. Substituting Equation 4.14 into Equation 4.13 yields the applied voltage as a function of deflection for the piston actuator design shown in Figure 4.1.

$$V(x) = \frac{4h [\varepsilon_n(d_a - x) + d_n]}{L_f} \sqrt{\frac{Ehfx}{2\varepsilon_o\varepsilon_n^2L_fA}} \quad (4.15)$$

The research is focused on in-situ measurements of the voltage-deflection relationship of the piston actuator. With the resources available, there is no convenient way to directly measure the amount of deflection of the piston actuator while being operated in a radiation environment. For this reason, the simple voltage-deflection relationship defined by Equation 4.15 must be manipulated further.

As shown in Equation 4.3, the capacitance associated with the piston actuator has an inverse relationship with the amount of deflection. It is possible then to characterize the deflection of the piston actuator by taking capacitance measurements. For modelling purposes, a Matlab program was written to calculate the voltage-capacitance relationship using Equations 4.15 and 4.3. The Matlab code can be found in Appendix A.

The previous derivation resulted in a foundational equation used to model the voltage-deflection relationship. Once the voltage-deflection relationship is known the capacitance-voltage relationship can be found by using the infinite parallel plate capacitor approximation. One shortfall of the model derived thus far is that it does not account for any charge build-up within the actuator.

The research accomplished to date on MEMS devices [2–5] have listed dielectric charging as a major contributor to degradation of the devices. Therefore, with the belief that charge build-up within the nitride layer will affect the operation of the electrostatic piston actuator, the model should be expanded to include effects of charge build-up.

A simple model, developed by Bochobza-Degani [6], approximates charge trapped within the dielectric layer with a sheet of charge,  $Q$ , at the nitride-air interface. Figure 4.3 illustrates this addition of a sheet charge  $Q$ .

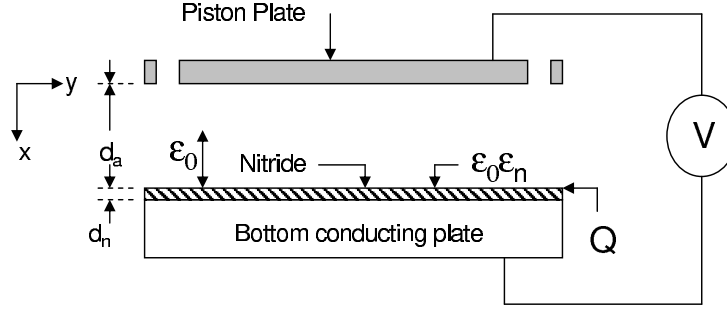


Figure 4.3 Schematic diagram of a cross-section of an electrostatic piston actuator with a sheet charge placed at the air-dielectric interface.

Bochabza-Degani defines the electrical stored energy in the system due to the sheet charge as:

$$U_Q = \frac{d_n}{2A\varepsilon_0\varepsilon_n} \frac{\frac{1}{\alpha} - \zeta}{1 - \zeta} Q^2 \quad (4.16)$$

where  $\alpha = 1 + \frac{\varepsilon_0 d_n}{\varepsilon_0 \varepsilon_n d_a}$ , and  $\zeta = \frac{x}{\alpha d_a}$ .

The force applied to the piston plate by the sheet charge is defined as:

$$F_Q = -\frac{dU}{dx} = \frac{d_a d_n (\alpha + 1)}{2A\varepsilon_0\varepsilon_n (\alpha d_a - x)^2} Q^2 \quad (4.17)$$

The force applied to the piston plate due to trapped holes opposes the force applied to the piston plate due to the actuation voltage. The new net force applied to the piston plate by the applied voltage, Equation 4.7, and the sheet charge (Equation 4.17) yields a new attracting force between the two conducting plates:

$$F_T = F_E - F_Q = \frac{1}{2} \frac{\varepsilon_0 \varepsilon_n^2 A V^2}{(\varepsilon_n (d_a - x) + d_n)^2} - \frac{d_a d_n (\alpha + 1)}{2A\varepsilon_0\varepsilon_n (\alpha d_a - x)^2} Q^2 \quad (4.18)$$

where  $F_T$  is the new attracting force between the two conducting plates. Equating Equation 4.18 with the restoring force of the four flexures, given by Equation 4.12, and solving for the voltage as a function deflection,  $x$ , yields:

$$V(x) = [\varepsilon_n(d_a - x) + d_n] \sqrt{\frac{8Efh^3x}{\varepsilon_0\varepsilon_n^2L_f^3} + \frac{d_ad_n(\alpha + 1)Q^2}{A^2\varepsilon_0^2\varepsilon_n^3(\alpha d_a - x)^2}} \quad (4.19)$$

Equation 4.19 can now be used to find the deflection-voltage relationship. Once the deflection-voltage relationship is known, Equation 4.3 can be used to find the capacitance-voltage relationship as a function of geometric parameters and charge trapped in the dielectric layer.

#### 4.2 *Electrothermal actuator*

The following analytical model calculates the thermal induced stresses for the electrothermal actuator and converts these stresses into pseudo forces which are used to calculate the amount of deflection. Comtois [7], Huang [8], Hickey [9]and, Yan [10] have derived different models to predict the operation of electrothermal actuators .

A three step procedure will be used to assemble the analytical model for the electrothermal model. The first step consists of modeling the temperature distribution due to Joule heating. The second step is to calculate the thermal expansion of the actuator. The final step will be determining the deformation or deflection using a finite element method (FEM).

Before beginning the derivation, two simplifying assumptions are made for the actuator. The first assumption is that the actuator can be accurately modelled in only one dimension. The second assumption is that the only avenue for heat loss from the actuator is through conduction to the substrate through air.

Simplifying the derivation to one dimension allows the actuator to be unwrapped along a single axis. Figure 4.4 illustrates the simplified coordinate system with top and side view of the unwrapped actuator.

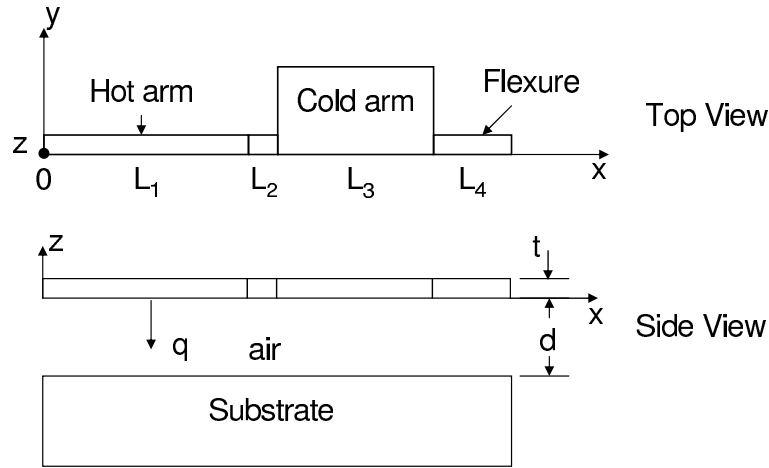


Figure 4.4 Top view of electrothermal actuator unwrapped along x axis and side view of actuator with elevation of actuator above substrate surface,  $d$ , and actuator thickness,  $t$ , labelled.

As mentioned earlier, the first step in assembly the model is to model the temperature distribution. This must be done for every element of the actuator. The temperature distribution within an element is dependent on the amount of internal heat generated, the amount of heat stored by the element, and the rate at which heat is transferred to the surrounding environment. The rate at which heat is transferred is governed by the material's thermal conductivity. The heat equation governs the temperature profile within each element.

$$\nabla^2 T + \frac{1}{k} q_{gen} = \frac{\rho c}{k} \frac{\partial T}{\partial t} \quad (4.20)$$

where  $q_{gen}$  is the power generated per unit volume,  $k$  is the thermal conductivity,  $\rho$  is the density,  $c$  is the specific heat for the material. For the actuator, the net amount of power generated per unit volume is equal to the amount of heat generated by joule heating minus the heat lost to the substrate by conduction. Mathematically, the net power generated is given by:

$$q_{gen} = q_{Joule} - \frac{hp}{A}(T - T_{substrate}) \quad (4.21)$$

where  $q_{Joule}$  is the amount of heat generated by joule heating,  $p$  is the parameter where convection occurs,  $A$  is the cross-sectional area,  $T_{substrate}$  is the temperature of the substrate, and  $h$  is the heat transfer coefficient. The heat transfer coefficient is defined by:

$$h = \frac{k_{air}}{d} \quad (4.22)$$

where  $k_{air}$  is the thermal conductivity of the air, and  $d$  is the distance to the substrate. Assuming steady-state, and substituting Equation 4.21 into Equation 4.20 yields the one-dimensional heat equation:

$$\frac{d^2T}{dx^2} + \frac{1}{k}q_{Joule} - \frac{hp}{kA}(T - T_{substrate}) = 0 \quad (4.23)$$

The temperature distribution in each actuator element can now be found by solving Equation 4.23:

$$\begin{aligned} T(x) &= Ae^{\gamma x} + Be^{-\gamma x} + \varepsilon \\ \gamma &= \sqrt{\frac{hp}{kA}} \\ \varepsilon &= \frac{qA}{hp} + T_{substrate} \end{aligned} \quad (4.24)$$

where  $A$  and  $B$  are proportionality constants found by applying boundary conditions. Equation 4.24 can be generalized to account for each element of the actuator model. The generalized equation is:

$$\begin{aligned} T_i(x) &= C_i e^{\gamma_i x} + D_i e^{-\gamma_i x} + \varepsilon_i \\ \gamma_i &= \sqrt{\frac{h\rho_i}{kA}} \\ \varepsilon_i &= \frac{q_i A_i}{h\rho_i} + T_{substrate} \end{aligned} \quad (4.25)$$



where  $i$  denotes the element number, and  $C_i$  and  $D_i$  are proportionality constants found by applying boundary conditions. The boundary conditions for the electrothermal actuator are that the temperature of each element must be continuous across the boundary of adjacent elements and the heat flow must be continuous across the element boundaries. Applying these boundary conditions to Equation 4.25 allows a system of equations to be assembled. The system of equations that must be solved, using the  $Ax=b$  notation is:

$$\begin{aligned}
 A = & \begin{bmatrix}
 1 & 1 & 0 & 0 & 0 & 0 & 0 & 0 \\
 e^{\gamma_1 L_1} & e_1^{-\gamma_1 L} & -e^{\gamma_2 L_1} & -e_1^{-\gamma_2 L} & 0 & 0 & 0 & 0 \\
 0 & 0 & e^{\gamma_2 L_2} & e^{-\gamma_2 L_2} & -e^{\gamma_3 L_2} & -e^{-\gamma_3 L_2} & 0 & 0 \\
 0 & 0 & 0 & 0 & e^{\gamma_3 L_3} & e^{-\gamma_3 L_3} & -e^{\gamma_4 L_3} & -e^{-\gamma_4 L_3} \\
 0 & 0 & 0 & 0 & 0 & 0 & e^{\gamma_4 L_4} & e^{-\gamma_4 L_4} \\
 A_1 \gamma_1 e^{\gamma_1 L_1} & -A_1 \gamma_1 e^{-\gamma_1 L_1} & -A_2 \gamma_2 e^{\gamma_2 L_1} & A_2 \gamma_2 e^{-\gamma_2 L_1} & 0 & 0 & 0 & 0 \\
 0 & 0 & A_2 \gamma_2 e^{\gamma_2 L_2} & -A_2 \gamma_2 e^{-\gamma_2 L_2} & -A_3 \gamma_3 e^{-\gamma_3 L_2} & A_3 \gamma_3 e^{\gamma_3 L_2} & 0 & 0 \\
 0 & 0 & 0 & 0 & A_3 \gamma_3 e^{\gamma_3 L_3} & -A_3 \gamma_3 e^{-\gamma_3 L_3} & -A_4 \gamma_4 e^{\gamma_4 L_3} & A_4 \gamma_4 e^{-\gamma_4 L_3}
 \end{bmatrix} \\
 x = & \begin{bmatrix} C_1 & C_2 & C_3 & C_4 & C_5 & C_6 & C_7 & C_8 \end{bmatrix}^T \\
 b = & \begin{bmatrix} T_0 - \varepsilon_1 & \varepsilon_2 - \varepsilon_1 & \varepsilon_3 - \varepsilon_2 & \varepsilon_4 - \varepsilon_3 & T_0 - \varepsilon_4 & 0 & 0 & 0 \end{bmatrix}^T
 \end{aligned}$$

Now that the temperature distribution for each of the elements is known, the thermal expansion and associated stress for each element can be calculated. This leads to the second step in assembling the analytical model. As the temperature of an element changes the length of that element also changes. The uniaxial strain in the x-direction is defined as the change in length divide by the original length. Mathematically it is stated as:

$$\varepsilon_x = \frac{\delta L}{L_0} \quad (4.26)$$

where  $\varepsilon_x$  is the uniaxial strain in the x-direction,  $\delta L$  is the change in length, and  $L_0$  is the original length. The change in length,  $\delta L$ , of each element is define by:

$$\delta L_i = \int_{L_{(i-1)}}^{L_i} \alpha [T_i(x) - T_0] dx \quad (4.27)$$

where  $\alpha$  is the coefficient of thermal expansion. The associated stress can be thought of as the external load required to compress the element back to its original length. This is also the stress that would stretch the element from its original length to its new length. Mathematically, the stress is define as:

$$\sigma_x = E \frac{\delta L}{L_0} \quad (4.28)$$

where  $\sigma_x$  is the stress in the x-direction, and  $E$  is Young's modulus of the material. Now a force in the x-direction can be calculated using Equations 4.28 and 4.27. The force defined for each element is:

$$F_i = \frac{EA_i}{L_i} \delta L_i \quad (4.29)$$

The next step is to calculate the deflection of the actuator. This was done using a finite element method. The actuator was broke into four elements. Each element has two associated nodes, and thus a total of 5 independent nodes are defined for the actuator. The finite element model was developed using a general beam with three degrees of freedom to model the elements of the actuator. The boundary conditions for the model consisted of two end nodes fixed in position and temperature. Next, the forces defined by Equation 4.29 are converted to a global coordinate system and applied to the applicable nodes. The reactions associated for each node is then calculated. The tip deflection of the actuator is found from these reactions. A Matlab<sup>®</sup> script, presented in Appendix B, was used to calculate the deflection.

The analytical model derived for the electrothermal actuator can be used to predict the deflection of the actuator when operated in the linear elastic region. The model fails to predict the deflection of the actuator when plastic deformation occurs.

### 4.3 Residual stress cantilever

The first step in building an analytical model for the bi-layer cantilever is to define the geometry of the device. The following model derivation will use the coordinate system and geometry illustrated in Figure 4.6. There are three sources of stress associated with the bi-layer cantilever. First, the fabrication process introduces internal stresses in the metal film layer. Second, the fabrication process introduces internal stresses in the polysilicon structural layer of the cantilever. Lastly, the mismatch in coefficient of thermal expansion between the gold metal layer and the polysilicon structural layer results in stresses between the layers.

Figure 4.5 can be referenced throughout the following discussion. Note that subscript  $f$  is used to denote parameters associated with the thin film of gold and subscript  $s$  is used to denote parameters associated with the structural layer of polysilicon.

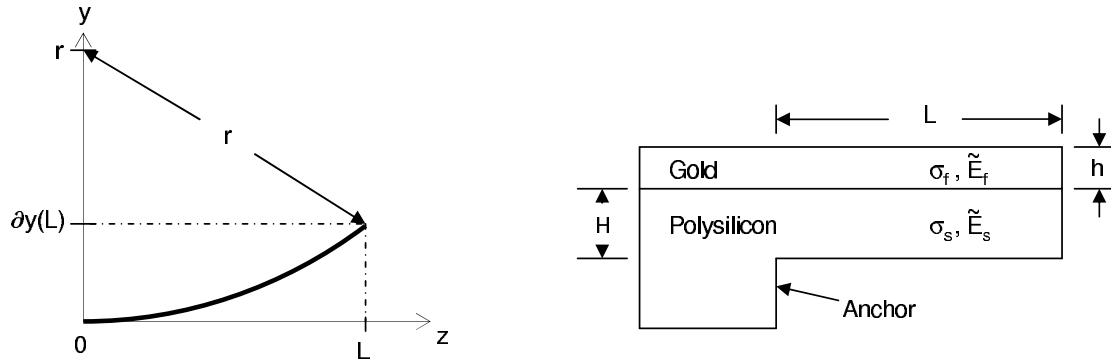


Figure 4.5 Definition of variables used in the derivation of the analytical model used to calculate radius of curvature and tip deflection of a residual stress cantilever

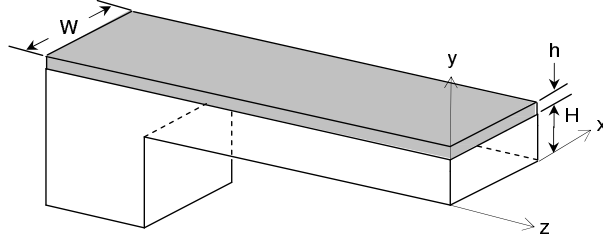


Figure 4.6 Isometric view of cantilever used to derive analytical model.

The analytical model derived in Senturia's Microsystem Design will be used to model the residual stress cantilever [11]. Senturia's starts the model derivation with the Basic Beam Bending Equation.

$$\frac{1}{r} \approx \frac{\partial^2 y}{\partial x^2} = \frac{M}{EI} \quad (4.30)$$

where  $r$  is the radius of curvature associated with the deflected cantilever,  $M$  is the internal bending moment,  $E$  is Young's modulus, and  $I$  is the moment of inertia. Young's modulus is a material property unique to the structural material of the cantilever. The moment of inertia is a parameter that is defined by the geometry of the cantilever. Equation 4.30 is the basic differential equation for small angle bending of slender beams. Since the length to width ratio of the cantilever that will be tested is 30, the basic beam bending formula is a justifiable starting point.

For the cantilever illustrated in Figure 4.6, the moment of inertia about the x-axis,  $I_x$ , is defined as:

$$I_x = \frac{WH^3}{12} \quad (4.31)$$

where  $W$  is the width of the cantilever, and  $H$  is the thickness of the cantilever. The internal bending moment,  $M$ , is found by calculating the first moment of the

distributed internal stress. Therefore, a next logical step is to define the internal stress.

The derivation of the internal stress begins with the assumption that the gold film is thin compared to the thickness of the cantilever. Prior to release, the gold layer has a tensile stress,  $\sigma_f$ . Two events happen immediately following the release of the cantilever. First, the cantilever contracts until the average stress reaches zero. Since this contraction occurs in both the x and z directions within the plain of the cantilever, the biaxial modulus,  $\tilde{E}$ , must be used in Equation 4.30. The biaxial modulus is defined as:

$$\tilde{E} = \frac{E}{(1 - \nu)} \quad (4.32)$$

where  $\nu$  is Poisson's ratio. Senturia [11] defines the net tensile stress in the film after the contraction occurs by :

$$\sigma_{f,new} = \frac{\tilde{E}_s H \sigma_f}{\tilde{E}_f h + \tilde{E}_s H} \quad (4.33)$$

where  $\tilde{E}_s$  is the biaxial modulus for the cantilever structural layer,  $\sigma_f$  is the tensile stress in the thin film before the contraction, and  $\tilde{E}_f$  is the biaxial modulus of the thin film layer. The net compressive stress in the cantilever is then given by:

$$\sigma_{cantilever} = \frac{\tilde{E}_s h \sigma_f}{\tilde{E}_f h + \tilde{E}_s H} \quad (4.34)$$

The second event that occurs after release and contraction is that a net bending moment is induced on the beam by the tensile gold film. The bending moment can then be found by summing the moments from the stresses defined in Equation 4.33 and Equation 4.34.

$$M = \int_{H/2}^{-H/2} \sigma_{cantilever} z dz + \int_{H/2-h}^{H/2} \sigma_{f,new} z dz \quad (4.35)$$

where  $z$  is the distance along the cantilever as defined in Figure 4.5. With the assumption that the gold film is thin compared to the cantilever thickness, the second integral in Equation 4.35 simplifies to:

$$\int_{H/2-h}^{H/2} \sigma_{f,new} z dz = \sigma_{f,new} \frac{Hh}{2} \quad (4.36)$$

If the small relaxation which occurred at release is ignored the bending moment simplifies to:

$$M = \sigma_f \frac{Hh}{2} \quad (4.37)$$

Equation 4.37 can now be combined with Equation 4.30 to obtain the radius of curvature of the cantilever. However, the EI product must now be replaced with the  $\tilde{E}I$  product to accommodate for the biaxial behavior. The  $\tilde{E}I$  product must also be calculated for the entire structure, the cantilever as well as the thin gold film. For the structure illustrated in Figure 4.6 Senturia [11] calculates the  $\tilde{E}I$  product as

$$\tilde{E}I = \tilde{E}_s \int_{-H/2}^{H/2} y^2 dy + \tilde{E}_f h \left( \frac{H}{2} \right)^2 \quad (4.38)$$

Which simplifies to:

$$\tilde{E}I = \frac{1}{12} H^2 (\tilde{E}_s H + 3\tilde{E}_f h) \quad (4.39)$$

Substituting Equation 4.37 and Equation 4.39 into the basic beam bending equation 4.30 yields the radius of curvature for the residual stress cantilever:

$$r = \frac{H(\tilde{E}_s H + 3\tilde{E}_f h)}{6\sigma_f h} \quad (4.40)$$

One important parameter to know for residual stress cantilevers is the maximum amount of deflection. Now that the radius of curvature of the cantilever is known, the maximum deflection can be calculated by referencing Figure 4.5. Note that the tip deflection can be defined as:

$$\partial y(L) = r - r \sin \left( \cos^{-1} \left( \frac{L}{r} \right) \right) \quad (4.41)$$

Substituting Equation 4.40 into Equation 4.41 yields:

$$\partial y(L) = \frac{H}{6\sigma_f h} (\tilde{E}_s H + 3\tilde{E}_f h) \left( 1 - \sin \left( \cos^{-1} \left( \frac{6\sigma_f h L}{H(\tilde{E}_s H + 3\tilde{E}_f h)} \right) \right) \right) \quad (4.42)$$

The previous derivation provided two important equations used to model the behavior of a residual stress cantilever. Equation 4.40 models the radius of curvature for a deflected, residual stress cantilever. Equation 4.41 models the maximum amount of deflection that occurs at the tip of the cantilever.

As stated earlier, the mismatch in coefficients of thermal expansion between the gold film and the polysilicon structural layer also results in stresses being introduced within the layers. Therefore, it is also possible to model the changes in tip deflection due to changes in the temperature of the cantilever. Hsueh [12] derived such a model. Hsueh defines the radius of curvature for a bi-layer structure with residual stress by:

$$\frac{1}{r} = \frac{6E_f h}{E_s H^2} \left[ 1 + \frac{h}{H} \left( 1 - 4 \frac{E_f}{E_s} \right) \right] (\alpha_f - \alpha_s) \Delta T \quad (4.43)$$

where  $\alpha_f$  is the coefficient of thermal expansion of the thin gold layer,  $\alpha_s$  is the coefficient of thermal expansion of the structural polysilicon layer, and  $\Delta T$  is a change in temperature that creates the residual stresses. Once the radius of curvature is calculated using Equation 4.43, Equation 4.41 can be used to calculate the tip deflection.

This section has presented three equations used to predict the amount of deflection obtained from a residual stress cantilever. Equation 4.40 and Equation 4.43 use two different methods to calculate the radius of curvature. Equation 4.41 can then be used to calculate the tip deflection.

#### 4.4 *Conclusions*

This chapter has focused on deriving first order analytical models capable of predicting the operation of the three MEMS actuators tested in this research. Two analytical models were derived which give a prediction for the deflection-voltage relationship for an electrostatic piston actuator. A finite element model was derived and programmed using Matlab<sup>®</sup> which predicts the deflection-voltage relationship for a general horizontally deflecting, electrothermal actuator. The last analytical model derived yields a prediction of the deflection of a residual stress cantilever. A model developed by Hsueh [12] was also presented that related the deflection of a residual stress cantilever to a change in temperature. Comparisons of the models results with actual operation of the MEMS actuators is presented in Chapter VI.



## Bibliography

1. Kovacs, G. T. A., *Micromachined Transducers Sourcebook*. Boston: McGraw Hill, 1998.
2. Knudson, A. R., S. Buchner, P. McDonald, W. J. Stapor, A. B. Campbell, K. S. Grabowski, and D. L. Knies, "The Effects of Radiation on MEMS Accelerometers," *IEEE Transactions on Nuclear Science*, vol. 43, pp. 3122–3126, December 1996.
3. Edmonds, L. D., G. M. Swift, and C. I. Lee, "Radiation Response of a MEMS Accelerometer: An Electrostatic Force," *IEEE Transactions on Nuclear Science*, vol. 45, pp. 2779–2788, December 1998.
4. Lee, C. I., A. H. Johnston, W. C. Tang, and C. E. Barnes, "Total Dose Effects on Microelectromechanical Systems (MEMS): Accelerometers," *IEEE Transactions on Nuclear Science*, vol. 43, pp. 3127–3132, December 1996.
5. Schanwald, L. P., J. R. Schwank, J. J. Sniegowski, D. S. Walsh, N. F. Smith, K. A. Peterson, M. R. Shaneyfelt, P. S. Winokur, J. H. Smith, and B. L. Doyle, "Radiation effects on surface micromachined comb drives and microengines," *IEEE Transactions on Nuclear Science*, vol. 45, pp. 2789–2798, December 1998.
6. Bochobza-Degani, O. and Y. Menirovsky, "On the effect of residual charges on the pull-in parameters of electrostatic actuators," *Sensors and Actuators A*, vol. 97-98, pp. 563–568, 2002.
7. Comtois, J. H., V. M. Bright, and M. W. Phipps, "Thermal microactuators for surface-micromachining processes," *The International Society for Optical Engineering*, vol. 2642, pp. 10–15, Oct. 1995.
8. Huang, Q. and N. K. S. Lee, "Analysis and design of polysilicon thermal flexure actuator," *Journal of Micromechanics and Microengineering*, vol. 9, pp. 64–70, 1999.
9. Hickey, R., D. Sameoto, T. Hubbard, and M. Kujath, "Time and frequency response of two-arm mmicromachined thermal actuators," *Journal of Micromechanics and Microengineering*, vol. 13, pp. 40–46, 2003.
10. Yan, D., A. Khajepour, and R. Mansour, "Modeling of two-hot-arm horizontal thermal actuator," *Journal of Micromechanics and Microengineering*, vol. 13, pp. 312–322, 2003.
11. Senturia, S. D., *Microsystem Design*. Boston: Kluwer Academic Publishers, 2001.

12. Hsueh, C. H., “Modeling of elastic deformation of multilayers due to residual stresses and external bending,” *Journal of Applied Physics*, vol. 91, pp. 9652–9656, 15 June 2002.

## *V. Experimental Setup*

This chapter presents the procedures and equipment used to characterize the MEMS actuators in an ionizing radiation environment. Section 5.1 discusses the equipment used to capture images of the MEMS devices. Section 5.2 presents the measurement equipment used in device characterization. Section 5.3 discusses the two radiation sources used to irradiate the actuators. Section 5.4 discusses the post-processing steps required to prepare the MUMPs<sup>®</sup> fabricated actuators for radiation testing. The last section of the chapter, Section 5.5 presents the procedures used to characterize the three MEMS actuators tested in this research.

### *5.1 Image Capture*

Two methods were used in this research to document devices and their operation. The first method utilized an Emcal Scientific, 1/3 inch color video camera mounted on an analytical probe station to capture both still images and video. The output of the video camera was connected to a computer through a video acquisition card. The software package Ulead<sup>®</sup> VideoStudio 5 by Ulead Systems Inc. was used to process both the captured video and still pictures. Figure 5.1 is a photograph of the Micromanipulator Probe station, test equipment rack and video image processing cart located in the AFIT MEMS Test Laboratory.

The second method used to record images was a Scanning Electron Microscope (SEM). All scanning electron micrographs for this research were taken with an International Scientific Instruments WB-6 SEM. The micrographs were taken using Polaroid Polapan 55PN black and white instant sheet film. The SEM was operated at 10 kV with an emission current of 100  $\mu$ m. The SEM is pictured in Figure 5.2.

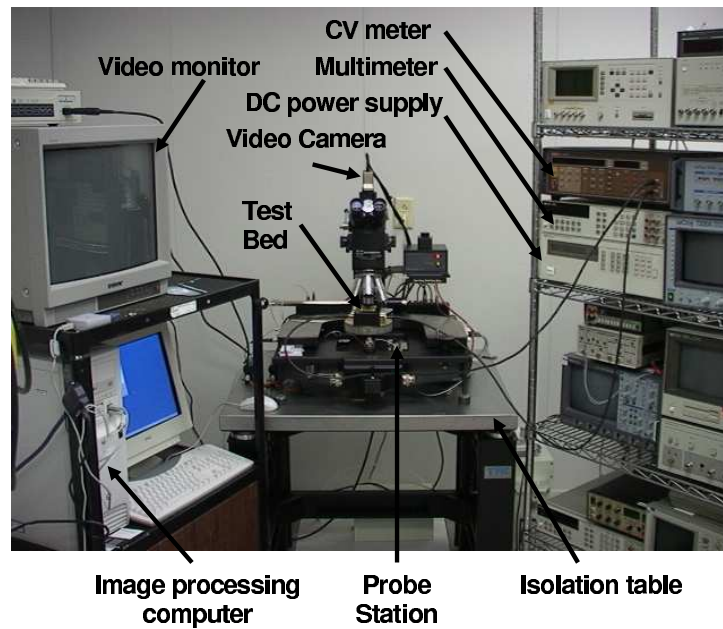


Figure 5.1 Photograph of Micromanipulator Probe Station, test equipment rack and video image processing cart.



Figure 5.2 Photograph of International Scientific Instruments WB-6 scanning electron microscope during this research.

## 5.2 Test Equipment

This section introduces the test equipment required for this research. Section 5.2.1 gives a brief overview of the measurement equipment used to characterize the actuators tested. Section 5.2.2 presents two electrical boxes used to connect the measurement equipment to the device under test (DUT).

*5.2.1 Measurement Equipment.* Three pieces of measurement equipment were used in characterizing the MEMS actuators. Characterizing the electrostatic piston actuator was accomplished using an HP6642A Direct Current (DC) power supply and a Keithley 590 CV meter. The electrothermal actuator was characterized using an HP 6642A DC power supply and an HP 3458A multimeter. The following is a short overview of the important details for each piece of measurement equipment.

*5.2.1.1 HP 6642A Direct Current Power Supply.* The HP 6642A DC power supply is a 4 output series regulated system power supply. Each output is capable of providing 40 watts with voltages ranging from 0 to 50 volts. The power supply is controllable through both front panel and General Purpose Interface Bus (GPIB). Output one was used for all biasing required for this research.

*5.2.1.2 HP 3458A Multimeter.* The HP 3458A multimeter is a 7 function all purpose multimeter. The meter is capable of measuring alternating current (AC) and DC voltages and currents, resistance, frequency and period. The meter is controllable through both front panel and GPIB. For this research the multimeter was used to measure DC current draw for the electrothermal actuators.

*5.2.1.3 Keithley 590 CV Meter.* The Keithley 590 CV Meter is capable of measuring capacitance and conductance. The measurement can be taken at either 100 kHz or 1 MHz. The CV meter has four measurement ranges: 2pF/2S, 20pF/20 $\mu$ S, 200pF/200 $\mu$ S and 2nF/2mS. The meter is controllable through both

front panel and GPIB. For this research the CV meter was used to measure the capacitance associated with the electrostatic piston actuator while varying the DC bias.

*5.2.2 Connection Boxes.* During this research, electrical connections were required between the measurement equipment and the DUT. There were two issues associated with these electrical connections that presented unique challenges. The first issue was how to connect the DIP mounted MUMPs® die to the test equipment. This was solved by building a test bed which connected BNC connectors to each pin of a 14 pin, dual in-line socket. Figure 5.3 is a picture of the test bed used throughout this research. The second issue was interconnecting measurement equipment with different electrical connectors. A splitter box (Figure 5.4) was built that facilitated connecting the DUT to the power supply and the multimeter. A circle with a dot centered in it was used to represent the BNC connections. This notation is used in all schematic diagrams containing BNC connectors. The circle represents the cable shield or ground connection and the centered dot represents the main coaxial conductor. Therefore, any lines connected to the outer circle represent electrical connections made to the grounding conductor while lines connected to the center dot represent electrical connections made to the main coaxial conductor.

### *5.3 Radiation Sources*

Two AFRL radiation sources were used for this research. The sources are maintained and operated by the Space Electronics and Protection Branch (AFRL/VSSE) at Kirtland AFB, New Mexico. The two sources used are the Co-60 gamma radiation source and the LEXR source. Section 5.3.1 discusses the Co-60 source and associated experimental setup. Section 5.3.2 describes the LEXR source and associated experimental setup.

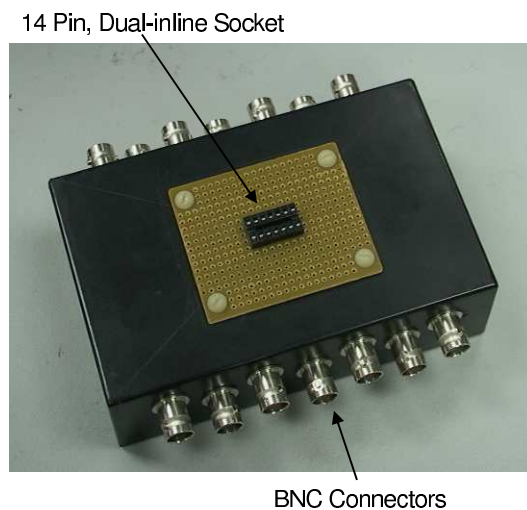


Figure 5.3 Picture of test bed used to provide electrical connections to the test die during irradiation. Each of the fourteen leads are connected to one of the BNC connectors on the side of the box.

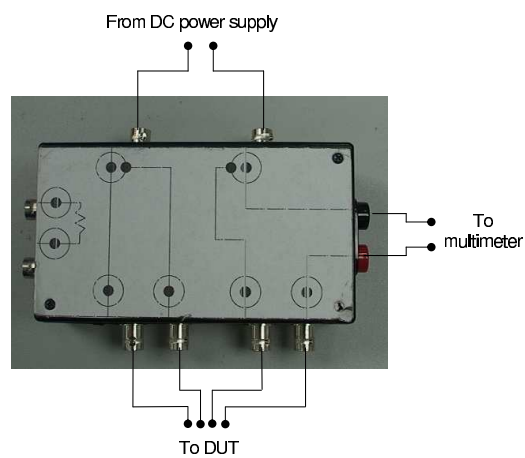


Figure 5.4 Picture of splitter box built to facilitate electrical connections between the DUT and the measurement equipment.

5.3.1 *Cobalt 60 Gamma Source.* The Co-60 source is housed in a 1500 square foot facility. The source can deliver a maximum total ionizing source of  $10 \frac{krad(Si)}{min}$  or a minimum of  $<1 \frac{rad(Si)}{min}$ . Co-60 is an unstable isotope which decays into the stable isotope Nickle-60 (Ni-60). Co-60 has a 5.27 year half-life. The energy level diagram for this decay is shown in Figure 5.5. The emitted  $\beta^-$  particle has an average energy of 0.0093 MeV and a maximum energy of 0.314 MeV. Since less than one in  $10^6$  Co-60 nuclei will decay directly to a Ni-60 ground state, the resulting Ni-60 nucleus will usually be in an excited state. The excited Ni-60 nucleus will decay into a stable state by emitting a 1.17 MeV gamma ray followed by a 1.33 MeV gamma ray.

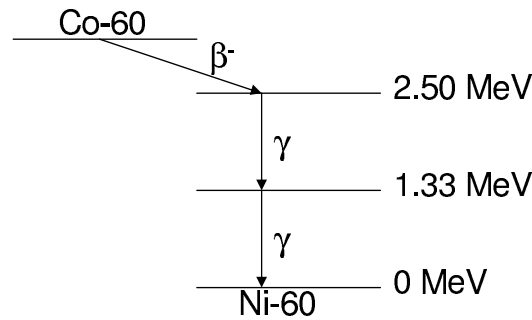


Figure 5.5 Cobalt decay scheme.

The experimental setup used to irradiate the MEMS actuators is illustrated in Figure 5.6. All three actuators were irradiated with the same experimental setup. The physical layout of the source provides plenty of room for placing all test equipment within the source facility. An eight inch thick lead brick wall was built between the source and the test equipment. This lead wall minimized the dose absorbed by the test equipment. The test equipment was controlled through a local computer using Agilent VEE software. The computer was interfaced from the control building located 120 feet from the source building. Remote computer access was accomplished using a ServSwitch<sup>TM</sup> Brand CAT5 KVM Micro Extender System. The system al-



allows the user to interface with the computer via a remotely located monitor, keyboard and mouse.

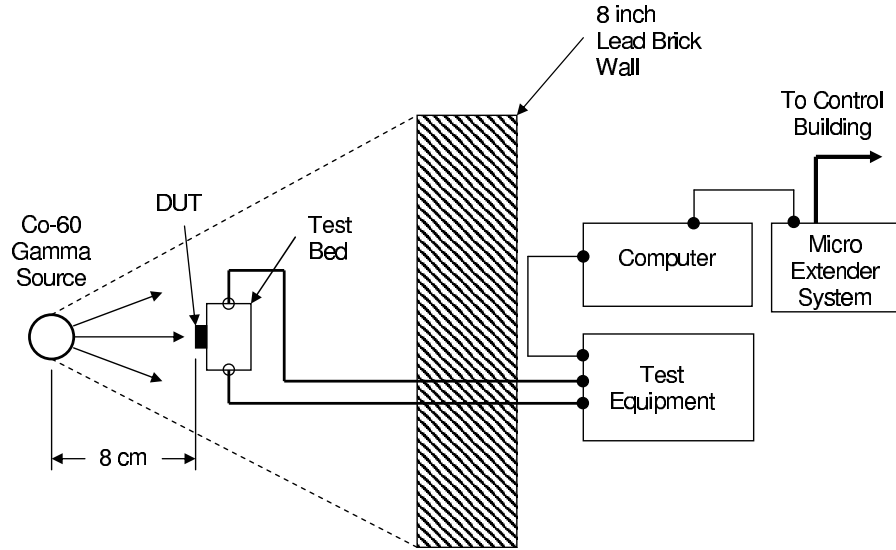


Figure 5.6 Experimental setup used for irradiating devices with the Co-60 source.

Figure 5.7 is a picture of the test bed mounted 8 cm from the Co-60 source. Figure 5.8 is a picture of the setup of the test equipment and computer in the Co-60 source building. Both Figures 5.7 and 5.8 show the lead brick walls built to shield the test equipment from ionizing radiation.

All dosimetry was provided by the source operator. The dose rate for the time of irradiation was calculated to be  $130.8 \frac{\text{rad}(\text{Si})}{\text{s}}$  at a distance of 8 cm from the center of the source tube. The high gamma energies of the Co-60 source eliminated the need to adjust the dose rate to account for the cellophane tape used to seal the packages. The experimental dose rate was confirmed using an electronic dosimeter.

The Co-60 source is operated from a control panel located 120 feet from the source building in the control building. The Co-60 source was operated by a certified operator. The operation started by programming the time required to irradiate the devices, at a dose rate of  $130.8 \frac{\text{rad}(\text{Si})}{\text{s}}$ , into the control panel. When the devices were

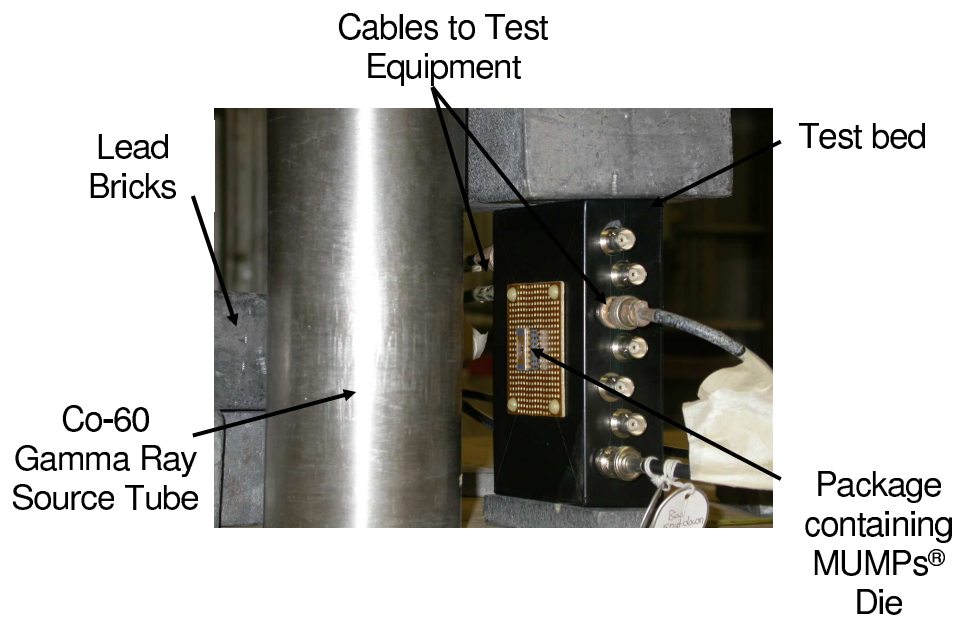


Figure 5.7 Picture of test bed mounted next to Co-60 source tube.

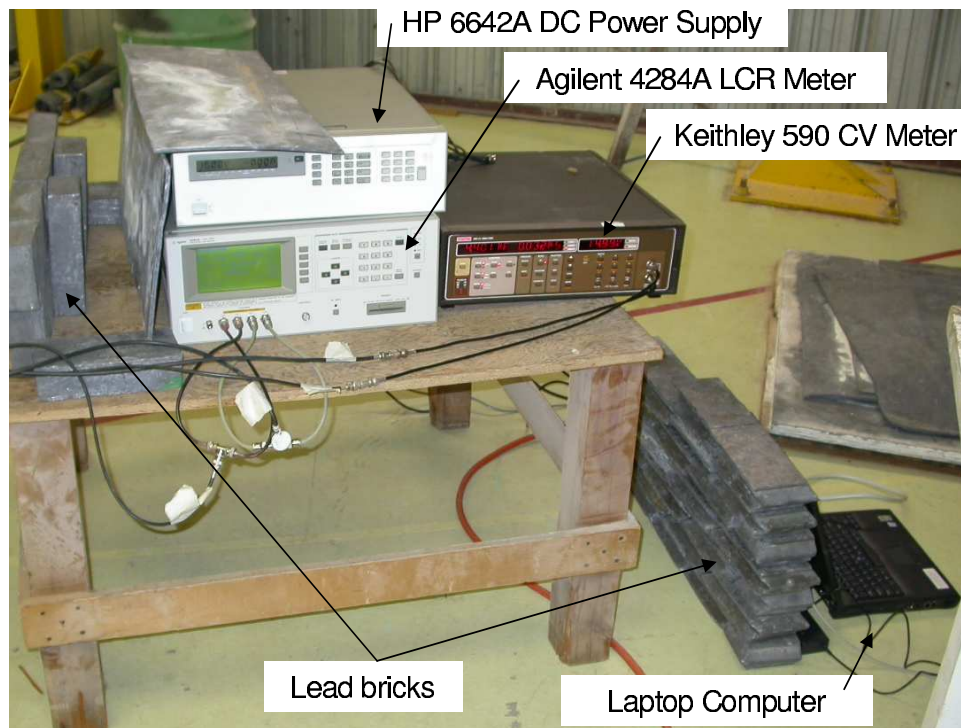


Figure 5.8 Picture of test equipment setup in Co-60 source building.

ready, the operator started the process to raise the radiation source from a shielded pit. From this point the source is automatically controlled. Approximately 30 seconds after initiating the raising process, the source reaches the full raised height. The source is automatically returned to its lowered position after the programmed time has elapsed.

*5.3.2 Low Energy X-ray Source.* AFRL's LEXR source is a Phillips MG 161 constant potential X-ray system. The system is capable of producing X-rays with end point energies ranging from 8 to 160 keV. The source can produce a maximum total ionizing dose of  $21 \frac{\text{krad(Si)}}{\text{min}}$ . The dose rate of the source is controlled by varying the X-ray tube current.

The experimental setup used to irradiate the MEMS actuators is illustrated in Figure 5.9. The same setup was used to irradiate all three actuators. The test equipment required for device characterization was placed outside the source room. Electrical connection was made to the DUT through a cable port. The test equipment was controlled through a local computer using Agilent VEE software.

Figure 5.10 is a picture of the lead shielded room housing the LEXR source. The picture also shows the location of the test equipment used for device characterization.

Figure 5.11 is a picture of the X-ray source tube, test bed and DUT. The test bed is held in place by lead bricks.

Like the Co-60 source, all required dosimetry was provided by the source operator. Initial dosimetry was accomplished using a 50 keV Pin-diode. The test consisted of measuring the dose rate 25 cm from the source with and without a cellophane window over the pin-diode. This was done to calculate the amount of attenuation the low energy X-rays would undergo after passing through the cellophane window. The cellophane window was made of the same cellophane tape used to seal the packages. Once the attenuation was known, the tube current could be adjusted so that the

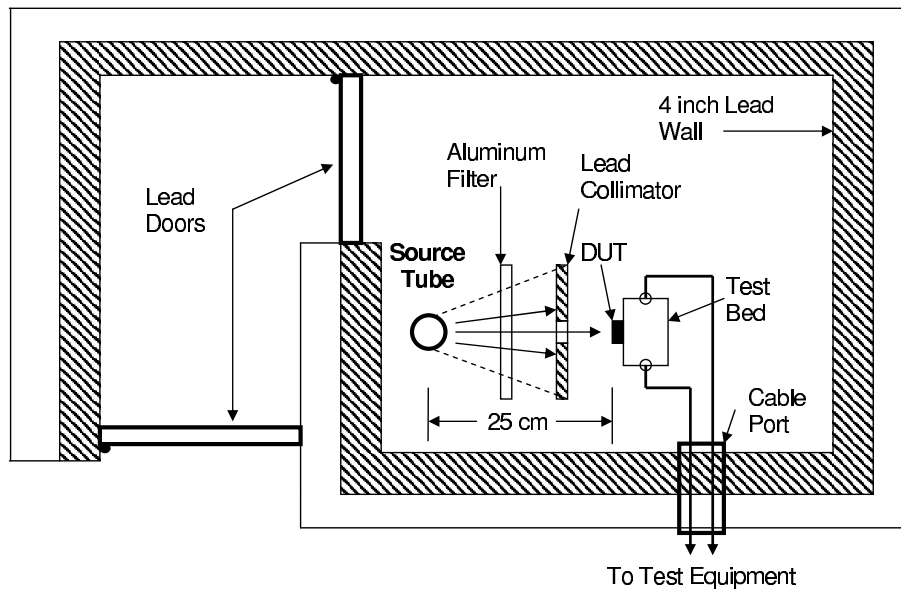


Figure 5.9 Experimental setup used for irradiating devices with the LEXR source.

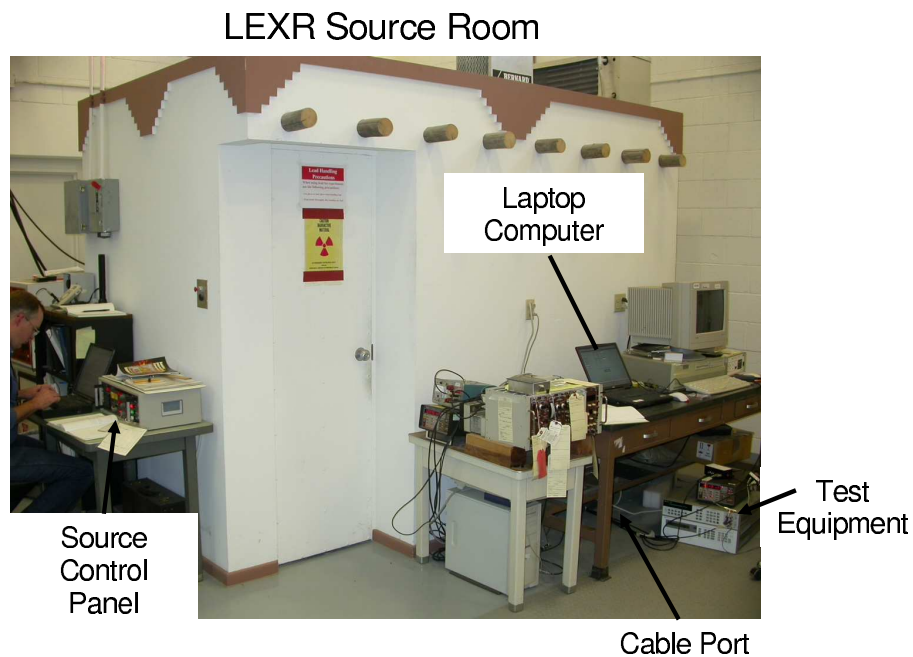


Figure 5.10 Picture of the exterior of the LEXR source room. The LEXR control panel, test equipment and computer are positioned outside the room.

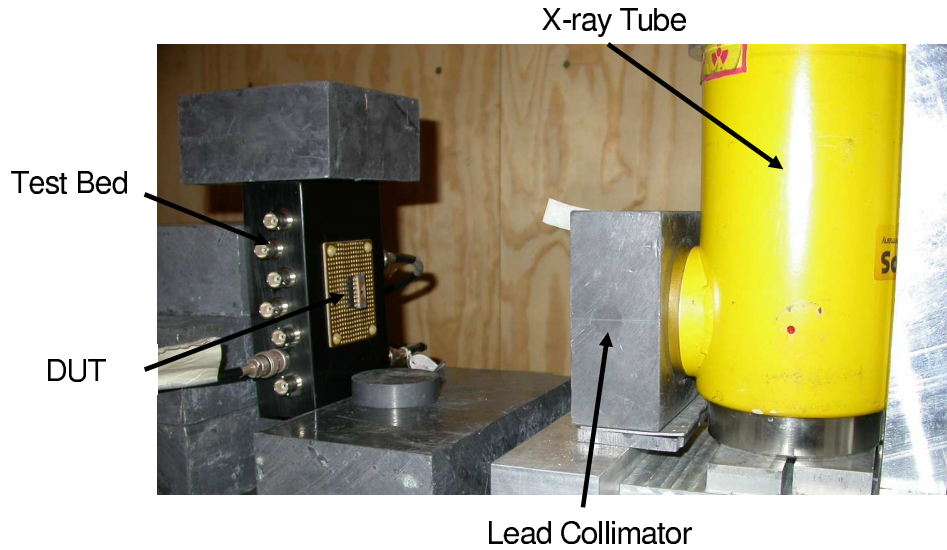


Figure 5.11 Picture of X-ray tube, test bed and DUT inside the LEXR source room.

desired dose rate was achieved. The cellophane window attenuated the low energy X-rays by approximately 18 percent which corresponds to a 10 keV reduction in energy. With this in mind, the tube current was set to 7.0 mA and the energy at 60 keV. These settings corresponded to a dose rate of  $134.5 \frac{\text{rad}(\text{Si})}{\text{s}}$ .

The LEXR source is operated from a control panel located outside the radiation room. The control panel is identified in Figure 5.10. The source is operated by a certified operator. The operation consists of programming in the required voltage tube current and radiation time and energizing the source. Once energized the source operates for the specified time and automatically de-energizes after the time has elapsed.

#### 5.4 Post-processing of MUMPs<sup>®</sup> Die

Every device tested had to first undergo post-processing before any experimental characterization could be accomplished. Section 5.4.1 explains the procedures and materials used to package the devices. Section 5.4.2 then explains the procedures used to release the devices. Wire bonding the die to the package is outlined in Sec-

tion 5.4.3. Once the devices were packaged, released, and wire bonded, they had to be sealed to avoid moisture and particulate damage. Section 5.4.4 discusses the sealing process used.

*5.4.1 Packaging Process.* Each die to be irradiated was packaged in a standard side-brazed package, commonly referred to as a DIP or dual-inline package. An appropriate size package was selected to accommodate the 2 mm by 2 mm die while providing the appropriate amount of electrical output leads. The package selected was procured from Spectrum Semiconductor Materials Incorporated. Figure 5.12 (a) is an illustration of the physical layout of the 14 pin, ceramic package used in this research. The Spectrum part number that was used is CSB01410.

The die was mounted in the DIP using Polysolder LTD. Polysolder LTD is a lead-free, silver filled, one part, electrically-conductive adhesive paste specifically designed for assembling electronic parts. A small amount of the paste was dispensed into the well of the package using a syringe. The die was pressed into the adhesive and positioned in the well using plastic tweezers. The Polysolder LTD was then cured in an Ultra Clean 100 curing oven and baked at 130 °C for 15 minutes. A packaged die is pictured in Figure 5.12 (b). Once the die were mounted, the packages were transported to the AFIT Class 10,000 Clean Room where the release process was accomplished.

*5.4.2 Release Process.* The release process was conducted in the AFIT Class 10,000 Clean Room. Some of the chemicals used in the release process can give off dangerous vapors and could cause injury if skin contact occurs. Therefore, the release process is accomplished under a chemical vapor hood within the Clean Room. While performing the release, an acid resistant laboratory apron and gloves along with eye protection are worn. Acid resistant tweezers were used to transfer the packaged die between petri dishes and acid resistant beakers. Figure 5.13 illustrates the experimental setup used throughout the release process.

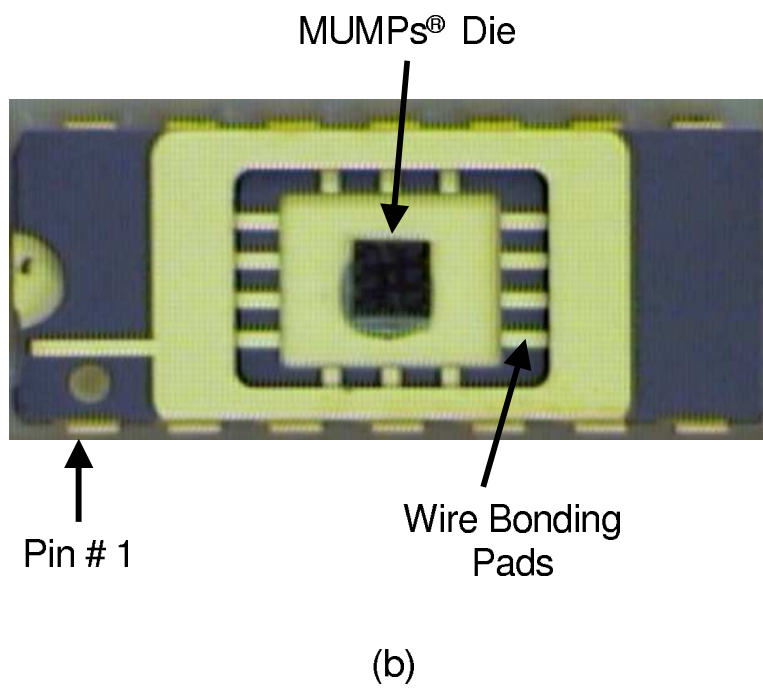
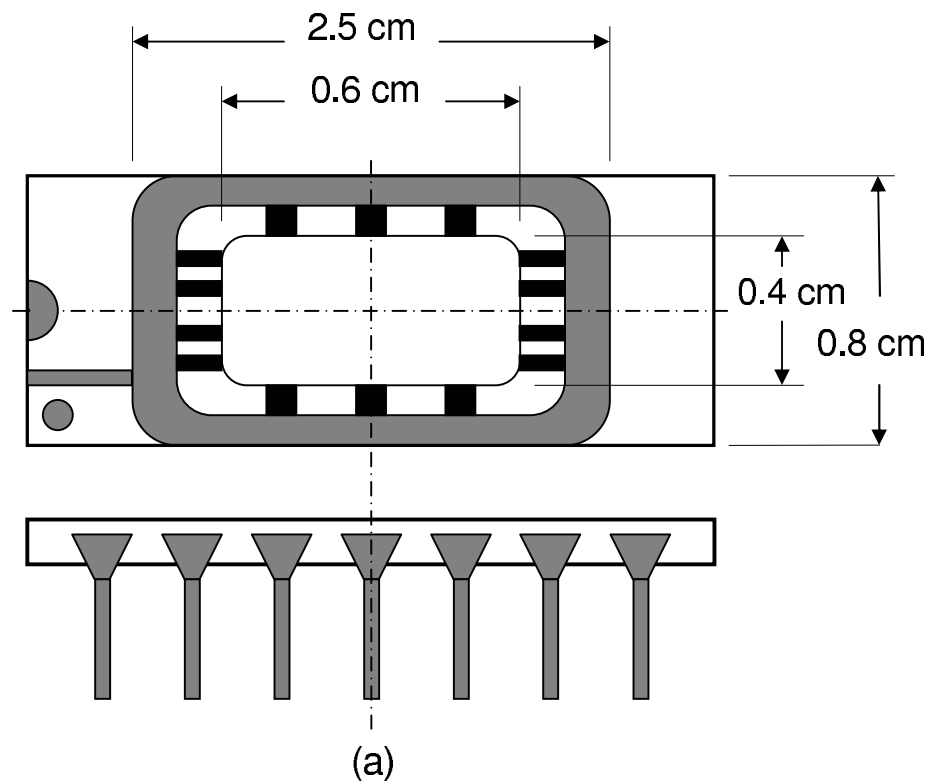


Figure 5.12 (a) Illustration and leading particulars of ceramic package used in this research and (b) picture of MUMPs® die packaged in ceramic 14 pin DIP.

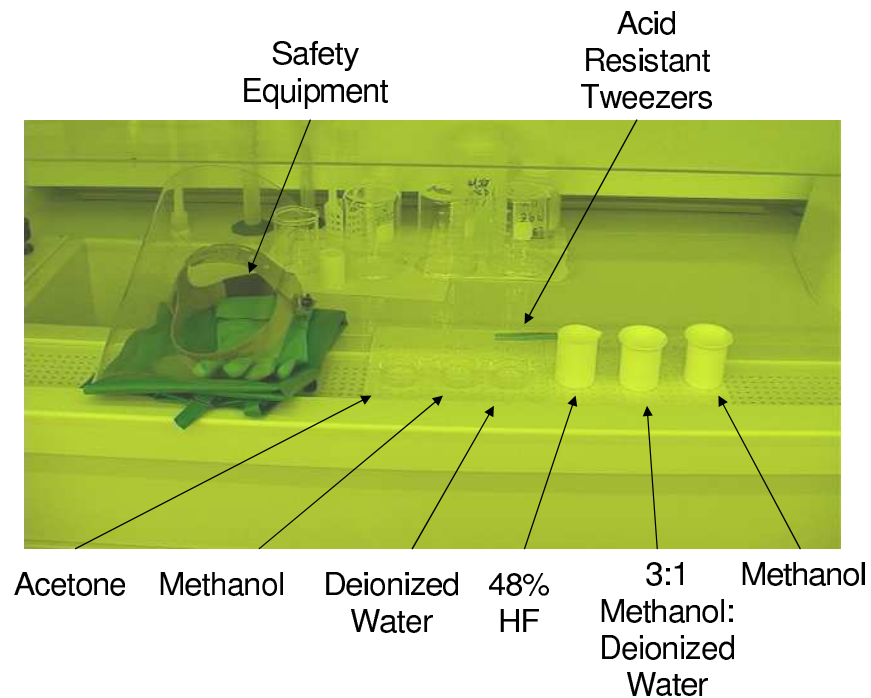


Figure 5.13 Picture of typical setup used to release packaged die in AFIT Class 10,000 Clean Room.

The following steps were used to perform the release:

- 1) Soak packaged die in 25 ml of acetone for 15 minutes. This step removes the protective layer of photoresist applied in the last step of the MUMPs® process.
- 2) Soak packaged die in 25 ml of methanol for 5 minutes. This step is used to rinse any acetone residue that may remain from step 1.
- 3) Dip packaged die in deionized water for 30 seconds. This step is used to displace the methanol from the die.
- 4) Soak package die in 50 ml 49% hydrofluoric acid for 4 minutes. This step is used to etch the sacrificial PSG layers thus releasing the micro-actuators on the die.
- 5) Dip packaged die in 25 ml 3:1, methanol:deionized water solution, for 5 seconds. This step is used to stop the etching by diluting the hydrofluoric acid.





Figure 5.14 Autosamdri® -815 CO<sub>2</sub> dryer.

6) Soak packaged die in methanol until ready to place die in Autosamdri® -815 automatic critical point dryer. This step is used to ensure the die remains clean and free from particulates.

7) Place packaged die in Autosamdri® -815 automatic critical point, CO<sub>2</sub> dryer. This step is used to completely dry the package while minimizing stiction. The Autosamdri® -815 is pictured in Figure 5.14. The Autosamdri® capitalizes on the supercritical region of CO<sub>2</sub> to avoid surface tension forces associated with drying solvents. Within the supercritical region, the interface between the liquid and gas states is eliminated and the CO<sub>2</sub> can transition directly to the gas phase. Once the CO<sub>2</sub> has transitioned to the gas phase, it can be safely vented. All processes used by the Autosamdri® -815 are automatically controlled with the exception of the purge time which is manually set with the PURGE Time Control on the front of the -815. The PURGE Time Control was set to position 1, corresponding to a 5 minute purge cycle, for all packaged die.

8) Remove the packages from the Autosamdri® -815 and store in a clean, dry, air tight container. This step ensures minimal contamination from particulates and

moisture. At this point the released die are ready to be wire bonded to the package leads.

*5.4.3 Wire Bonding Process.* All wire bonding required for this research was accomplished at AFRL's Packaging facility located at Wright-Patterson Air Force Base, Ohio. The facility is operated by the Sensors Directorate. The MUMPs die were wire bonded to the 14 pin ceramic DIP with a Kulicke & Soffa 4123 Wedge bonder using 0.0007 inch diameter, 99.99% gold wire with 0.5% - 2.0 % elongation. Figure 5.15 is a picture of a released MUMPs die wire bonded to the bond pads of a 14 pin ceramic DIP. After being wire-bonded the packaged die were returned to the AFIT Class 10,000 Clean Room where the last step of the packaging process was completed.

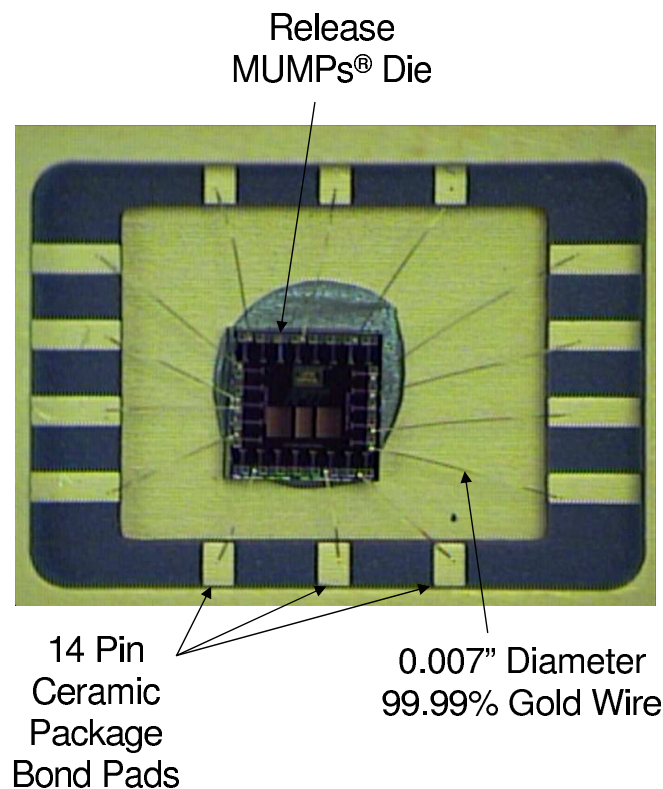


Figure 5.15 Picture of released, MUMPs® die mounted in well of 14 pin ceramic DIP and wire bonded to package bond pads.

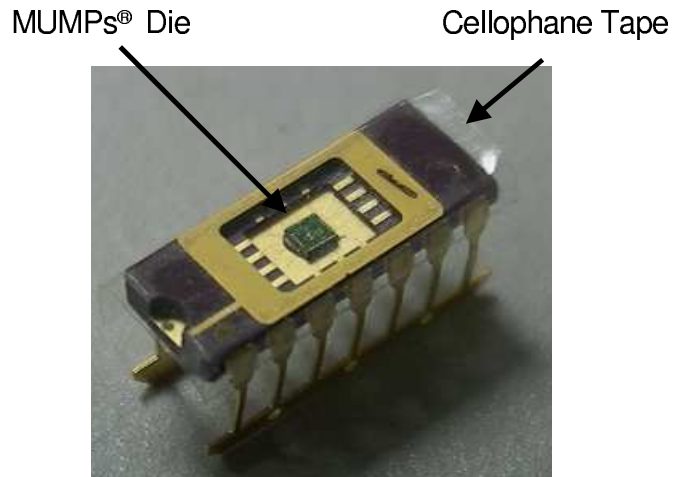


Figure 5.16 Picture of MUMPs® die mounted in 14 pin ceramic package and sealed with cellophane tape.

*5.4.4 Sealing Process.* The last step in the packaging process was to seal the package to minimize contamination from particulates and moisture, while allowing future inspection of the die. The preformed epoxy alumina lids that were designed for use with these packages would not satisfy the post inspection requirement. Once the epoxy was heat cured the lids were nearly impossible to remove. As an alternative, the packages were sealed using double-sided cellophane tape. Cellophane tape had two main advantages over the alumina lids. First, the tape could be easily removed without damaging the die or micro-actuators. Second, the die could be irradiated with low-energy (50 keV) radiation with minimal degradation in dose rate. Figure 5.16 is a picture of a 14 pin ceramic package sealed with cellophane tape.

The cellophane tape was applied to the package in the AFIT Class 10,000 Clean Room. This again ensured minimal contamination from particulates and moisture. Once sealed the packages were stored in a nitrogen purged dry-box located in the AFIT MEMS Test Laboratory until they were transported to the radiation sources. During transportation to the radiation sources, the packages were stored in an air-tight plastic container. Desiccant pouches were placed in the container to remove excess moisture from the air.

The post-processing steps that have been explained yielded contaminate-free micro-actuators, electrically connected to and sealed in a DIP. The packaged die are now ready for characterization.

## 5.5 *Device Characterization*

The next step in the research process, after designing, fabricating and post-processing the devices was to characterize their operation. Section 5.5.1 outlines the procedures used to characterize the electro-static piston actuator. Section 5.5.2 outlines the procedures used in the characterization of the electrothermal actuator. Finally, the procedures used to characterize the residual stress cantilever are covered in Section 5.5.3.

*5.5.1 Electrostatic Piston Actuator.* The operation of the electrostatic piston actuator is defined by the relationship between the amount of horizontal deflection and the applied voltage. Typically, this relationship can be found using a DC power supply and an interferometric microscope. This research required that the operation of the actuator be recorded within a radiation environment, precluding the use of an interferometric microscope. Instead, the capacitance-voltage relationship outlined in Section 4.1 was used to characterize the actuator. Section 5.5.1.1 presents the electrical connections required to connect the electrostatic piston actuator to the test equipment. Section 5.5.1.2 outlines the procedures used to characterize the operation of the piston actuator before being subjected to a radiation environment. Section 5.5.1.3 discusses the procedures used to characterize the operation of the piston actuator while being irradiated. Finally, Section 5.5.1.4 presents the procedures used to characterize the piston actuator after being irradiated.

*5.5.1.1 Electrical Connections between Electrostatic Piston Actuator and Test Equipment.* In order to obtain the capacitance-voltage relationship for the electrostatic piston actuator, outlined in Section 4.1, electrical connections had to

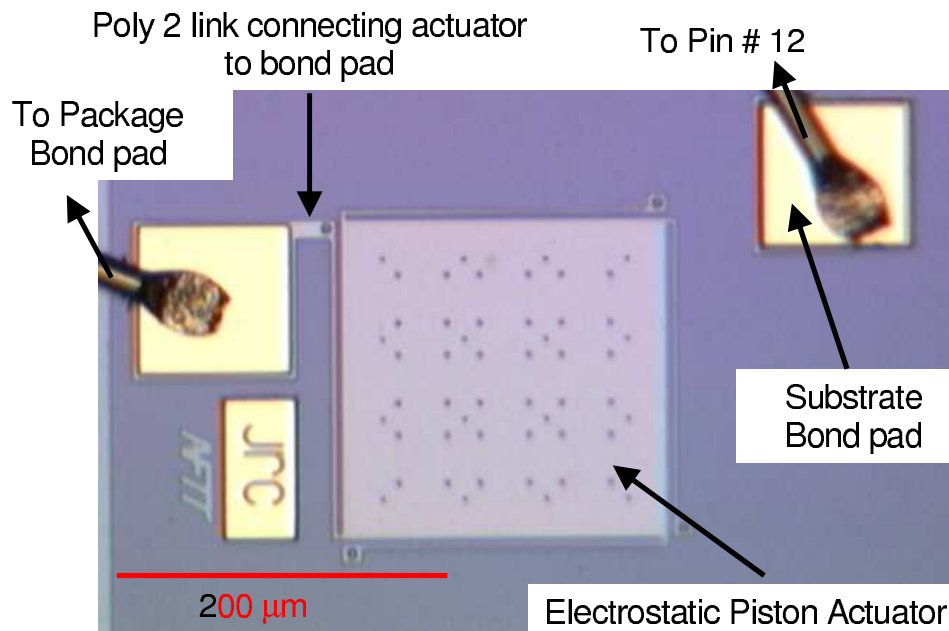


Figure 5.17 Picture illustrating the electrical connection between the electrostatic piston actuator and the 100  $\mu\text{m}$  by 100  $\mu\text{m}$  bond pad, and the 100  $\mu\text{m}$  by 100  $\mu\text{m}$  substrate bond pad.

be made between the actuator and the test equipment. First, electrical connections had to be made between the 100  $\mu\text{m}$  by 100  $\mu\text{m}$  bond pads and the electrostatic actuator. These connections were made using a POLY 2 connecting link to connect the bond pad to one anchor of the actuator. Electrical connection was made to the substrate using a 100  $\mu\text{m}$  by 100  $\mu\text{m}$  that was connected to the substrate by breaching the silicon nitride. Figure 5.17 shows the POLY 2 connecting link connecting the actuator to the bond pad and the substrate bond.

The second set of electrical connections were those required to connected the 100  $\mu\text{m}$  by 100  $\mu\text{m}$  bond pads to the 14 pin ceramic DIP. 0.0007 inch diameter, 99.99 gold wire was used to make these connections. Figure 5.18 illustrate the typical wiring configuration used to connect the die to the 14 pin ceramic package.

The last set of electrical connections that were required to connect the electrostatic piston actuator to the test equipment were those made between the ceramic

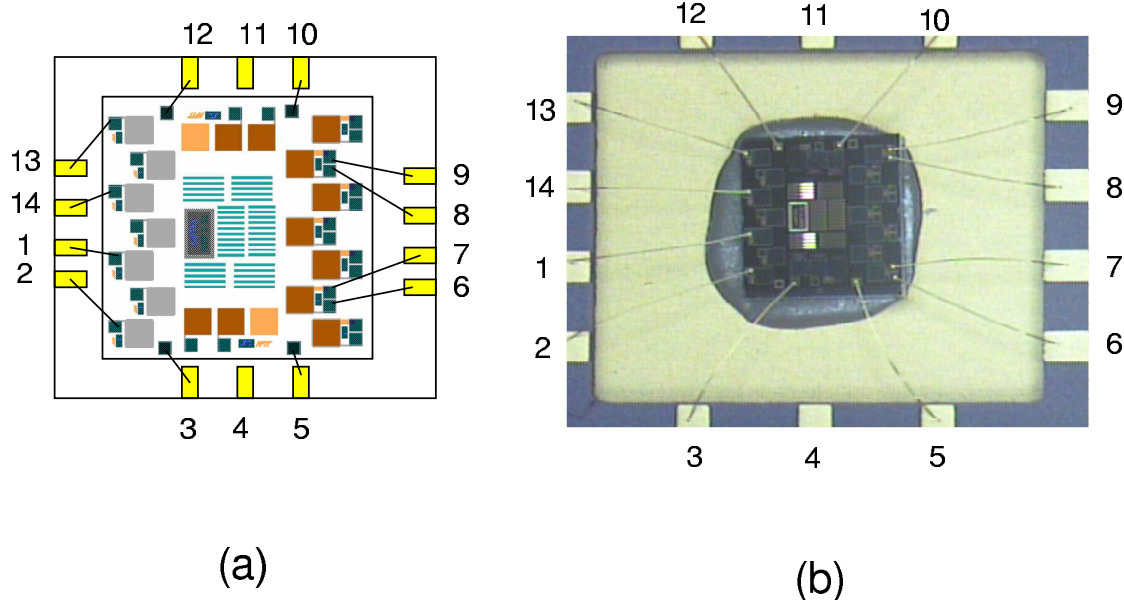


Figure 5.18 (a) Illustration of L-Edit schematic detailing the wire bond connections. (b) Picture of MUMPs<sup>®</sup> Die, containing the electrostatic piston actuators, wire bonded to to 14 PIN ceramic DIP.

package and the test equipment. Figure 5.19 is a picture of the 14 pin ceramic DIP mounted in the test bed. Each of the 14 pins are connected to one of the BNC connectors on the side of the test bed. Coaxial cables were then used to connect the test bed directly to the test equipment.

A schematic diagram depicting all the electrical connections between the test equipment used and the DUT is illustrated in Figure 5.20. The output from the DC power supply is connected to the external bias connection on the rear panel of the CV meter. The positive and ground cable connectors on the front panel of the CV meter were then connected to the DUT. Both the CV meter and the DC power supply were connected to the computer using GPIB cables.

Recall from Section 3.3.1, the electrostatic piston actuators will be tested under three biasing configurations; positive, negative, and snapdown. Under the positive configuration a positive voltage will be placed on the piston plate of the actuator

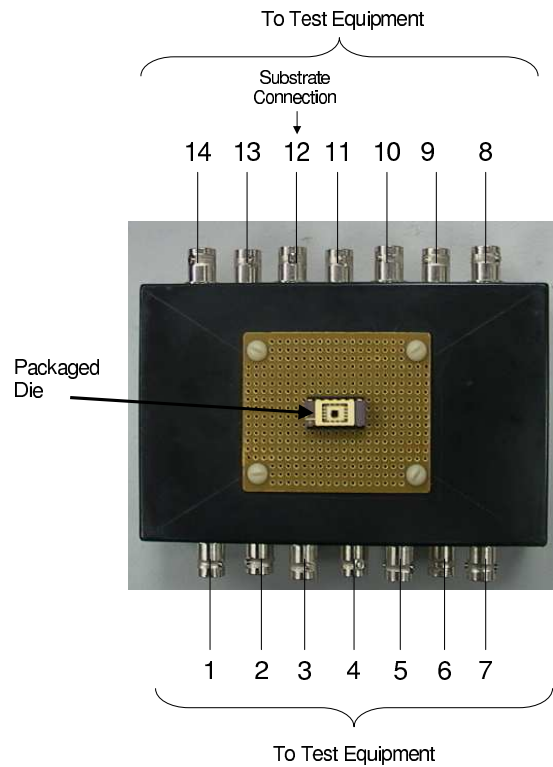


Figure 5.19 Picture of 14 pin ceramic package, containing MUMPs® Die, mounted in the test bed.

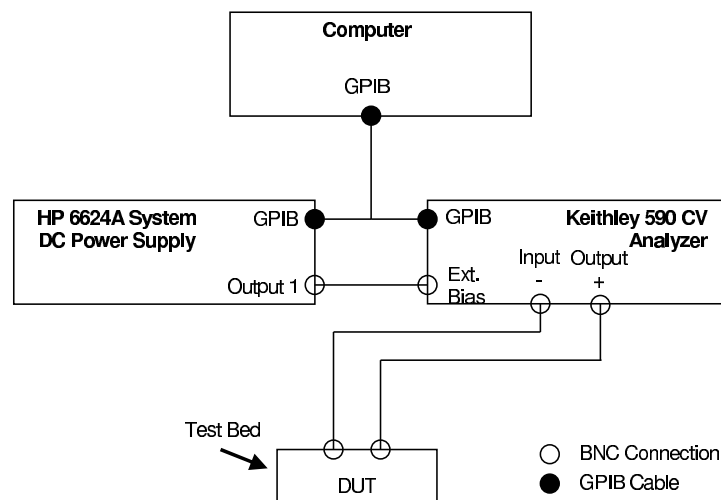


Figure 5.20 General test configuration used to measure capacitance-voltage relationship for electrostatic piston actuator.

during irradiation. For the negative configuration, a negative voltage will be placed on the piston plate of the actuator during irradiation. The snapdown configuration entails applying a positive voltage while irradiating and, at a specified total ionizing dose, sweeping the voltage from 0 to 20 volts in 1 volt increments. For the positive and snap-down bias configurations, the positive cable from the CV meter was connected to the piston plate and the ground cable to the substrate. Figure 5.21 illustrates the electrical connections made between the DUT and the test equipment for both the positive and snapdown biasing configurations. For the negative bias configuration, the positive cable from the CV meter was connected to the substrate and the ground cable to the piston plate. The electrical connections made between the DUT and the test equipment for the negative bias configuration are illustrated in Figure 5.22.

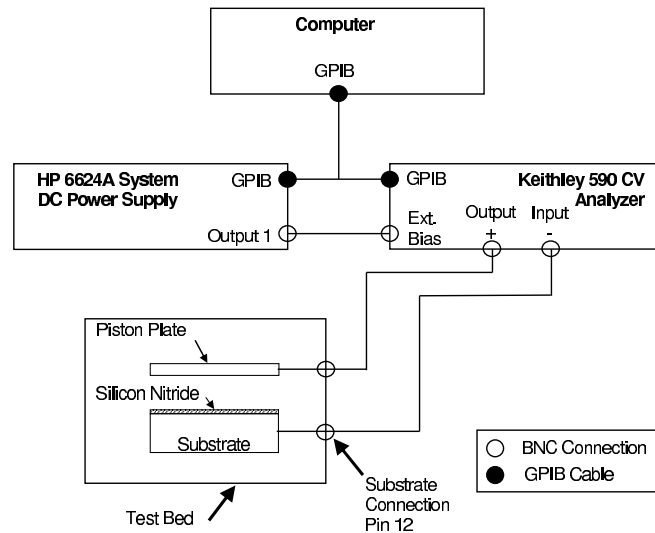


Figure 5.21 Electrical connections required to measure capacitance-voltage relationship for electrostatic piston actuator tested under positive and snapdown biasing configurations.

*5.5.1.2 Pre-Irradiation Characterization of Electrostatic Piston Actuator.* The pre-irradiated capacitance-voltage relationship was obtained using the applicable test configuration illustrated in Figures 5.21 and 5.22. The power supply



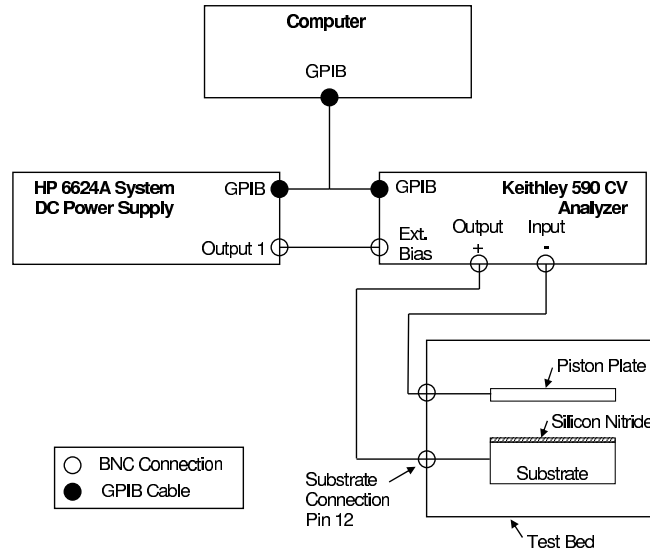


Figure 5.22 Electrical connections required to measure capacitance-voltage relationship for electrostatic piston actuator tested under negative biasing configuration.

and CV meter were controlled by a computer using the Agilent VEE software. An Agilent VEE program was developed that stepped the DC power supply through a pre-determined voltage range and read the capacitance measurement, associated with each voltage step, from the CV meter. Using the Agilent VEE software allowed the desired data to be taken and recorded with minimal operator interface. This minimized the amount of systematic errors introduced by the operator. The Agilent VEE program used to control the test equipment and record the applicable data is presented in Appendix C.

The pre-irradiation measurements were obtained by running the Agilent VEE program. The program stepped the voltage from 0 to 20 volts in 1 volt increments. Each voltage step was held for 1 second before the next step was initiated. The capacitance measurement was taken 0.5 seconds after the voltage was stepped. This allowed the piston actuator to reach a steady deflected position and helped to reduce the amount of deviation in the measurements. Both the applied voltage and the capacitance measurements were recorded in a Microsoft® Excel spreadsheet for

later analysis. Each measurement cycle was repeated eight times so that statistical analysis could be accomplished. Next, the actuators were characterized within an ionizing radiation environment.

#### *5.5.1.3 In-situ Characterization of Electrostatic Piston Actuator .*

The electro-static piston actuator was irradiated with 50 keV X-rays and 1.25 MeV gamma rays. The procedures used to irradiate and characterize the piston actuator will now be presented.

As mentioned in Section 3.3.1, the piston actuators were irradiated under three different biasing configurations using both the LEXR and Co-60 radiation sources. A total of 24 die containing piston actuators were irradiated, 12 using the LEXR source and 12 using the Co-60 source.

The same biasing configurations were used for die irradiated in both radiation sources. Four devices were irradiated under a constant, positive 10 volt bias and four under a constant, negative 10 volt bias. Capacitance measurements were taken at one second intervals for one device on each die. The die were irradiated to a total ionizing dose of 250, 500, 750 and 1000 krad(Si) for each of the biasing configurations.

The last 4 die were irradiated to a total ionizing dose of 1000 krad(Si). They were biased at a constant 10 volt bias until the specified dose was absorbed and then the applied voltage was swept from 0 to 20 volts in 1 volt steps. The voltage sweep was initiated at doses of 250, 500, 750 and 1000 krad(Si), for each of the four die. Tables 5.1 and 5.2 lists the irradiation time, dose rate, total ionizing dose and biasing configuration for the piston actuators irradiated with the LEXR and Co-60 sources. Two numbers appear in the Dose column for the actuator irradiated under the snapdown biasing configuration. The first number indicates the dose level at which the applied bias was stepped from 0 to 20 volts in 1 volt increments. The second number indicates the total ionizing dose the die was exposed to.

LEXR

Die	irradiation time [sec]	Dose Rate [rad(Si)/s]	Dose [krad(Si)]	Bias [V]
1	1858	134.5	250	+ 10
2	3720	134.5	500	+ 10
3	5575	134.5	750	+ 10
4	7450	134.5	1000	+ 10
5	1858	134.5	250	- 10
6	3720	134.5	500	- 10
7	5575	134.5	750	- 10
8	7450	134.5	1000	- 10
9	7450	134.5	250/1000	0-20 Sweep
10	7450	134.5	500/1000	0-20 Sweep
11	7450	134.5	750/1000	0-20 Sweep
12	7450	134.5	1000/1000	0-20 Sweep

Table 5.1 Irradiation time, Dose, Dose rate and biasing configuration for the 12 piston actuator die irradiated with 50 keV X-rays from the LEXR. For those die irradiated using the snapdown biasing configuration, the first number in the Dose column indicates the dose level at which the applied bias was swept from 0 to 20 volts, and the second number indicates the total ionizing dose the die were exposed to.

Co-60

Die	irradiation time [sec]	Dose Rate [rad(Si)/s]	Dose [krad(Si)]	Bias [V]
1	1914	130.8	250	+ 10
2	3825	130.8	500	+ 10
3	5725	130.8	750	+ 10
4	7632	130.8	1000	+ 10
5	1914	130.8	250	- 10
6	3825	130.8	500	- 10
7	5725	130.8	750	- 10
8	7632	130.8	1000	- 10
9	7632	130.8	250/1000	0-20 Sweep
10	7632	130.8	500/1000	0-20 Sweep
11	7632	130.8	750/1000	0-20 Sweep
12	7632	130.8	1000/1000	0-20 Sweep

Table 5.2 Irradiation time, Dose, Dose rate and biasing configuration for the 12 piston actuator die irradiated with 1.25 MeV gamma rays from the Co-60 source. For those die irradiated using the snapdown biasing configuration, the first number in the Dose column indicates the dose level at which the applied bias was swept from 0 to 20 volts, and the second number indicates the total ionizing dose the die were exposed to.

The in-situ measurements were obtained by running an Agilent VEE program while irradiated the die. The Agilent VEE program is presented in Appendix C. The program controlled the DC power supply to maintain the appropriate biasing voltage and polled the CV meter to obtain the capacitance reading every second. Both the applied voltage and capacitance measurements were recorded in a Microsoft® Excel spreadsheet for later analysis. The final step in characterizing the operation of the piston actuator was to monitor its operation after irradiation.

*5.5.1.4 Post-Irradiation Characterization of Electrostatic Piston Actuator .* Immediately following irradiation, the capacitance-voltage relationship was again measured. The characterization procedures followed exactly those detailed in Section 5.5.1.2 for the pre-characterization of the piston actuator. These procedures were then repeated every 24 hours for seven days in order to track any time dependent changes in the capacitance-voltage relationship.

The procedures followed to characterize the piston actuator provided data detailing the operation of the actuator prior to, during, and following irradiation by both 1.25 MeV gamma rays and 50 keV X-rays.

*5.5.2 Electrothermal Actuator.* The electrothermal actuator is typically characterized by the relationship between the amount of tip deflection and applied voltage. However, the actuator can also be characterized by the resistance-voltage relationship. Both methods of characterizing the electrothermal actuator were used in this research. Section 5.5.2.1 presents the electrical connections required to connect the horizontally deflecting electrothermal actuator to the test equipment. Section 5.5.2.2, outlines the methods and experimental setup used to obtain the deflection-voltage relationship and current-voltage relationship before subjecting the actuator to radiation. The procedures and setup used to obtain the current-voltage relationship while subjecting the actuator to both 1.25 MeV gamma rays and 50 keV X-rays are presented in Section 5.5.2.3. Section 5.5.2.4 outlines the procedures and experi-

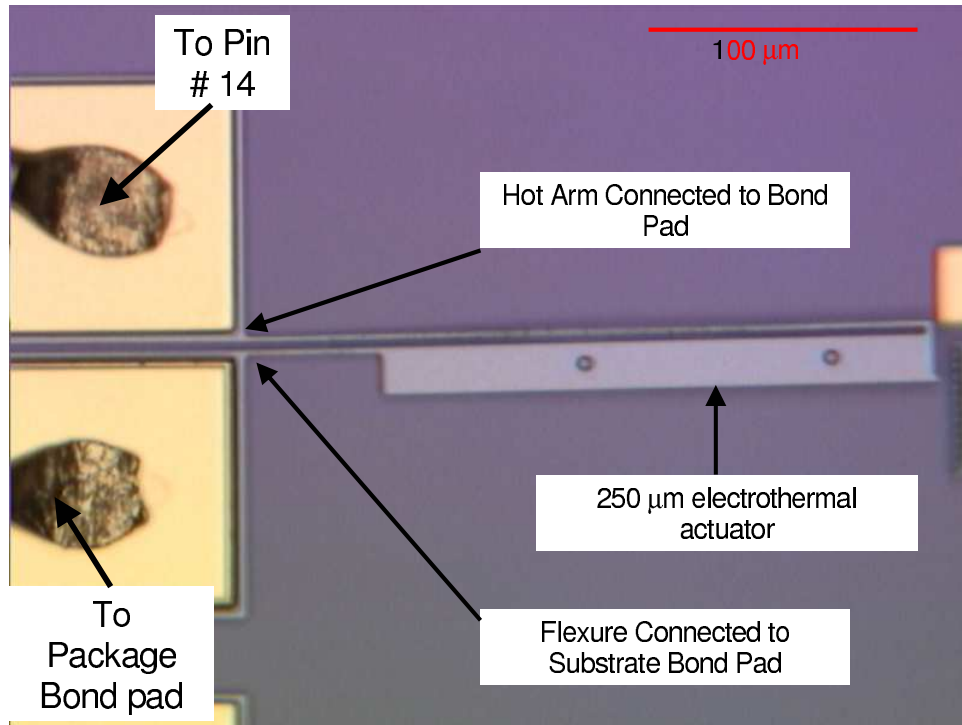


Figure 5.23 Picture illustrating the electrical connections between the electrothermal actuator and the 100  $\mu\text{m}$  by 100  $\mu\text{m}$  bond pads.

mental setup used to characterize the operation of the electrothermal actuator after being irradiated.

*5.5.2.1 Electrical Connections between Electrothermal Actuator and Test Equipment.* In order to obtain the resistance-voltage relationship for the electrothermal actuator, electrical connections had to be made between the actuator and the test equipment. First, electrical connections had to be made between the

100  $\mu\text{m}$  by 100  $\mu\text{m}$  bond pads and the actuator. These connections were made by connection the hot arm and the flexure of the actuator directly to the bond pads. Figure 5.23 show the hot arm and the flexure connected to the bond pads.

The second set of connections that were required was between the 100  $\mu\text{m}$  by 100  $\mu\text{m}$  bond pads and the 14 pin ceramic DIP. 0.0007 inch diameter, 99.99 gold wire was used to make the electrical connections between the bond pads and the ceramic

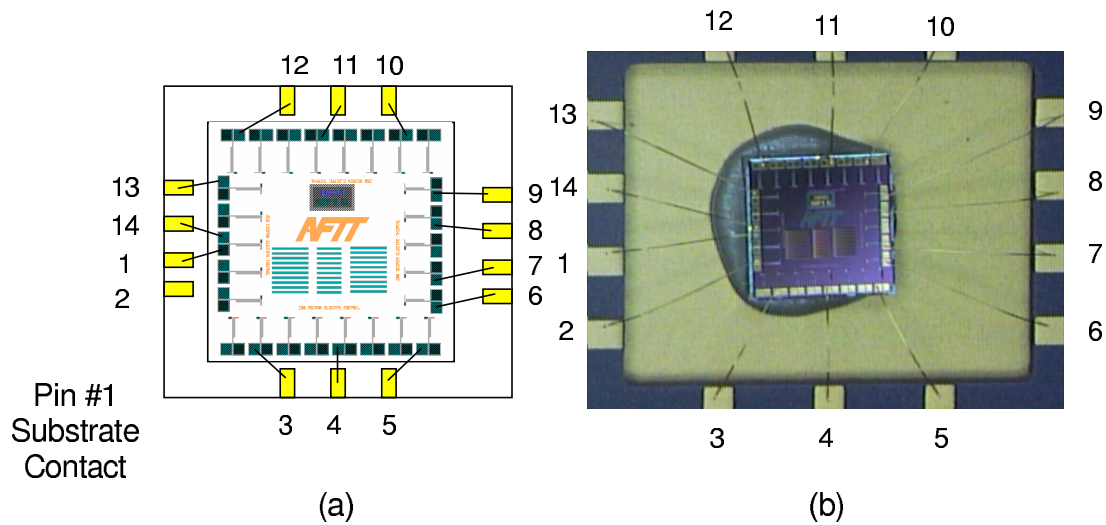


Figure 5.24 (a) Illustration of L-Edit schematic detailing the wire bond connections for the electrothermal actuators. (b) Picture of MUMPs® Die containing the electrothermal actuators wire bonded to to 14 PIN ceramic DIP.

DIP. Figure 5.24 illustrates the typical wiring configuration used to connect the die to the 14 pin ceramic package. Only one electrical connection was made between the ceramic package and the substrate, since all the electrothermal actuators were fabricated with a substrate bond pad. The substrate connection is made through pin 1 on the ceramic package.

The final set of electrical connections that were required to connect the electrothermal actuator to the test equipment were those made between the ceramic package and the test equipment. These connections were made using the test bed discussed in Section 5.2.2 and pictured in Figure 5.3. Figure 5.25 is a picture of the 14 pin ceramic DIP mounted in the test bed. Each of the 14 pins are connected to one of the BNC connectors on the side of the test bed. Coaxial cables were then used to connect the test bed to the splitter box detailed in Section 5.2.2. The splitter box was used so that the multimeter could be connected in series with the electrothermal actuator.

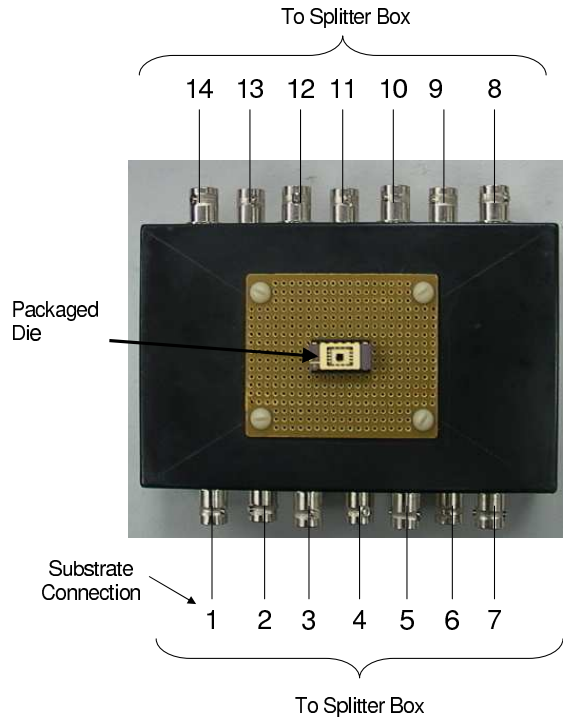


Figure 5.25 Picture of packaged MUMPs<sup>®</sup> die containing electrothermal actuators mounted in test bed.

A schematic diagram depicting all the electrical connections between the test equipment and the DUT is illustrated in Figure 5.26. The output from the DC power supply was connected to the splitter box, described in Section 5.2.2. The multimeter was connected in series with the electrothermal actuator to accommodate current measurement. All connections between the splitter box, test bed and test equipment were made using coaxial cables. Both the DC power supply and multimeter were connected to the computer using GPIB cables.

#### 5.5.2.2 Pre-Irradiation Characterization of Electrothermal Actuator.

Pre-irradiation characterization of the electrothermal actuator consisted of measuring the deflection-voltage and the current-voltage relationships. Obtaining the deflection-voltage relationship proved to be more challenging than the current-voltage relationship. The deflection-voltage relationship was measured using an analytical probe station, an HP 6642A DC power supply and the video capture system outlined

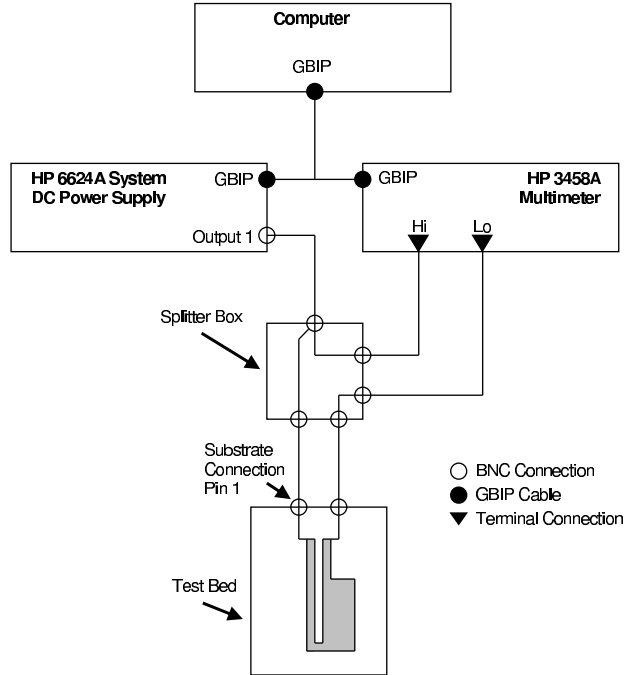


Figure 5.26 Test configuration used to measure resistance-voltage relationship for an electrothermal actuator.

in Section 5.1. The measurement procedures consisted of applying a DC voltage and monitoring the tip deflection using the video capture software. As the voltage was incrementally increased, the location of the tip of the actuator was marked on a piece of masking tape placed on the video monitor. The voltage was stepped in 1 volt increments from 0 to 10 volts and a deflection measurement was taken for each voltage step. After completing the voltage sweep the total length of the deflection scale was recorded on the masking tape so that the actual tip deflection could be extrapolated. This was accomplished by measuring the tip deflection, recorded on the masking tape, with a millimeter rule. This measurement was then scaled by multiplying it by the known length of the deflection scale (50 microns) and dividing it by the measured length of the deflection scale in millimeters. Once the deflection-voltage measurements were complete, the current-voltage measurements were taken.



The current-voltage measurements were taken using the test bed, an HP 6642A DC power supply, HP Multimeter, computer and Agilent VEE software. The DUT was placed in the test bed and connected to the power supply and multimeter as illustrated in Figure 5.26. An Agilent VEE program was run to sweep the voltage between 0 and 11 volts in 1 volt increments and measure the current flow for each voltage step. Each voltage step was held for 1 second and the current measurement was taken 0.5 seconds after the voltage was incremented. This time frame allowed the current to stabilize before being measured. Both the applied voltage and measured current values were recorded in a Microsoft<sup>®</sup> Excel spreadsheet for later analysis. The Agilent VEE program is presented in Appendix C

Having characterized the electrothermal actuator with current and deflection measurements as a function of applied voltage, the actuator was ready to be irradiated.

*5.5.2.3 In-situ Characterization of Electrothermal Actuator .* A total of eight die containing electrothermal actuators were irradiated with 50 keV X-rays and 1.25 MeV gamma rays. Four of these were irradiated using the LEXR source and four using the C0-60 source. The die were irradiated to total ionizing doses of 250, 500 750 and 1000 krad(Si) for both radiation sources. Table 5.3 indicates the irradiation time, dose rate and total dose for the four die irradiated using the LEXR source. Table 5.4 indicates the irradiation time, dose rate and total dose for the four die irradiated using the Co-60 source.

LEXR			
Die	Irradiation Time (sec)	Dose Rate [ $\frac{rad(Si)}{s}$ ]	Dose [krad(Si)]
1	1858	134.5	250
2	3720	134.5	500
3	5575	134.5	750
4	7450	134.5	1000

Table 5.3 Irradiation time, Dose and Dose rate for the 4 electrothermal actuator die irradiated with 50 keV X-rays from the LEXR source.

Co-60

Die	Irradiation Time (sec)	Dose Rate [ $\frac{rad(Si)}{s}$ ]	Dose [krad(Si)]
1	1914	130.8	250
2	3825	130.8	500
3	5725	130.8	750
4	7632	130.8	1000

Table 5.4 Irradiation time, Dose and Dose rate for the 4 electrothermal actuator die irradiated with 1.25 MeV gamma rays from the Co-60 source.

The in-situ characterization of the electrothermal actuators consisted of measuring the current-voltage relationship. The same measurement process and Agilent VEE program used during the pre-irradiation characterization (See Section 5.5.2.2) was used for the in-situ characterization.

The final step in radiation testing the electrothermal actuator was post-characterization which began immediately after the die were irradiated.

#### *5.5.2.4 Post-radiation Characterization of Electrothermal Actuator .*

Immediately following the irradiation process, current-voltage measurements were again taken. The measurement procedures were the same used during pre- and in-situ characterization. The current-voltage relationship was measured every 24 hours over a 7 day period. Deflection-voltage measurements were not taken immediately following the irradiation process since the equipment required to perform the measurements was not available at the radiation test site. However, deflection-voltage measurement were made 3 days after the devices were irradiated.

The procedures followed to characterize the electrothermal actuator provided data detailing the operation of the actuator prior to, during and following irradiation by both 1.25 MeV gamma rays and 50 keV X-ray environments.

*5.5.3 Residual stress cantilever.* As presented in Section 4.3, the residual stress cantilever is characterized by tip deflection. A common method used to measure the tip deflection of a residual stress cantilever is with an interferometric

microscope. Although AFIT does not have an interferometric microscope, access to one was provided by AFRL/SN. Section 5.5.3.1 outlines the procedures used to characterize the residual stress cantilever before and after being subjected to the ionizing radiation sources.

*5.5.3.1 Characterization of Residual Stress Cantilever .* The pre-irradiated cantilevers were transported to the AFRL/SN Class 100 Clean Room in an air tight plastic container. Each of the die containing residual stress cantilevers were mounted on the Zygo's movable stage. The stage was adjusted so the substrate surface of the die was level. A 100  $\mu\text{m}$  scan was performed by the microscope software and a deflection profile was obtained. From the deflection profile the tip deflection was measured for each of the cantilevers. Figure 5.27 illustrates the typical cross-sectional profile obtained using MetroPro software distributed by Zygo Corporation. The amount of deflection was measured from the top of the anchor to the tip of the cantilever. Deflection measurements were taken for two sets of five cantilevers located on each die.

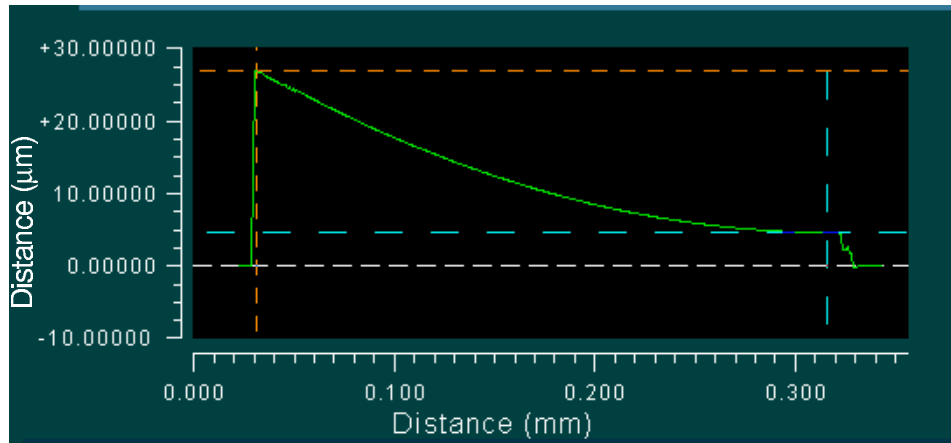


Figure 5.27 Cross-sectional profile plots of residual stress cantilever plotted using MetroPro Software distributed by Zygo Corporation.

Eight residual stress cantilever die were irradiated with the LEXR and Co-60 sources. Four were irradiated using the LEXR source and four using the Co-60

source. Since the cantilevers were collocated on the same die as the electrostatic piston actuators they were irradiated at the same time as the electrostatic piston actuators. This was possible because no in-situ measurements were taken for the cantilevers.

The cantilevers were exposed to total ionizing doses of 250, 500, 750 and 1000 krad(Si) by both radiation sources. The four die containing the cantilevers irradiated in the LEXR source are numbered die 1 through 4 in Table 5.1. The four die containing the cantilevers irradiated in the Co-60 source are numbered die 1 through 4 in Table 5.2. As indicated in the tables, the cantilevers were irradiated with 50 keV x-rays at a dose rate of  $134.5 \frac{\text{rad}(\text{Si})}{\text{s}}$  with the LEXR source and 1.25 MeV average energy gamma rays at a dose rate of  $130.8 \frac{\text{rad}(\text{Si})}{\text{s}}$  by the Co-60 source.

The final step in characterizing the residual stress cantilevers was to reaccomplish the interferometric measurements outlined in the pre-characterization step.

The measurement procedures allow characterization of the residual stress cantilever prior to and after being irradiated with 1.25 MeV gamma rays and 50 keV X-rays.

## 5.6 Conclusions

The focus of this chapter centered on the experimental procedures followed in characterizing the MEMS actuators for operation in an ionizing radiation environment. A brief overview was given for all the equipment required to conduct the research. In addition, all the steps taken during the research were discussed to include post-processing of the MUMPs® die and characterization of the MEMS actuators.

## VI. Results and Analysis

This chapter presents the results and analysis pertaining to the characterization of the three MEMS actuator subjected to an ionizing radiation environment. The results include characterization of each device before, during, and after being irradiated with ionizing radiation from a LEXR source and a Co-60 gamma source. Section 6.1 contains the results and analysis for measurements taken on the electrostatic piston actuator. The results and analysis for the electrothermal actuator is presented in Section 6.2. Section 6.3 presents results and analysis for the residual stress cantilever.

### 6.1 Characterization of Electro-static Piston Actuator

This section presents the results and analysis for the characterization of the electrostatic piston actuator. Section 6.1.1 discusses the results of the analytical model and compares the model to deflection measurement taken prior to irradiating the actuator. The results and analysis of the experimental measurements are categorized according to the radiation source. Section 6.1.2 discusses the results for the characterization accomplished using the LEXR source. The results for the actuators irradiated using the Co-60 gamma ray source are discussed in Section 6.1.3.

#### 6.1.1 Comparison of Analytical Model and Experimental Measurements.

The two analytical models derived in Section 4.1 describe the applied voltage as a function of geometrical and material parameters of the piston actuator. Equation 4.15 yields the voltage as a function of deflection. Equation 4.19 yields the voltage as a function of both deflection and charge trapped in the dielectric layer. The geometrical parameters listed in Table 6.1 and the material parameters listed in Table 6.2 will be used in the models to predict the capacitance as a function of applied voltage. The Matlab<sup>®</sup> script used to for the calculation is present in Appendix A.

Parameter	Value
Area of piston plate, A	40,000 $\mu\text{m}^2$
Width of flexures, w	3 $\mu\text{m}$
Thickness of flexures, h	1.5 $\mu\text{m}$
Length of flexures, L	185 $\mu\text{m}$
Initial air gap, $d_a$	2.75 $\mu\text{m}$
Thickness of silicon-nitride, $d_n$	0.6 $\mu\text{m}$

Table 6.1 Geometrical parameters used in the analytical model of the piston actuator.

Parameter	Value
Young's moduls for polysilicon, E	169 GPa [1]
Relative permittivity of silicon-nitride, $\varepsilon_n$	8 [2]

Table 6.2 Material parameters used in the analytical model of the piston actuator.

Figure 6.1 allows the changes in capacitance as a function of voltage to be compared between the values predicted by the two models and those obtained experimentally. Figure 6.1 illustrates the correlation of the two models when the charge is set to zero in Model #2. The black line represents the prediction obtained from Model #1. The red \*'s represent the values predicted by Model #2. The models predict the snap through voltage to be between 4 and 5 volts. Figure 6.1 also compares the two models to the experimentally obtained change in capacitance values. The change in capacitance is calculated experimentally by subtracting the average of the zero voltage capacitance. The green +'s represent experimental data.

When compared to the experimental data, the models accurately predict the snap through voltage to within 1 volt. The experimentally-measured snap through voltage is between 3 and 4 volts. The predicted trend associated with the change of capacitance as the voltage is increased is visible in the experimentally obtained measurements. Also visible in the experimental results is an increase of capacitance after snapdown has occurred. This increase is not predicted by the models. The increase in capacitance is attributed to the fact that the actuator is not a rigid parallel plate but rather a thin curved film and an increase in the actuation voltage

causes the plate to flatten out. In addition, differences between the models and the measured data can be attributed to the use of widely varying material parameters in the model. The values used for Young's modulus and the dielectric permittivity were not experimentally measured and therefore could introduce errors into the model. The significance of the results illustrated by Figure 6.1 is that both models predict the snapdown voltage of the actual electrostatic piston actuator to within 1 volt. In addition, the two models equate to each other when no charge is trapped in the dielectric layer.

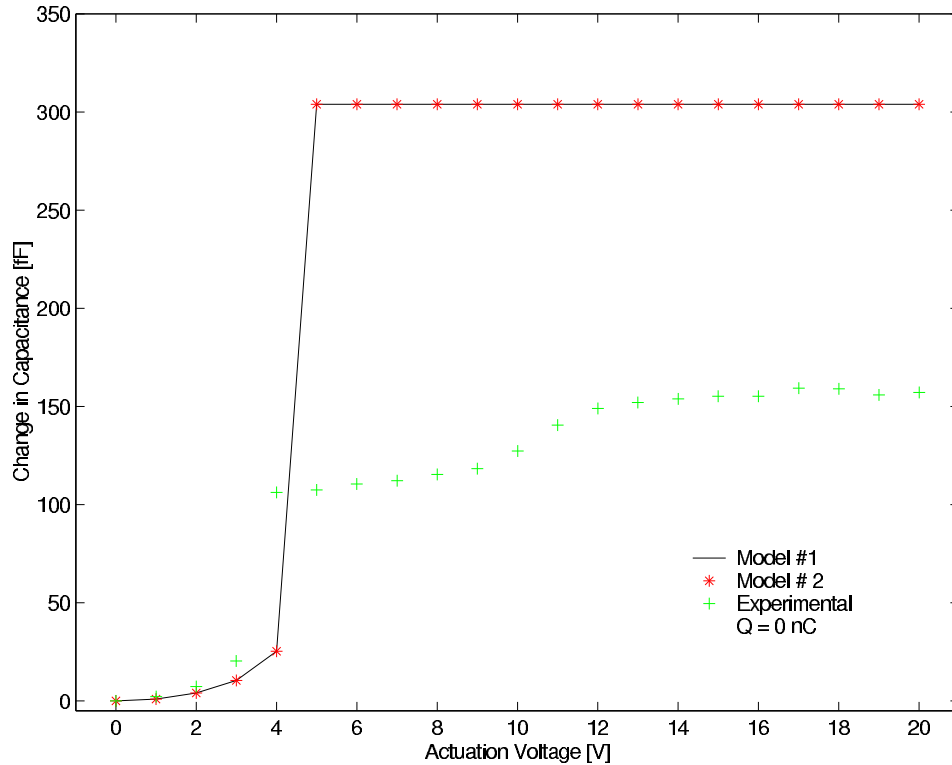


Figure 6.1 Change in capacitance versus actuation voltage predicted by Model #1, Model #2, and experimentally measured.

The next step is to see what changes the models will yield when trapped charge is taken into account. Srour [3] defines the electron-hole density per krad(Si) as:

$$\frac{Pair\ Density}{rad(Si)} = \frac{\left(100 \frac{ergs}{g-rad}\right) \rho}{\left(10^7 \frac{ergs}{J}\right) \left(1.6 \times 10^{-19} \frac{J}{eV}\right) E_p} \quad (6.1)$$

where  $\rho$  is the density of the silicon nitride layer in grams per cubic centimeter, and  $E_p$  is the pair generation energy in electron-volts for silicon nitride. Using a density of  $3.4 \frac{g}{cm^3}$ , and a pair generation energy of 11.7 eV the pair density per rad(Si) is approximately  $18 \times 10^{12} \frac{pair}{cm^3 \cdot krad(Si)}$ . For this illustration, it was assumed that 10 percent of the generated holes are trapped within the silicon nitride layer. This equates to a trapped charge density within the silicon nitride layer of  $2.88 \frac{C}{cm^3 \cdot krad(Si)}$ . If we take the volume of silicon nitride directly under the  $200 \mu m$  by  $200 \mu m$  actuator plate, the charge trapped is  $6.9 \times 10^{-15} \frac{C}{krad(Si)}$ . For a 250 krad(Si) dose, the trapped charge equates to  $1.7 \times 10^{-12} C$ .

Figure 6.2 illustrates the predicted change in capacitance when 1.7 picoCoulombs of charge is placed at the nitride-air interface. Again the black line represents the results using the first model that neglects the trapped charge. The red ‘\*’s represent the change in capacitance predicted by the second model. The model predicts that the 1.7 pC of charge will increase the snap through voltage from 4.52 volts to 5.48 volts.

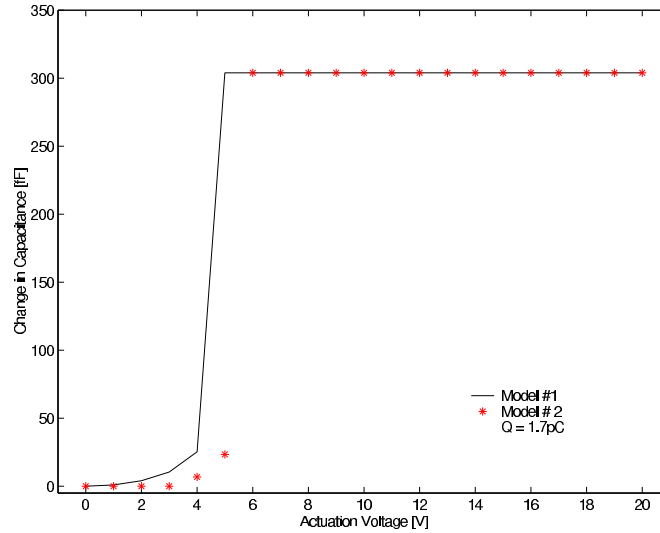


Figure 6.2 (a) Analytical predictions of Capacitance versus voltage when 1.7 pC of charge is placed at the nitride-air interface. The x- and y-axis are scaled in (b) to emphasize the differences between the two model prior to snapdown.



The two analytical models derived predict the trend in the capacitance-voltage relationship. The second model predicts that the operation of the actuator will be affected when charge is trapped in the dielectric layer. The model predicts an increase in snap through voltage and a decrease in change in capacitance before snapdown. These changes in snapdown and capacitance are consistent with positive charge trapping. Positive charge trapped within the dielectric layer will reduce the amount of deflection obtained for a given applied potential. The reduced deflection corresponds to a decrease in the capacitance associated with the applied potential. Positive charge trapping within the dielectric layer is expected when the devices are exposed to ionizing radiation environments.

*6.1.2 Characterization of Electrostatic Piston Actuator Subjected to Low Energy X-rays.* Characterizing the electrostatic piston actuators irradiated in the LEXR source consisted of taking ten sets of measurements. Table 6.3 details the time frame between the ten measurements and the duration of all measurements taken at each total ionizing dose. The time at which the pre-irradiation measurements were initiated is denoted by T.

Measurement Sequence	Measurement	250 krad(Si) Dose		500 krad(Si) Dose		750 krad(Si) Dose		1000 krad(Si) Dose	
		Start Time	Duration	Start Time	Duration	Start Time	Duration	Start Time	Duration
1	Pre-Irradiated Capacitance	T	3 min	T	3 min	T	3 min	T	3 min
2	In-situ Capacitance	T + 5 min	31 min	T + 5 min	62 min	T + 5 min	93 min	T + 5 min	124 min
3	Post-irradiated Capacitance	T + 40 min	3 min	T + 72 min	3 min	T + 103	3 min	T + 135	3 min
4	Post-irradiated Capacitance	T + 21 hr	3 min	T + 18 hr	3 min	T + 16 hr	3 min	T + 29 hr	3 min
5	Post-irradiated Capacitance	T + 45 hr	3 min	T + 42 hr	3 min	T + 40 hr	3 min	T + 55 hr	3 min
6	Post-irradiated Capacitance	T + 71 hr	3 min	T + 68 hr	3 min	T + 66 hr	3 min	T + 78 hr	3 min
7	Post-irradiated Capacitance	T + 94 hr	3 min	T + 90 hr	3 min	T + 89 hr	3 min	T + 100 hr	3 min
8	Post-irradiated Capacitance	T + 117 hr	3 min	T + 113 hr	3 min	T + 115 hr	3 min	T + 135 hr	3 min
9	Post-irradiated Capacitance	T + 152 hr	3 min	T + 148 hr	3 min	T + 150 hr	3 min	T + 158 hr	3 min
10	Post-irradiated Capacitance	T + 176 hr	3 min	T + 171 hr	3 min	T + 173 hr	3 min	T + 181 hr	3 min

Table 6.3 Time table detailing the time elapsed between the ten measurements taken, and the duration of the measurements, for electrostatic piston actuators irradiated to the specified total dose using the LEXR Source. T is taken to be the start of the pre-irradiation capacitance measurements.

The procedures outlined in Section 5.5.1 were used to characterize the electrostatic piston actuator. The actuators were irradiated under three different bias configurations. However, each biasing configuration received the same measurement schedule as shown in Table 6.3. All data plotted in this section is the average of seven measurements. The data is plotted with error bars which represent the standard error obtained in the measurements. The standard error was calculated by dividing the standard deviation of the measurement by the square root of the number of measurements.

Figure 6.3 illustrates the change in capacitance versus actuation voltage for the actuators irradiated to a total ionizing dose of 500 krad(Si) (Die #2, Table 5.1) prior to irradiation (Pre-irradiation), immediately following irradiation (Post-irradiation), and seven days following irradiation (7 day Post-irradiation). Figure 6.3 (a) illustrates the capacitance changes for an actuator held at +10 volts during irradiation. Figure 6.3 (b) illustrates the capacitance changes for a device with no actuation voltage applied during irradiation. Both devices are collocated on the same die. Figure 6.4 illustrates the absolute capacitance measurements taken for the actuators irradiated to a total ionizing dose of 500 krad(Si) (Die #2, Table 5.1).

The first significant result illustrated by Figure 6.3 is that the actuator is already snapped down. This is evident from the lack of a significant capacitance change associated with snapdown of the actuator. Figure 6.5 is a scanning electron micrograph showing flexures of an electrostatic actuator stuck to the silicon-nitride layer. It is believed that the test signal generated by the Keithley CV meter could be attributing to the actuators being stuck down. The magnitude of the test signal is 2 volts peak to peak which is on the same order of magnitude as the snapdown voltage. In addition, wire-bonding the actuators could also be attributing to the actuator being stuck down. Electrostatic charge generated by the wire-bonder could cause the actuator plate to be attracted to silicon nitride layer. It is also believed that any charging of the dielectric layer by the application of the actuation voltage could

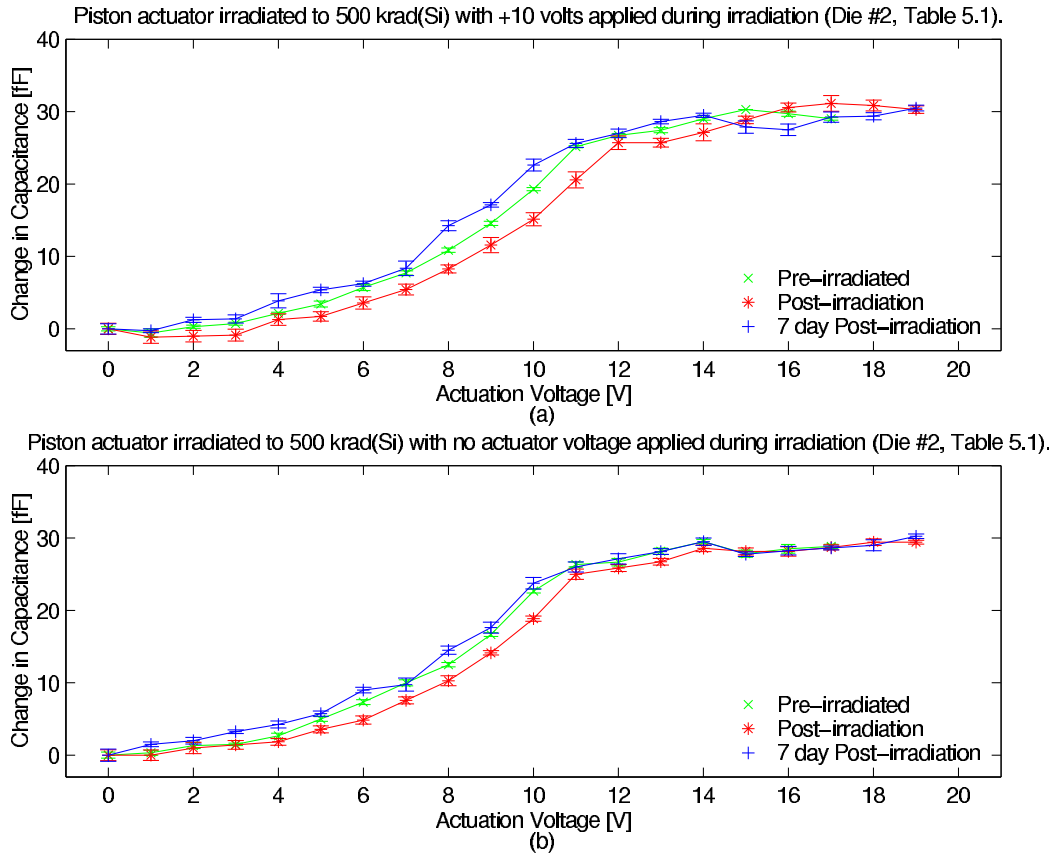


Figure 6.3 Change in capacitance versus actuation voltage for piston actuator irradiated to total dose of 500 krad(Si) (Die #2, Table 5.1) with (a) 10 volts actuation voltage applied during irradiation and (b) no actuation voltage applied during irradiation.

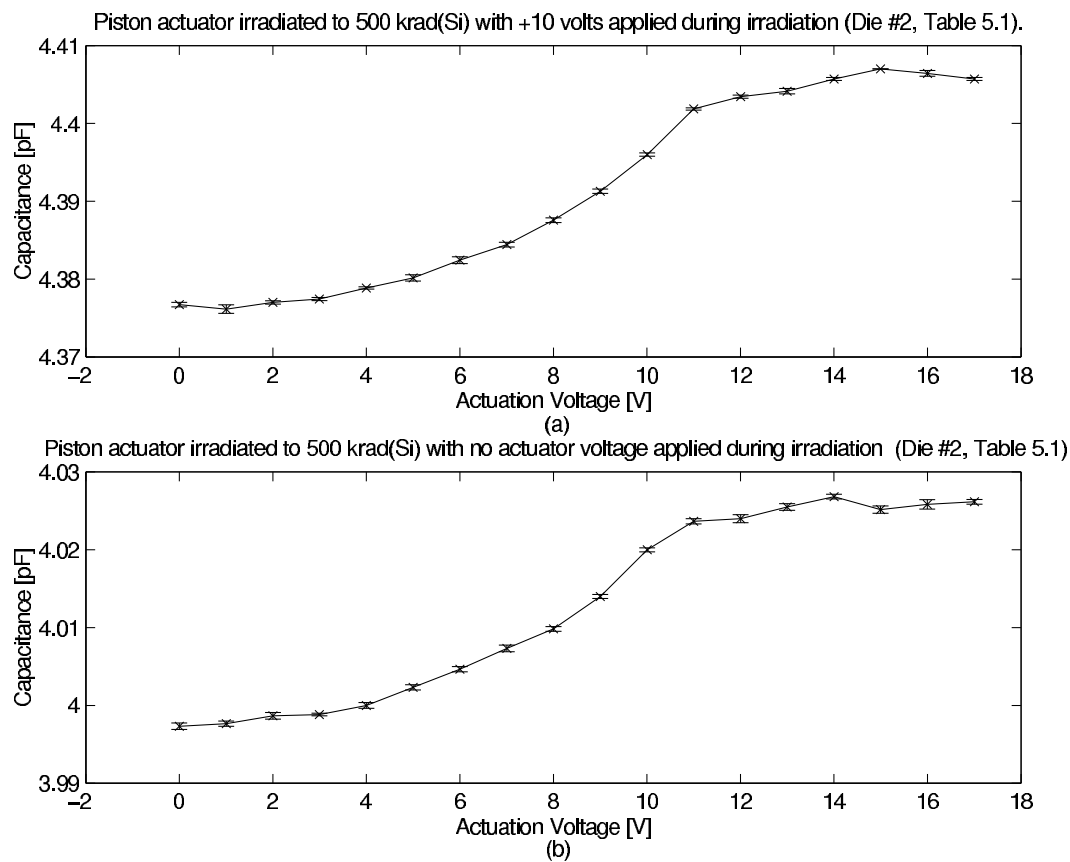


Figure 6.4 Capacitance versus actuation voltage for piston actuator irradiated to total dose of 500 krad(Si) (Die #2, Table 5.1) with (a) 10 volts actuation voltage applied during irradiation and (b) no actuation voltage applied during irradiation.

attribute to the actuator being stuck down. All actuators tested in this radiation study were stuck down before irradiation.

Two actuators were found after radiation testing that showed a change in capacitance versus actuation voltage similar to that demonstrated by the two models (Figure 6.1). The actuators were located on Die #5 and Die #6 (Table 5.2) irradiated under negative bias in the Co-60 Source. The change in capacitance as a function of actuation voltage for the actuator located on Die #5 is illustrated in Figure 6.1.

The trend noted in the change of capacitance versus actuation voltage is similar to the trend noted in the experimental measurements plotted in Figure 6.1 after snapdown occurs. The plots in Figure 6.3 illustrate a decrease in capacitance immediately following irradiation. This decrease in capacitance is attributed to charge trapping within the silicon nitride layer. The differences in the pre-irradiated data and the post-irradiated data follow the predictions made by the Model #2 discussed in Section 6.1.1. Little difference is noted between the device irradiated with a bias applied (Figure 6.3 (a)) and the one irradiated with no bias applied (Figure 6.3 (b)). This is somewhat unexpected since without an applied bias the generated charge would not be separated and thus a more recombination would occur leading to few charge carriers to be trapped. However, the density of electron-hole pairs generated by the low energy X-rays is low. Therefore, the amount of recombination that occurs is minimal and thus carriers are available for trapping. This data therefore implies that even in the absence of an electric field charges are still trapped within the dielectric layer.

Figure 6.3 also illustrates that the change in capacitance noted immediately following irradiation disappears after seven days. The capacitance-voltage relationship for both devices plotted in Figure 6.3 returned to the pre-irradiated values after seven days. This suggests that the charge trapped within the silicon nitride layer is annihilated over time.

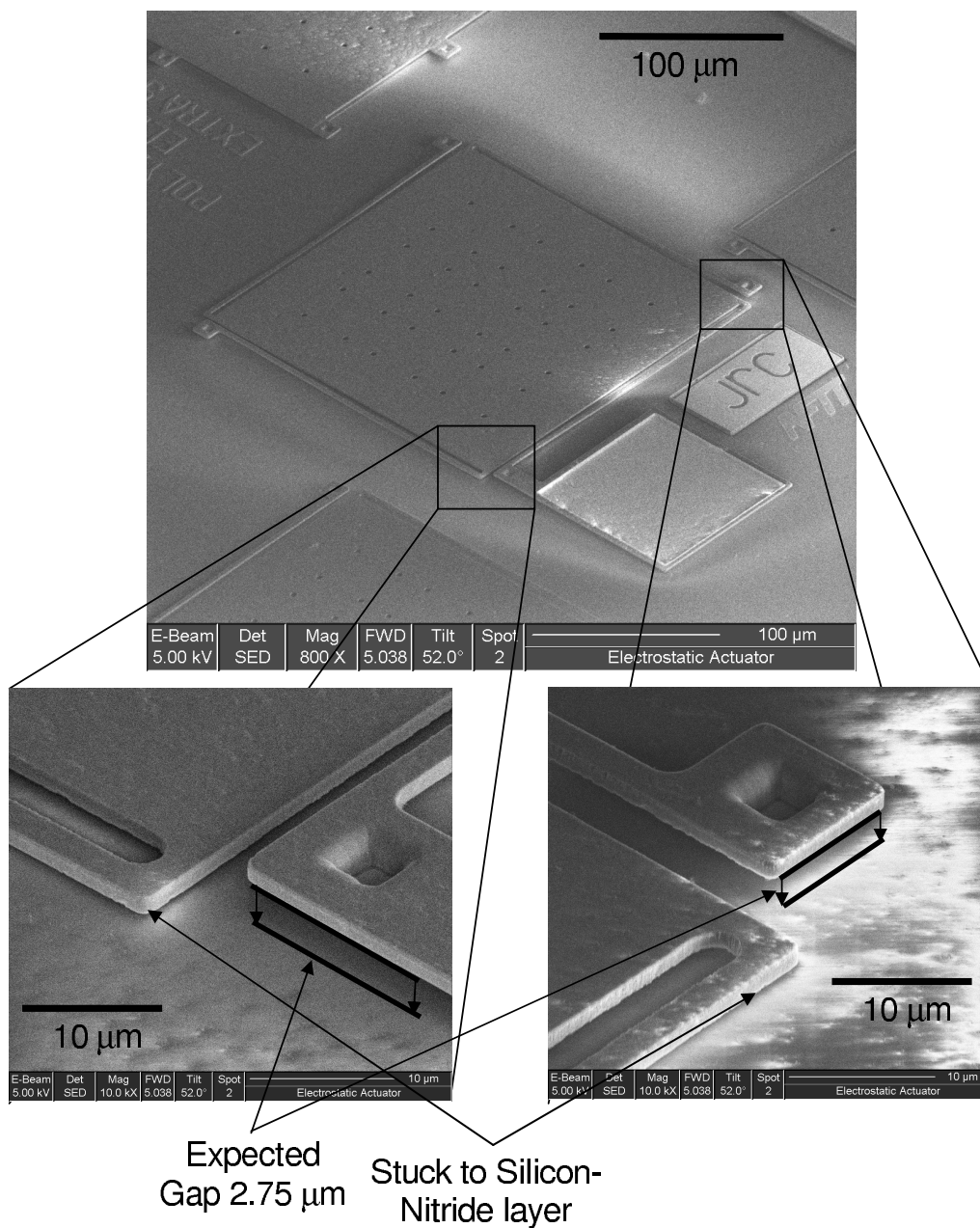


Figure 6.5 Scanning electron micrograph showing the flexures of the electrostatic piston actuator stuck to the silicon-nitride layer.

The significance of the results plotted in Figure 6.3 is that radiation exposure does affect the operating parameters of the piston actuator. The charge trapped within the silicon nitride layer causes a short lived change in capacitance and an increase in the voltage-deflection relationship as evidenced through increase in voltage-capacitance relationship of the piston actuator.

Results similar to those just presented were noted for devices irradiated to total doses of 250, 750, and 1000 krad(Si). At higher doses the change in capacitance between the pre-irradiated devices and the post-irradiated devices became more pronounced. This is illustrate in Figure 6.6 which presents the change in capacitance for actuators irradiated to total ionizing dose of 750 krad(Si) immediately following irradiation, and seven days after irradiation. Figure 6.6 (a) illustrates change in capacitance versus actuation voltage for an actuator irradiated with +10 volts applied, and Figure 6.6 (b) illustrates change in capacitance versus actuation voltage for an actuator irradiated with no bias applied. The significance of the results plotted in Figure 6.6 is that the decrease in capacitance associated with the actuation voltage is more prevalent for the devices irradiated to a total ionizing dose of 750 krad(Si) than for those devices irradiated to 500 krad(Si) (Figure 6.3).

Figure 6.7 illustrates the change of capacitance measured while the actuators were irradiated to total doses of (a) 250 (Die #1, Table 5.1), (b) 500 (Die #2, Table 5.1), (c) 750 (Die #3, Table 5.1), and (d) 1000 krad(Si) (Die #4, Table 5.1) and biased with 10 volts. The device irradiated to 750 krad(Si) total dose shows a decrease of 7 fF which corresponds directly with the difference between pre-irradiation and post-irradiation measurements plotted in Figure 6.6 (a) for the same device. The significance of this result is that the change in capacitance and thus deflection can be directly related to radiation exposure. Differences in the amount of capacitance decrease that occurred among the different doses illustrated in Figure 6.7 may be attributed to the differences in the capture cross-section of the silicon nitride layer. The amount of charging that occurs within the dielectric layer is dependent

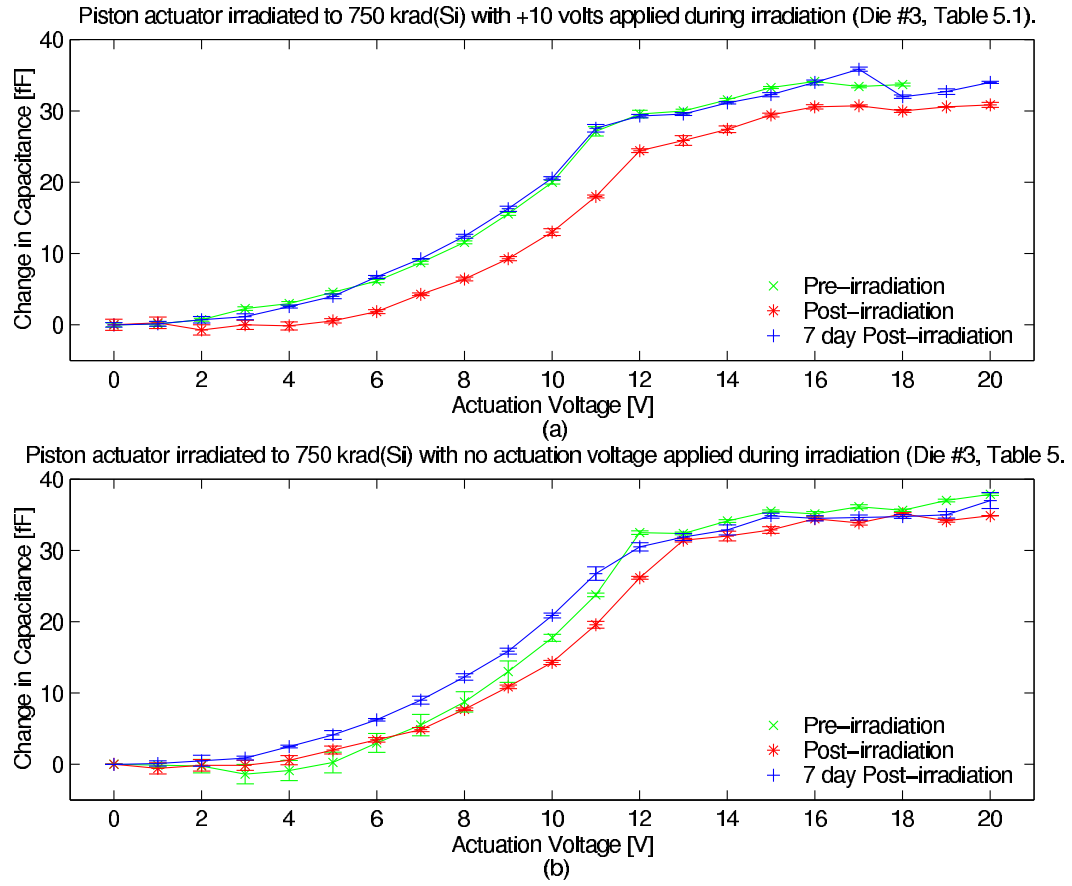


Figure 6.6 Change in capacitance versus actuation voltage for piston actuator irradiated to total dose of 750 krad(Si) (Die #3, Table 5.1) with (a) 10 volts actuation voltage applied during irradiation and (b) no actuation voltage applied during irradiation.



on both the amount of carriers available for trapping and the amount of trap site within the dielectric layer. Both these factors could change with position on the die and also between different die.

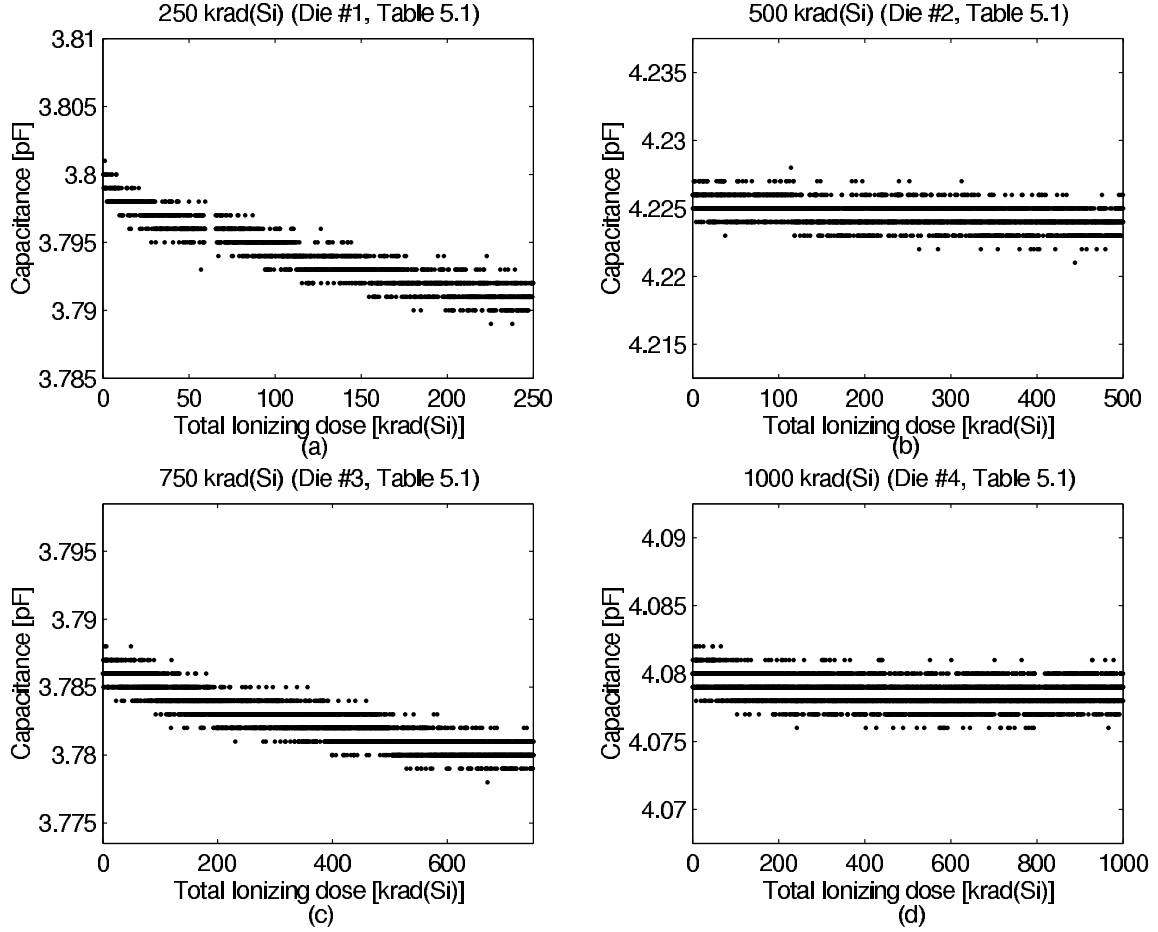


Figure 6.7 In-situ measured change in capacitance versus total ionizing dose for piston actuator irradiated to total doses of 250 (Die #1, Table 5.1) (a), 500 (Die #2, Table 5.1) (b), 750 (Die #3, Table 5.1) (c), and 1000 krad(Si) (Die #4, Table 5.1) (d) while biased with 10 volts.

The piston actuators irradiated under a negative bias did not follow the same trends in the change of capacitance as those irradiated under a positive bias. Actuators irradiated under a negative bias experienced an increase in capacitance after irradiation. Figure 6.8 (a) illustrates this increase for an actuator irradiated to a total ionizing dose of 500 krad(Si) (Die #6, Table 5.1) under a negative bias. This

increase in the change of capacitance is attributed to holes being trapped at the silicon nitride-air interface. Holes trapped at the interface add to the attractive force applied between the substrate and the actuator plate. The increase in force causes the plate to experience more deflection for a particular voltage and thus a greater change in capacitance is noted. The significance of this result is that charge trapping is not limited to the silicon nitride-substrate interface but also occurs within the bulk region of the silicon nitride and at the silicon nitride-air interface. Unlike the actuators irradiated under a positive bias, the actuators irradiated under a negative bias did not return to pre-irradiated conditions after a 7 day time frame. This is probably due to the fact that electrons are not readily available to annihilate holes trapped within the bulk region, and at the silicon nitride-air interface.

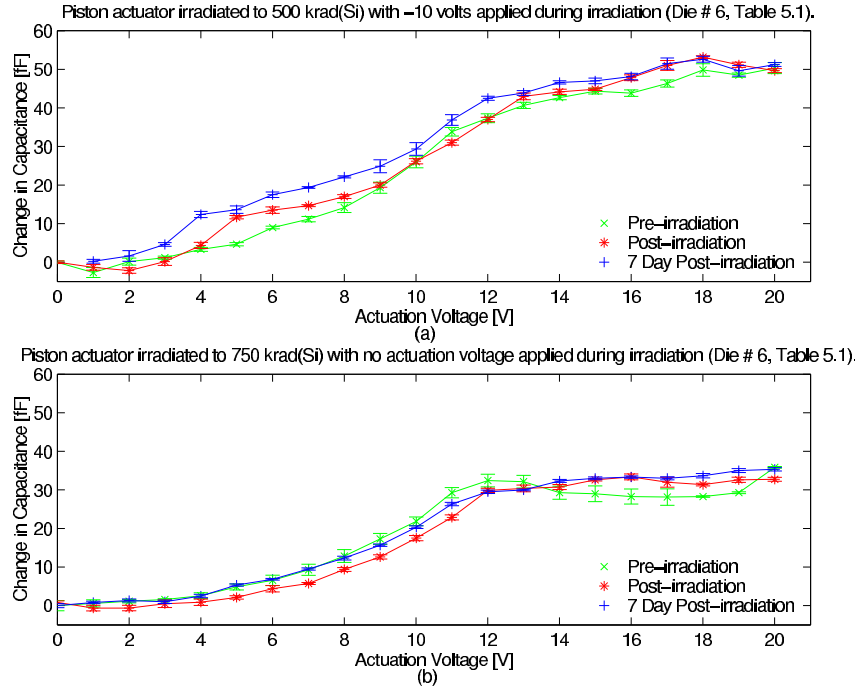


Figure 6.8 Change in capacitance versus actuation voltage for piston actuator irradiated to total dose of 500 krad(Si) (Die #6, Table 5.1). The top plot illustrates changes for an actuator held at a -10 volt constant bias during irradiation. The bottom plot illustrates changes for an actuator with no actuation voltage applied during irradiation.

Figure 6.8 (b) illustrates typical changes seen in the piston actuators irradiated with no actuation voltage applied during irradiation. These results are similar to the actuator tested under a positive bias scheme but with no actuation voltage applied during irradiation. The significance of this result is that minimal hole trapping is seen to occur when no biasing is applied during irradiation. With no bias applied the electrons and holes experience a higher rate of recombination leaving fewer carriers for trapping.

Figure 6.9 illustrates the in-situ capacitance measurement taken for an actuator irradiated under a negative bias to a total ionizing dose of 500 krad(Si) (Die #6, Table 5.1). The significance of the plotted results is that no change in capacitance was noted and this corresponds with the pre- and post-irradiated capacitance measurements taken for an actuation voltage of 10 volts plotted in Figure 6.8 (a).

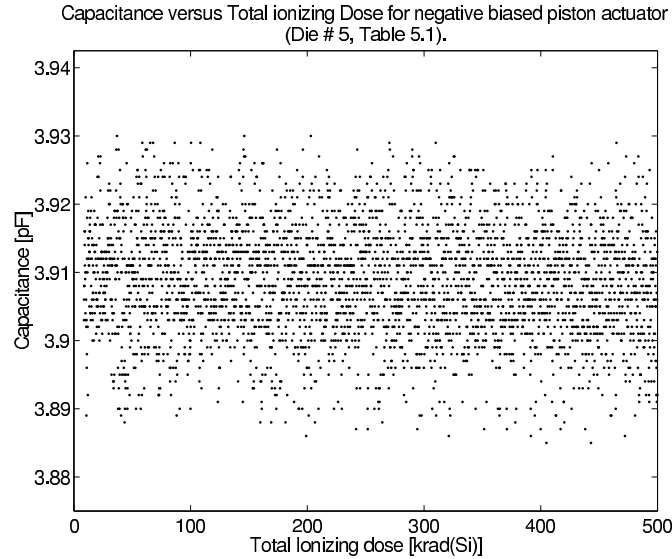


Figure 6.9 In-situ measured change in capacitance versus total ionizing dose for piston actuator bias with -10 volts and irradiated to total dose of 500 krad(Si) (Die #6, Table 5.1).

The last biasing configuration tested in the LEXR source was the snapdown biasing. It is important to note that the actuators are already stuck down. The snapdown bias is independent of the operation of the actuator snapdown voltage.

This biasing configuration was denoted as being snapdown since the voltage was swept from 0 to 20 volts, a voltage much higher than the actual snapdown voltage of the actuators tested. This test was accomplished to see if the applying high electric field during irradiation would alter the charge trapping behavior of the dielectric layer, and is therefore still a valid experiment. Figure 6.10 illustrates the capacitance measurements for two devices. Both devices were irradiated to a total dose of 1000 krad(Si). Figure 6.10 (a) illustrates the capacitance measurements taken for a device when a snapdown bias was applied after a total dose of 500 krad(Si) (Die #10, Table 5.1). Figure 6.10 (b) illustrates the capacitance measurements taken for a device when a snapdown bias was applied after a total dose of 750 krad(Si) (Die #11, Table 5.1). Applying the snapdown bias to the actuator after a total dose of 500 krad(Si) was absorbed seemed to cause the capacitance to saturate. The same behavior was not shown when the snapdown bias was applied after receiving a dose of 750 krad(Si) since the dielectric layer was already saturated with trapped holes. The significance of these results is that there is a point at which no more charge can be trapped within the dielectric layer. This is expected since the number of trapped charges is dependent not only on the amount of charge generated but also the finite number of traps present within the dielectric.

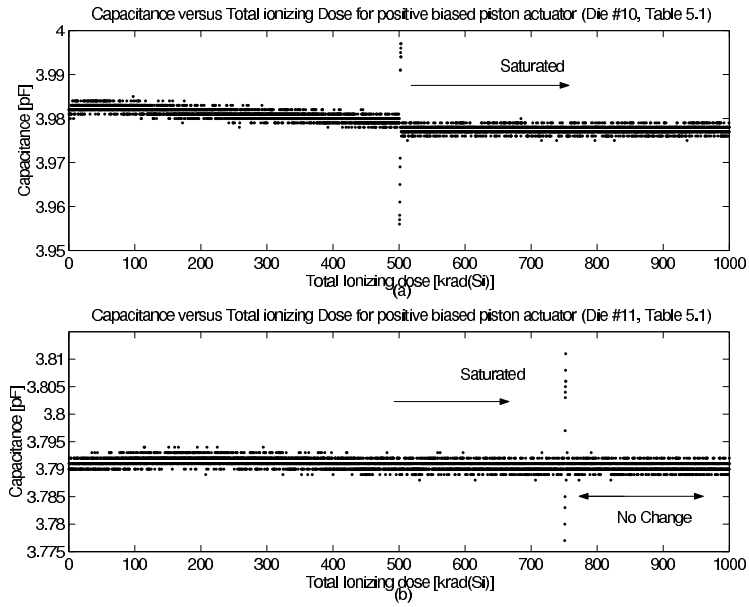


Figure 6.10 Change in capacitance versus total ionizing dose for two piston actuators irradiated to total dose of 1000 krad(Si) using the snapdown biasing configuration. (a) represents changes in capacitance when snapdown voltages were applied after absorbing a total dose of 500 krad(Si) (Die #10, Table 5.1). (b) represents changes in capacitance when snapdown voltages were applied after absorbing a total dose of 750 krad(Si) (Die #11, Table 5.1).

*6.1.3 Characterization of Electrostatic Piston Actuator Subjected to Gamma rays.* Characterizing the electrostatic piston actuators irradiated in the Co-60 source consisted of taking ten sets of measurements. Table 6.4 details the time frame between the ten measurements and the duration of all measurements taken at each total ionizing dose. The time at which the pre-irradiation measurements were initiated is denoted by T. All graphs detailing data obtained during these measurements will be denoted with the applicable measurement sequence number listed in Table 6.4.

Measurement Sequence	Measurement	250 krad(Si) Dose		500 krad(Si) Dose		750 krad(Si) Dose		1000 krad(Si) Dose	
		Start Time	Duration	Start Time	Duration	Start Time	Duration	Start Time	Duration
1	Post-irradiation Capacitance	T	3 min	T	3 min	T	3 min	T	3 min
2	In-situ Capacitance	T + 5 min	31.9 min	T + 5 min	63.8 min	T + 5 min	95.7 min	T + 5 min	127.6 min
3	Post-irradiation Capacitance	T + 42 min	3 min	T + 72 min	3 min	T + 105 min	3 min	T + 137 min	3 min
4	Post-irradiation Capacitance	T + 24 hr	3 min	T + 24 hr	3 min	T + 24 hr	3 min	T + 24 hr	3 min
5	Post-irradiation Capacitance	T + 47 hr	3 min	T + 47 hr	3 min	T + 47 hr	3 min	T + 47 hr	3 min
6	Post-irradiation Capacitance	T + 70 hr	3 min	T + 70 hr	3 min	T + 70 hr	3 min	T + 70 hr	3 min
7	Post-irradiation Capacitance	T + 94 hr	3 min	T + 94 hr	3 min	T + 94 hr	3 min	T + 94 hr	3 min
8	Post-irradiation Capacitance	T + 108 hr	3 min	T + 108 hr	3 min	T + 108 hr	3 min	T + 108 hr	3 min
9	Post-irradiation Capacitance	T + 144 hr	3 min	T + 144 hr	3 min	T + 144 hr	3 min	T + 144 hr	3 min
10	Post-irradiation Capacitance	T + 168 hr	3 min	T + 168 hr	3 min	T + 168 hr	3 min	T + 167 hr	3 min

Table 6.4 Time table detailing the time elapsed between the ten measurements taken, and the duration of the measurements, for electrostatic piston actuators irradiated to the specified total dose using the Co-60 Source. T is taken to be the start of the pre-irradiation capacitance measurements.

No significant changes were noted for electrostatic actuators irradiated in the Co-60 gamma source. Figure 6.11 illustrates the typical change in capacitance as a function of actuation voltage for devices irradiated in the Co-60 source. Unlike the devices irradiated in the LEXR source, the devices irradiated in the Co-60 source showed little change in capacitance. This is likely due to the different energy deposition profiles for the two sources. The low energy X-rays deposit more of their energy within the polysilicon structural layer and the silicon nitride insulating layer. The higher energy gamma rays in the Co-60 source deposit most of their energy within the silicon substrate, away from the actuators.

Figure 6.12 depicts in-situ capacitance measurements take on devices irradiated to 250 (Die # 1, Table 5.2), and 500 krad(Si) (Die #2, Table 5.2) respectively. Again,

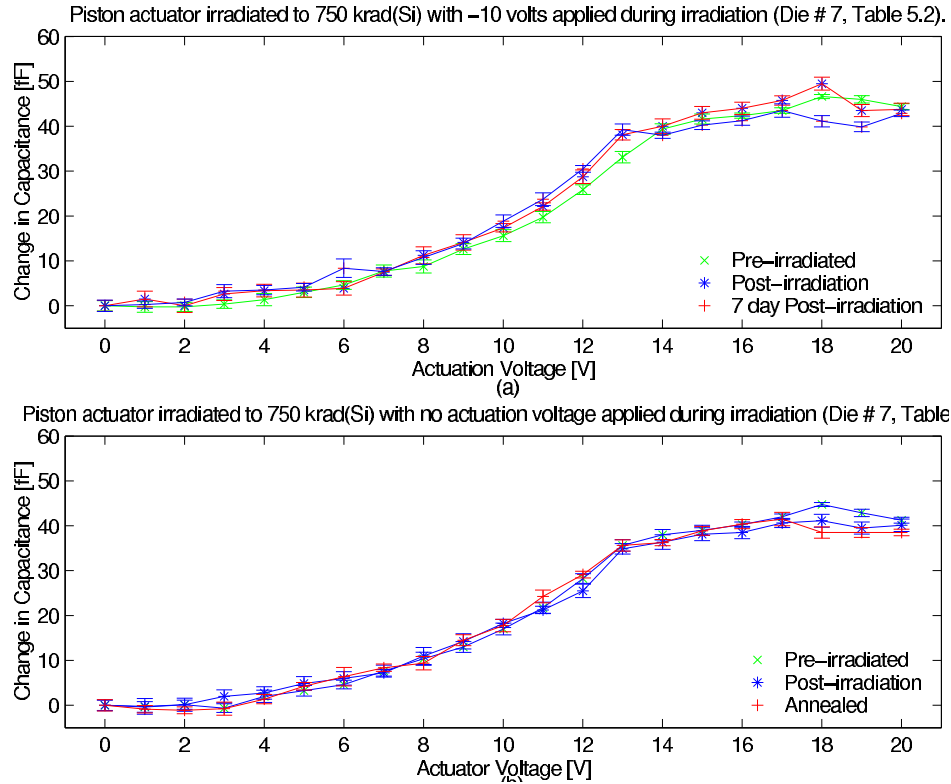


Figure 6.11 Change in capacitance versus actuation voltage for piston actuator irradiated to total dose of 750 krad(Si) (Die # 7, Table 5.2). The top plot illustrates changes for an actuator held at a -10 volt constant bias during irradiation. The bottom plot illustrates changes for an actuator with no actuation voltage applied during irradiation.

unlike the devices irradiated in the LEXR source, little change of capacitance is noted over the dose range. The capacitance plots illustrated in Figure 6.12 are indicative of all the devices irradiated at all dose levels. The significance of these results is that the operation of the electrostatic piston actuator was not effected by exposure to 1.25 MeV gamma rays.

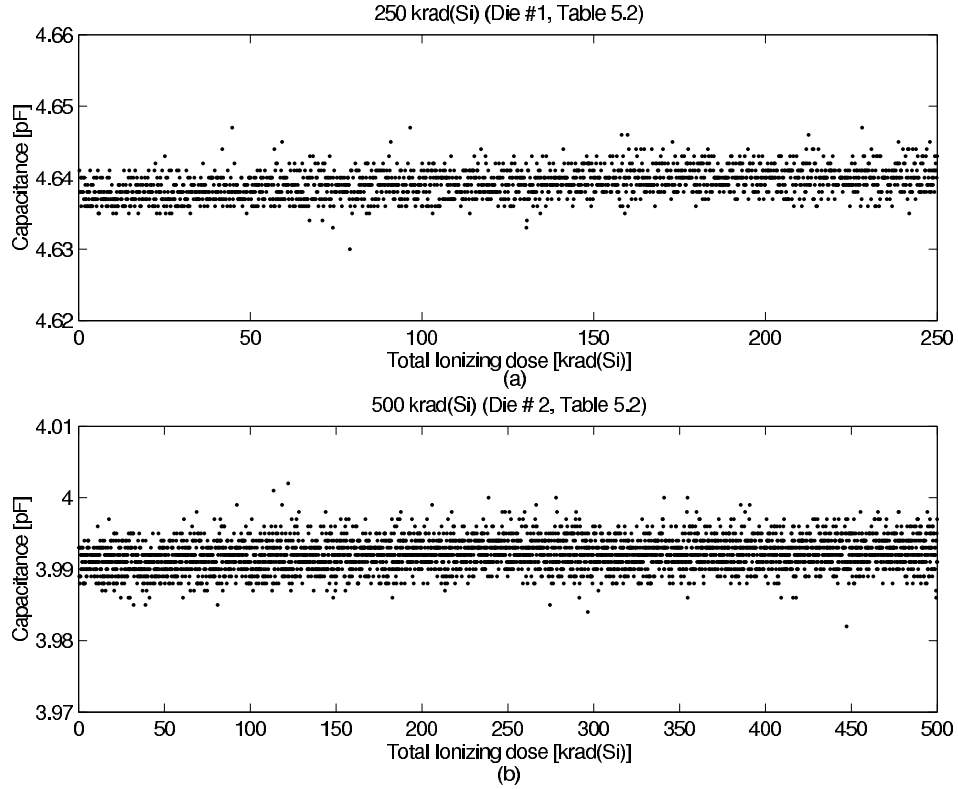


Figure 6.12 Change in capacitance versus total ionizing dose for piston actuator irradiated to total doses of 250 (Die #1, Table 5.2) (a), and 500 krad(Si) (Die #2, Table 5.2) (b) while biased with -10 volts.

It is important to note that the electrostatic piston actuators were not tested under charged particle equilibrium. Under charged particle equilibrium, charged particles carry an incremental energy out of a volume are replaced by charged particles carrying the same amount of energy into the volume. Since for this research the actuators were not irradiated under charge particle equilibrium, the silicon nitride layer did not receive the same dose as did the substrate material. It is believed



that had the test been accomplished under charged particle equilibrium different results would have occurred. Under charge particle equilibrium the dielectric layer would have been bombarded with charged carriers and more ionization would have occurred within the dielectric layer. Charge particle equilibrium can be placing a piece of silicon material over the package well, thus the actuator would be irradiated by charged particles created in the piece of silicon material. It would therefore be possible that the results of the C0-60 tests would have been similar to those reported for the LEXR testing.

From the results of this research, it is believed that ionizing radiation would have no long lived effects on the operation of the electrostatic piston actuator irradiated under a positive bias. Actuators irradiated under a negative bias could be prone premature snapdown due to hole trapping at the dielectric-air interface. Therefore, the best biasing configuration for electrostatic piston actuators operating within a radiation environment is the positive configuration.

## 6.2 *Characterization of Electrothermal Actuator*

This section presents the results and analysis for the characterization of the electrothermal actuator. Section 6.2.1 discusses the results of the analytical model and compares the model to experimental deflection measurements. The results and analysis of the experimental measurements are categorized according to the radiation source. Section 6.2.2 discusses the results for the characterization accomplished using the LEXR source. The results for the actuators irradiated using the Co-60 gamma ray source are discussed in Section 6.2.3.

### 6.2.1 *Comparison of Analytical Model and Experimental Measurements.*

Using the Analytical model discussed in Section 4.2 gives the deflection-voltage relationship illustrated in Figure 6.13 using the parameters given in Table 6.5 and Table

6.1. The pre-characterized deflection measurements are plotted on the same graph for comparison reasons.

Parameter	Value
Young's Modulus for polysilicon, $E_s$	169 GPa [1]
Resistivity of polysilicon, $\rho$	20 $\Omega\mu\text{m}$ [4]
Coefficient of thermal expansion, $\alpha$	$3.5 \times 10^{-6} \text{ C}^{-1}$ [4]
Thermal conductivity of air, $k_a$	$0.026 \times 10^{-6} \text{ W}\mu\text{m}^{-1}\text{C}^{-1}$ [4]
Thermal conductivity of polysilicon, $k_p$	117 $\text{W}\mu\text{m}^{-1}\text{C}^{-1}$ [5]
Temperature of substrate, $T_{\text{substrate}}$	30 C

Table 6.5 Material parameters used in the electrothermal actuator analytical model.

Parameter	Value
Length of hot arm, $L_h$	250 $\mu\text{m}$
Length of flexure, $L_f$	50 $\mu\text{m}$
Length of cold arm, $L_c$	200 $\mu\text{m}$
Length of gap, $g$	2.5 $\mu\text{m}$
Width of cold arm, $W_c$	18 $\mu\text{m}$
Width of hot arm, $W_h$	2.5 $\mu\text{m}$
Width of flexure, $W_f$	2.5 $\mu\text{m}$
Thickness of polysilicon, $t$	1.5 $\mu\text{m}$

Table 6.6 Geometrical parameters used in the electrothermal actuator analytical model.

The plot in Figure 6.13 illustrates the accuracy of the analytical model of the electrothermal actuator. At the higher voltages the model diverges from the actual measured tip deflection. This is somewhat expected since the model does not account for the temperature dependence of the resistance of the polysilicon material and the material parameters used were obtained from published reports and not measured.

*6.2.2 Characterization of Electrothermal Actuator Subjected to Low Energy X-rays.* Characterizing the electrothermal actuators irradiated in the LEXR source consisted of taking eight sets of measurements. Table 6.7 details the time frame between the eight measurements and the duration of all measurements taken at each total ionizing dose. The time at which the pre-irradiation measurements

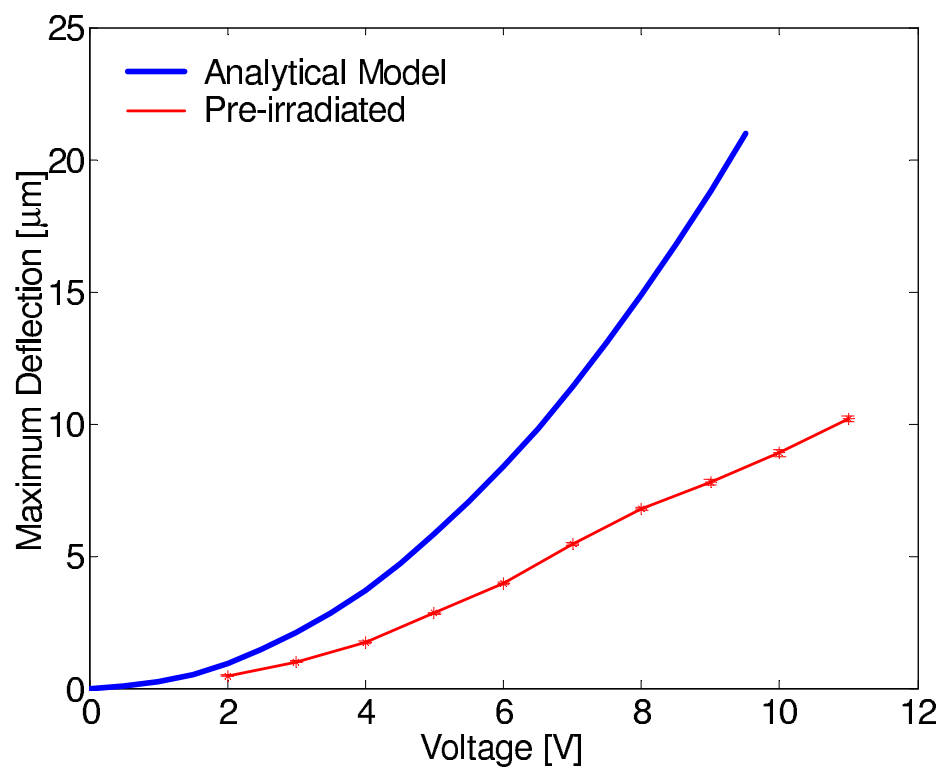


Figure 6.13 Analytical prediction and pre-characterization measurement of Electrothermal actuator tip deflection versus voltage.

were initiated is denoted by T. All graphs detailing data obtained during these measurements will be denoted with the applicable measurement sequence number listed in Table 6.7.

Measurement Sequence	Measurement	250 krad(Si) Dose		500 krad(Si) Dose		750 krad(Si) Dose		1000 krad(Si) Dose	
		Start Time	Duration	Start Time	Duration	Start Time	Duration	Start Time	Duration
1	Pre-irradiated Deflection	T - 454 hr	45 min	T - 454hr	45 min	T - 454 hr	45 min	T - 454hr	45 min
2	Pre-irradiated Resistance	T	2 min	T	2 min	T	2 min	T	2 min
3	In-situ Resistance	T + 5 min	31 min	T + 5 min	62 min	T + 5 min	93 min	T + 5 min	124
4	Post-irradiated Resistance	T + 40 min	2 min	T + 70 min	2 min	T + 102 min	2 min	T + 133 min	2 min
5	Post-irradiated Resistance	T + 24 hr	2min	T + 24 hr	2 min	T + 24 hr	2 min	T + 24 hr	2 min
6	Post-irradiated Resistance	T + 50 hr	2min	T + 50 hr	2 min	T + 51 hr	2 min	T +51 hr	2 min
7	Post-irradiated Resistance	T + 75 hr	2min	T + 75 hr	2 min	T + 74 hr	2 min	T + 74 hr	2 min
8	Post-irradiated Deflection	T + 100 hr	45 min	T + 100 hr	45 min	T + 100 hr	45 min	T + 100 hr	45 min

Table 6.7 Time table detailing the time elapsed between the eight measurement taken, and the duration of the measurements, for electrothermal actuators irradiated to the specified total dose using the LEXR Source. T is taken to be the start of the pre-irradiation resistance measurements.

The deflection-voltage response for electrothermal actuators irradiated with 50 keV X-rays using the LEXR source to total ionizing doses of 250 (Die #1, Table 5.3), 500 (Die #2, Table 5.3), 750 (Die #3, Table 5.3), and 1000 krad(Si) (Die #4, Table 5.3) are presented in Figure 6.14. The plots represent the average measured tip deflection plus and minus the standard error in the measurements. The pre-irradiation measurement are plotted in green and the post-irradiation measurements are plotted in red. The pre-irradiation measurements were the first measurements taken in the sequence of measurements and the post-irradiation measurements were the last measurement in the sequence as indicated by Measurement Sequence #1 and #8 respectively in Figure 6.14. The measured tip deflection for all the irradiated actuators shows a decrease. The change in tip deflection seems to extend to lower voltage levels as the total ionizing dose is increases. This dose behavior, however, is not noted in the resistance-voltage measurement taken before and after irradiation.

Figure 6.15 presents the pre- and post-irradiation resistance measurements for actuators irradiated to total ionizing doses of (a) 250 (Die #1, Table 5.3), (b) 500 (Die #2, Table 5.3), (c) 750 (Die #4, Table 5.3), and (c) 1000 krad(Si) (Die #4, Table 5.3). The plots for actuators irradiated to 250, and 1000 krad(Si), plots (a)

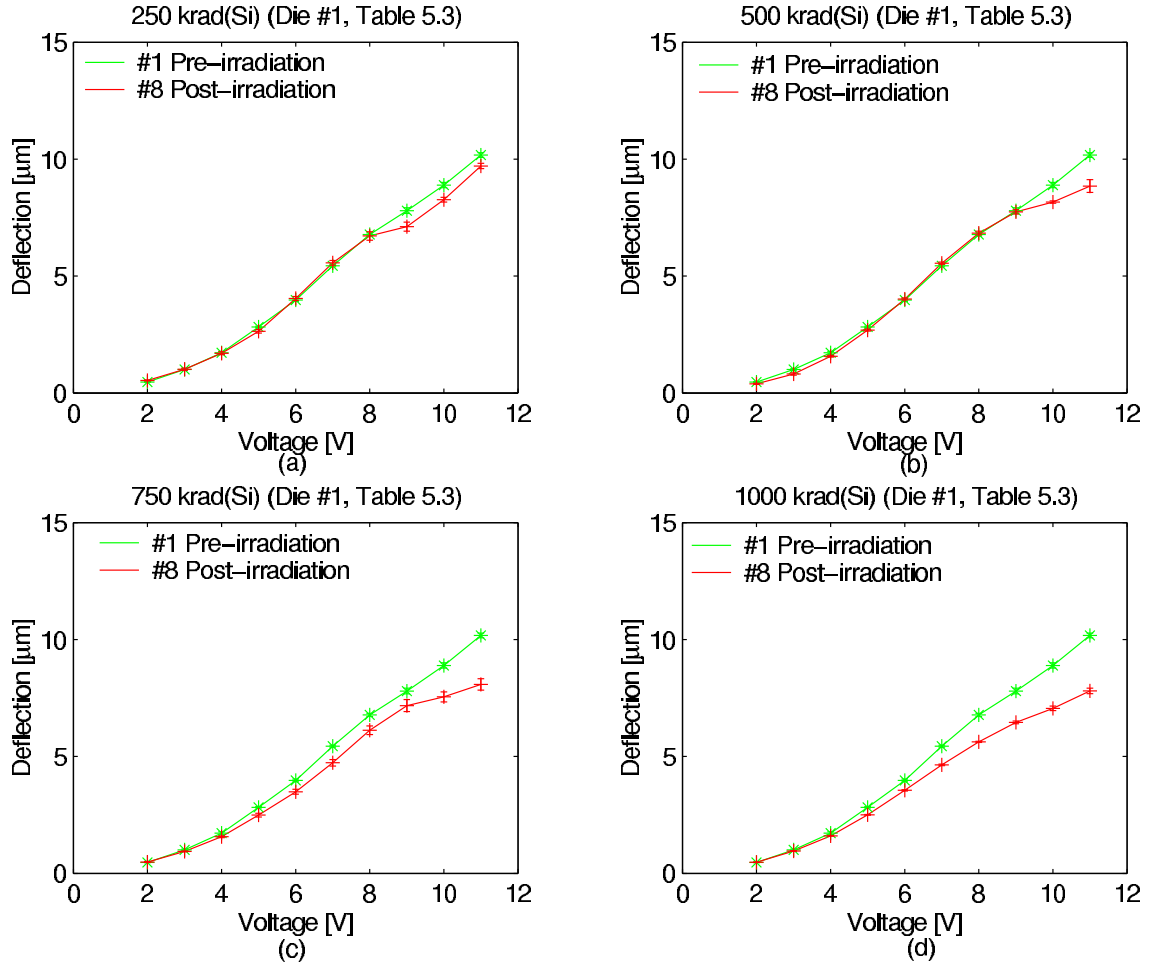


Figure 6.14 Pre- and post-irradiation deflection measurements for 250  $\mu\text{m}$  long electrothermal actuators subjected to total ionizing doses of (a) 250 krad(Si), (b) 500 krad(Si), (c) 750 krad(Si), and (d) 1000 krad(Si) in LEXR source.

and (d) in Figure 6.15, show essentially no change in resistance. This indicates that power dissipation at these two dose levels were unchanged. The significance of this result is that the decrease in the tip deflection measured at these two doses cannot be attributed to the radiation but rather to a break-in phenomena that occurred after the devices were irradiated. In Figure 6.15, the actuators irradiated to total doses of 500 krad(Si) (a), and 750 krad(Si) (c) show changes in resistance. Both actuators show an increase in resistance at the higher voltages and a decrease in resistance at the lower voltages. The magnification of this trend at the higher dose indicates a possible dose dependence. However, once again, this dependence is voided by the in-situ resistance measurements taken during irradiation.

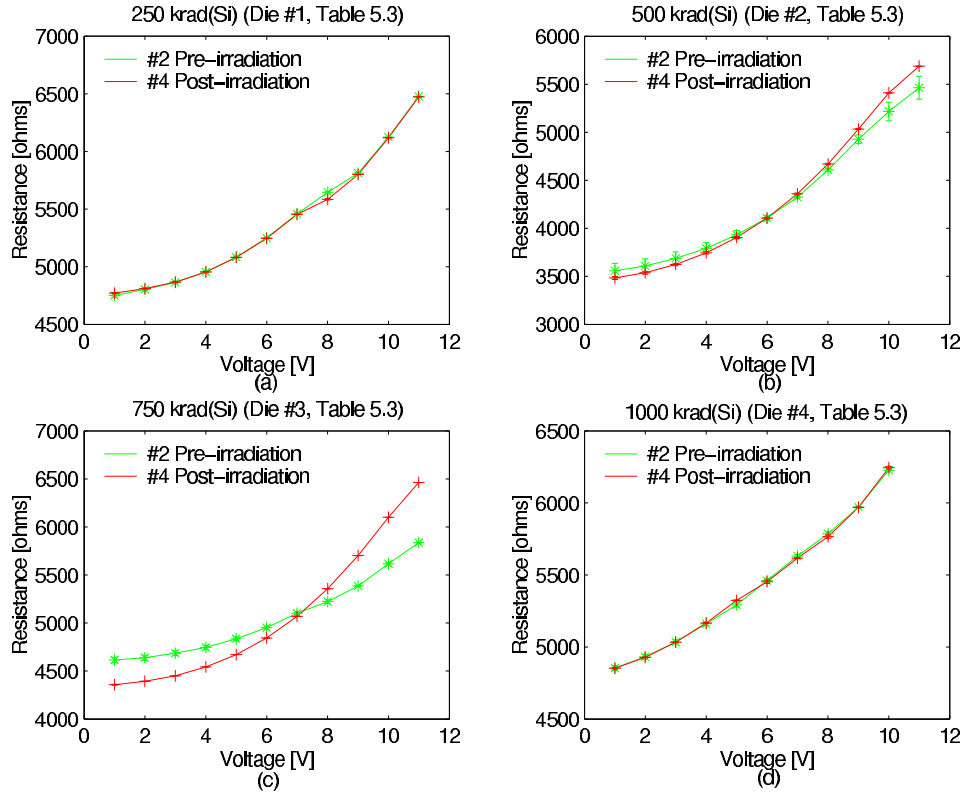


Figure 6.15 Pre- and post-irradiation resistance measurements for 250  $\mu\text{m}$  long electrothermal actuators subjected to total ionizing doses of (a) 250 krad(Si) (Die #1, Table 5.3), (b) 500 krad(Si) (Die #2, Table 5.3), (c) 750 krad(Si) (Die #3, Table 5.3), and (d) 1000 krad(Si) (Die #4, Table 5.3) in LEXR source.

Figure 6.16 illustrates in-situ resistance measurements as a function of total ionizing dose for each voltage step from 1 to 11 volts. Recall, the actuators were irradiated at a dose rate of  $134.5 \frac{\text{rad}(\text{Si})}{\text{s}}$ , therefore, the resistance measurements plotted in Figure 6.16 (a) and (b) span a 63.7 minute (Die #2, Table 5.3) and 95.4 minute (Die #3, Table 5.3) time frame respectively. A significant change in resistance is noted for the actuator irradiated to a total dose of 750 krad(Si). This noted change in resistance correlates to the change in resistance illustrated in Figure 6.15 for the same actuator. A similar correlation in resistance for the actuator irradiated to 500 krad(Si) was not noted. However, investigating the pre-irradiated IV relationship for the actuator irradiated to 500 krad(Si) reveals that the change in resistance actually occurred before the device was irradiated.

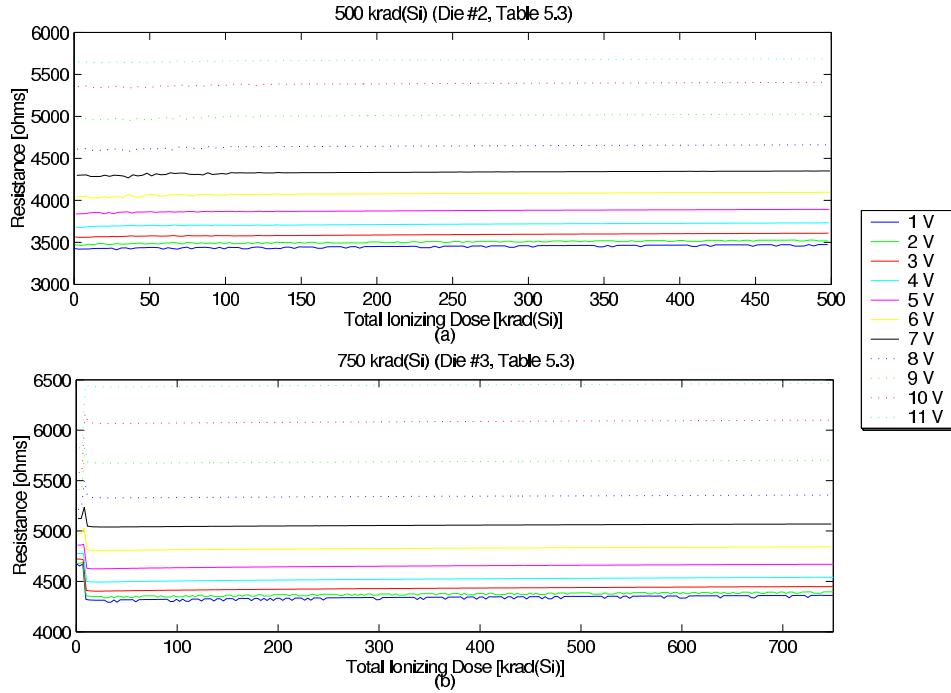


Figure 6.16 In-situ resistance measurements taken on  $250 \mu\text{m}$  long electrothermal actuators subjected to total ionizing doses of (a) 500 krad(Si), and (b) 750 krad(Si), at a dose rate of  $134.5 \frac{\text{rad}(\text{Si})}{\text{s}}$ , in LEXR source.

The pre-irradiation characterization consisted of measuring the IV relationship for the actuator several times. Figure 6.17 (a) illustrates the measured IV

relationship for the actuator irradiated to 500 krad(Si). Each cycle represents steps of voltage from 1 to 11 volt. A definite changes is noted between the second and third cycle. Figure 6.17 (b) illustrates plots of the average resistance for the first two and last five cycles of the measurement process. The change in the IV profile between the second and third cycles explains the change in resistance between the pre- and post-characterization of the actuator irradiated to a dose of 500 krad(Si) (See Figure 6.17 (c)).

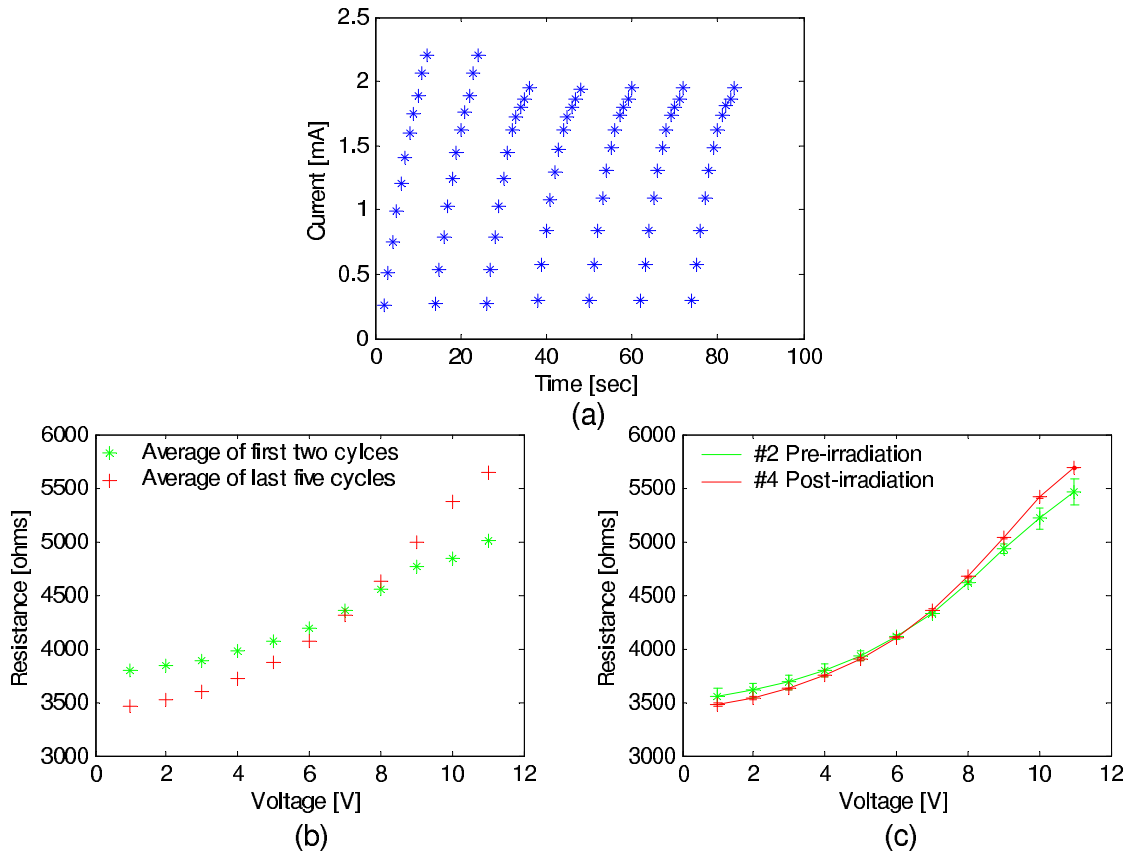


Figure 6.17 (a) Current measurements for  $250\ \mu\text{m}$  electrothermal actuator taken immediately before irradiating the actuator to a total ionizing dose of 500 krad(Si) (Die #2, Table 5.3) in LEXR source. (b) Average resistance for first two and last five cycles of the pre-irradiation resistance measurements plotted in (a). (c) Pre- and post-irradiation resistance measurements.

For the actuators irradiated to 500, and 750 krad(Si), the change in deflection can be attributed to changes in the resistance of the polysilicon. Yang [6] notes that



thresholds exist for the electrical input value and duration above which deformation phenomenon begins. In addition, it has been documented [7] that thermal anneal can affect the mass density and grain size of polysilicon. This, in turn could alter both the resistivity and Young's modulus of the material. During this research, resistance changes were noted to occur both before, during, and after irradiation. In order to confirm that there was no correlation between the change in resistance and the radiation exposure a control experiment was performed.

The control experiment consisted of performing deflection and IV measurements on electrothermal actuators not subjected to any radiation. First, deflections measurements were taken for an electrothermal actuator. The deflection-voltage relationship was measured four different times. The actuator was cycled through a voltage sweep from 0 to 20 volts for approximately 8.5 minutes and IV measurement taken every second. The same procedures used to characterize the actuators before and after irradiation were followed. After the resistance measurements were complete, deflection measurements were again taken. Figure 6.18 illustrates the measured tip deflection before and after the actuator was broke-in. The amount of tip deflection associated with a given voltage decreases after break-in. This is the same phenomena noted for the irradiated actuators.

Figure 6.19 (a) illustrates the resistance of the electrothermal actuator as a function of time and applied voltage, and Figure 6.19 (b) illustrates the average resistance measured before and after break-in of the actuator. It should be noted that the resistance measured for 10 volts, plotted in Figure 6.19 (a), does not follow the trend seen for the other applied voltages. There is no explanation for why this occurred. The significance of the results plotted in Figure 6.19 (a) is that the same change in resistance noted for the irradiated actuators is noted for the non-irradiated actuator. The significance of these results for the irradiation and control experiment is that the electrothermal actuator's deflection and power consumption are unaffected by 50 keV X-rays up to a total ionizing dose of 1000 krad(Si).

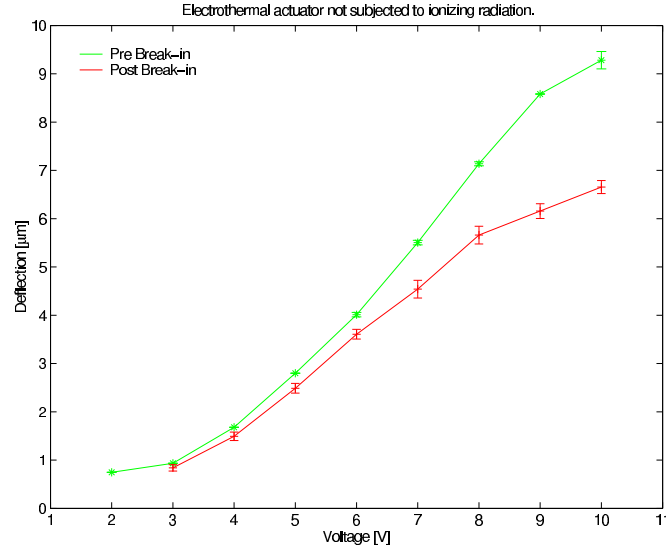


Figure 6.18 Pre and post break-in tip deflection measurements for electrothermal actuators not subjected to ionizing radiation.

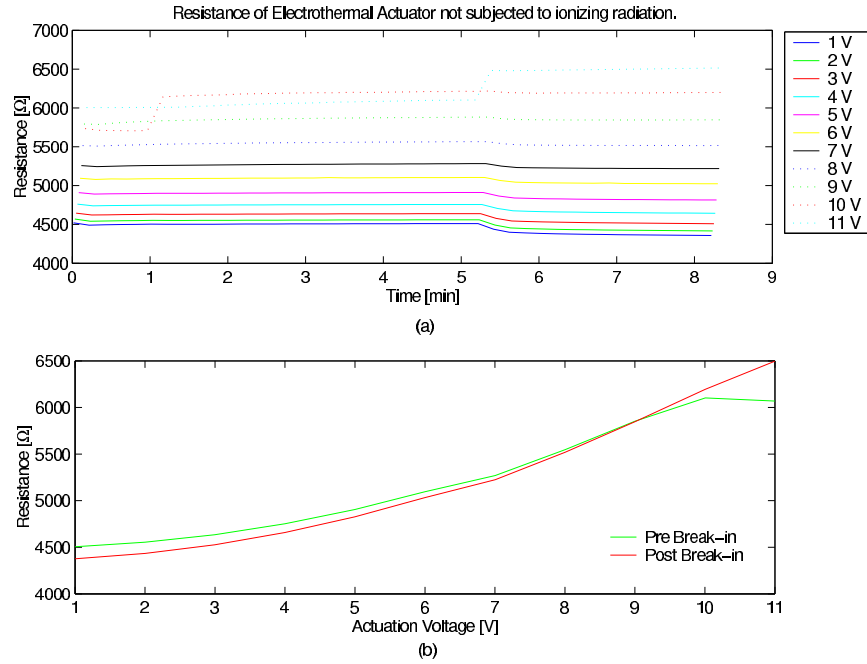


Figure 6.19 (a) Current measurements for electrothermal actuators not subjected to ionizing radiation. (b) Average resistance for pre and post break-in of electrothermal actuator not subjected to ionizing radiation.

### 6.2.3 Characterization of Electrothermal Actuator Subjected to Gamma rays.

Characterizing the electrothermal actuators irradiated in the Co-60 source consisted of taking eight sets of measurements. Table 6.8 details the time frame between the eight measurements and the duration of all measurements taken at each total ionizing dose. The time at which the pre-irradiation measurements were initiated is denoted by T. All graphs detailing data obtained during these measurements will be denoted in the legend with the applicable measurement sequence number listed in Table 6.8.

Measurement Sequence	Measurement	250 krad(Si) Dose		500 krad(Si) Dose		750 krad(Si) Dose		1000 krad(Si) Dose	
		Start Time	Duration	Start Time	Duration	Start Time	Duration	Start Time	Duration
1	Pre-irradiated Deflection	T - 430 hr	45 min	T - 430 hr	45 min	T - 430 hr	45 min	T - 430 hr	45 min
2	Pre-irradiated Resistance	T	2 min	T	2 min	T	2 min	T	2 min
3	In-situ Resistance	T + 5 min	31.9 min	T + 5 min	63.7 min	T + 5 min	95.4 min	T + 5 min	127.2 min
4	Post-irradiated Resistance	T + 38 min	2 min	T + 68 min	2 min	T + 100 min	2 min	T + 131 min	2 min
5	Post-irradiated Resistance	T + 27 hr	2min	T + 27 hr	2 min	T + 25 hr	2 min	T + 25 hr	2 min
6	Post-irradiated Resistance	T + 57 hr	2min	T + 57 hr	2 min	T + 49 hr	2 min	T +49 hr	2 min
7	Post-irradiated Resistance	T + 75 hr	2min	T + 75 hr	2 min	T + 74 hr	2 min	T + 74 hr	2 min
8	Post-irradiated Deflection	T + 99 hr	45 min	T + 99 hr	45 min	T + 99 hr	45 min	T + 99 hr	45 min

Table 6.8 Time table detailing the time elapsed between the eight measurement taken, and the duration of the measurements, for electrothermal actuators irradiated to the specified total dose using the Co-60 Source. T is taken to be the start of the pre-irradiation resistance measurements.

The deflection-voltage response for electrothermal actuators irradiated with 1.25 MeV gamma rays using the Co-60 source to total ionizing doses of 250 (Die #1, Table 5.4), 500 (Die #2, Table 5.4), 750 (Die #3, Table 5.4), and 1000 krad(Si) (Die #4, Table 5.4) are presented in Figure 6.20. The plots represent the average measured tip deflection plus and minus the standard error in the measurements. The pre-irradiation measurement are plotted in red and the post-irradiation measurements are plotted in blue. The post-irradiation measurement were taken seven days after the actuators were irradiated. Only the actuator irradiated to 250 krad(Si) shows a change in measured deflection outside the 3 sigma measurement error.

Figure 6.21 illustrates the resistance as a function of voltage for actuators irradiated to the specified dose before and after irradiation. As with the deflection

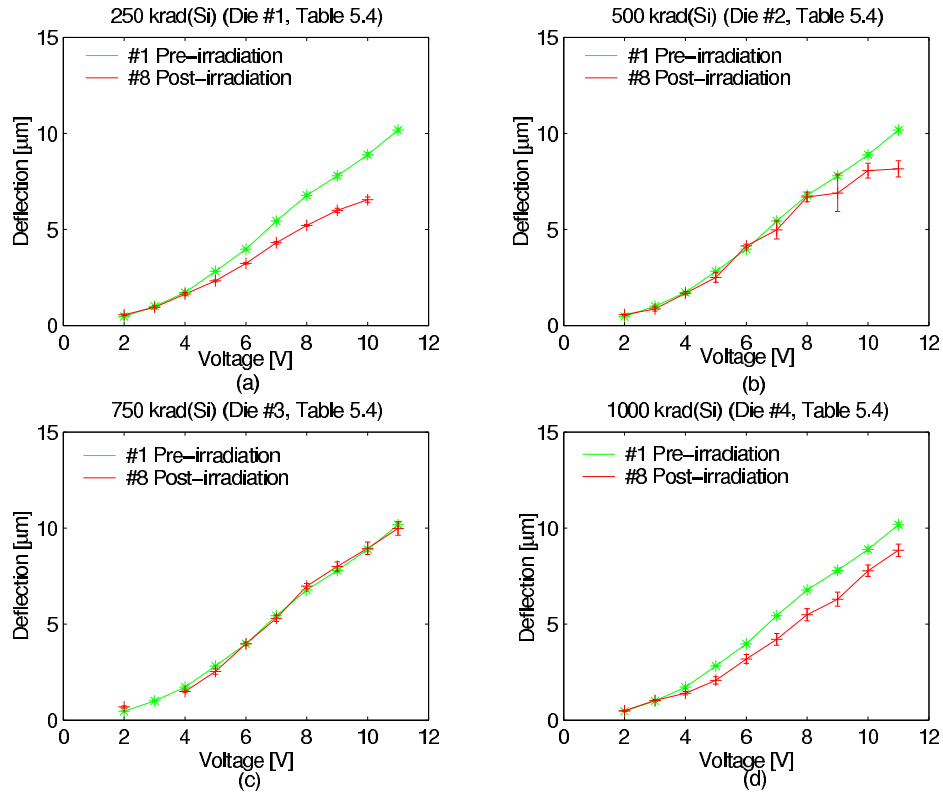


Figure 6.20 Pre- and post-irradiation deflection measurements for 250  $\mu\text{m}$  long electrothermal actuators subjected to total ionizing doses of 250 (Die #1, Table 5.4), 500 (die #2, Table 5.4), 750 (Die #3, Table 5.4) and 1000 krad(Si) (Die #4, Table 5.4) in Co-60 gamma source.

measurements, the post-irradiation resistance measurements were taken seven days after irradiating. Only the actuator irradiated to 750 krad(Si) shows any change in resistance. Figure 6.22 illustrates the resistance measurement while irradiating the this actuator. The change in resistance during irradiation is similar to the change of resistance reported for the electrothermal actuators irradiated with the LEXR source. This change of resistance is seen to occur randomly with no correlation to radiation exposure. The significance of these results is that the operation of the electrothermal actuators is not effected by 1.25 MeV gamma ray exposure up to a total ionizing dose of 1000 krad(Si).

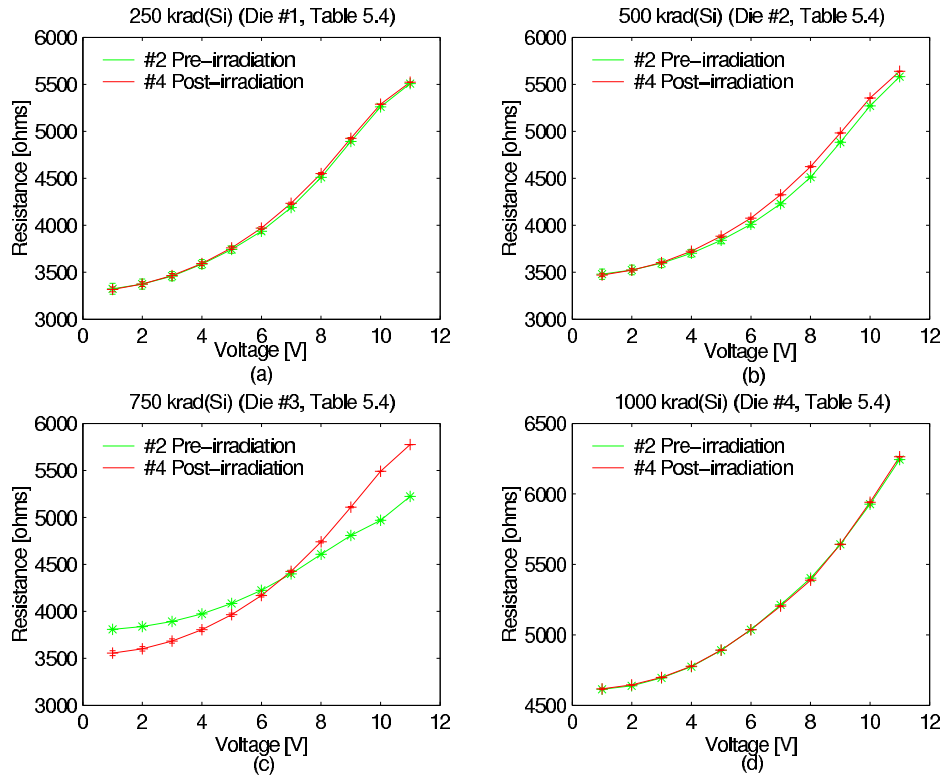


Figure 6.21 Pre- and post-irradiation resistance measurements for 250  $\mu\text{m}$  long electrothermal actuators subjected to total ionizing doses of 250 (Die #1, Table 5.4), 500 (Die #2, Table 5.4), 750 (Die #3, Table 5.4), and 1000 krad(Si) (Die #4, Table 5.4) in Co-60 gamma source.

During post-characterization of the electrothermal actuator, a discoloration in the irradiated actuators was noted. Figure 6.23 contains pictures of an actuator not

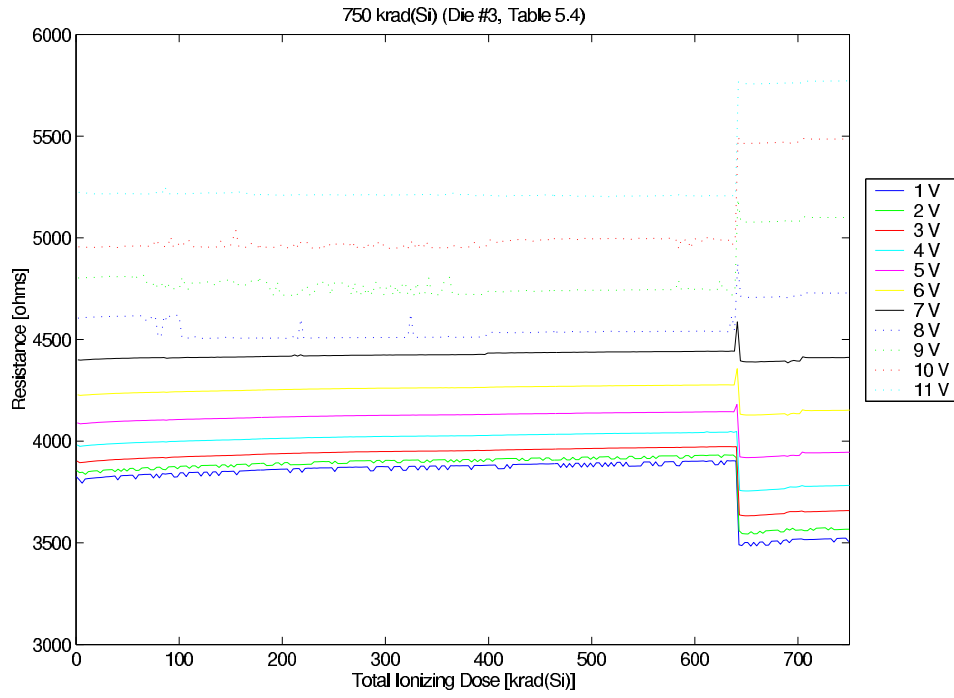


Figure 6.22 In-situ resistance measurements taken on 250  $\mu\text{m}$  long electrothermal actuator subjected to total ionizing dose of 750 krad(Si) (Die #3, Table 5.4), at a dose rate of  $130.8 \frac{\text{rad}(\text{Si})}{\text{s}}$ , in Co-60 gamma source.

subjected to irradiation and one subjected to a total dose of 1 Mrad(Si) in the Co-60 source (Die #4, Table 5.4). Similar color changes were noted on electrothermal actuators irradiated to different dose; however, not as drastic as the changes illustrated in Figure 6.23. The change in color leads to the conclusion that some changes have occurred within the polysilicon layer. Radiation studies have documented color center formation within optical materials [8]. Color centers are essentially new energy state, or filled existing energy states, within the forbidden energy gap of the material thus changing the absorption spectra of the material. The formation of new energy states would be a product of radiation induced displacement damage discussed in Section 2.4.2. Interestingly, this research concludes that displacement damage has occurred within the polysilicon layer.

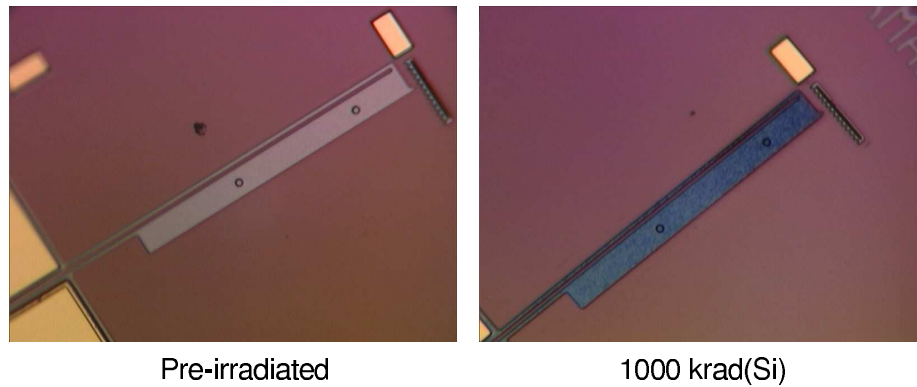


Figure 6.23 Pictures of electrothermal actuator before irradiation and after irradiating to 1000 krad(Si) in Co-60 gamma source.

The results of the characterization of the electrothermal actuator, along with the results of the control experiment discussed in Section 6.2.2, lead to the conclusion that the operation of the actuator is unaffected by gamma radiation up to a total ionizing dose of 1 MradSi.

In both ionizing radiation environments, 50 keV X-ray and 1.25 MeV gamma, the operation of the electrothermal actuator was unaffected. This same conclusions were drawn by Johnstone [9] and Taylor [10] after subjecting the actuators to gamma,

protons and copper ions. It is suspected that the changes in tip deflection that were noted were due to the actuator being physically changed as is evidenced by the change of resistance noted after break-in of the actuator.

### 6.3 Characterization of Residual Stress Cantilever

This section presents the results and analysis for the characterization of the residual stress cantilever. The pre- and post- characterization results will be presented together since no in-situ measurements were taken for the cantilever. However, a distinction will be made between the radiation source. Section 6.3.1 presents the results obtained from the analytical model derived in Section 4.3. Section 6.3.2 presents the results and analysis for the residual stress cantilevers irradiated using the LEXR source. Section 6.3.3 presents the results and analysis of the residual stress cantilevers irradiated using the Co-60 Gamma ray source.

*6.3.1 Analytical Model Results.* The amount of deflection that a residual stress cantilever will undergo upon release is given by Equation 4.42.

Figure 6.24 illustrates the amount of deflection as a function of the distance from the anchor for the analytical model and pre-characterized cantilevers. The analytical results were obtained using Equation 4.42 and the parameters listed in Table 6.9.

The experimental deflection measurement plotted in Figure 6.24 is the average deflection measured for 80 cantilevers. The deflection as a function of distance from the anchor was calculated by converting the experimentally obtained tip deflection to a radius of curvature. The radius of curvature was then used in Equation 4.42 to calculate the deflection versus distance. The standard deviation of the experimentally obtained tip deflection was  $0.48 \mu\text{m}$ . The analytical model is seen to underestimate the deflection of the cantilever. A structure whose width is much smaller than its



Parameter	Value
Young's modulus of polysilicon, $E_s$	169 GPa [1]
Poisson's ratio for polysilicon, $\nu_s$	0.22 [1]
Young's modulus of gold film, $E_f$	78 GPa [11]
Poisson's ratio for gold film, $\nu_f$	0.35 [11]
Thickness of polysilicon, $H$	$1.5 \mu\text{m}$ [12]
Thickness of gold film, $h$	$0.5 \mu\text{m}$ [12]
Length of cantilever, $L$	$295 \mu\text{m}$

Table 6.9 Parameters used in analytical model of residual stress cantilever.

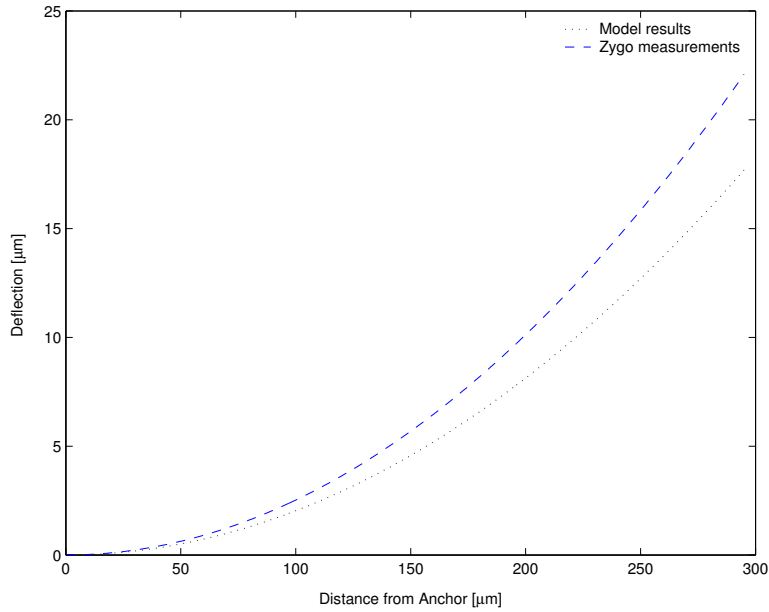


Figure 6.24 Modelled and experimentally measured deflection of  $300 \mu\text{m}$  by  $20 \mu\text{m}$  cantilever.

length will experience less stiffening then one whose width and length are comparable [13]. For the cantilever design tested in this research the width is fifteen times shorter then the length of the actuator and thus the effects of stiffening would be small. In addition, the difference between the model and experimental measurements can also be attributed to varying material parameters. The material parameters used in the analytical model were found in published reports and not measured.

The analytical model was derived for the sole purpose of providing a first order prediction of the amount of deflection associated with a residual stress cantilever. The model has accomplished this within a 20 percent tolerance.

### *6.3.2 Results for Residual Stress Cantilever irradiated with LEXR Source.*

Table 6.10 presents the deflection measurements for residual cantilevers before and after being irradiated with 50 keV X-rays to total ionizing doses of 250 (Die #1, Table 5.1), 500 (Die #2, Table 5.1), 750 (Die #3, Table 5.1) and 1000 krad(Si) (Die #4, Table 5.1). Each measurement listed is an average of measurements on 20 cantilevers. A small change in tip deflection was measured between the pre-characterization and the post-characterization. Although no significant changes were noted, no correlation can be made between the measured changes and the radiation dose absorbed. Two reasons explain why no correlation can be made. First, A time lapse of two weeks occurred between the time the cantilevers were irradiated and the time deflection measurement were taken. Secondly, from Equation 4.43 it can be shown that up to a 10 percent change in deflection will occur with a 5° C change in temperature. It is believed that a 5° C change is possible within the Clean room environment; however, the actual temperature of the Clean Room was not recorded. The significance of these results is that the radiation exposure did not cause significant damage to the residual stress cantilevers.

*6.3.3 Results for Residual Stress Cantilever irradiated with Co-60 Gamma Source.* Table 6.11 presents the deflection measurements for residual cantilevers

Total Ionizing Dose [krad(Si)]	Pre-characterization Tip Deflection [ $\mu\text{m}$ ]	Standard Deviation	Post-characterization Tip Deflection [ $\mu\text{m}$ ]	Standard Deviation	Percent Change
250 (Die #1, Table 5.1)	22.162	0.204	21.460	.0265	3.3
500 (Die #2, Table 5.1)	21.352	0.376	21.318	0.226	0.2
750 (Die #3, Table 5.1)	22.246	0.295	21.508	0.213	3.4
1000 (Die #4, Table 5.1)	22.280	0.312	21.232	0.319	4.9

Table 6.10 Measured Tip deflection and standard deviation for residual stress cantilever prior to after being irradiated with LEXR source to specified total ionizing dose. The percent change is given for comparison purposes.

before and after being irradiated with 1.25 MeV gamma rays to total ionizing doses of 250 (Die #1, Table 5.2), 500 (Die #2, Table 5.2), 750 (Die #3, Table 5.2) and 1000 krad(Si) (Die #4, Table 5.2). Each measurement listed is an average of deflection measurements taken on 20 cantilevers. A small change in tip deflection was measured between the pre-characterization and the post-characterization. Although no significant changes were noted, no correlation can be made between the measured changes and the radiation dose absorbed for the same reasons present in Section 6.3.2.

Total Ionizing Dose [krad(Si)]	Pre-characterization Tip Deflection [ $\mu\text{m}$ ]	Standard Deviation	Post-characterization Tip Deflection [ $\mu\text{m}$ ]	Standard Deviation	Percent Change
250 (Die #1, Table 5.2)	22.589	0.188	19.814	0.239	14.0
500 (Die #2, Table 5.2)	21.138	0.204	19.754	0.386	7.0
750 (Die #3, Table 5.2)	22.397	0.208	19.774	0.383	13.3
1000 (Die #4, Table 5.2)	22.552	0.241	19.359	0.192	16.5

Table 6.11 Measured Tip deflection and standard deviation for residual stress cantilever prior to after being irradiated with Co-60 source to specified total ionizing dose. The percent change is given for comparison purposes.

## 6.4 Conclusion

This chapter present the results for radiation testing of electrostatic piston actuators, electrothermal actuators, and residual stress cantilevers. The operation of the electrostatic actuators were affected when irradiated with low energy X-rays; however, few changes were noted when irradiated with 1.25 MeV gamma rays. All

radiation induced deflection changes measured for devices irradiated under no bias and positive bias disappeared after 7 days. Radiation induced deflection changes for devices irradiated under negative bias did not anneal out after seven days. From these results a negative bias configuration should be avoided when the electrostatic actuators are to be used in an ionizing radiation environment. No degradation in tip deflection of the electrothermal actuator was attributed to radiation exposure. Actuator break-in was noted and confirmed with control experiment to have no radiation dependence. No correlation between tip deflection and absorbed dose can be made for the residual stress cantilevers. However, a direct correlation was made between tip deflection and radiation energy. Cantilevers irradiated with 50 keV X-rays experienced up to 5 % decrease in tip deflection while cantilevers irradiated with 1.25 MeV gamma rays experienced up to 16 % decrease in tip deflection.

## Bibliography

1. Sharpe, W. N., Jr., B. Yuan, and R. Vaidyanathan, "Measurements of Young's Modulus, Poisson's Ratio, and Tensile Strength of Polysilicon," *Proceedings of the Tenth IEEE International Workshop on Microelectromechanical Systems, Nagoya, Japan*, pp. 424–429, 1997.
2. Neamen, D. A., *Semiconductor Physics & Devices Basic Principles*. Boston: Irwin McGraw-Hill, 2<sup>nd</sup> ed., 1997.
3. Srour, J. R., "Basic mechanisms of radiation effects on electronic materials, devices, and integrated circuits," *IEEE Nuclear and Space Radiation Effects Conference Short Course*, 1982.
4. Yan, D., A. Khajepour, and R. Mansour, "Modeling of two-hot-arm horizontal thermal actuator," *Journal of Micromechanics and Microengineering*, vol. 13, pp. 312–322, 2003.
5. McConnell, A. D., S. Uma, and K. E. Goodson, "Thermal Conductivity of Doped Polysilicon Layers," *Journal of Microelectromechanical Systems*, vol. 10, pp. 360–369, September 2001.
6. Yang, E. H. and H. Fujita, "Determination of the modification of Young's modulus due to Joule heating of polysilicon microstructures using U-shaped beams," *Sensors and Actuators A*, vol. 70, pp. 185–190, 1998.
7. Maier-Schneider, D., A. Köprülü, S. Ballhausen Holm, and E. Obermeier, "Elastic properties and microstructure of LPCVD polysilicon films," *Journal of Micromechanics and Microengineering*, vol. 6, pp. 436–446, 1996.
8. Holmes-Siedle, A., *Handbook of Radiation Effects*. Oxford: Oxford University Press, 1993.
9. Johnstone, R. W., K. F. Ko, J. C. Yang, M. Parameswaran, and L. S. Erhardt, "The effects of proton irradiation on electrothermal micro-actuators," *Canadian Journal of Electrical and Computer Engineering*, vol. 27, pp. 3–5, January 2002.
10. Taylor, E. W., A. H. Paxton, H. Schöne, J. H. Comtois, A. D. Sanchez, M. A. Michalicek, J. E. Winter, S. J. Mckinnew, M. Osinski, P. Perlin, R. F. Carson, J. P. G. Bristow, J. Lehman, and M. K. Hibbs Brenner, "Radiation induced effects research in emerging photonic technologies: vertical cavity surface emitting lasers, GaN light emitting diodes and microelectromechanical devices," *Photonics for Space Environments V, Proceedings of SPIE*, vol. 3124, pp. 9–20, July 1997.

11. Pamula, V. K., A. Jog, and R. B. Fair, “Mechanical property measurement of thin-film gold using thermally actuated bimetallic cantilever beams,” *Modeling and Simulation of Microsystems*, pp. 410–413, 2001.
12. Koester, D., A. Cowen, R. Mahadevan, and B. Hardy, *PolyMUMPs Design Handbook: a MUMPS<sup>®</sup> process*. Revision 8.0, MEMSCAP, 2002.
13. Kovacs, G. T. A., *Micromachined Transducers Sourcebook*. Boston: McGraw Hill, 1998.

## *VII. Conclusions*

This chapter discusses the results of this research as it relates to the goal presented in Chapter I. Sections 7.1 and 7.2 discuss the ending stages of the current research and its contributions to the scientific community. Section 7.3 presents a direction for future research.

### *7.1 Actuator Characterization*

This section presents an overview of the results obtained from testing the electrostatic piston actuator, the electrothermal actuator, and the residual stress cantilever in an ionizing radiation environment.

The electrostatic piston actuators were tested in two ionizing radiation environments. The actuators were tested before, during, and after irradiation. The measurements for actuators irradiated under a positive bias taken during and after irradiation showed a decrease in capacitance and thus an increase in the voltage per deflection when compared to pre-irradiation measurements. Actuators irradiated under a negative bias showed an increase in capacitance and thus a decrease in the voltage per deflection. Both results are attributed to radiation induced charge that is trapped within the exposed silicon nitride layer. The differences noted between the two biasing configurations is due to the location of the trapped holes. The results of the experimental measurements are qualitatively predicted by the analytical model developed in Chapter IV. All actuators irradiated under a positive bias returned to their pre-irradiated condition within seven days after irradiation. This annealing of the trapped charge was not noted for actuators irradiated under negative bias.

The horizontal deflecting electrothermal actuators were irradiated in two ionizing radiation environments. The operation of the devices was measured before, during, and after irradiation. Neither the X-ray nor gamma irradiation affected the operation of the actuators. Although some changes in resistance were noted for

a few actuators, no correlation can be made between the changes and the radiation exposure. This test confirms test results published by two separate research groups [1, 2].

The residual stress cantilevers were tested in two ionizing radiation environments. The actuators were characterized before and after irradiation. Although a slight ( $<14\%$ ) decrease was noted in the tip deflection, no correlations could be made with respect to the absorbed dose. Changes due to radiation energy are noted.

For space applications, positive biasing electrostatic actuators will allow the radiation induced trapped holes to anneal thus minimizing any degradation in operating parameters. The same cannot be said for actuators operated under a negative bias. Electrothermal actuators will not be affected by ionizing radiation; however, the break-in of the actuators should be considered in the design phase. Residual stress structures may experience an energy dependent decrease in deflection probably due to accelerated annealing of gold on polysilicon.

## *7.2 Contributions to Scientific Community*

The following is a list of noteworthy scientific contributions made during this research.

- Test and characterizes electrostatic piston actuator in an ionizing radiation environment.
- Demonstrates that the operation of electrostatic piston actuators are affected by radiation induced charge trapping within exposed dielectric layers.
- Reports successful experimental packaging of MEMS devices for testing and post characterization in an ionizing radiation environment.
- Demonstrates high yields for MUMPs<sup>®</sup> fabricated MEMS devices for testing within radiation environments.



- Confirms previously published radiation testing results for the horizontally deflecting electrothermal actuator.

### 7.3 *Future Work*

This section presents a direction for future research. I believe there are two possible avenues to build on the research accomplished for this thesis: continued radiation testing of MEMS actuators, and modeling resistance changes.

*7.3.1 Testing Actuators in Different Radiation Environments.* The research accomplished for this thesis focused on testing the actuators in an ionizing radiation environment. Other types of radiation such as neutrons and heavy ions could cause changes in the actuators operability not noted within the ionizing radiation environment. Therefore, further testing could be accomplished using the same actuators tested for this research and different radiation sources.

*7.3.2 In-situ Characterization.* Although plans were made in this thesis to test the residual stress cantilevers during irradiation, the testing was not accomplished due to time conflicts between getting devices back from Cronos and scheduling the radiation sources. No conclusions could be made with the cantilever measurements taken during this research. This was mainly due to the fact that in-situ measurement were not taken. Therefore, the next logical step in characterizing the residual stress cantilever would be to perform in-situ deflection measurements on them.

*7.3.3 Quantify and Model Changes in Resistance Due to Joule Heating.* Throughout the extensive literature search accomplished for this research, no published research was found on to quantify or model the changes of resistance noted for the electrothermal actuators. The change of resistance was strongly dependent on the actuation voltage applied to the actuator. Modelling this change in resistance

could lead to an improved analytical model capable of predicting the deflection of the actuator when operated in the plastic deformation region.

#### *7.3.4 Redesign Electrostatic Actuator and Confirm Snapdown Behavior.*

The electrostatic actuators should be redesigned to have a higher snapdown voltage. It is believed that the low snapdown voltage of the actuators tested in this research contributed to the fact that all the actuators were stuck down. Redesigning the actuators to have a higher snapdown voltage should allow the actuators to be tested over their entire deflection range and not just in the snapdown region. Testing over the entire deflection range would allow the effects of radiation on the snapdown behavior to be completely characterized.

#### *7.4 Conclusions*

This concludes the research focused on characterizing the electrostatic piston actuator, electrothermal actuator and residual stress cantilever within an ionizing radiation environment. This research should be viewed as a stepping stone in the maturation process of MEMS technology.

## *Bibliography*

1. Johnstone, R. W., K. F. Ko, J. C. Yang, M. Parameswaran, and L. S. Erhardt, "The effects of proton irradiation on electrothermal micro-actuators," *Canadian Journal of Electrical and Computer Engineering*, vol. 27, pp. 3–5, January 2002.
2. Taylor, E. W., A. H. Paxton, H. Schöne, J. H. Comtois, A. D. Sanchez, M. A. Michalicek, J. E. Winter, S. J. Mckinnew, M. Osinski, P. Perlin, R. F. Carson, J. P. G. Bristow, J. Lehman, and M. K. Hibbs Brenner, "Radiation induced effects research in emerging photonic technologies: vertical cavity surface emitting lasers, GaN light emitting diodes and microelectromechanical devices," *Photonics for Space Environments V, Proceedings of SPIE*, vol. 3124, pp. 9–20, July 1997.

*Appendix A. Matlab<sup>®</sup> Script for Modelling Electrostatic Piston  
Actuator*

This appendix presents the Matlab<sup>®</sup> code written as part of the analytical models for the electrostatic piston actuator.



```

% Resize the voltage and deflection vectors
% model #1
    Vsnap=V(1:snappoint);
    xsnap=x(1:snappoint);
% model #2
    Vqsnap=Vq(1:snappoint);
    xsnapq=x(1:snappoint);
% Interpolate the data for experimental voltage values
% model #1
    volt=[0:1:V(snappoint)];
    deflection = spline(Vsnap,xsnap,volt);
% model #2
    voltq=[0:1:Vq(snappoint)];
    deflectionq= spline(Vqsnap,xsnapq,voltq);
% extend the length of Voltage vector out to max experimental measurement
% model #1
    while volt(end)<max_test_volt
        volt(end+1)=volt(end)+1;
    end
% model #2
    while voltq(end)<max_test_volt
        voltq(end+1)=voltq(end)+1;
    end
% extend the length of the deflection vector out to 2.0 microns
% model #1
    for j=length(deflection)+1:1:length(volt)
        deflection(j)=2.0e-6;
    end
% model #2
    for j=length(deflectionq)+1:1:length(voltq)
        deflectionq(j)=2.0e-6;
    end
%%%%%%%%%%%%%%%%%%%%%%%%%%%%%%%%%%%%%%%%%%%%%%%%%%%%%%%%%%%%%%%%%%%%%%%%%%%%%%
% Calculate the capacitance
%%%%%%%%%%%%%%%%%%%%%%%%%%%%%%%%%%%%%%%%%%%%%%%%%%%%%%%%%%%%%%%%%%%%%%%%%%%%%%
% model #1
    for i=1:length(deflection)
        C(i)=eps0*epsn*A/(epsn*(d_a-deflection(i))+d_n);
    end
% model #2
    for i=1:length(deflectionq)
        Cq(i)=eps0*epsn*A/(epsn*(d_a-deflectionq(i))+d_n);
    end
% read in the pre-characterization measurements
[status sheetnames]=xlsinfo('D:\Analyzed_data\Piston\Piston_Lexr.xls')
pre=xlsread('D:\Analyzed_data\Piston\Piston_Lexr.xls',sheetnames{1,1});
% plot the results
% define text string to plot charge value on plots
charge=cat(2,'Q = ',num2str(Q), 'C')
% Begin Plot Sequence
figure
hold on
% Plot the Capacitance versus voltage w/ unconstrained axis
subplot(2,1,1)
plot(volt,(C-C(1))*10^15,'k',voltq,(Cq-Cq(1))*10^15,'r*', pre(2:20,1),pre(2:20,12)*10^15,'g+')
legend('Model #1', 'Model # 2','Experimental',charge,2)
legend boxoff
ylabel('Change in capacitance [fF]')
xlabel('Voltage [V]')
axis([0 20 -1 400])
% Plot the Capacitance versus voltage w/ constrained axis
subplot(2,1,2)
plot(volt,(C-C(1))*10^15,'k',voltq,(Cq-Cq(1))*10^15,'r*', pre(2:20,1),pre(2:20,12)*10^15,'g+')
legend('Model #1', 'Model # 2','Experimental',charge,2)
legend boxoff
ylabel('Change in capacitance [fF]')
xlabel('Voltage [V]')
axis([0 20 0 65])

```

## *Appendix B. Matlab<sup>®</sup> Script for Modelling Electrothermal Actuator*

This appendix presents the Matlab<sup>®</sup> code written as part of the analytical model for the horizontally deflection electrothermal actuator.

```
% Analytical model for electro-thermal actuator.
% Written by Jared R. Caffey
% Actuator is broken into five segments.
% Initialize
close all
clear all;
file=cat(2,'c:\Caffey\EEENG777\300etherm');
format long g
% for variable voltages
Volt=[0:.5:15];
k=1
while k<length(Volt)
%%%%%%%%%%%%%%%%%%%%%%%%%%%%%%%%%%%%%%%%%%%%%%%%%%%%%%%%%%%%%%%%%%%%%%%%
% Variable Definitions
%%%%%%%%%%%%%%%%%%%%%%%%%%%%%%%%%%%%%%%%%%%%%%%%%%%%%%%%%%%%%%%%%%%%%%%%
% The temperature of the substrate
ToC=30;
To=ToC+273;
% The width of each segment [hot,connect,cold,flex] [m]
W=[2.5,2.5,18,2.5]*10^-6;
% The length of each segment [hot,connect,cold, flex] [m]
L=[250,2.5,500,50]*10^-6;
% The thickness of the structural layer [m]
t=1.5*10^-6;
% The distance to substrate P1=2, P2=2.75 [m]
d=2.75*10^-6;
% The thermal conductivity of polysilicon [W/(mK)]
Kp=117;
% The thermal conductivity of air [W/(mK)]
Kair=0.035;
% The resistivity of the structural layer [ohm-m]
p=3.22e-5;
% Define the applied voltage
V=Volt(k);
% Define the coefficient of Thermal expansion [1/C]
CTE=2.6*10^-6;
% Define Young's Modulus [pa]
E=1.69*10^5*10^6;
%%%%%%%%%%%%%%%%%%%%%%%%%%%%%%%%%%%%%%%%%%%%%%%%%%%%%%%%%%%%%%%%%%%%%%%%
% Calculations using defined variables
%%%%%%%%%%%%%%%%%%%%%%%%%%%%%%%%%%%%%%%%%%%%%%%%%%%%%%%%%%%%%%%%%%%%%%%%
% Calculate the Area for each segment
A=t*W;
% Calculate the resistance of the structure
R=p*(sum(L./A));
```



```

% Calculate the Total current
current=V/R;
% Calculate the heat generated
qdot=current^2*p./(A.^2);
% Calculate the heat transfer coefficient (d is in meters)
h=Kair/(d);
% Calculate the characteristic length
lc=W;
% Calculate gamma
gamma=sqrt(h*lc./(Kp.*A));
% Calculate epsilon
Epsilon=qdot.*A./(h*lc)+To;
% Calculate the composite lengths [m]
l=[L(1), L(1)+L(2), L(1)+L(2)+L(3), L(1)+L(2)+L(3)+L(4)];
% Calculate the second moment of inertia
I=W.^3*(t/12);

%%%%%%%%%%%%%%%%%%%%%%%%%%%%%%%%%%%%%%%%%%%%%%%%%%%%%%%%%%%%%%%%%%%%%%%%
% Define the Temperature matrix
%%%%%%%%%%%%%%%%%%%%%%%%%%%%%%%%%%%%%%%%%%%%%%%%%%%%%%%%%%%%%%%%%%%%%%%%
T1=[1 1 0 0 0 0 0];
T2=[exp(gamma(1)*l(1)) exp(-gamma(1)*l(1)) -exp(gamma(2)*l(1)) -exp(-
gamma(2)*l(1)) 0 0 0 0];
T3=[0 0 exp(gamma(2)*l(2)) exp(-gamma(2)*l(2)) -exp(gamma(3)*l(2)) -exp(-
gamma(3)*l(2)) 0 0];
T4=[0 0 0 0 exp(gamma(3)*l(3)) exp(-gamma(3)*l(3)) -exp(gamma(4)*l(3)) -exp(-
gamma(4)*l(3))];
T5=[0 0 0 0 0 exp(gamma(4)*l(4)) exp(-gamma(4)*l(4))];
T6=[A(1)*gamma(1)*exp(gamma(1)*l(1)) -A(1)*gamma(1)*exp(-gamma(1)*l(1)) -
A(2)*gamma(2)*exp(gamma(2)*l(1)) A(2)*gamma(2)*exp(-gamma(2)*l(1)) 0 0 0 0];
T7=[0 0 A(2)*gamma(2)*exp(gamma(2)*l(2)) -A(2)*gamma(2)*exp(-gamma(2)*l(2)) -
A(3)*gamma(3)*exp(gamma(3)*l(2)) A(3)*gamma(3)*exp(-gamma(3)*l(2)) 0 0];
T8=[0 0 0 0 A(3)*gamma(3)*exp(gamma(3)*l(3)) -A(3)*gamma(3)*exp(-
gamma(3)*l(3)) -A(4)*gamma(4)*exp(gamma(4)*l(3)) A(4)*gamma(4)*exp(-
gamma(4)*l(3))];

T=[T1;T2;T3;T4;T5;T6;T7;T8];
%%%%%%%%%%%%%%%%%%%%%%%%%%%%%%%%%%%%%%%%%%%%%%%%%%%%%%%%%%%%%%%%%%%%%%%%
% Define result matrix
%%%%%%%%%%%%%%%%%%%%%%%%%%%%%%%%%%%%%%%%%%%%%%%%%%%%%%%%%%%%%%%%%%%%%%%%
Result=[To-Epsilon(1);Epsilon(2)-Epsilon(1);Epsilon(3)-Epsilon(2);Epsilon(4)-
Epsilon(3);To-Epsilon(4);0;0;0];
%%%%%%%%%%%%%%%%%%%%%%%%%%%%%%%%%%%%%%%%%%%%%%%%%%%%%%%%%%%%%%%%%%%%%%%%
% Solve for C vector
%%%%%%%%%%%%%%%%%%%%%%%%%%%%%%%%%%%%%%%%%%%%%%%%%%%%%%%%%%%%%%%%%%%%%%%%
format short g
C=TVResult;

```

```

%%%%%%%%%%%%%%%%%%%%%%%%%%%%%%%%%%%%%%%%%%%%%%%%%%%%%%%%%%%%%%%%%%%%%%%%
% Calculate the temperature distribution for each element
%%%%%%%%%%%%%%%%%%%%%%%%%%%%%%%%%%%%%%%%%%%%%%%%%%%%%%%%%%%%%%%%%%%%%%%%
clear T1
clear T2
clear T3
clear T4
x1=[0:.5*10^-6:l(1)];
x2=[l(1):.5*10^-6:l(2)];
x3=[l(2):.5*10^-6:l(3)];
x4=[l(3):.5*10^-6:l(4)];
% segment (1) hot arm
    Tmax=0;
    distance=0;
    for i=1:length(x1)
        T1(i)=[exp(gamma(1)*x1(i)) exp(-gamma(1)*x1(i)) 0 0 0 0]*C+Epsilon(1);
        if T1(i)>Tmax
            Tmax(k)=T1(i);
            distance=x1(i);
        end
    end
% segment (2) connection
for i=1:length(x2)
    T2(i)=[0 0 exp(gamma(2)*x2(i)) exp(-gamma(2)*x2(i)) 0 0 0]*C+Epsilon(2);
end
% segment(3) cold arm
for i=1:length(x3)
    T3(i)=[0 0 0 0 exp(gamma(3)*x3(i)) exp(-gamma(3)*x3(i)) 0 0]*C+Epsilon(3);
end
% segment(4) flexure
for i=1:length(x4)
    T4(i)=[0 0 0 0 0 exp(gamma(4)*x4(i)) exp(-gamma(4)*x4(i))]*C+Epsilon(4);
end
% plot the results of the temperature distribution
figure
plot(x1*10^6,T1,x2*10^6,T2,x3*10^6,T3,x4*10^6,T4)
heading=cat(2,'Temperature distribution for electro-thermal actuator biased with',num2str(V),' volts. ');
str1=cat(2,'Tmax= ',num2str(round(Tmax(k))),' K');
str2=cat(2,'at ',num2str(distance*10^6),' \mum');
title(heading)
axis([0,600,0,2000])
xlabel('Distance from hot arm anchor [\mum]')
ylabel('Temperature [K]')
text(350,1400,str1,'fontsize',16)

```

```

text(350,1300,str2,'fontsize',16)
legend('Hot-Arm','Connection','Cold-Arm','Flexure')
M(k)=getframe(gcf);
%% Find the thermal expansion and associated stress
T1ave=sum(T1)/length(T1);
T1aveC=T1ave-273;
T2ave=sum(T2)/length(T2);
T2aveC=T2ave-273;
T3ave=sum(T3)/length(T3);
T3aveC=T3ave-273;
T4ave=sum(T4)/length(T4);
T4aveC=T4ave-273;
TaveC=[T1aveC T2aveC T3aveC T4aveC];
% calculate the change in length and the pseudo forces for each segment
for i=1:length(L)
    delta(i)=CTE*L(i)*(TaveC(i)-ToC);
    Force(i)=E*A(i)*delta(i)/L(i);
end
% Define the local stiffness matrices
i=1;
kprime1=[E*A(i)/L(i) 0 0 -E*A(i)/L(i) 0 0;
    0 12*E*I(i)/L(i)^3 6*E*I(i)/L(i)^2 0 -12*E*I(i)/L(i)^3 6*E*I(i)/L(i)^2;
    0 6*E*I(i)/L(i)^2 4*E*I(i)/L(i) 0 -6*E*I(i)/L(i)^2 2*E*I(i)/L(i);
    -E*A(i)/L(i) 0 0 E*A(i)/L(i) 0 0;
    0 -12*E*I(i)/L(i)^3 -6*E*I(i)/L(i)^2 0 12*E*I(i)/L(i)^3 -6*E*I(i)/L(i)^2;
    0 6*E*I(i)/L(i)^2 2*E*I(i)/L(i) 0 -6*E*I(i)/L(i)^2 4*E*I(i)/L(i)];
i=2;
kprime2=[E*A(i)/L(i) 0 0 -E*A(i)/L(i) 0 0;
    0 12*E*I(i)/L(i)^3 6*E*I(i)/L(i)^2 0 -12*E*I(i)/L(i)^3 6*E*I(i)/L(i)^2;
    0 6*E*I(i)/L(i)^2 4*E*I(i)/L(i) 0 -6*E*I(i)/L(i)^2 2*E*I(i)/L(i);
    -E*A(i)/L(i) 0 0 E*A(i)/L(i) 0 0;
    0 -12*E*I(i)/L(i)^3 -6*E*I(i)/L(i)^2 0 12*E*I(i)/L(i)^3 -6*E*I(i)/L(i)^2;
    0 6*E*I(i)/L(i)^2 2*E*I(i)/L(i) 0 -6*E*I(i)/L(i)^2 4*E*I(i)/L(i)];
i=3;
kprime3=[E*A(i)/L(i) 0 0 -E*A(i)/L(i) 0 0;
    0 12*E*I(i)/L(i)^3 6*E*I(i)/L(i)^2 0 -12*E*I(i)/L(i)^3 6*E*I(i)/L(i)^2;
    0 6*E*I(i)/L(i)^2 4*E*I(i)/L(i) 0 -6*E*I(i)/L(i)^2 2*E*I(i)/L(i);
    -E*A(i)/L(i) 0 0 E*A(i)/L(i) 0 0;
    0 -12*E*I(i)/L(i)^3 -6*E*I(i)/L(i)^2 0 12*E*I(i)/L(i)^3 -6*E*I(i)/L(i)^2;
    0 6*E*I(i)/L(i)^2 2*E*I(i)/L(i) 0 -6*E*I(i)/L(i)^2 4*E*I(i)/L(i)];
i=4;
kprime4=[E*A(i)/L(i) 0 0 -E*A(i)/L(i) 0 0;

```

```

0 12*E*I(i)/L(i)^3 6*E*I(i)/L(i)^2 0 -12*E*I(i)/L(i)^3 6*E*I(i)/L(i)^2;
0 6*E*I(i)/L(i)^2 4*E*I(i)/L(i) 0 -6*E*I(i)/L(i)^2 2*E*I(i)/L(i);
-E*A(i)/L(i) 0 0 E*A(i)/L(i) 0 0;
0 -12*E*I(i)/L(i)^3 -6*E*I(i)/L(i)^2 0 12*E*I(i)/L(i)^3 -6*E*I(i)/L(i)^2;
0 6*E*I(i)/L(i)^2 2*E*I(i)/L(i) 0 -6*E*I(i)/L(i)^2 4*E*I(i)/L(i)];

%%
%% Define the global transformation matrices
%%
theta=[0,pi/2,pi,pi];
i=1;
trans1=[cos(theta(i)),sin(theta(i)),0,0,0,0;
        -sin(theta(i)),cos(theta(i)),0,0,0,0;
        0,0,1,0,0,0;
        0,0,0,cos(theta(i)),sin(theta(i)),0;
        0,0,0,-sin(theta(i)),cos(theta(i)),0;
        0,0,0,0,0,1];
i=2;
trans2=[cos(theta(i)),sin(theta(i)),0,0,0,0;
        -sin(theta(i)),cos(theta(i)),0,0,0,0;
        0,0,1,0,0,0;
        0,0,0,cos(theta(i)),sin(theta(i)),0;
        0,0,0,-sin(theta(i)),cos(theta(i)),0;
        0,0,0,0,0,1];
i=3;
trans3=[cos(theta(i)),sin(theta(i)),0,0,0,0;
        -sin(theta(i)),cos(theta(i)),0,0,0,0;
        0,0,1,0,0,0;
        0,0,0,cos(theta(i)),sin(theta(i)),0;
        0,0,0,-sin(theta(i)),cos(theta(i)),0;
        0,0,0,0,0,1];
i=4;
trans4=[cos(theta(i)),sin(theta(i)),0,0,0,0;
        -sin(theta(i)),cos(theta(i)),0,0,0,0;
        0,0,1,0,0,0;
        0,0,0,cos(theta(i)),sin(theta(i)),0;
        0,0,0,-sin(theta(i)),cos(theta(i)),0;
        0,0,0,0,0,1];
%%
%% Transform to global coordinates
%%
K1=trans1*kprime1*trans1;
K2=trans2*kprime2*trans2;
K3=trans3*kprime3*trans3;
K4=trans4*kprime4*trans4;

```

```

%% Expand to structure size matrix
structure=zeros(15,15);
% Insert K1 matrix
for j=1:6
    for i=1:6
        structure(j,i)=structure(j,i)+K1(j,i);
    end
end
% Insert K2 matrix
for j=4:9
    for i=4:9
        structure(j,i)=structure(j,i)+K2(j-3,i-3);
    end
end
% % Insert K3 matrix
for j=7:12
    for i=7:12
        structure(j,i)=structure(j,i)+K3(j-6,i-6);
    end
end
% % Insert K4 matrix
for j=10:15
    for i=10:15
        structure(j,i)=structure(j,i)+K4(j-9,i-9);
    end
end
% Define result vector
Fx2=Force(1);
Fy2=-Force(2);
Fx3=Force(3);
Fy3=Force(2);
Fx4=Force(4)-Force(3);
Fy4=0;
R=[0;0;0;Fx2;Fy2;0;Fx3;Fy3;0;Fx4;Fy4;0;0;0;0];
%% pick off required parts of structure
reqstructure=structure(4:12,4:12);
reqR=R(4:12);
% Define displacement vector
Disp=reqstructure\reqR;

```

```

defnode2(k)=Disp(2);

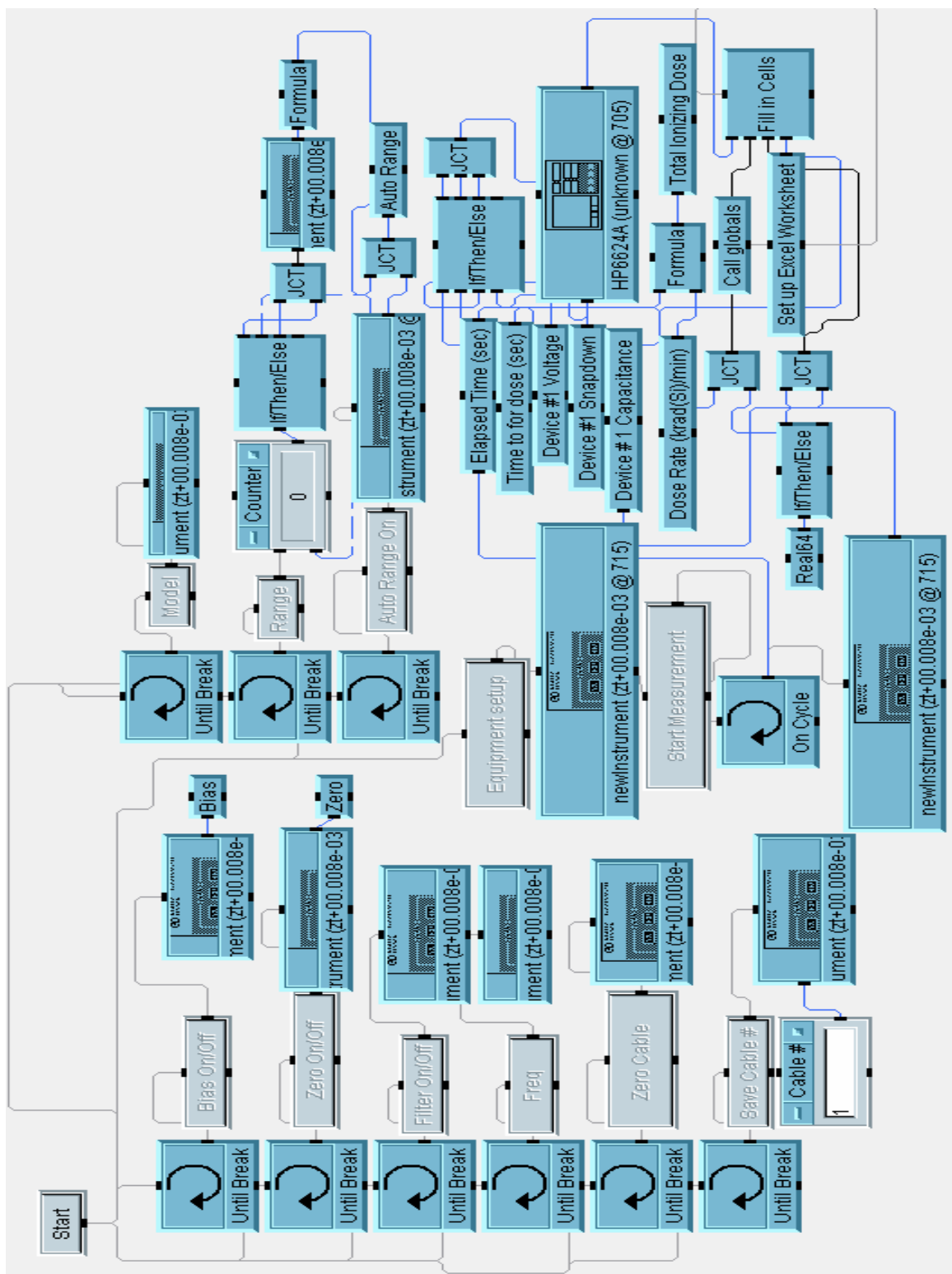
if Tmax(k)>1683
    Volt=Volt(1:k);
    k=length(Volt)+1;
end
k=k+1;
end % end while loop
% write movie file
movie2avi(M,file,'fps',2,'compression','Indeo5','quality',100);
expdef=[2.3 3.5 5.2 6.6];
expvolt=[4 5 6 7];
Cdef=[2.57e-1 5.76e-1 1.02 1.59 2.28 3.09 4.02 5.05 6.1 7.35 8.58 9.84 11.1 12.3 13.6
14.9 16.0 17.3 18.3];
Cvolt=[1 1.5 2 2.5 3 3.5 4 4.5 5 5.5 6 6.5 7 7.5 8 8.5 9 9.5 10];
figure
plot(Volt,defnode2*10^6)
% plot(Volt,defnode2*10^6,expvolt,expdef,'+',Cvolt,Cdef,'r')
% legend('Analytical','Experimental','Finite Element')
plot2title=cat(2,'Deflection vs Applied Voltage for ',num2str(L(1)*10^6),'\mum long
Electro-Thermal Actuator');
% title(plot2title)
str1=cat(2,'CTE = ',num2str(CTE),' C^-^1');
str2=cat(2,'Thermal Conductivity = ',num2str(Kp),' W/(mK)')
% text(2,(defnode2(end))*10^6-5,str2);
% text(2,(defnode2(end))*10^6-10,str1);
xlabel('Voltage [V]')
ylabel('Maximum Deflection [\mum]')

% read in postitive in-situ results form lexr source
[status sheetnames]=xlsinfo('D:\Analyzed_data\etherm\etherm_deflection.xls')
% % plot positive in-situ results from the lexr source
pre=xlsread('D:\Analyzed_data\etherm\etherm_deflection.xls',sheetnames{9,1});
hold on
plot(pre(14:23,1),pre(14:23,11),'r')
legend('Analytical Model','Pre-irradiated')
errorbar(pre(14:23,1),pre(14:23,11),pre(14:23,13),'r*')

```

## *Appendix C. Agilent VEE Pro Programs*

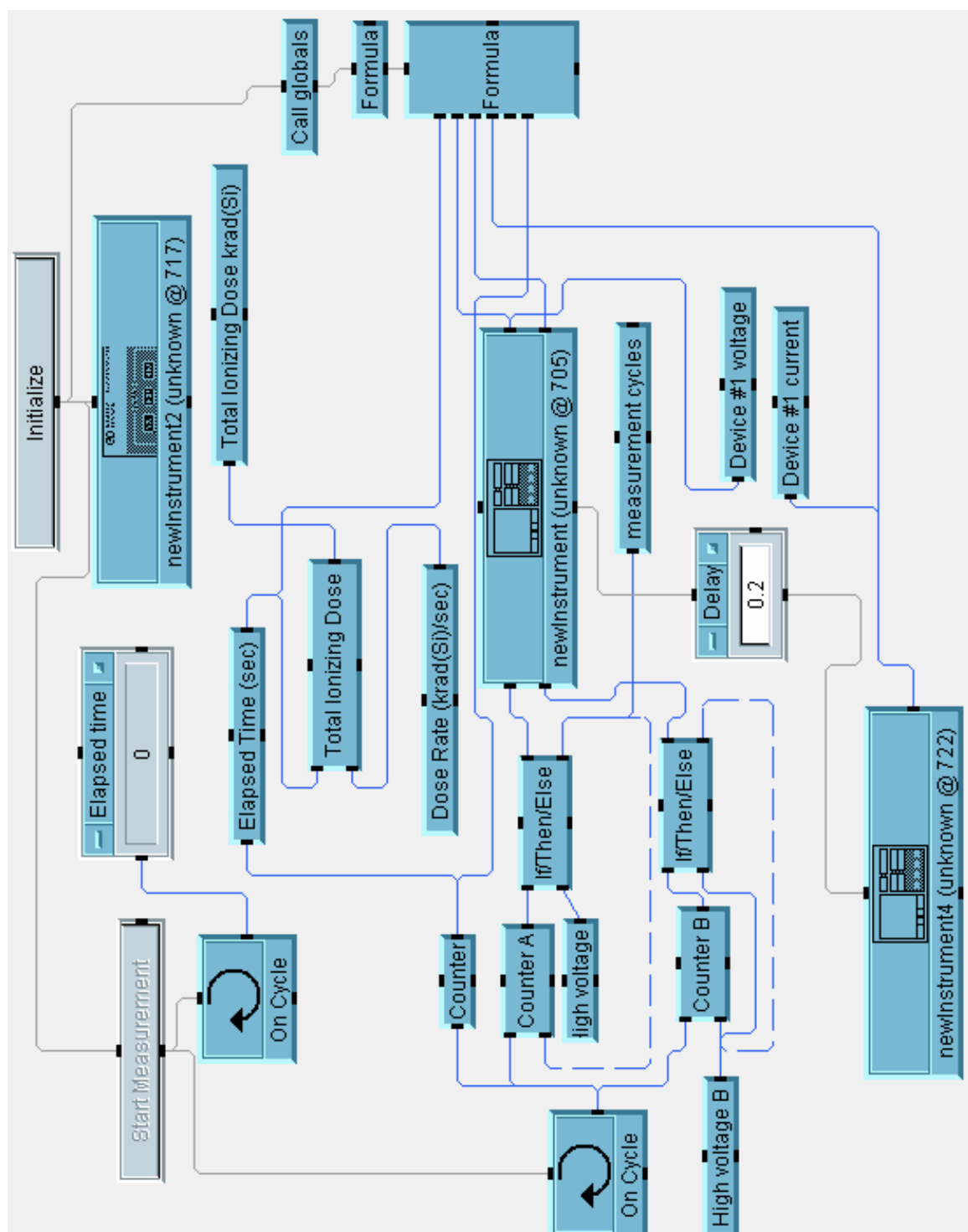
### *C.1 Agilent VEE Pro Program Used for Electrostatic Piston Actuator*







## *C.2 Agilent VEE Pro Program Used for Electrothermal Actuator*



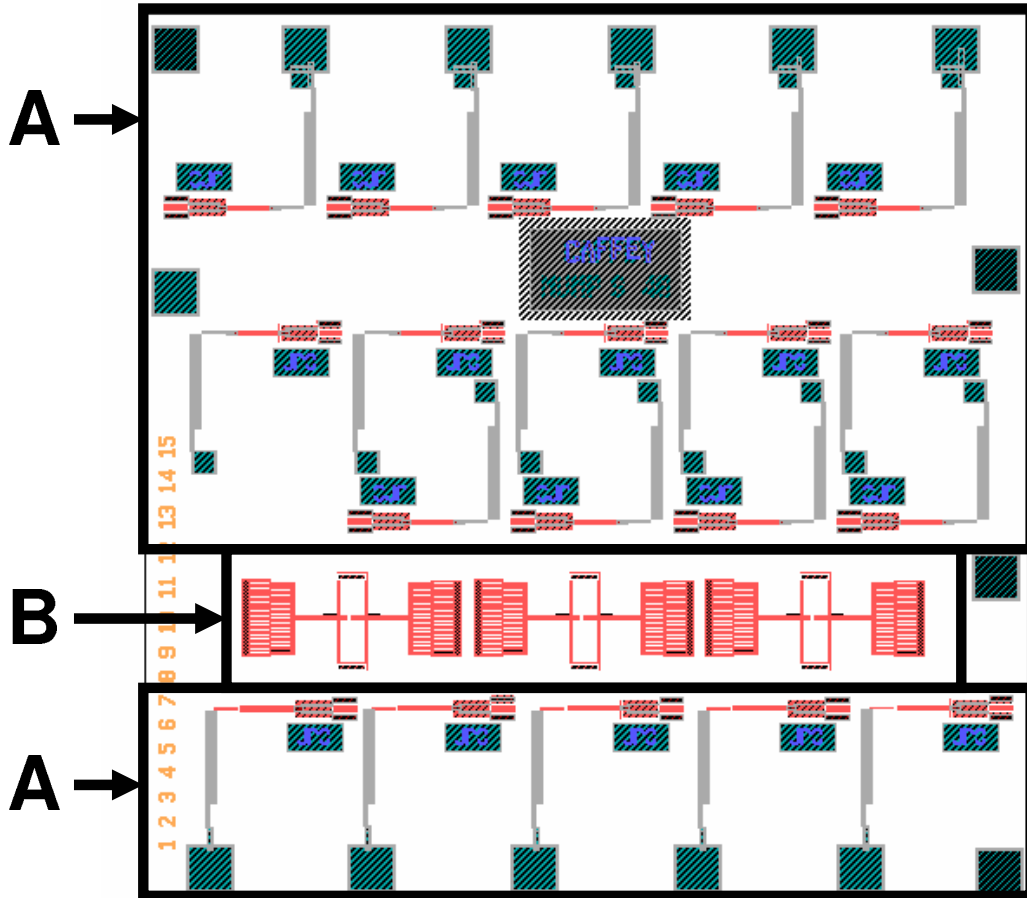


## Appendix D. PolyMUMPs Designs

### D.1 PolyMUMPs Run 48 Designs

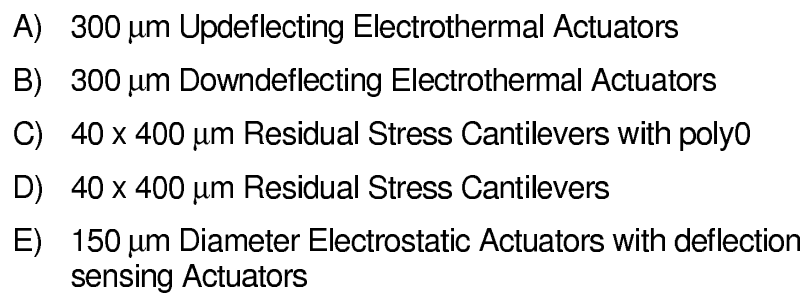
Chip A

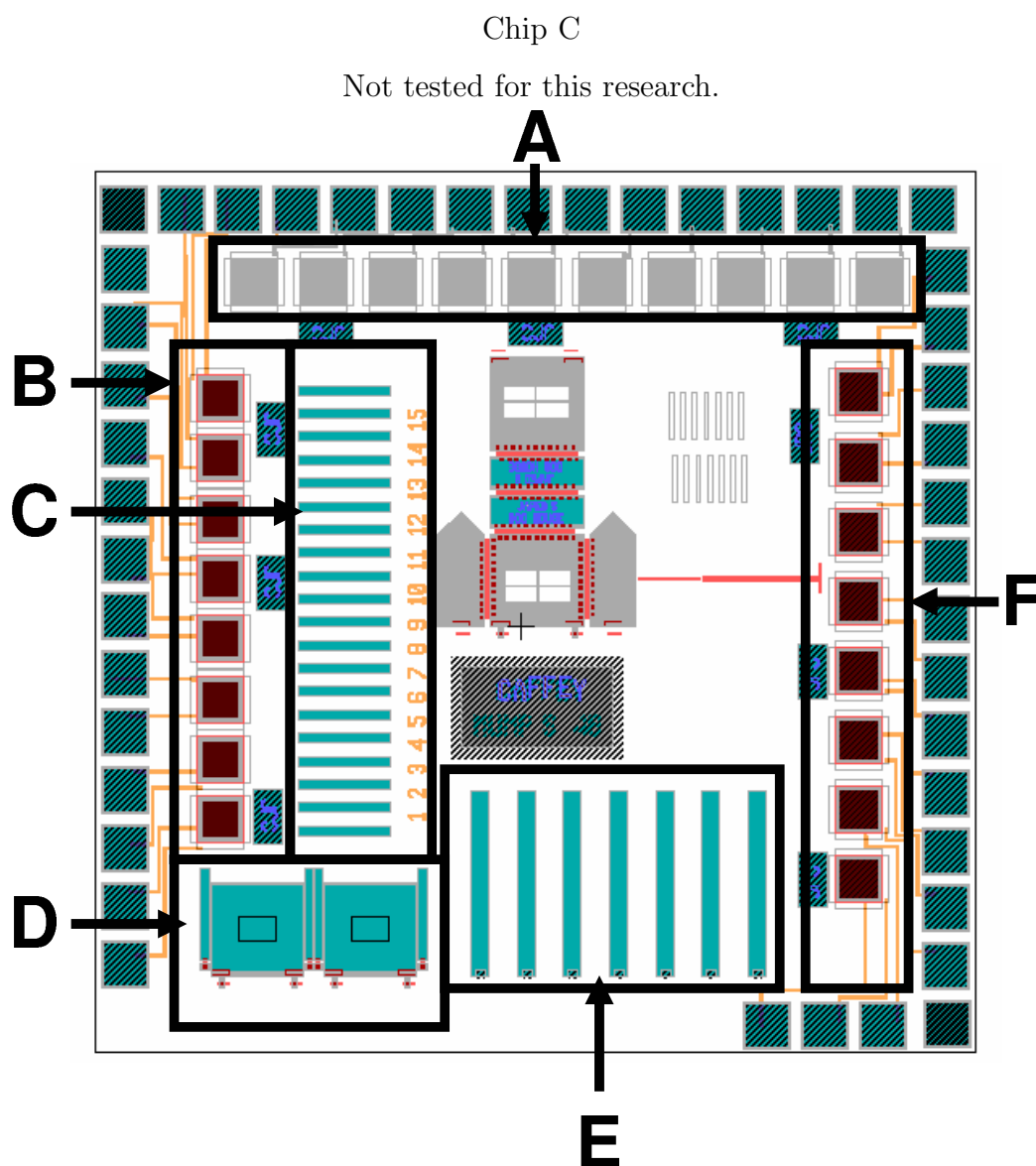
Not tested for this research.



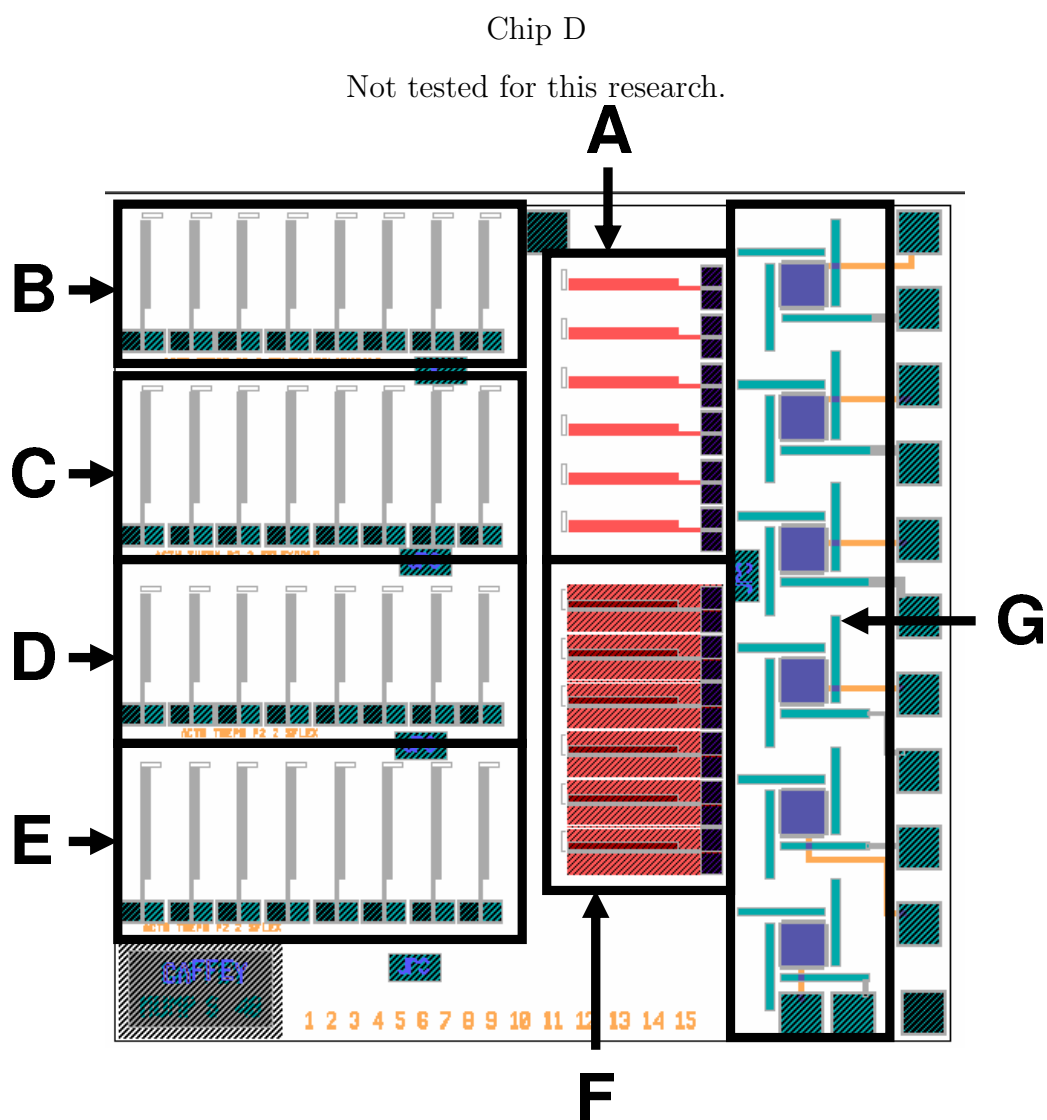
- A) 250  $\mu\text{m}$  poly2 Electrothermal Actuators with Locking Mechanism
- B) Simply Comb-drive design

Not tested for this research.





- A) 100 x 100  $\mu\text{m}$  poly 2 Electrostatic Actuators
- B) 100 x 100  $\mu\text{m}$  poly1-oxide2-poly2 Electrostatic Actuators
- C) 20 x 200  $\mu\text{m}$  poly2 Residual Stress Cantilevers
- D) 200 x 200  $\mu\text{m}$  poly2-metal mirrors with residual stress lifts
- E) 40 x 400  $\mu\text{m}$  Residual Stress Cantilevers
- F) 100 x 100  $\mu\text{m}$  poly1-poly2 Electrostatic Actuators

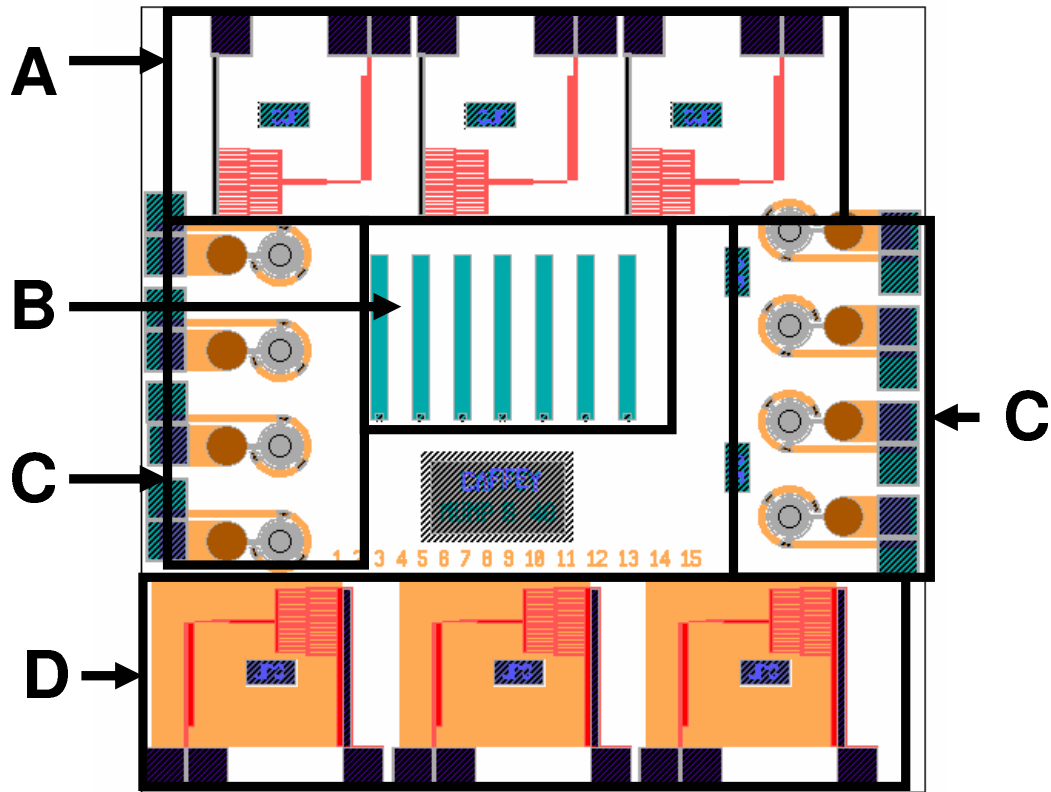


- A) 250  $\mu\text{m}$  poly1 Horizontally deflecting Electrothermal Actuator
- B) 250  $\mu\text{m}$  poly1-poly2 Horizontally deflecting Electrothermal Actuator
- C) 250  $\mu\text{m}$  poly2 Horizontally deflecting Electrothermal Actuator with gold dots
- D) 300  $\mu\text{m}$  poly2 Horizontally deflecting Electrothermal Actuator with gold dots
- E) 250  $\mu\text{m}$  poly2 Horizontally deflecting Electrothermal Actuator
- F) 250  $\mu\text{m}$  poly2 Horizontally deflecting Electrothermal Actuator
- G) 100 x 100  $\mu\text{m}$  poly2-metal Electrostatic Actuators with 20 x 200  $\mu\text{m}$  Residual Stress Cantilevers



# Chip E

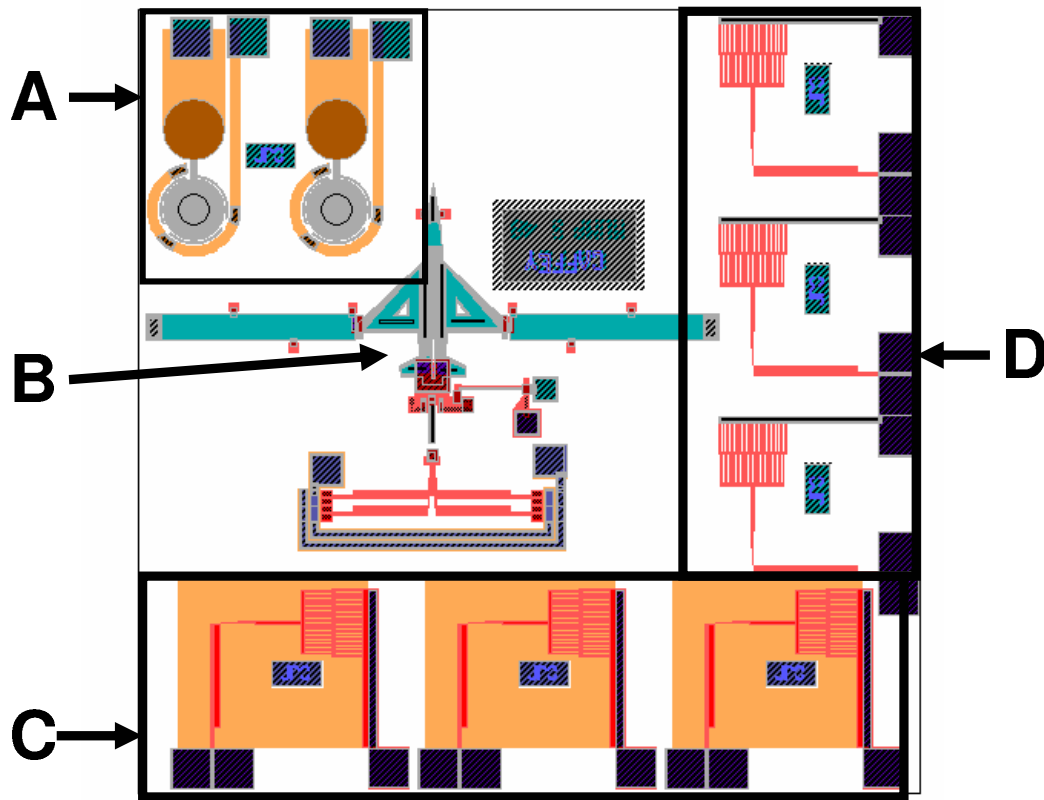
Not tested for this research.



- A) 300  $\mu\text{m}$  poly 1 Electrothermal Actuators with Capacitive Sensing
- B) 40 x 400  $\mu\text{m}$  Residual Stress Cantilevers
- C) 150  $\mu\text{m}$  Diameter Electrostatic Actuators with deflection sensing
- D) 300  $\mu\text{m}$  poly1 Electrothermal Actuators with Capacitive Sensing shielded with poly0

# Chip F

Not tested for this research.

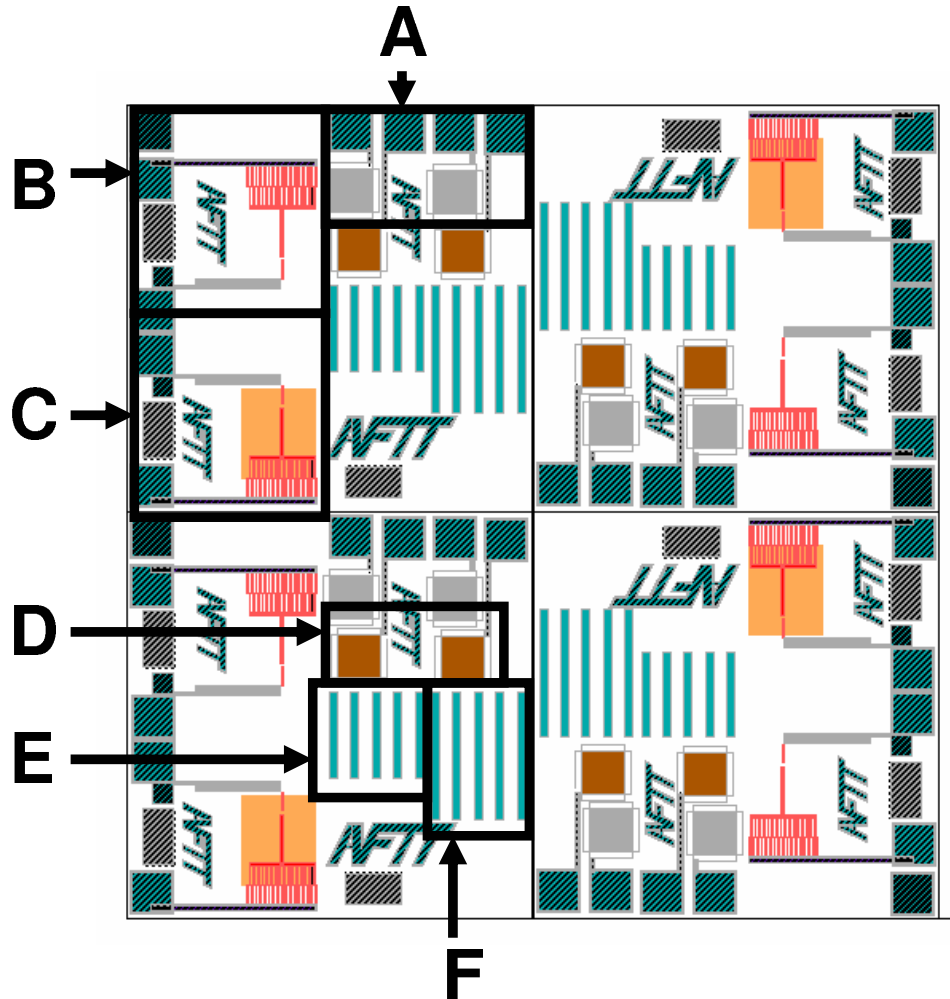


- A) 150  $\mu\text{m}$  Diameter Electrostatic Actuators with deflection sensing
- B) Airplane Model with Residual Stress Cantilevers
- C) 300  $\mu\text{m}$  poly 1 Electrothermal Actuators with Capacitive Sensing shielded with poly0
- D) 300  $\mu\text{m}$  poly 1 Electrothermal Actuators with Capacitive Sensing

D.2 PolyMUMPs Run 49 Designs

Chip A

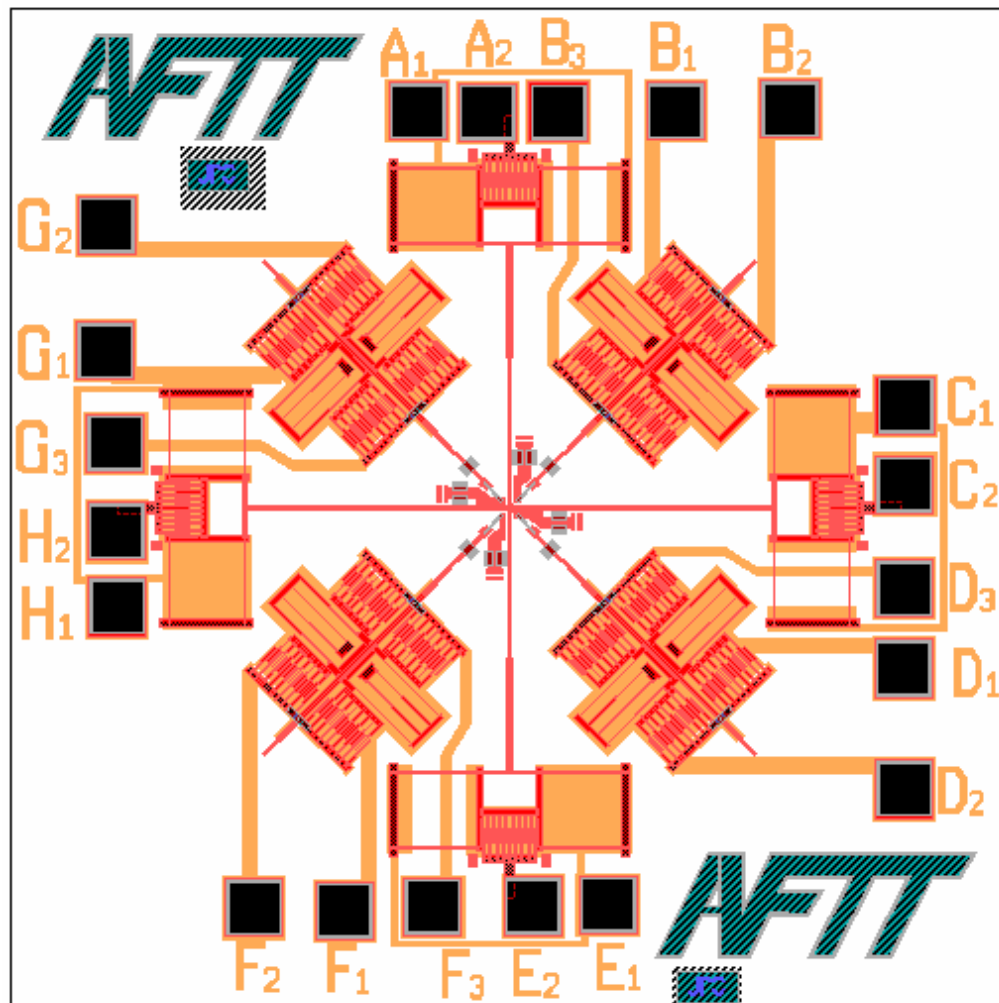
Not tested for this research.



- A) 100 x 100  $\mu\text{m}$  poly2 Electrostatic Actuators
- B) 250  $\mu\text{m}$  Electrothermal Actuators with Capacitive Sensing
- C) 250  $\mu\text{m}$  Electrothermal Actuators with Capacitive Sensing shielded with poly0
- D) 100 x 100  $\mu\text{m}$  poly2 Electrostatic Actuators with poly0 electrode
- E) 20 x 200  $\mu\text{m}$  Residual Stress Cantilevers
- F) 20 x 300  $\mu\text{m}$  Residual Stress Cantilevers

Chip B

Not tested for this research.

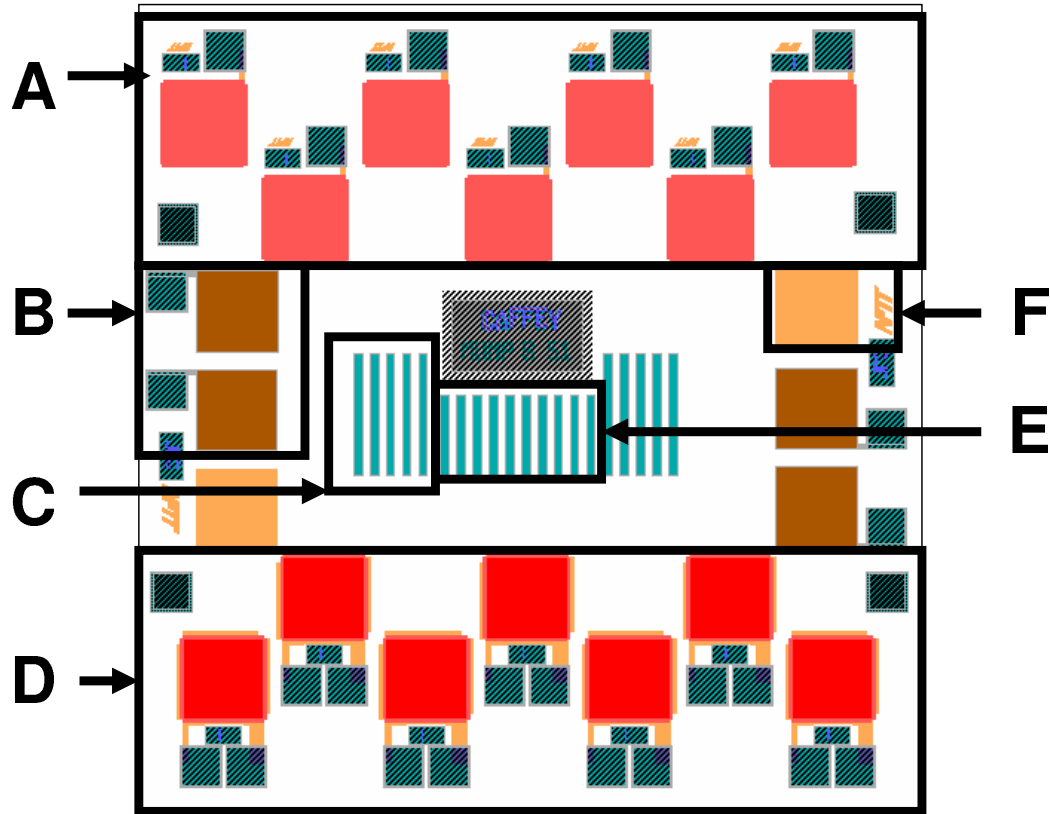


Microstage with two dimensional movement and four adjustable probes

### D.3 PolyMUMPs Run 51 Designs

Chip A

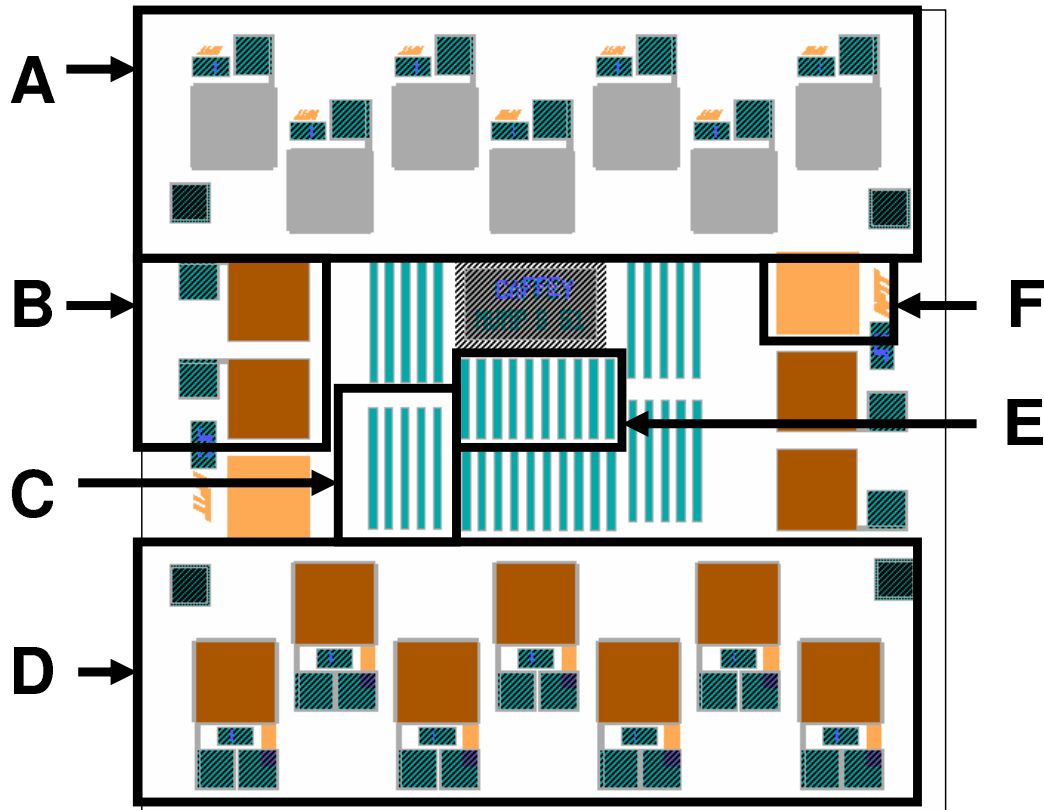
Not tested for this research.



- A) 200 x 200  $\mu\text{m}$  poly1 Electrostatic Actuators
- B) 200 x 200  $\mu\text{m}$  poly2 Electrostatic Actuators with poly0 electrode
- C) 20 x 300  $\mu\text{m}$  Residual Stress Cantilevers
- D) 200 x 200  $\mu\text{m}$  poly1 Electrostatic Actuators with poly0 electrode
- E) 20 x 200  $\mu\text{m}$  Residual Stress Cantilevers
- F) 200 x 200  $\mu\text{m}$  poly0 plate

## Chip B

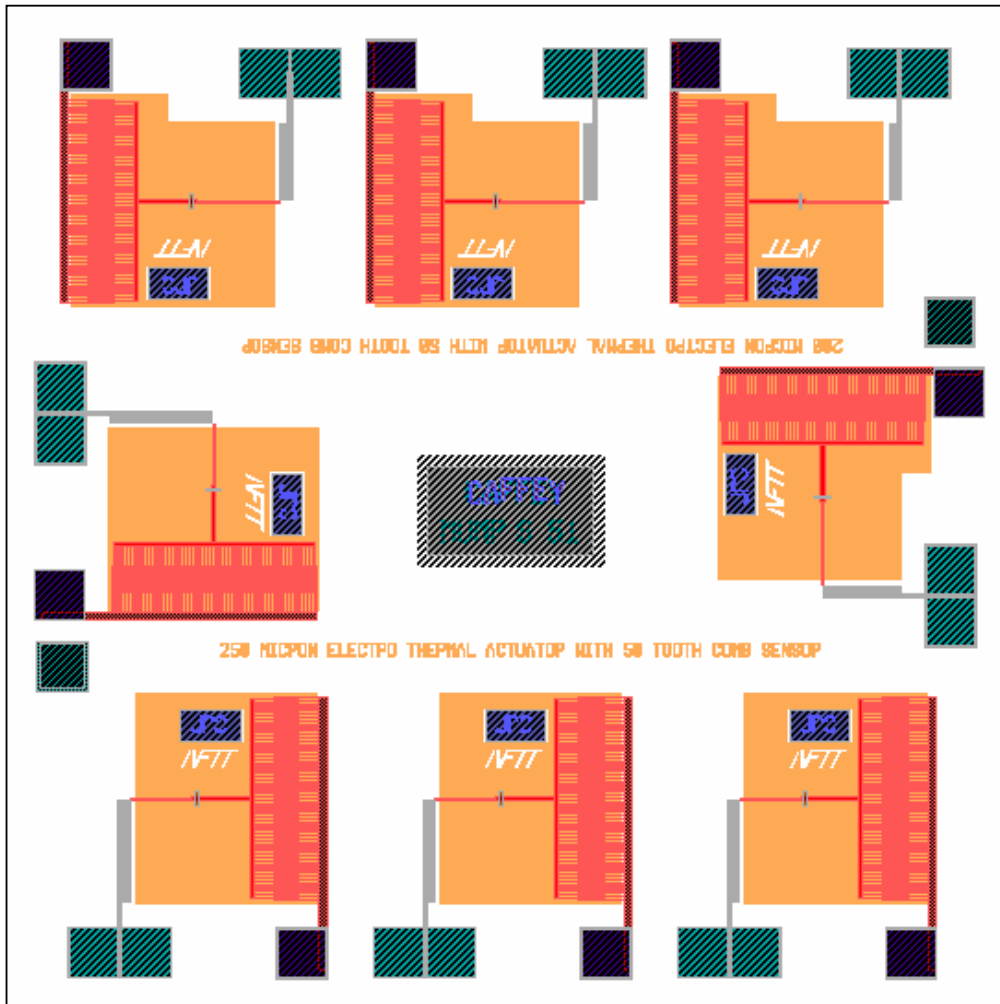
The electrostatic actuators and residual stress cantilevers tested for this research were fabricated using this chip design. In particular, the electrostatic actuators tested are labelled “A” and the residual stress cantilevers tested are labelled “C”.



- A) 200 x 200  $\mu\text{m}$  poly2 Electrostatic Actuators
- B) 200 x 200  $\mu\text{m}$  poly2 Electrostatic Actuators with poly0 electrode
- C) 20 x 300  $\mu\text{m}$  Residual Stress Cantilevers
- D) 200 x 200  $\mu\text{m}$  poly2 Electrostatic Actuators with poly0 electrode
- E) 20 x 200  $\mu\text{m}$  Residual Stress Cantilevers
- F) 200 x 200  $\mu\text{m}$  poly0 plate

# Chip C

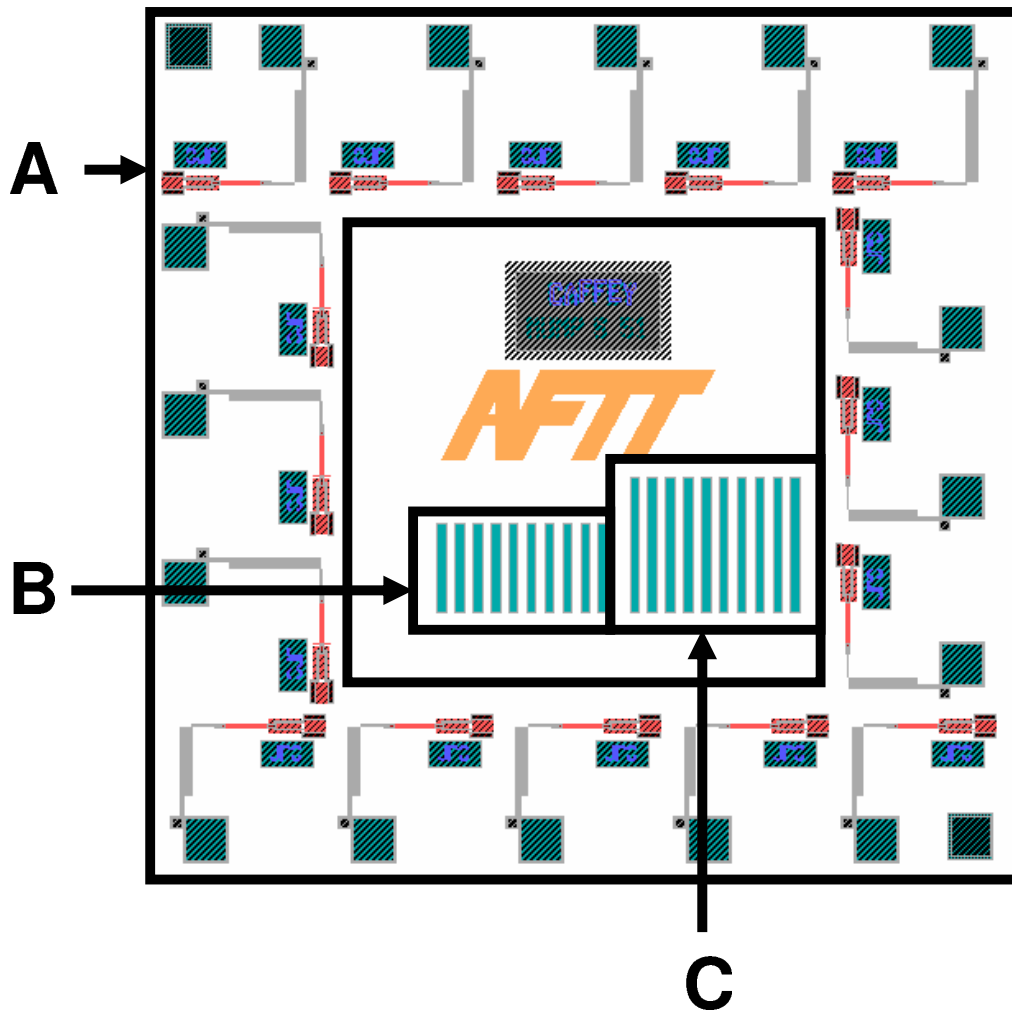
Not tested for this research.



250  $\mu\text{m}$  Electrothermal Actuators with capacitive sensing shielded with poly0

Chip D

Not tested for this research.

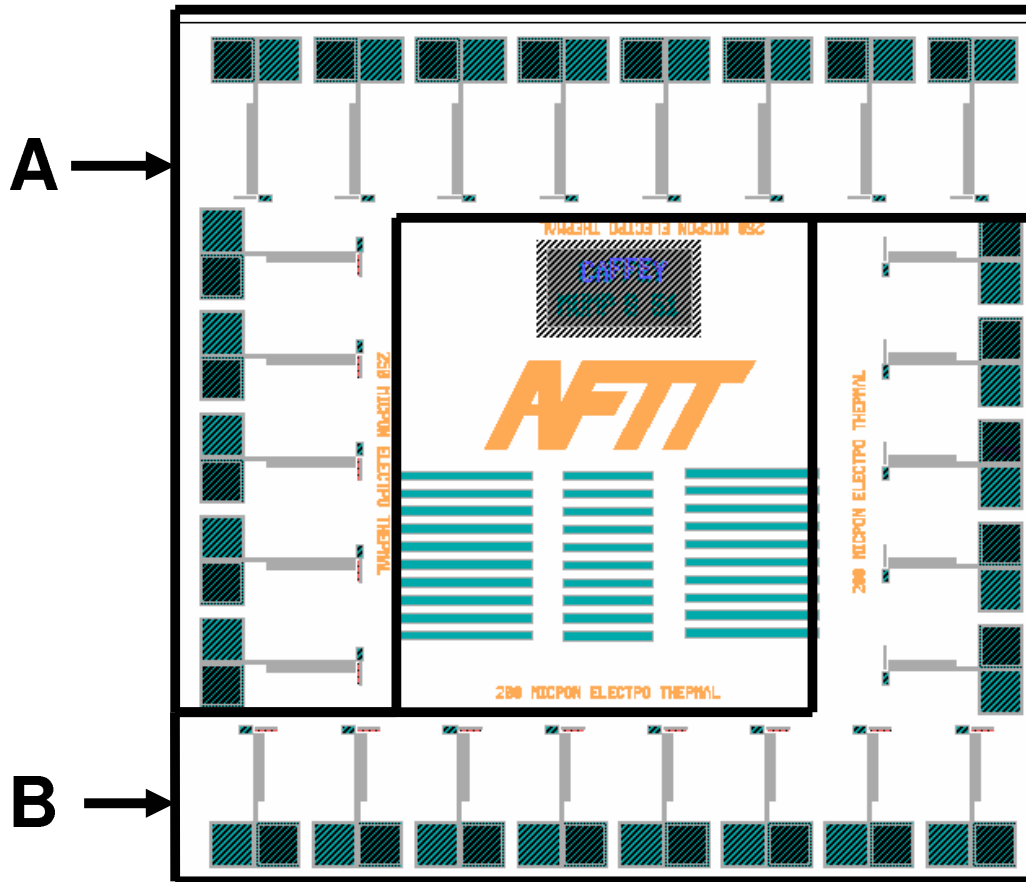


- A) 250  $\mu\text{m}$  poly2 Electrothermal Actuators with locking mechanism
- B) 20 x 200  $\mu\text{m}$  Residual Stress Cantilevers
- C) 20 x 300  $\mu\text{m}$  Residual Stress Cantilevers



### Chip E

The electrothermal actuators tested for this research were fabricated using this chip design. The 250  $\mu\text{m}$  actuators tested are labelled “A”.

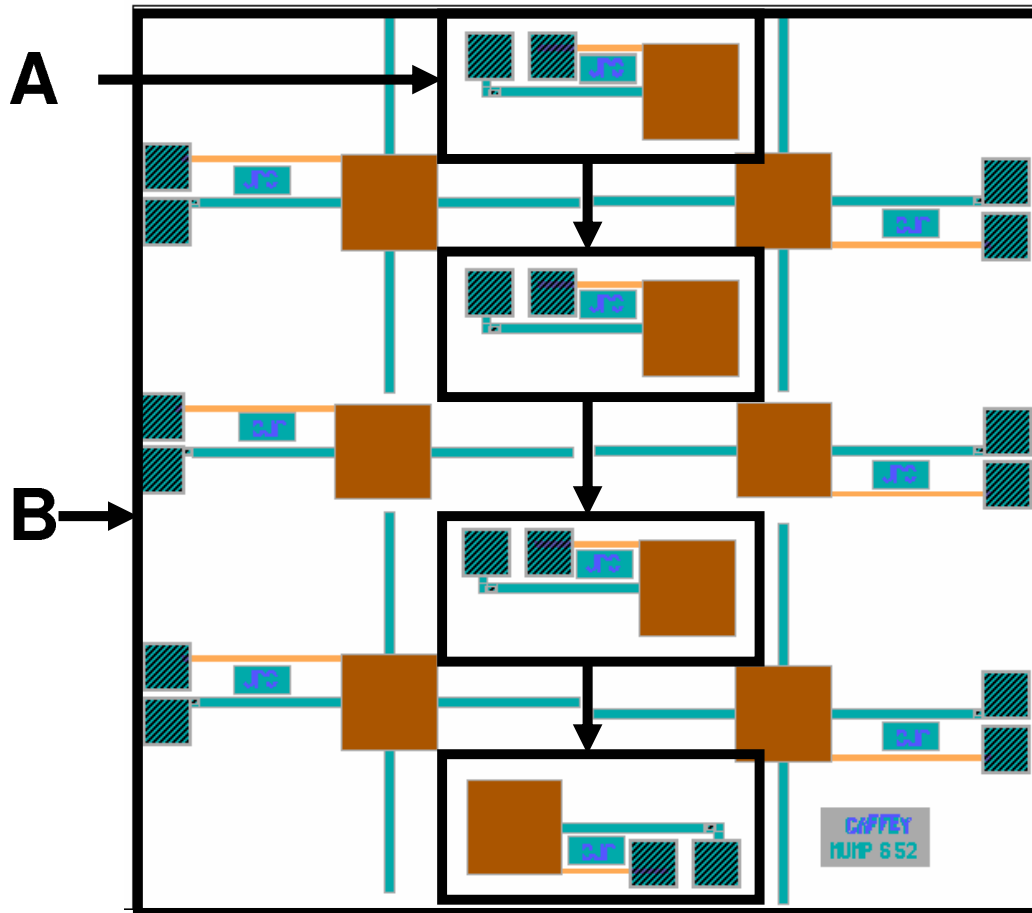


- A) 250  $\mu\text{m}$  poly2 Electrothermal Actuators
- B) 200  $\mu\text{m}$  poly2 Electrothermal Actuators

D.4 PolyMUMPs Run 52 Designs

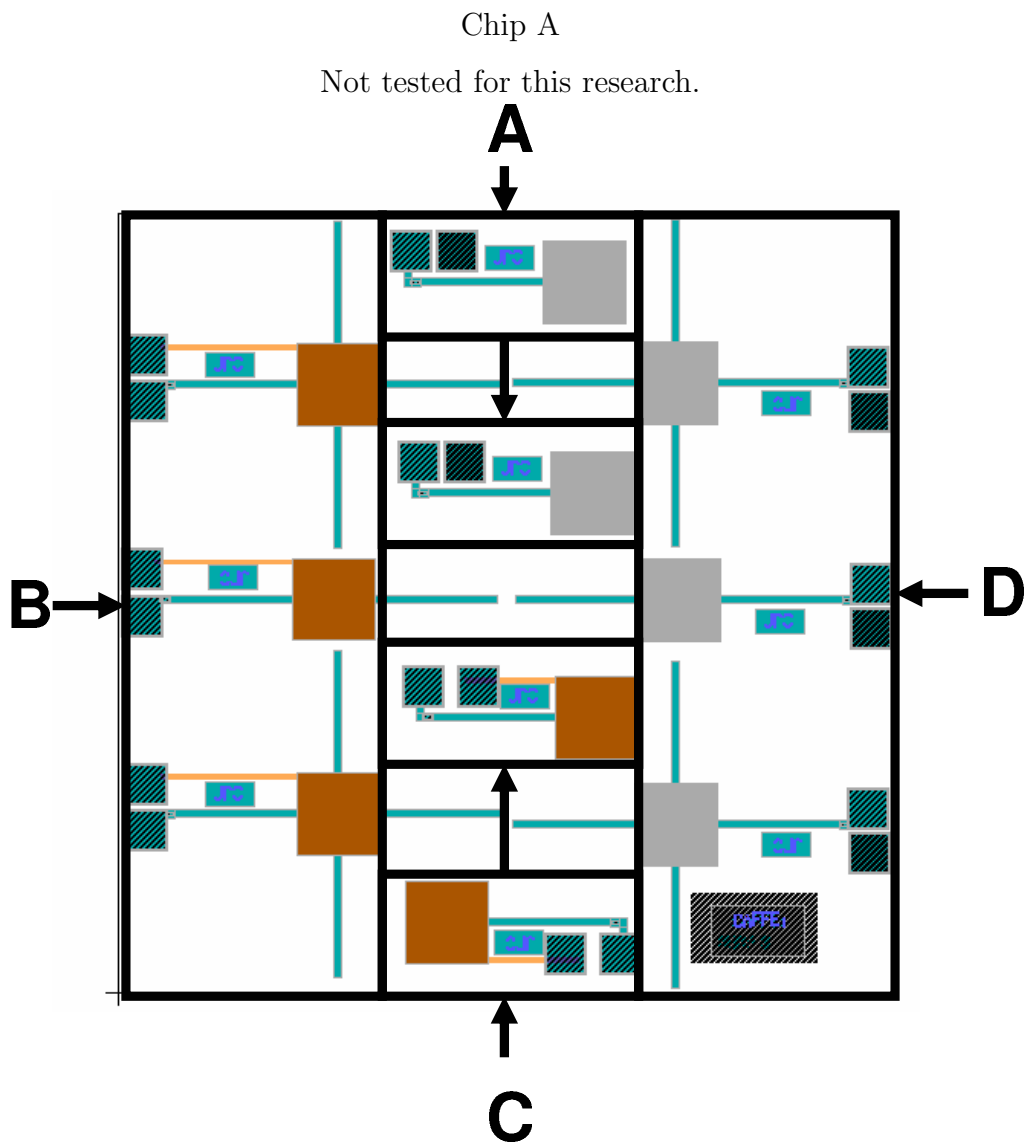
Chip A

Not tested for this research.



- A) 4 - 20 x 300  $\mu\text{m}$  Residual Stress Cantilevers with capacitive sensing
- B) 20 x 300  $\mu\text{m}$  Residual Stress Cantilevers with capacitive sensing

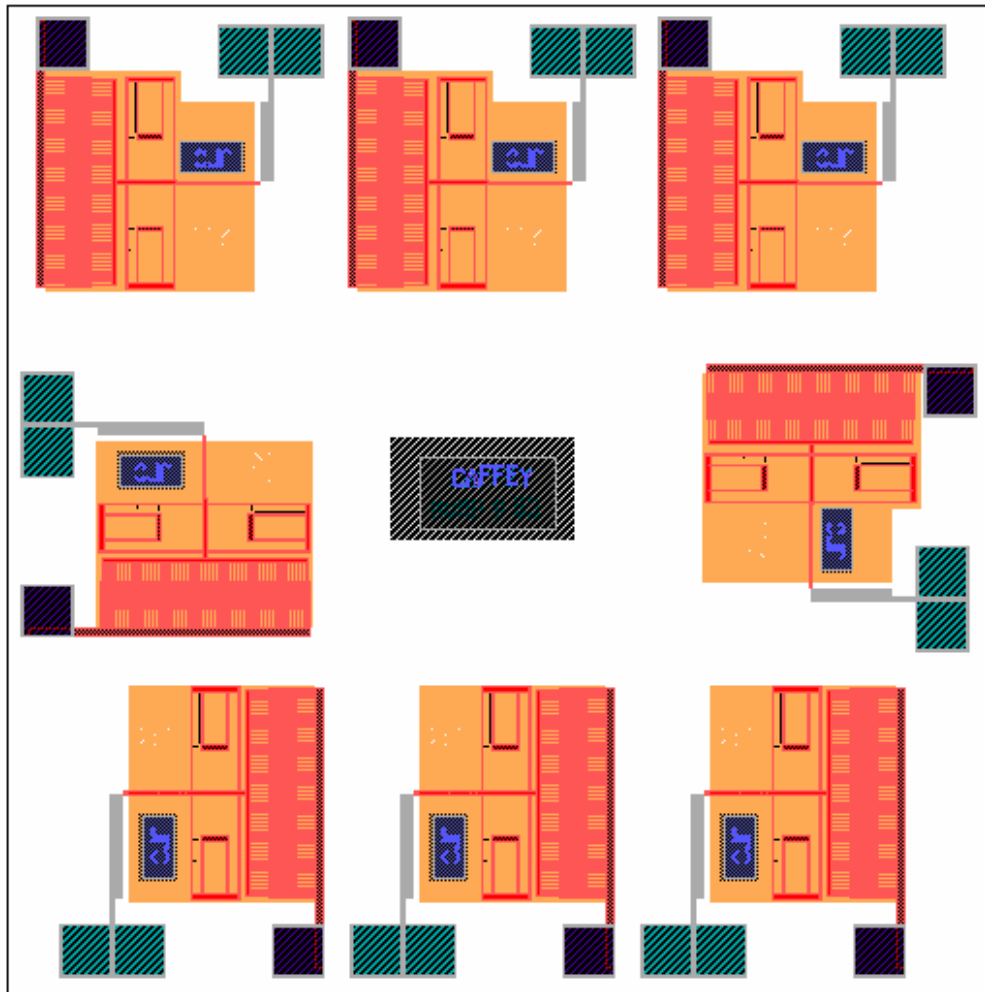
## D.5 PolyMUMPs Run 53 Designs



- A) 20 x 300  $\mu\text{m}$  Residual Stress Cantilevers with poly2-substrate capacitive sensing
- B) 4 – 20 x 300  $\mu\text{m}$  Residual Stress Cantilever with poly2-poly0 capacitive sensing
- C) 20 x 300  $\mu\text{m}$  Residual Stress Cantilevers with poly2-poly0 capacitive sensing
- D) 4 – 20 x 300  $\mu\text{m}$  Residual Stress Cantilever with poly2-substrate capacitive sensing
- E) 100 x 100  $\mu\text{m}$  poly1-poly2 Electrostatic Actuators

# Chip B

Not tested for this research.



250 mm poly2 Electrothermal Actuators with capacitive sensing  
shielded with poly0

REPORT DOCUMENTATION PAGE				Form Approved OMB No. 074-0188	
<p>The public reporting burden for this collection of information is estimated to average 1 hour per response, including the time for reviewing instructions, searching existing data sources, gathering and maintaining the data needed, and completing and reviewing the collection of information. Send comments regarding this burden estimate or any other aspect of the collection of information, including suggestions for reducing this burden to Department of Defense, Washington Headquarters Services, Directorate for Information Operations and Reports (0704-0188), 1215 Jefferson Davis Highway, Suite 1204, Arlington, VA 22202-4302. Respondents should be aware that notwithstanding any other provision of law, no person shall be subject to a penalty for failing to comply with a collection of information if it does not display a currently valid OMB control number.</p> <p><b>PLEASE DO NOT RETURN YOUR FORM TO THE ABOVE ADDRESS.</b></p>					
1. REPORT DATE (DD-MM-YYYY) 25-03-2002		2. REPORT TYPE Master's Thesis		3. DATES COVERED (From - To) Aug 2001 - Mar 2003	
4. TITLE AND SUBTITLE  THE EFFECTS OF IONIZING RADIATION ON MICROELECTROMECHANICAL SYSTEMS (MEMS) ACTUATORS: ELECTROSTATIC, ELECTROTHERMAL, AND RESIDUAL STRESS				5a. CONTRACT NUMBER	
				5b. GRANT NUMBER	
				5c. PROGRAM ELEMENT NUMBER	
6. AUTHOR(S)  Caffey, Jared, R., 2d Lieutenant, USAF				5d. PROJECT NUMBER ENR # 2002-025	
				5e. TASK NUMBER	
				5f. WORK UNIT NUMBER	
7. PERFORMING ORGANIZATION NAMES(S) AND ADDRESS(S) Air Force Institute of Technology Graduate School of Engineering and Management (AFIT/EN) 2950 Hobson Way, Building 640 WPAFB OH 45433-7765				8. PERFORMING ORGANIZATION REPORT NUMBER  AFIT/GE/ENG/03-05	
9. SPONSORING/MONITORING AGENCY NAME(S) AND ADDRESS(ES) AFRL/VSSSE Attn: Capt. Joseph W. Tringe 3550 Aberdeen Ave SE Kirtland AFB NM 87117-5776 DSN: 246-4049 e-mail: Joseph.Tringe@kirtland.af.mil				10. SPONSOR/MONITOR'S ACRONYM(S)	
				11. SPONSOR/MONITOR'S REPORT NUMBER(S)	
12. DISTRIBUTION/AVAILABILITY STATEMENT  APPROVED FOR PUBLIC RELEASE; DISTRIBUTION UNLIMITED.					
13. SUPPLEMENTARY NOTES					
14. ABSTRACT The effects of ionizing radiation on the operation of polysilicon microelectromechanical system (MEMS) electrostatic actuators, electrothermal actuators, and residual stress cantilevers were examined. Pre-irradiation, in-situ, and post-irradiation measurements were taken for the electrostatic and electrothermal actuators. The residual stress cantilevers were characterized before and after irradiation. All three devices were irradiated to a total ionizing dose of 1 megarad(Si) using both the Air Force Research Laboratory's low energy X-ray source and Co-60 gamma source. In both radiation environments, the electrostatic piston actuators exhibited a decrease in capacitance and thereby an increase in voltage per deflection. Both effects are attributed to dielectric charging phenomena. All devices irradiated under positive bias returned to pre-irradiation conditions within seven days of being irradiated. The electrothermal actuator operation was not affected by exposure to either type of ionizing radiation. The tip deflection measurements of the residual stress cantilevers showed a slight decrease between pre- and post characterization. The tip deflection of residual stress cantilevers irradiated with 50 keV X-rays, to 1 megarad(Si) total ionizing dose, decreased by less than 5 % from pre-irradiation measurements. Tip deflection of residual stress cantilevers irradiated with 1.25 MeV gamma rays, to 1 megarad(Si) total ionizing dose, decreased by less than 16.5 % of pre-irradiated measurements. No correlation was made between change in tip deflection and radiation dose.					
15. SUBJECT TERMS Microelectromechanical Systems, Micromachining, Actuators, Radiation Effects, Ionizing Radiation, Gamma rays, X rays, Residual Stress					
16. SECURITY CLASSIFICATION OF:			17. LIMITATION OF ABSTRACT	18. NUMBER OF PAGES	19a. NAME OF RESPONSIBLE PERSON
a. REPORT	b. ABSTRACT	c. THIS PAGE			Paul E. Kladitis, Capt, USAF (ENG)
U	U	U	UU	217	19b. TELEPHONE NUMBER (Include area code) (937) 255-3636, ext 4595; e-mail: Paul.Kladitis@afit.edu